

Avalanche statistics and single electron counting with a Timepix-InGrid detector

BY MICHAEL LUPBERGER

*28th of September 2010
Corrected Edition*

Diploma thesis

handed in and prepared at the Physikalisches Institut of the Albert-Ludwigs Universität
Freiburg



in cooperation with service de physique de particules (SPP) at the Commissariat à
l'énergie atomique et aux énergies alternatives (CEA) at Saclay



Diploma thesis Supervisors:

Dr. Paul Colas, CEA/Irfu/SPP

and

Prof. Markus Schumacher, Physikalisches Institut Universität Freiburg

Advisors:

Dr. David Attié, CEA/Irfu/Sedi

and

Uwe Renz, Physikalisches Institut Universität Freiburg

Statistique des avalanches et comptage des électrons avec un détecteur Timepix-InGrid

PAR MICHAEL LUPBERGER

28 septembre 2010

Édition corrigée

Thèse de diplôme

soutenue et préparée au Physikalisches Institut de l'Albert-Ludwigs Universität Freiburg



en cotutelle avec le service de physique de particules (SPP) au Commissariat à l'énergie atomique et aux énergies alternatives (CEA) à Saclay



Directeurs de thèse de diplôme
Dr. Paul Colas, CEA/Irfu/SPP
et

Prof. Markus Schumacher, Physikalisches Institut Universität Freiburg

Responsables:
Dr. David Attié, CEA/Irfu/Sedi
et

Uwe Renz, Physikalisches Institut Universität Freiburg

Lawinenstatistik und Einzelelektronenzählung mit einem Timepix-Ingrid Detektor

VON MICHAEL LUPBERGER

*28. September 2010
Korrigierte Ausgabe*

Diplomarbeit

vorgelegt und erstellt am Physikalischen Institut der Albert-Ludwigs Universität Freiburg



in Zusammenarbeit mit dem Service de physique de particules (SPP) am Commissariat à l'énergie atomique et aux énergies alternatives (CEA) in Saclay



Betreuung der Diplomarbeit:
Dr. Paul Colas, CEA/Irfu/SPP
und
Prof. Markus Schumacher, Physikalisches Institut Universität Freiburg

Betreuer:
Dr. David Attié, CEA/Irfu/Sedi
und
Uwe Renz, Physikalisches Institut Universität Freiburg

Table of contents

1 Introduction	1
1.1 Context of this thesis	1
1.1.1 Detector development	1
1.1.2 The International Linear Collider	2
ILC baseline	2
ILC detectors	3
1.2 Gaseous Tracking Detectors	4
1.2.1 Wire tubes	4
1.2.2 Multi-Wire Proportional Chambers	5
1.2.3 Time Projection Chambers	6
1.2.4 Micro Pattern Gas Detectors	10
2 Interaction of particles with matter	11
2.1 Particle interaction with gas	11
2.1.1 Charged particles	12
2.1.2 Photons	15
Photo effect	15
Compton effect	16
Pair production	16
2.1.3 Fano factor	16
2.1.4 Drift	17
2.1.5 Diffusion	18
2.2 Amplification process	19
Ion backflow	19
2.2.1 Townsend coefficient	19
2.2.2 UV photons	20
2.2.3 Penning effect	20
2.2.4 Avalanche statistics	21
2.2.5 Polya distribution	21
2.3 ^{55}Fe -spectrum	22
2.3.1 Argon based mixtures	22
2.3.2 Other gas mixtures	23
3 Experimental setup	24
3.1 Pixel readout	24
3.1.1 Medipix2	24
3.1.2 Timepix	25
3.1.3 Threshold equalisation	27
3.1.4 InGrid	28
3.2 Detector	32
3.2.1 Saclay gas box	32
3.2.2 Freiburg gas box	35
3.3 MUROS Readout	35
3.3.1 Test pulses	36
3.3.2 Threshold calibration	36
3.3.3 TOT calibration	38
3.4 Laser test bench	39
4 Measurements and results	42
4.1 Data acquisition and analysis	43

4.1.1	Data acquisition	43
4.1.2	Data analysis and cuts	44
	Photon separation	44
	RMSratio cut	44
	Centre cut	45
	RMS cut	46
	Clustering	47
4.2	Primary electron counting	48
4.2.1	Remark to the measured ^{55}Fe spectrum for the primary electron counting	49
4.2.2	Field ratio	57
4.2.3	Gas flux	59
4.2.4	Single Electron detection efficiency	59
4.2.5	Number of primary electrons in ArIso 80/20	62
4.2.6	Peak resolution and Fano factor	63
4.3	Charge measurements	64
4.3.1	Ingrid gain measurements	65
4.3.2	Micromegas gain measurements	71
4.4	Theory of the Influence of SiProt on gas amplification in an InGrid setup	74
4.5	Measurements of the time constant of SiProt	79
4.5.1	Measurements of the time constant	79
4.5.2	Low frequency gain measurements	80
4.5.3	Low frequency Θ measurements	82
4.5.4	Single electron detection efficiency	83
4.5.5	LASER test bench measurements	84
5	An eight chip panel for the large LC TPC prototype	92
5.1	The LC TPC prototype	92
5.2	Octopuce	94
5.3	Detector tests	96
6	Summary and outlook	97
6.1	Summary	97
6.1.1	Avalanche statistics	98
6.1.2	Single electron counting	98
6.2	Outlook	99
6.3	Résumé	99
6.3.1	Statistique des avalanches	100
6.3.2	Comptage des électrons	101
6.4	Perspective	101
6.5	Zusammenfassung	102
6.5.1	Lawinenstatistik	103
6.5.2	Einzelelektronenzählung	104
6.6	Ausblick	104
	Bibliography	106
	Appendix A Primary electrons in the photo peak	108
	Appendix B Long term measurements and temperature effects	111
	Appendix C SiProt influence on electric field without avalanches	112
	Appendix D Measurement summary table	113
	Acknowledgement	116
	Declaration	119

1 Introduction

Chapter one is an introduction to the diploma thesis (herein called thesis). In the first section of this chapter the content of this thesis will be set in context with the research in particle physics. The second section will briefly illustrate some milestones in the history of the particle detector development.

1.1 Context of this thesis

This thesis pertains to the field of particle physics and more precisely to the development of future detectors for high energy particle physics experiments. At present the *Large Hadron Collider* (LHC) at the *Conseil Européen pour la Recherche Nucléaire* (CERN) with its experiments is the outstanding accelerator in particle physics. The LHC project was approved by the CERN council in December 1994 and in October 1995 the technical design report was published, though the planning of the accelerator machine and the experiments and detectors started even 16 years before. Presently the LHC is in operation with the first collisions being performed in March 2010. The focus of detector development is to make improvements of the LHC experiments (super LHC) and future accelerator projects. One of these, the *International Linear Collider* ILC, will briefly be presented in this section. The topic of this thesis will be set in context with detector development.

1.1.1 Detector development

Since the discovery of the first elementary particle, detectors were built to prove their existence and measure their properties. The interaction of a particle with the detector material leaves a fingerprint to identify the particle. This identification can sometimes be ambiguous. Sometimes more than one detector is necessary or even large detector systems are needed to get enough information to tell which particle just passed and its momentum. Figure 1 shows four layers of different detectors and the fingerprints which several particles leave in the detector system. The first layer is a tracking detector where charged particles will leave a signal. The *electromagnetic calorimeter* (ECAL) is built to obtain the energy of electromagnetically interacting particles. The same is done for particles interacting via the strong force in the *hadronic calorimeter* (HCAL). Muons penetrate all these layers and will then leave a trace in the muon detectors in the outermost layer. Usually there is an additional layer called the vertex detector included in the tracker to detect the interaction point. As an example the *international large detector concept* (ILD) for the ILC is shown in Figure 3.

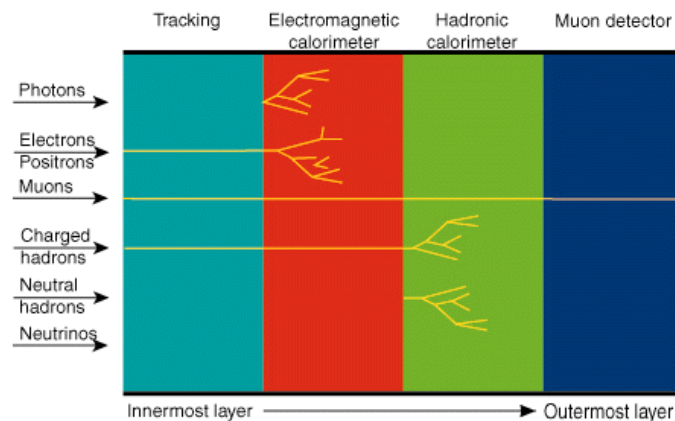


Figure 1. Detector layer interactions with different particle types, from [Phy]

There are different technologies for each sub detector and the improvement upon current technologies is an ongoing process. This thesis will mainly focus on tracking detectors. Upon the last few years gaseous detectors have become of interest again. The combination of new technologies with old ideas has led to inventions such as that of *Micro Pattern Gas Detectors* (MPGD) or the *Integrated Grid* (InGrid). It should be noted that the technology discussed here can also be applied to other sub detectors. There are, for example, efforts in constructing a gaseous vertex detector (GOSSIP [Cam06]) or a hadronic calorimeter using Micromegas as readout [Adl08]. The research of this thesis is supported by the EUDET project. This thesis is related to the research and development project RD51 on MPGDs.

1.1.2 The International Linear Collider

The LHC is often called a discovery machine. Its aim is in particular to find and study the Higgs boson and new physics¹ at the tera electron volt energy scale. A linear collider would increase the understanding as well as be able to precisely measure properties of new particles. Even if the Higgs boson can not be found with the LHC, a linear collider would be able to find hints of new physics of an alternate theory. One machine being designed is the *International Linear Collider* (ILC) [Lin]. In order to achieve highly precise measurements, the requirements for the ILC accelerator and detectors are ambitious and specified in the reference design report (RDR [Bra07]).

ILC baseline The ILC is an electron-positron collider with an initial centre of mass (CM) energy of 500 GeV using superconducting radio frequency accelerating cavities. After the extension of the baseline, an energy of 1 TeV can be reached. It should arrive at a total luminosity of 500fb^{-1} within the first four years of operation. The polarisation of the electron beam must be better than 80%. The ILC consists of two linear accelerators as show in Figure 2. The whole length of the first construction stage is 31km and can be extended to 42km for the second stage. The design luminosity at 500 GeV is $2 \times 10^{34} \text{ cm}^{-2} \text{ s}^{-1}$. Table 1 shows the basic design parameters for the ILC. The beam is structured as pulses with a rate of 5Hz and each pulse consists of 1000–5400 bunches with 10^{10} particles per bunch. The bunch separation is 337ns or 100 m. Still after the RDR has been published these parameters are adopted slightly.

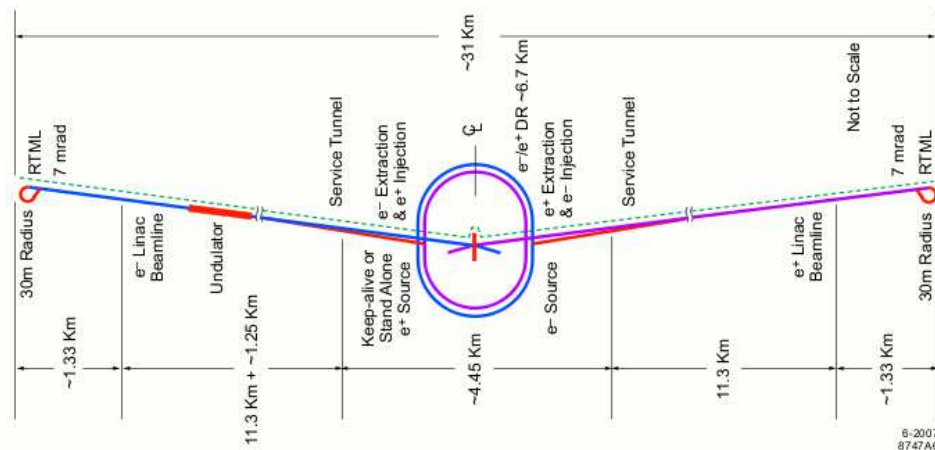


Figure 2. Schematic of the ILC baseline for a energy of 500 GeV CM, from [Bra07]

1. The current standard model of particle physics would become inconsistent without a Higgs boson at a certain energy of the order of 1 TeV. Theories have been developed and included to the standard model to save it in the high energy regime. New particles are predicted for example by the supersymmetry theory which should be found with the LHC.

<i>Parameter</i>	<i>Unit</i>	<i>Value</i>
CM energy range	GeV	200–500
Peak luminosity*	$\text{cm}^{-2} \text{s}^{-1}$	2×10^{34}
Average beam current in pulse	mA	9.0
Pulse rate	Hz	5.0
Pulse length (beam)	ms	~ 1
Number of bunches per pulse		1000–5400
Bunch separation	ns	337
Charge per bunch	nC	1.6–3.2
Accelerating gradient*	MV/m	31.5
RF pulse length	ms	1.6
Beam power (per beam)*	MW	10.8
Typical beam size at interaction point* ($h \times v$)	nm	640×5.7
Total AC power consumption*	MW	230

Table 1. Basic design parameters for the ILC, from [Bra07] *: for 500 GeV CM energy

ILC detectors The RDR proposes four different detector concepts. The two² most promising and furthest developed concepts are the *Silicon Detector* (SiD) and the *International Large Detector* (ILD). The focus will be put on the ILD as it uses a gaseous central tracking device, while the SiD uses a pure silicon tracker. Figure 3 shows a schematic of the detector. The four layers explained in section 1.1.1 are clearly visible. The vertex detector is realised with five layers of silicon strip and pixel detectors. The tracker (yellow) is a large volume *Time Projection Chamber* (TPC) that will be explained in section 1.2.3. For a typical track it will record up to 200 three dimensional space points with a point-resolution better than $100 \mu\text{m}$ in the $r - \phi$ plane. The ECAL (blue) and HCAL (green) are the next layers. Then a super-conduction 4 Tesla magnet coil and a cryostat system follow. The muon detectors are embedded in the iron yoke (brown).

Detector requirements are:

- For the vertex detector a precision of $\sigma_{r\phi,z}(\text{IP}) \leq 5 \mu\text{m} \oplus \frac{10 \mu\text{m GeV}/c}{p \sin^{3/2}\theta}$ to detect secondary vertices and tag the quarks in processes like $HZ, H \rightarrow b\bar{b}, c\bar{c}, gg$ or $b\bar{b}$ quark asymmetries.
- For the tracker a resolution of the transverse momentum of $\sigma\left(\frac{1}{p_t}\right) \leq 5 \times 10^{-5} \left(\frac{\text{GeV}}{c}\right)^{-1}$ to measure for example the Higgs recoil mass in the process $e^+ e^- \rightarrow ZH \rightarrow l^+ l^- X$ or supersymmetry (SUSY) particle masses like in the decay of the supersymmetric partner of the muon.
- For the calorimeters a jet energy resolution of $\frac{\sigma_E}{E} \simeq 0.3 \frac{1}{\sqrt{E(\text{GeV})}}$ to measure missing energy in multi jet events like ZHH (Triple Higgs coupling), $HZ \rightarrow q \bar{q} b \bar{b}$ (Higgs mass) or $ZH \rightarrow ZWW^*$ (branching ratio).
- Hermiticity down to $\theta = 5 \text{ mrad}$ to detect missing energy signatures in SUSY.

². There is only one collision point with this accelerator. A cavern for two detectors would contain a rail to move the two detectors, one in a parking position, the other at the interaction point.

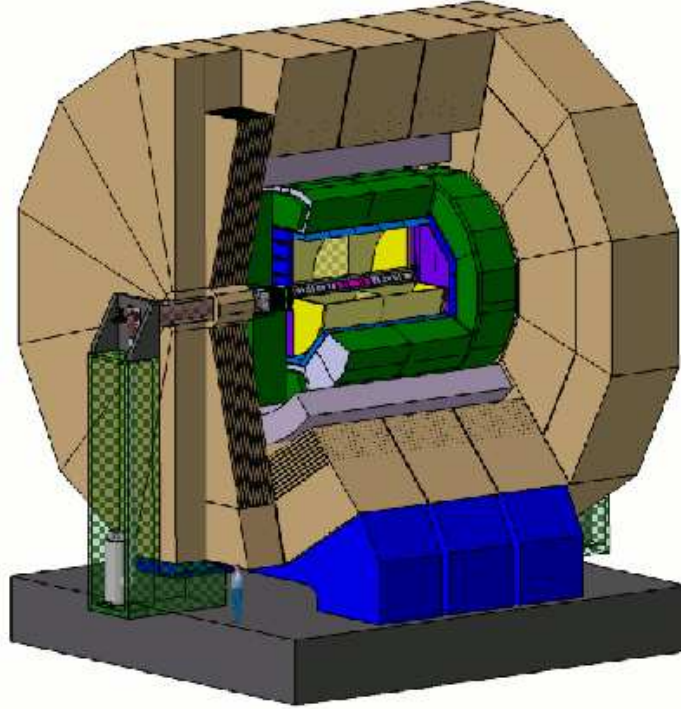


Figure 3. Schematic of ILD, the International Large Detector concept, from the ILD collaboration [ILD09]

1.2 Gaseous Tracking Detectors

Since the end of the 1970s gas based detectors have played an important role in the detection and reconstruction of particle tracks. The invention of the *Multi Wire Proportional Chamber* (MWPC, [Cha68]) by Georges Charpak in 1968 at CERN (Nobel Price 1992) triggered the replacement of the photographic technology that was used, for example, in bubble and spark chambers.

All gaseous detectors are based on the same principle which will be explained in detail in section 2.1. High energy charged particles ionise molecules in the gas (primary ionisation). Electric fields are used to separate ionised atoms and electrons (primary electrons). However the signal from the primary particles is, in most cases, too small to be detected directly. For that reason an amplification of the primary charge is necessary. Charged particles are accelerated in an electric field. They will gain enough energy to ionise other gas molecules (secondary ionisation) and, if the field is strong enough, an avalanche is created.

Tracking detectors are used to measure the momentum p of charged particles. This is usually done by measuring the radius r of the curvature of the track in a magnetic field B :

$$p = qBr \text{ or } p[\text{GeV}/c] = 0.3B[T] \cdot r[m] \quad (1)$$

In this section, the development of gaseous particle trackers will be presented. There are other technologies using liquids (e.g. bubble chambers) or solids (e.g. silicon trackers) which will not be discussed in this thesis.

1.2.1 Wire tubes

A wire tube is a cylinder of metal filled with gas and a wire stretched along its symmetry axis. The wire

is held at a positive potential with respect to the cylinder wall and is connected to readout electronics. The equipotential surfaces have a cylindrical shape for an infinitely long tube. The equations for the electric field $E(r)$ and the potential $V(r)$ are given by

$$E(r) = \frac{U_0}{r \ln \frac{R_1}{R_2}} \text{ and } V(r) = \frac{U_0 \ln(r)}{\ln \frac{R_1}{R_2}}, \quad (2)$$

where U_0 is the potential of the wire compared to the grounded cylinder barrel, R_1 is the inner radius of the barrel, R_2 is the wire radius and $R_1 < r < R_2$. The field increases close to the wire and the amplification can be strong in this region.

Figure 4 shows the different modes the detectors can be operated in. If the voltage is very low, the electric field is not strong enough to separate the charge in most of the cylinder volume and the electrons and ionised atoms will recombine. In the region of a moderate voltage, all the primary charges will be collected but no amplification will occur (ionisation chamber). If the voltage is higher, the amplification process will start. In the region of proportional counters the amplified charge is proportional to the primary charge. If the voltage is raised further, this is not the case anymore. Finally, every primary ionisation will lead to a discharge of the wire tube (Geiger counter). At voltages higher than the breakdown voltage of the gas the wire tube will start to spark.

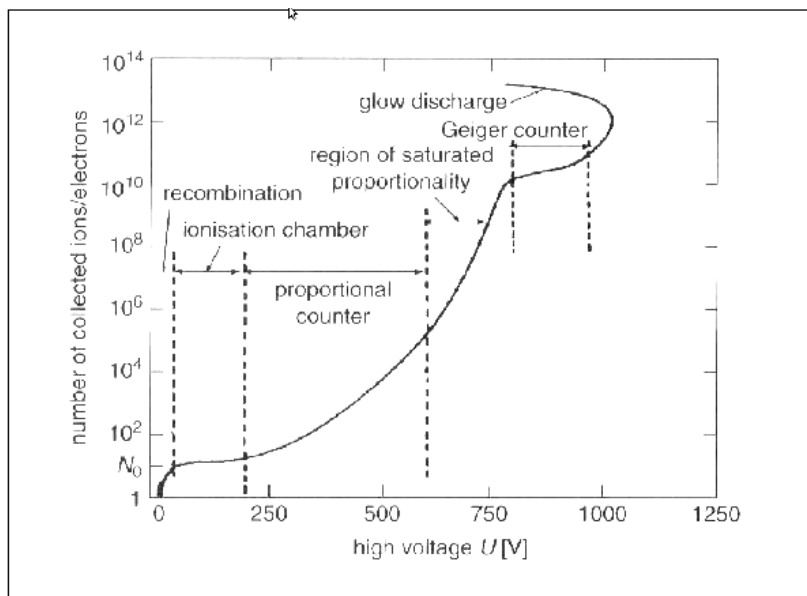


Figure 4. Different operation modes for a wire tube [GS08]

When several wire tubes are combined to arrays, tracks of charged particles can be detected as, for example, in the ATLAS muon spectrometer.

1.2.2 Multi-Wire Proportional Chambers

A *Multi-Wire Proportional Chamber* (MWPC) consists of two parallel plates at ground potential. Between the plates several wires at a positive potential are stretched along the x -axis with equal distance p in y -direction. The high voltage is set such that the chamber works in the proportional mode. Typical dimensions are a gap size of $d = 6$ mm and a spacing between the wires of $p = 2$ mm. The chambers are built to detect particles traversing perpendicular to the plane of the plates along the z -axis. A charged

particle produces a signal on the closest wire. Putting two chambers on top of each other, when the wires are orthogonal with respect to the wires in the other chamber, allows the reconstruction of the x and y position of the track. Another method, where just one chamber is necessary, is to separate the ground cathodes into segments perpendicular to the wires and read out the signal induced by the ions drifting towards the plates.

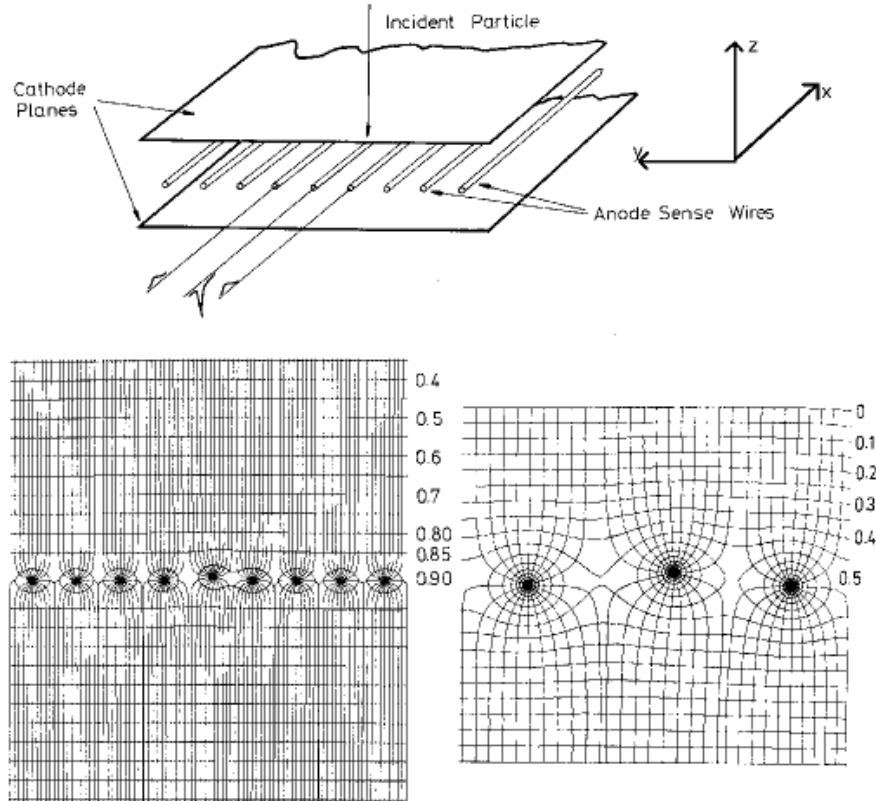


Figure 5. Schematic of a MWPC (top), and field lines with potential. Wires on potential 1, walls on potential 0 (bottom), from [CRS70]

A chamber making use of the drift time of the primary charge is called a **drift chamber**. The signals coming from the wires and plates can be used to get an even more precise position of the track. For different field geometries there is always a relation between drift distance and time of drift. Measuring the charge and the time of arrival of the signals on different wires allows a precision even better than $p/\sqrt{12}$ in y -direction and $d/\sqrt{12}$ in z -direction.

1.2.3 Time Projection Chambers

The Time Projection Chamber (TPC) was invented by David R. Nygren in 1975 [Nyg75]. The concept of a TPC is still up to date and is used as a tracking system, for example, at the ALICE experiment at the LHC or the STAR experiment at RHIC (Brookhaven). In Figure 6 the concept of a TPC is shown. It consists of a cylinder separated into two drift regions by a cathode. On each side there is an anode end plate equipped with MWPC where the amplification process and readout takes place. Inside the TPC there is another cylinder which hosts the beam line, the inner detector and the interaction point of the colliding beams. Charged particles coming from the interaction point will ionise the gas along their tracks through the drift volume. Electrons are separated from ions. The electrons will drift towards the end plate, are

amplified and a two-dimensional image of the track is recorded with the resolution of the MWPC. The third dimension of the track points is obtained by measuring the arrival time at the end-plate. As the TPC covers almost the whole volume around the interaction point it is said to be a 4π -detector.

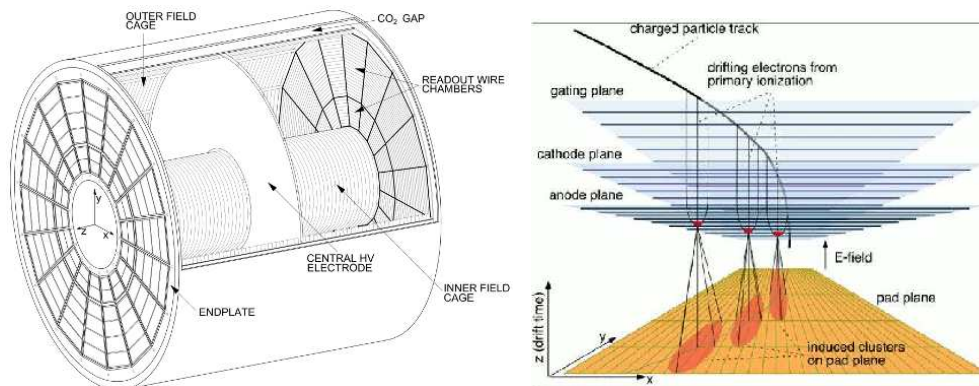


Figure 6. Schematic of a TPC (left), operation principle of a TPC (right), from the ALICE collaboration

To provide uniform drift times for all regions of the TPC, it is necessary that the electric field be homogeneous. For this reason a field cage (or better a voltage degrader) is included in the TPC. The inner wall of the cylinder consists of ring segments which are set to the right potential. As a TPC is used to measure the momentum of charged particles the magnetic field B is set parallel³ to the electric field E (Figure 6, left). In this setup the transverse diffusion of the primary charge on its way to the end-plate is strongly reduced, see section 2.1.5. Still the transverse diffusion is limiting the $r - \varphi$ resolution of the primary ionisation point. In argon for example, electrons coming from one point would be distributed with a root mean square (rms) of $200\ \mu\text{m}$ after a drift distance of 2mm. Limitations coming from the MWPC like pad size and wire pitch are less important. For the resolution in z direction the longitudinal diffusion is the limiting factor. As the interaction material is a gas, the radiation length of this tracking detector is very small. Including walls and the end-plate it is of the order of one radiation length X_0 . Other sub detectors, especially the calorimeters, can benefit from this feature and a more precise energy measurement is possible.

Ions created in the gas amplification and not attracted by the pads can leave the amplification region and disturb the field inside the drift volume (*ion backflow*). In MWPC based TPCs an additional wire plane called *gating grid* is installed to prevent ions getting into the drift volume. It can be switched off in order to let pass primary electrons. In Figure 8, the drift field maps with closed and open gating grid are shown. For a TPC using a gating grid it is necessary that there be enough time between two collisions to close the gate and collect the ions. For the ILC experiment the time between the collision of two bunches is far too small to collect the ions before the next bunches collide. We can see from Figure 7 that typical drift velocities of ions are of the order of $10\ \text{cm}/10^{-4}\text{s}$. 1000 – 5400 bunches will collide within 1ms. The gating grid can not be closed between the collision of two bunch trains as the pulse rate is 5Hz (200ms bunch train separation). An ion disc from the collisions of one bunch train has a width of $\approx 1\text{cm}$ and can drift $\approx 200\text{cm}$ towards the cathode before the next bunch train is injected. A gating grid at the right position in front of the amplification structure can prevent the ions from entering the drift volume. The signals coming from the events of one bunch train are added up in the readout (pile up). Since the end of the 90s, technologies with low ion backflow have been developed and will be presented in section 1.2.4. At high rates ions can also disturb the field inside the amplification region. For example in a MWPC it takes a time of the order of $100\ \mu\text{s}$ for the ions to reach a cathode. During this time the positive space charge lowers the gas gain. Figure 9 shows the gain drop in depend-

3. There are different TPC setups. In some experiments the magnetic field is set perpendicular to the electric field

ence of the rate. A copper target X -ray tube was used to generate a primary particle flux [Gar05]. A uniform gain can be used for particle identification on the basis of ionisation per track length.

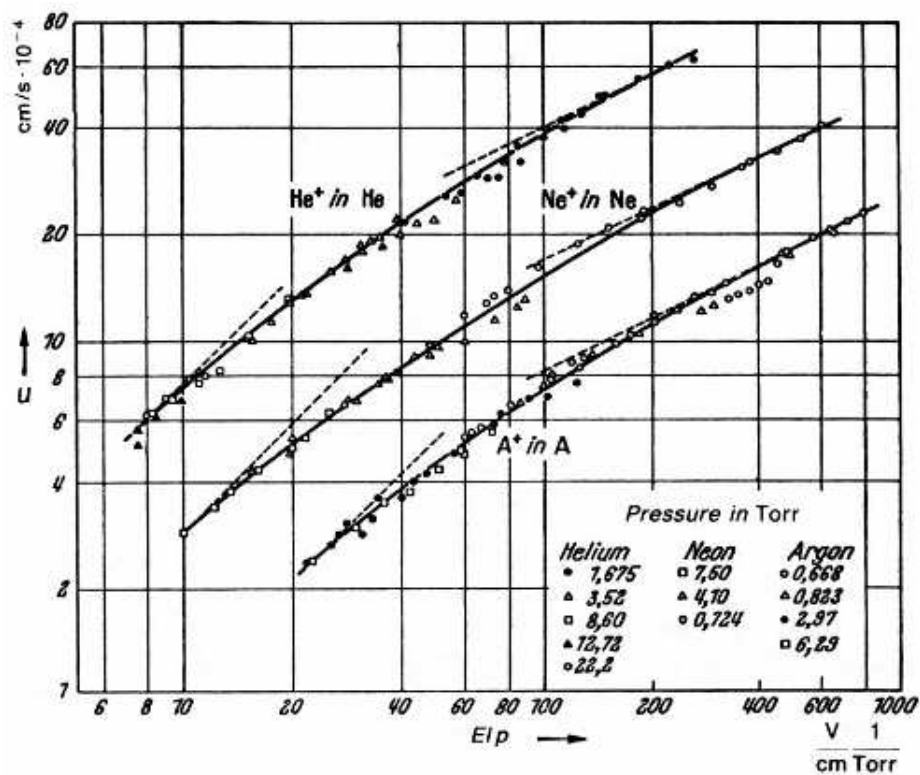


Figure 7. Drift velocity u of positive noble gas ions in their own gas as function of the reduced electric field, from [BR93]

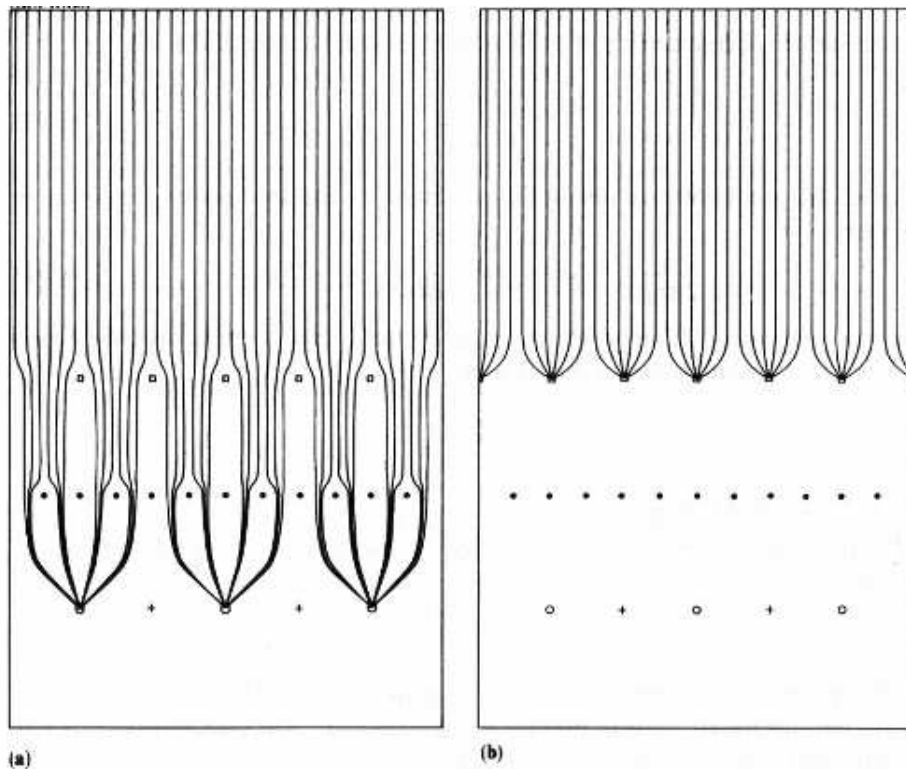


Figure 8. Drift field lines in a standard wire grid detector (see [BR93], Ch. 3.3). The field lines between the sense wires and the other electrodes have been omitted for clarity. *Squares*: gating grid; *black circles*: zero-grid; *open circles*: sense wires; *crosses*: field wires, (a): gating grid open (maximal transparency), (b): gating grid closed, from [BR93]

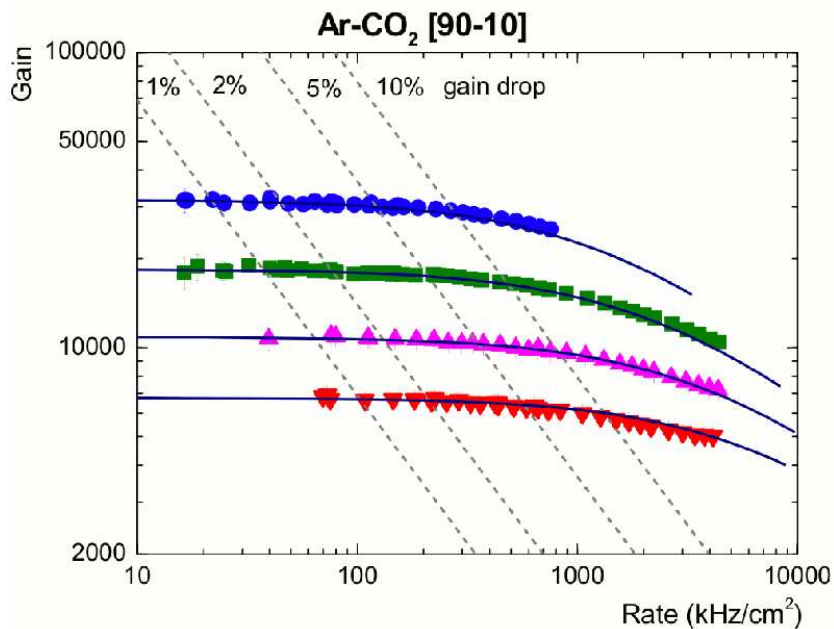


Figure 9. Rate per unit area dependence of the gas gain of a MWPC with a 2mm wire pitch and a gas thickness of 6mm. Primary particles are created at a copper plate with a X-ray tube. Curves referring to different wire voltages. Higher voltages are related to higher gain.[Gar05]

1.2.4 Micro Pattern Gas Detectors

Higher rates and the need for better resolution led to the invention of new concepts. In 1988, the first concept of a micro pattern gas detector (MPGD) was presented by Oed [Oed88]. This detector, a *Micro Strip Gas Counter* (MSGC) consists of an empty region between the cathode and the anode. In general MPGD have a segmented anode with electrodes of the order of $100\ \mu\text{m}$. In the case of the MSGC the anode consists of alternating anode and cathode strips printed on a glass plate. The strips are separated by some tens of microns of insulating material. A field map is shown in Figure 10. The field is homogeneous in most of the drift region. The amplification takes place shortly before the primary particles are focused to the anode. Ions created in the avalanche will quickly be pulled to the neighbouring cathode strips which are close by.

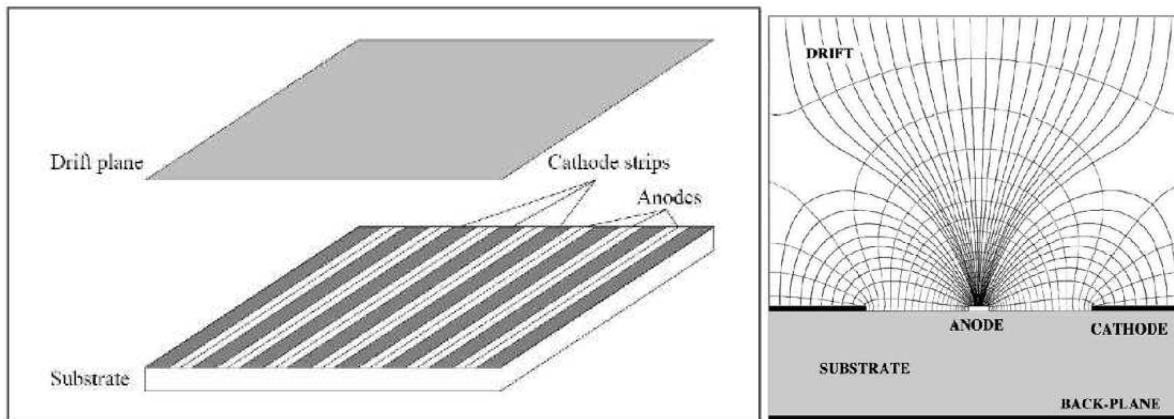


Figure 10. Setup of a MSGC (left) and field map of segmented readout structure (right), from [Che09]

Spatial resolutions of down to $30\ \mu\text{m}$ are reported [Ang90]. However a disadvantage of this detector are shortcuts between cathode and anode strips. After irradiation the isolation will charge up and lead to discharges that can possibly melt the strips.

The *Micro Mesh Gaseous Detector* (Micromegas) was invented by Giomataris et al. in 1995 [Gio96]. With this concept the gas volume is separated into a drift and an amplification region by a metal grid that is set to a potential of the order of $400\ \text{V}$ with respect to the readout anode. The electric field in the drift region is of the order of $1\ \text{kV/cm}$, while it is around $80\ \text{kV/cm}$ in the amplification region with a gap size of $10 - 100\ \mu\text{m}$. Both fields are almost uniform except for the region near the grid holes and the read out structure depending on its segmentation. The design of the anode plate is independent of the amplification structure. Unsegmented anodes, strips, pads or even pixels can be used as readout.

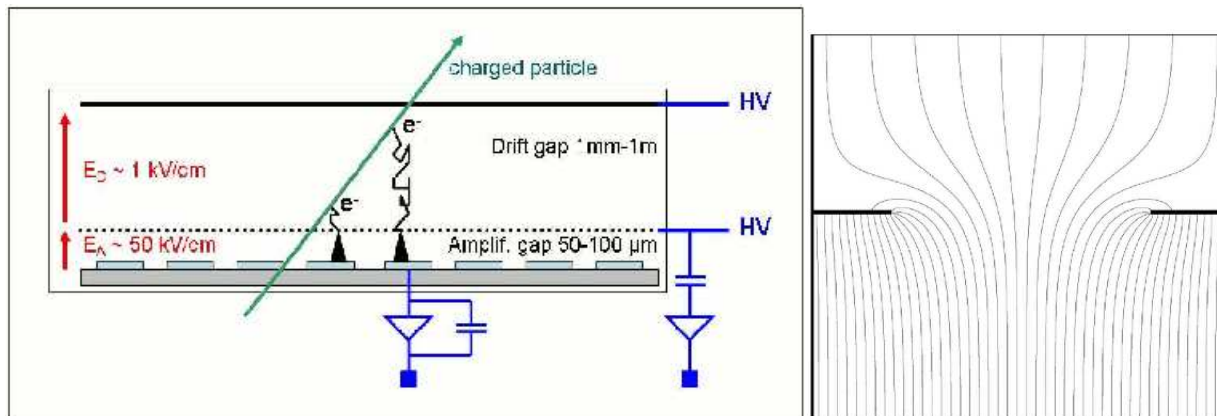


Figure 11. Setup of a Micromegas (left) and field map of grid holes (right), from [Che09].

Due to the compression of the field lines from the drift region at the grid the transmission of the electrons to the amplification region is higher than 99%. The amplification process happens in about 1ns and the ion backflow in about 30 – 100ns. Experiments where Micromegas detectors are used are, for example, COMPASS and CAST at CERN or the T2K experiment in Japan.

Another concept is the *Gas Electron Multiplier* (GEM). It was invented in 1996 by Sauli [Sau97] at CERN. A GEM foil is a $50\ \mu\text{m}$ thick Kapton® layer with $5\ \mu\text{m}$ of copper on both sides. Holes are etched into the foil with a radius of $70\ \mu\text{m}$ at the surface and $55\ \mu\text{m}$ in the centre as shown in Figure 12. The optical transparency is of the order of 20%. A high voltage of roughly 400V is applied between the top and the bottom of the GEM foil and amplification can take place in the holes. Ions drifting back are mainly pulled to the upper surface of the foil. The amplification of a single GEM foil is in most of the cases not sufficient. Several GEM foils are placed on top of each other with transfer fields in between. Because of diffusion the signal coming from one primary electron is smeared over several holes. A segmented readout anode can be used to get a precise position of the primary ionisation by the *centre of gravity method*. Detectors using GEMs are used for example at COMPASS, LHCb or TOTEM at CERN.

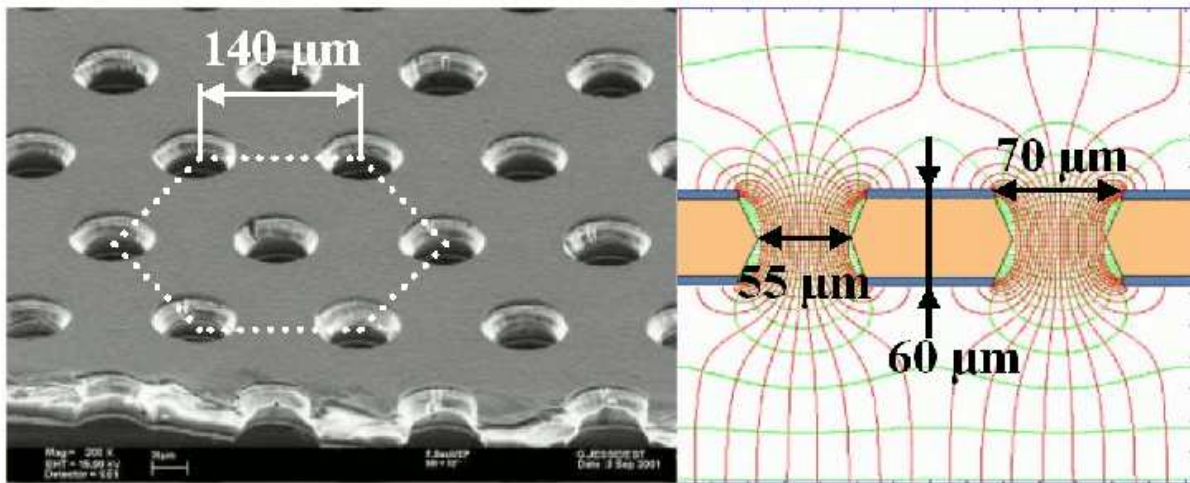


Figure 12. Microscope image of a GEM foil (left) and field map of foil holes (right), from [Ren07].

2 Interaction of particles with matter

This chapter will summarise the physics of the processes relevant to this thesis. The first section will concentrate on the interaction of particles with a gas. The second section will introduce the amplification process in a gas which is necessary to obtain a measurable signal of the primary interaction process. Finally the third section will explain the production of primary electrons in argon based mixtures which were mainly used and other gases also used in the experiments.

2.1 Particle interaction with gas

In this section the processes of interaction of a particle entering the detection gas will be explained. The particles will interact with the molecules of the gas mainly via the electromagnetic force which is at least

one order of magnitude stronger than the other forces⁴. The six processes a particle can undergo in gas are:

- elastic scattering with the electrons of the gas atoms.
- excitation or ionisation of gas atoms.
- deflection of charged particles in the coulomb field of the nucleus and emission of bremsstrahlung.
- elastic scattering and recoil of the nucleus (mainly interesting for neutron detection).
- inelastic scattering with the nucleus leading to an excitation and emission of γ -quanta.
- emission of Cerenkov light when the particle is faster than the speed of light in the medium.

2.1.1 Charged particles

A charged particle entering a gas will lose its energy by interactions with the gas atoms. If it has a high energy it will ionise many atoms along its path through the gas. The loss of energy dE along a path length dx can be described by the Bethe-Bloch equation.

For charged particles like protons, alpha particles or ions the formula is:

$$\frac{dE}{dx} = - \frac{Z_1^2 e^4 n_e}{4 \pi \varepsilon_0^2 v^2 m_e} \left[\ln \frac{2 m_e v^2}{\langle E_b \rangle} - \ln (1 - \beta^2) - \beta^2 \right] \quad (3)$$

with:

- Z_1 = charge number of the entering particle
- e = electron charge
- n_e = electron density of the medium
- ε_0 = dielectric constant
- v = velocity of the entering particle
- m_e = electron mass
- $\beta = \frac{v}{c}$
- $\langle E_b \rangle$ = mean binding energy of the material electrons

Corrections that can be added are *Fermi's density correction* for very high energies and the *shell correction* taking into account that the atomic electrons are not stationary.

From Equation 3 we see that the energy loss depends like $\frac{1}{E} \ln \frac{E}{E_b}$ on the energy of the particle. Using

4. The weak and the strong force are important if the energy of the entering particle gets so high that it enters a region of the atomic gas cores where those two forces become strong. Such high energies are not given in our experiments. In contrast to the weak and the strong force, the electromagnetic force has infinite range.

$\rho = n_a M_a \approx n_a A m_p$ (with n_a = atomic density, m_p = proton mass, A = mass number), we get the dependence on the material density ρ and kinetic energy E_{kin} of the particle:

$$\frac{dE}{dx} \propto \rho \frac{Z_1^2}{E_{\text{kin}}} \quad (4)$$

Hence $\frac{1}{\rho} \frac{dE}{dx}$, often in units $1 \text{ eV} \cdot \text{kg}^{-1} \cdot \text{m}^2$, is only weakly dependant on the material, see Figure 13. One can see in the figure on the left that the energy loss has a minimum at $\beta\gamma \approx 4$ for typical atomic numbers. Particles with a momentum higher than this value are called *Minimum Ionising Particles* (MIPs).

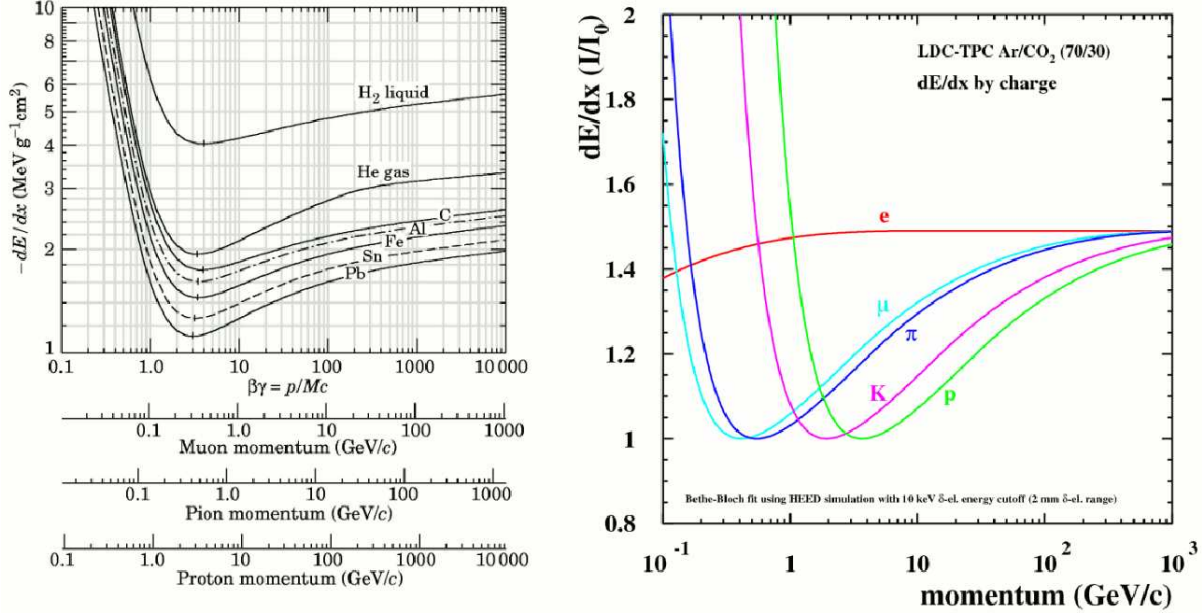


Figure 13. Energy loss (in units of $\text{MeV} \cdot \text{g}^{-1} \cdot \text{cm}^2$) as function of $\gamma\beta$ for different materials (left) and for different particles (electrons e , muons μ , pions π , kaons K and protons p) in an argon based gas mixture Ar/CO_2 70/30 as a function of momentum in GeV/c versus energy loss in units of the ionisation minimum $I_0 = 1.73 \text{ keV}/\text{cm}$ for MIPs in Ar/CO_2 70/30 (right), from [Ren07].

For electrons and positrons the energy loss is dominated by the emission of bremsstrahlung, Møller-scattering (for electrons) and Bhabha-scattering (for positrons). Bremsstrahlung is the radiation that is generated when an electron is accelerated. Møller-scattering is the interaction of two indistinguishable electrons. Bhabha-scattering is the interaction of a positron and an electron. Bremsstrahlung is dominating the energy loss for electrons with high energies (for example higher than 10 MeV in lead), see Figure 14.

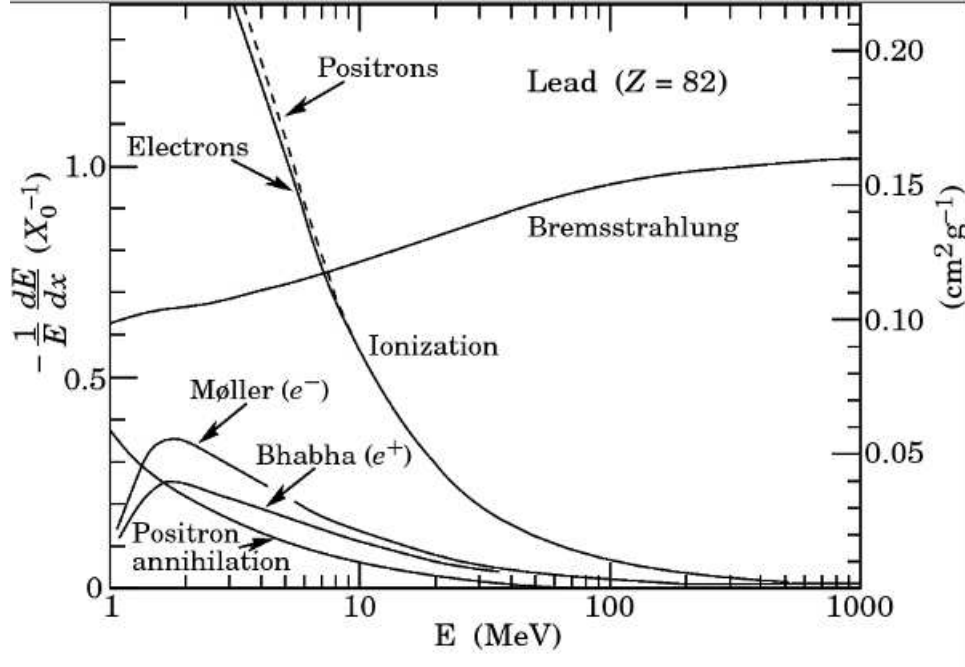


Figure 14. Fractional energy loss per radiation length in lead as a function of electron or positron energy. Electron (positron) scattering is considered as ionisation when the energy loss per collision is below 0.255 MeV, and as Møller (Bhabha) scattering when it is above, from [Ams08]

For slow, charged particles the electronic shell of the atom needs to be taken into account. They are deflected stronger. The deflection leads to the emission of bremsstrahlung. In this case, the energy $E(x)$ after a distance x can be approximated by $E(x) = E(0) e^{-\frac{x}{x_{\text{rad}}}}$.

The *radiation length* x_{rad} is the distance after which the energy has fallen to $1/e$:

$$x_{\text{rad}} = \left[\frac{4 n_a Z^2 \alpha^3 (\hbar c)^2}{m_e^2 c^4} \ln \frac{a(E)}{Z^{1/3}} \right]^{-1} \quad (5)$$

with:

- α =fine structure constant,
- $a(E)$ = numerical factor describing at which the impact parameter the incoming electron approaches the core close enough to be deflected sufficiently. ([Dem04] chap. 4.2.2).

If the absorber consists of a mixture with fraction proportions w_i in weights of an individual element the radiation length also needs to be weighted:

$$\frac{1}{x_{\text{rad}}} = \sum_{i=1}^n \frac{w_i}{x_{\text{rad}_i}} \quad (6)$$

Gas mixture	x_{rad}	$\sigma_{\text{mult scat}}$
Ar/CO ₂	125m	49 μm
He/CO ₂	565m	23 μm

Table 2. Radiation length x_{rad} track rms due to multiple scattering $\sigma_{\text{mult scat}}$, from [Ren07].

Multiple scattering will prevent a charged particle from flying straight on. Deflections on the coulomb fields of the atoms smear the track and lead to an additional factor $\sigma_{\text{mult scat}}$ for the resolution.

2.1.2 Photons

There are three basic processes for the interaction of photons with a material:

- Photo effect, primarily⁵ for energies E lower than 200 keV.
- Compton effect, primarily for $200 \text{ keV} < E < 5 \text{ MeV}$.
- Pair production, primarily for $E > 1.022 \text{ MeV}$.

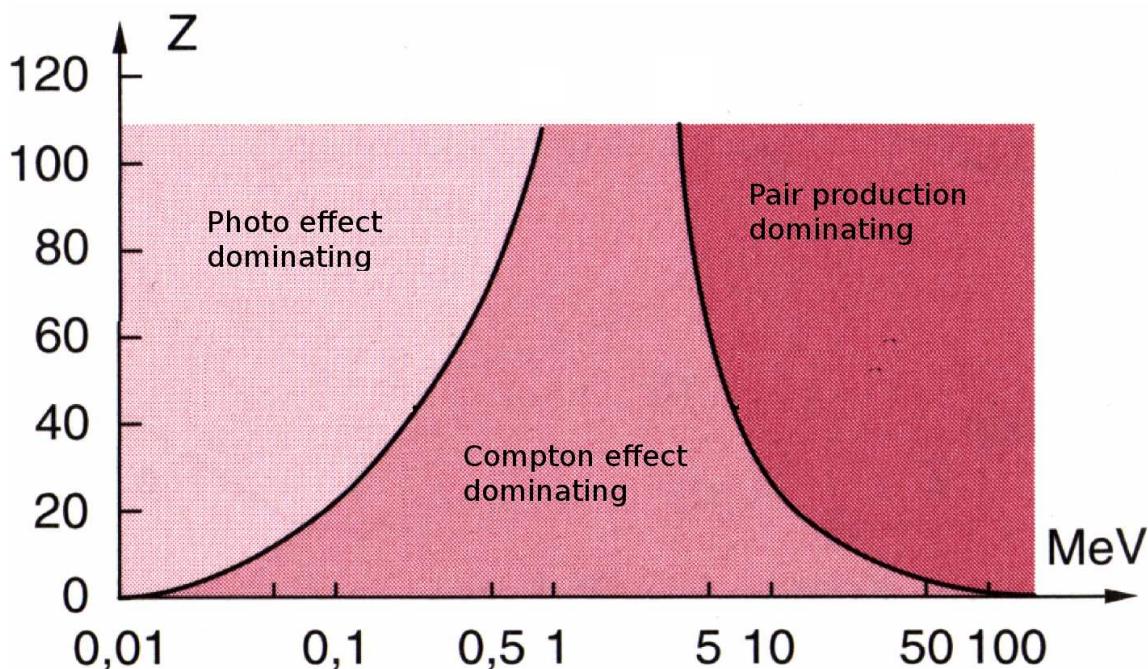


Figure 15. Fraction of the three processes on photon absorption depending on energy and atomic number, from [Dem04]. The lines between the different regions are lines of same cross sections for the adjacent processes.

Photo effect A photon (γ -quantum) with energy $h\nu$ hits the shell of an atom and transfers all its energy to an electron at the energy level E_k that then leaves the atom:

$$h\nu + A(E_k) \rightarrow A^+(E_{\text{ion}}) + e^-(E_{\text{kin}})$$

where E_{ion} is the ionisation energy. The kinetic energy of the free electron is $E_{\text{kin}} = h\nu - (E_{\text{ion}} - E_k)$. Hence for the photo effect a minimum energy is necessary. The free electrons (photo electrons) can have different, but discrete energies depending on the energy level they came from. The free place in the atom shell can be replaced by electrons on higher energy levels E_j . The energy difference $E_j - E_k$ can be emitted by a photon or it is transferred to another electron that can then leave the atom (*Auger effect*). This secondary radiation results in additional peaks in the spectrum. The photo peak refers to the original energy of the incoming γ -quantum⁶. The probability that a γ -quantum is absorbed by photo effect is proportional to $\frac{Z^5}{E^{3.5}}$ ([Dem04], p. 87), hence it is high for heavy atoms and low photon energy. If a photon has the exact binding energy of an electron $h\nu = E_k$ the absorption of photons is most likely. Absorption edges are visible in the spectrum in this case.

5. Primarily means, in this case, that the cross section for this process is the biggest of the three processes for most of the materials, see Figure 15.

6. All the secondary processes are added up by the detector and the correct energy is reconstructed

Compton effect This effect is the scattering of a γ -quantum with frequency ν on a free or weakly bounded electron. The interaction leads to an energy transfer:

$$h\nu + e^- \rightarrow e^-(E_{\text{kin}}) + h\nu'$$

with $E_{\text{kin}} = h(\nu - \nu')$, assuming that the electron was at rest before the collision. ν' is the frequency of the photon after the scattering. Using energy and momentum conservation leads to the Compton scattering formula ([Dem04], Chap. 3.1.6):

$$\lambda' - \lambda = \frac{h}{cm_0} (1 - \cos(\Theta)) \quad (7)$$

$$\Leftrightarrow \frac{1}{E_\nu} - \frac{1}{E_{\nu'}} = \frac{1}{E_0} (1 - \cos(\Theta)) \quad (8)$$

with E_ν the energy of the photon before the scattering, $E_{\nu'}$ the energy of the photon after the scattering, m_0 the rest mass of the electron, E_0 the rest energy of the electron and Θ the scattering angle. For the kinetic energy of the electron after the collision it is:

$$E_{\text{kin}} = E_\nu - E_{\nu'} = \frac{\frac{E_\nu^2}{E_0} (1 - \cos(\Theta))}{1 + \frac{E_\nu}{E_0} (1 - \cos(\Theta))}. \quad (9)$$

For a central collision ($\Theta = 180^\circ$) the maximum transferred energy to the electron is:

$$E_{\text{kin, max}} = \frac{E_\nu}{1 + \frac{E_0}{2E_\nu}}, \quad (10)$$

leading to the Compton edge in the spectrum. For the scattered photons the energy after the collisions is $E_{\nu'} = E_\nu - E_{\text{kin}}$. For $0^\circ < \Theta < 180^\circ$ the function $E_{\text{kin}}(\Theta)$ is continuous leading to a Compton continuum in the spectrum until down to $E_{\text{kin}} = 0$ eV for $\Theta = 0^\circ$.

Pair production In the electromagnetic field of a nucleus an incoming photon can undergo a spontaneous conversion into an electron positron pair. The whole energy of the photon is transferred to the two particles.

$$h\nu \rightarrow e^- + e^+ + E_{\text{kin}}$$

To create the two particles at least the rest energy of 1.022 MeV is necessary. The excessive energy can be shared by the nucleus, the electron and the positron. The created positron annihilates with the surrounding electrons producing two γ -quanta emitted in opposite direction.

2.1.3 Fano factor

The number of electrons produced in the conversion of a photon depends on the gas as they have different ionisation energies or molecular gases have different excitation states. The *mean energy per ion pair* W can be calculated from the number of primary electrons N_e and the energy of the photon E_0 if the photon loses all its energy by ionisation:

$$W = \frac{E_0}{N_e} \quad (11)$$

In hydrocarbons and noble gases, like Ar, Kr and Xe, W is about 20 – 30 eV, 41 eV for He and 36 eV for Ne. For photon energies higher than 1 keV, W is constant. The dependence of the gas mixture is complex [Che09].

The number of primary electrons N_e created by a photon conversion fluctuates and is a Poisson distribution with variance N_e if the different steps of ionisation are independent. But as $N_e \leq E_0/U_i$ where U_i is the ionisation potential this independence is broken. For that reason the Poisson distribution has a variance reduced by a factor F called *Fano factor*.

$$\sigma_{N_e}^2 = F \cdot N_e \quad (12)$$

F depends on the gas mixture and the photon energy. It is of the order of 0.15 – 0.2 for noble gases and 0.2 – 0.4 for molecular gases. Mixing gases can lead to different values, especially in Penning mixtures (see section 2.2.3). Factors down to 0.05 are reported in pure gases with additions of less than 1% [AKV67].

2.1.4 Drift

Almost all the interactions between particles and materials will lead to a separation of gas ions and primary electrons. Usually they will recombine and the atoms will emit a photon. In this case the material is a scintillator that can be used as a detector. But it is also possible to separate the primary electrons and drift them along the lines of an electric field E towards a structure where they can be measured. Usually a magnetic field B is also present in a detector setup. The equation of motion is:

$$m \frac{d\vec{v}}{dt} = e (\vec{E} + \vec{v} \times \vec{B}) \quad (13)$$

An additional term must be added to take the friction force \vec{f} of the gas into account which is assumed to be proportional to the velocity (proportional constant K) or the momentum (proportional constant $1/\tau$): $\vec{f} = -K\vec{v} = -\frac{m\vec{v}}{\tau}$. For $t \rightarrow \infty$ a constant *drift velocity* \vec{v}_d will be reached:

$$\frac{\vec{v}_d}{\tau} - \frac{e}{m} \vec{v}_d \times \vec{B} = \frac{e}{m} \vec{E}. \quad (14)$$

The solution for \vec{v}_d is the *Langevin formula*:

$$\vec{v}_d = \frac{e}{m} \tau E \frac{1}{1 + \omega^2 \tau^2} (\hat{e}_E + \omega \tau (\hat{e}_E \times \hat{e}_B) + \omega^2 \tau^2 (\hat{e}_E \cdot \hat{e}_B) \hat{e}_B) \quad (15)$$

where $\omega = (e/m)B$ is the cyclotron frequency and \hat{e}_B and \hat{e}_E are the unit vectors of the magnetic and electric field respectively. In first order in $\omega \tau$ (which is < 1 for typical magnetic field strengths) \vec{v}_d points in the direction of \vec{E} . The velocity fractions in the direction perpendicular to the electric field can be calculated from the cyclotron frequency. If there is no magnetic field ($\omega \tau = 0$) the drift velocity is:

$$\vec{v}_d = \frac{e}{m} \tau \vec{E} = \mu \vec{E} \quad (16)$$

where μ is called the *mobility*. For a given magnetic field the magnitude of \vec{v}_d is reduced by:

$$\frac{|\vec{v}_d(\omega)|}{|\vec{v}_d(0)|} = \frac{1 + \omega^2 \tau^2 \cos \phi}{1 + \omega^2 \tau^2} \quad (17)$$

where ϕ is the angle between \vec{B} and \vec{E} . Thus in the case of parallel fields the drift velocity is not affected.

In a microscopic model the friction force introduced in the equation above is the effect of collisions with gas molecules. Without electric field the direction of movement of an particle is randomly orientated and the velocity is Maxwell distributed. In an electric field the electron is accelerated between two collisions (along the free path length λ in the free time Δt) in the direction of the field.

$$\vec{v}_d = (e/m) \Delta t \vec{E} \quad (18)$$

Comparing Equation 16 and 18 one can see that the characteristic time τ introduced in the macroscopic model is related to the free time Δt in the microscopic model. They are equal for $B = 0$.

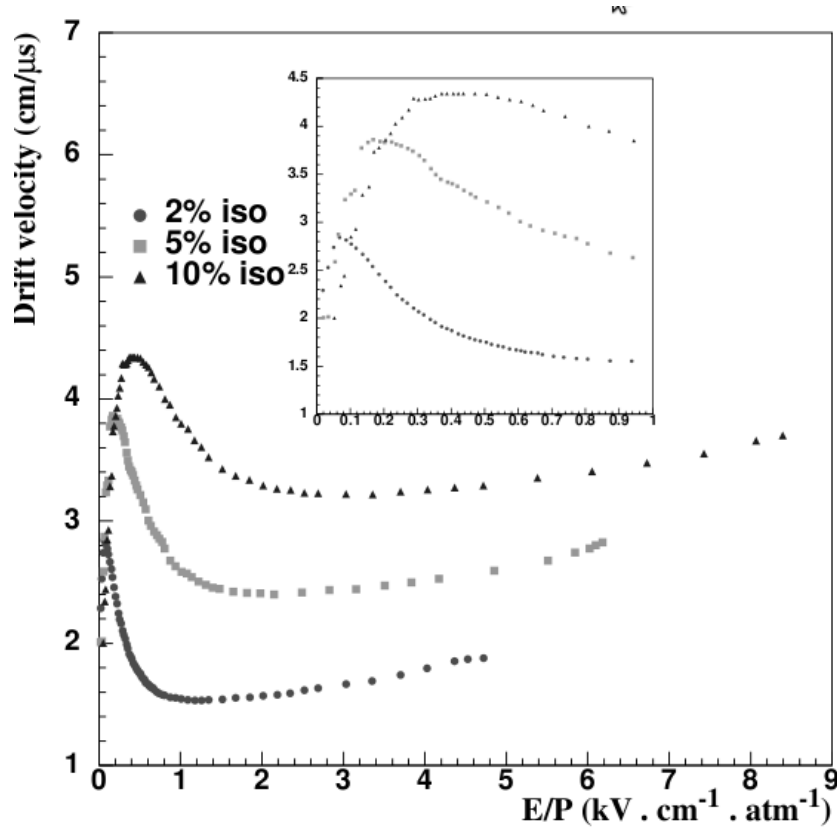


Figure 16. Drift velocities in different Argon/Iso gases mixtures as a function of the reduced electric fields. Measurements from [Col02].

2.1.5 Diffusion

Assuming a point-like accumulation of primary electrons at a position $(x, y, z) = (0, 0, 0)$ at the time $t = 0$. The electrons drift in an electric field in positive z -direction. They will not drift along the field lines but scatter off the gas molecules. The point-like accumulation of electrons will spread out to a cloud in x , y (transverse)- and z -(longitudinal) direction. The effect is similar for the ions drifting in the opposite direction with a difference due to their higher mass. For simplification consider that the diffusion for electrons is the same in transverse and longitudinal direction. Then the particle density n in each direction is a Gaussian distribution with a centre at $(0, 0, v_d t)$:

$$n(r) = \left(\frac{1}{4\pi D_c t} \right)^{3/2} \exp\left(\frac{-r^2}{4D_c t} \right) \quad (19)$$

The mean square deviation $\sigma_i^2 = 2 D_c t$ for any direction widens with time. D_c is the diffusion constant. Looking at the microscopic picture from the last section one can also calculate σ_i^2 and see that $D_c = \frac{2\epsilon\mu}{3e}$ [Che09], where $\epsilon = \frac{mu^2}{2}$ is the average energy of the drifting particles with u the average drift velocity and μ the mobility. Using $t = \frac{L}{\mu E}$, where L is the drift distance one gets

$$\sigma_i = D \sqrt{L} \quad (20)$$

with $D = \sqrt{\frac{2D_c}{\mu E}} = \sqrt{\frac{4\epsilon}{3eE}}$ the diffusion coefficient. As the electron cloud widens after a drift distance L diffusion sets a limit to the accuracy of track measurements of $\sigma_i(L)$. To keep the diffusion as small as possible high drift fields and low electron energies are necessary. For the second case cold gases are preferable. In the thermal limit the lowest energy for an electron is $\epsilon = (3/2) k_B T$. In this limit the diffusion only depends on the field and temperature:

$$D = \sqrt{\frac{2k_B T}{eE}} \quad (21)$$

At room temperature one gets $D \approx 230 \mu m / \sqrt{\text{cm}}$ for a field of $E = 100 \text{ V/cm}$ or $D \approx 70 \mu m / \sqrt{\text{cm}}$ for a field of $E = 1 \text{ kV/cm}$ for all gases as a limiting value. If the field strength gets too high, the electrons are not thermal any more. For argon based mixtures this is the case for fields higher than $E \approx 18 \text{ kV/cm}$.

The assumption that the diffusion is the same in longitudinal and transverse direction is not true [Wag67]. There are two diffusion coefficients D_t and D_l which usually are of the same order of magnitude.

In the presence of a magnetic field the diffusion orthogonal to \vec{B} is highly suppressed. Formula 17 can be applied for the diffusion coefficient D_t with $\phi = 90^\circ$ as the drift is perpendicular to \vec{B} :

$$\frac{D_t(\omega)}{D_t(0)} = \frac{1}{1 + \omega^2 \tau^2} \quad (22)$$

The Lorentz force will pull electrons with a velocity component perpendicular to \vec{B} on helical trajectories circling around the magnetic field lines. For that reason a TPC setup with a drift distance of several meters usually has parallel magnetic and electric fields. For example in a mixture of Ar/CH₄ 95/5 at a drift field of 40 V/cm and a magnetic field of 4 T the transverse diffusion is lowered by a factor 40. The longitudinal diffusion is not affected by this process.

2.2 Amplification process

In a tracking detector the electrons and ions created in the primary ionisation drift towards a readout structure. The few electrons created in the primary process are not enough to produce a measurable signal in the electronics. Therefore it is necessary to multiply the few electrons in a gas multiplication process. In Figure 4 we have seen the different operation modes of a wire tube. The primary ionisation takes place in a region where the field is as strong as in an ionisation chamber. In the amplification region the electric field is as strong as in a proportional chamber. The amplification process is based on inelastic collisions resulting in excitation and ionisation of gas molecules. A primary electron enters the amplification region. It gains enough energy in the electric field to ionise a gas molecule and a second free electron is created. This process is called the secondary ionisation. The two electrons are again accelerated and can ionise other gas molecules and so on. This leads to an avalanche of electrons and gains of typically $10^3 - 10^5$ are achieved. The gain can not be increased to infinity. If the electric field gets too strong the amplification zone will operate in the Geiger mode shown in Figure 4. Avalanches are more and more likely to create discharges if the electric field is increased. A breakdown happens at gains of 10^8 and is called the *Raether limit*.

Ion backflow In the amplification process ions are created that drift in the opposite direction. They can disturb the electric field and lower the gain, see section 1.2.3.

2.2.1 Townsend coefficient

To calculate the number of secondary electrons many factors have to be taken into account. The amplification depends on the Penning effect, pressure, temperature, recombination, attachment and space charge effects. In the following calculation all these effects will not be taken into account and the reader is referred to [BR93], [Che09], [Sip79].

The ionisation cross section $\sigma_i(\epsilon)$ (index i for ionisation) of an electron with energy ϵ is proportional to the probability that a electron ion pair is created. For independent ionising collisions the mean free path λ_i for ionisation is related to the cross section by

$$\lambda_i(\epsilon) = \frac{1}{n \sigma_i(\epsilon)}, \quad (23)$$

where n is a proportional constant. The Townsend coefficient $\alpha(\epsilon)$ is the mean number of ionisations per unit length and defined as:

$$\alpha(\epsilon) = \frac{1}{\lambda_i(\epsilon)}. \quad (24)$$

It is more practical to have the Townsend coefficient as a function of the electrical field E in the amplification region. The transformation can be done using the normalised electron energy distribution $p(E, \epsilon)$. This distribution describes the energy of an electron in the electric field.

$$\alpha(E) = \int_0^\infty p(E, \epsilon) \alpha(\epsilon) d\epsilon \quad (25)$$

The energy distribution is not known and an analytic formula does not exist for electric field strengths like in an amplification region. Numerical calculations and measurements are used to get $\alpha(E)$. There are different parametrisation in different ranges of field strength [PS75]. A parametrisation for field strengths up to 50 kV/cm for cylindrical and parallel plate chambers from [RK41] is commonly used:

$$\alpha/P = \bar{A} \exp(-\bar{B}P/E) \quad (26)$$

where P is the pressure and \bar{A} and \bar{B} are coefficients depending on the gas.

The number of electrons in the avalanche can be calculated from the Townsend coefficient. Let $n(x)$ be the number of electrons at a drift distance x . The change of this number dn on a distance dx is:

$$dn = n(x) \alpha(E(x)) dx. \quad (27)$$

For a drift distance $\Delta x = x_1 - x_0$ and n_0 electrons at x_0 the integration of Equation 27 leads to:

$$n(\Delta x) = n_0 \exp\left(\int_{x_0}^{x_1} \alpha(E(x)) dx\right). \quad (28)$$

The gain G is the multiplication of the primary charge in the amplification distance Δx :

$$G(\Delta x) = \frac{n(\Delta x)}{n(0)} \quad (29)$$

For a uniform electric field one gets:

$$G(\Delta x) = \exp(\alpha \cdot \Delta x). \quad (30)$$

The gain dependence on the electrical field is given by [Che09]:

$$G(E) = A \cdot \exp(B^* \cdot E) \text{ or } G(\Delta U) = A \cdot \exp(B \cdot \Delta U) \quad (31)$$

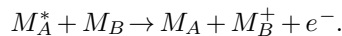
when ΔU is the potential difference in the amplification region. The parameters A and B (or B^*) can be obtained by a fit of the gain curve.

2.2.2 UV photons

As the cross sections for ionisation and excitation are of the same order of magnitude, UV photons are also created in the avalanche process. These photons can release electrons from the gas or detector material via photo effect. Additional delayed and displaced avalanches are created lowering the energy and position resolution of the detector or even cause breakdowns. For that reason UV photons should be stopped as soon as possible. Molecular gases like CO_2 , CH_4 , CF_4 or C_4H_{10} (isobutane) are added to noble gases as *quenching gases*. They have absorption lines in the UV regime. Vibrations of the molecules are excited and the energy is transferred to the noble gas or emitted by infrared photons.

2.2.3 Penning effect

Mixing different gases can lead to the *Penning effect*. This effect is the ionisation of molecules M_B of a gas B by excitation of molecules M_A^* of a gas A :



The energy from the de-excitation of a molecule M_A^* is transferred to a molecule M_B . If the ionisation potential of B is low enough it can be ionised ($M_B^+ + e^-$). The Penning effect can increase the primary ionisation and also the gain.

2.2.4 Avalanche statistics

The amplification of a primary charge is a statistic process as probabilities play an important role in the avalanche. The gain G is only a mean value of a gain distribution also called gain curve, single electron response or avalanche size distribution. The shape of this distribution is important for the detector performance, for example, for the energy resolution or the detection efficiency. There are many theories for the stochastic avalanche process and three of them will be presented in the following.

- Snyder's model [Sny47]: In this simple model the ionisation probability is constant and an exact solution is possible. The gain curve is an exponential distribution.
- Legler's model [Leg55]: The ionisation probability is a step function. It is zero for low energies and constant if the electron has achieved the ionisation energy of the gas. Only after a minimum acceleration distance x_0 , the electrons can again ionise gas molecules.
- Alkhozov's theory [Alk70]: The probability distribution of inelastic collision is a step function, the probability of an ionisation in an inelastic collision is not one.

2.2.5 Polya distribution

The distributions of the Legler and Alkhozov models can not be expressed analytically, but moments of the distribution can be calculated. A Polya distribution is a good approximation for both of the models. Compared to the Legler distribution the tail is longer. The Polya distribution depends on two parameters: the mean gain \bar{G} (centre of the distribution) and the variance Θ of the distribution sometimes written as $m = 1 + \Theta$.

$$P(G/\bar{G}, \Theta) = \frac{(\Theta + 1)^{\Theta + 1}}{\Gamma(\Theta + 1)} \left(\frac{G}{\bar{G}}\right)^{\Theta} \exp\left(-(\Theta + 1)\left(\frac{G}{\bar{G}}\right)\right) \quad (32)$$

$\Gamma(\Theta + 1)$ is the gamma function. Figure 17 shows Polya distributions for several values of the parameter θ . Tuning this parameter makes it possible to fit measured data.

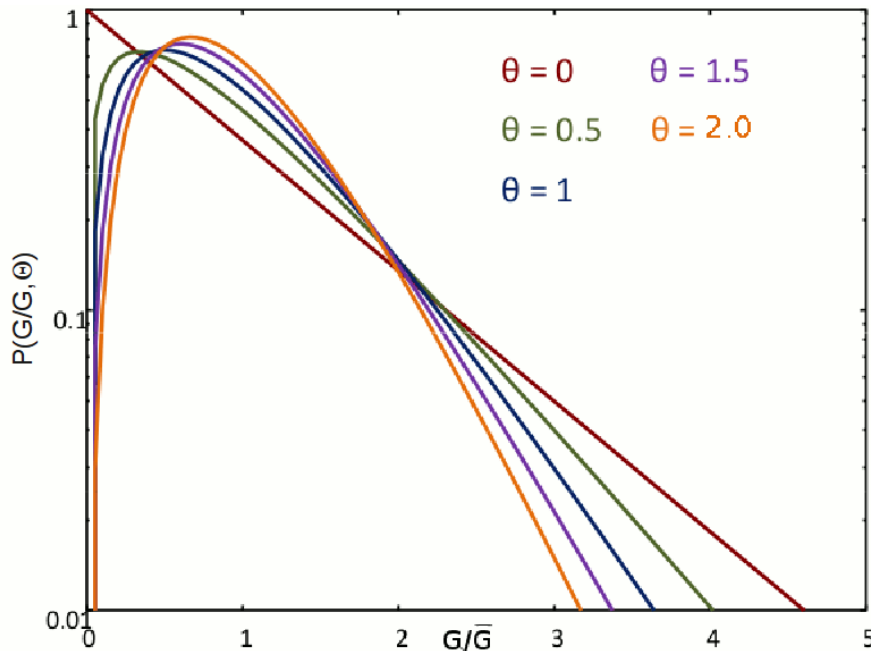


Figure 17. Normalised Polya distribution for different values of Θ ; from [Sch10]

2.3 ^{55}Fe -spectrum

In this experiments, an ^{55}Fe source was used to generate primary electrons in gas mixtures. ^{55}Fe decays with a life time of 2.73 years into ^{55}Mn by electron capture in the K -shell. The ^{55}Mn isotope goes to the ground state mainly emitting photons of energy 5.899 keV ($K_{\alpha 1}$) and 6.490 keV ($K_{\beta 3}$) in a ration of 8:5:1. The K_{β} line was strongly absorbed before entering the detector by a chromium foil. Cr has a Compton edge (see section 2.1.2) at 5.989 keV. The transmission for the K_{α} photon is higher than 80% and less than 15% for the K_{β} photon for a foil of a thickness of $10\ \mu\text{m}$. As the K_{α} and K_{β} energies are close-by, a higher resolution for the K_{α} photo peak can be achieved this way as a single Gauss curve can be fitted to the data.

2.3.1 Argon based mixtures

As an ^{55}Fe photon has an energy of about 6 keV, pair production is not possible. Argon has a atomic number of 18. We can already see from Figure 15 that the photo effect should be more likely than Compton effect. From Table 3, where the mean free paths for the two effects are listed, we can see that the difference is at least three orders of magnitude. We assume that all energy transfers in the gases listed in the table are due to photo effect. This is still true if fractions of less than 20% of quenching gases (see Section 2.2.2) are added [Che09].

	$\lambda_{\alpha}^{\text{p.e.}}$ (cm)	$\lambda_{\alpha}^{\text{c.s.}}$ (cm)	$\lambda_{\alpha}^{\text{t}}$ (cm)	$\text{P}_{\alpha}^{\text{p.e.}}$ (%)
	$\lambda_{\beta}^{\text{p.e.}}$ (cm)	$\lambda_{\beta}^{\text{c.s.}}$ (cm)	$\lambda_{\beta}^{\text{t}}$ (cm)	$\text{P}_{\beta}^{\text{p.e.}}$ (%)
Air	33.46	8064.52	33.32	
	44.80	7331.38	44.56	
Kapton	$4.29 \cdot 10^{-2}$	6.40	$4.27 \cdot 10^{-2}$	
	$5.82 \cdot 10^{-2}$	6.07	$5.73 \cdot 10^{-2}$	
Fe	$1.46 \cdot 10^{-3}$	2.16	$1.46 \cdot 10^{-3}$	
	$1.92 \cdot 10^{-3}$	2.00	$1.92 \cdot 10^{-3}$	
Ar	2.08	8153.81	2.08	17.49
	2.70	7643.51	2.70	13.77
$i\text{C}_4\text{H}_{10}$	65.16	4073.49	64.11	0.61
	88.32	3913.74	86.41	0.45
CH_4	166.73	8468.83	163.59	0.24
	225.47	8169.93	219.41	0.18

Table 3. From [Che09]: Mean free paths for the photo-electric effect ($\lambda^{\text{p.e.}}$), Compton scattering ($\lambda^{\text{c.s.}}$) and total absorption (λ^{t}) at normal conditions, in the various elements of the detector. The indexes α and β refer to the energy of the K_{α} and K_{β} quanta emitted by the ^{55}Fe source. The mean free paths are calculated using the gas mass densities and the mass attenuation coefficients taken from [BR93] and [XCO] respectively. In the last column, the probability that a photon entering the drift gap of the detector converts by the photo-electric effect within 4 mm is quoted.

There is a probability of 11% that the photo electron comes from the L or M shell. Most of the electrons are hit out in the K shell and have an energy of 2.694 keV and 3.286 keV for the K_{α} and K_{β} photons respectively. As mentioned in section 2.1.2 there are two possibilities of what can happen when the free

place in the K shell is filled. In 13.5% of the cases a photon with an energy between 2.957 keV and 3.190 keV (depending on from which shell the free space is filled) is emitted. In 86.5% of the cases the energy is transferred to one or several Auger electrons. The highest energy an Auger electron can get is 2.660 keV. From Figure 18 we can see that photo electrons as well as Auger electrons are stopped within less than $200\ \mu\text{m}$. High energetic electrons leaving the photo ionisation zone are called δ -electrons. For the photons, the free path of total absorption is 3.2cm. They can leave the detector. Their energy is not recorded by the detector and escape peaks are visible in the energy spectrum. In Figure 19 the main lines of the spectrum are plotted. Only the strongest escape line for K_α and K_β are shown. The photo peaks consist of three lines, each for a different Auger cascade.

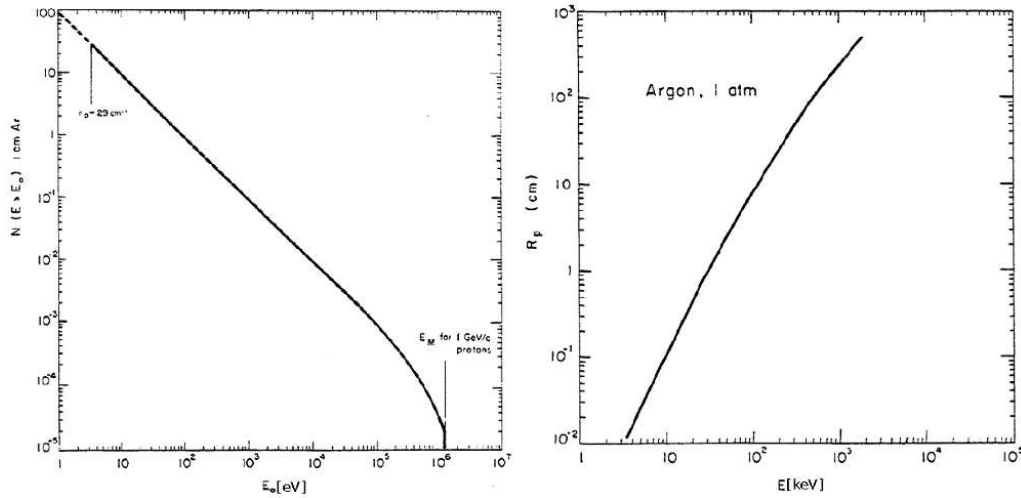


Figure 18. Number of electrons with energy higher than E_0 in 1 cm of argon for protons of 1 GeV/c (left), range of electrons in argon at 1013.25 hPa and 20°C (right), from [Ren07]

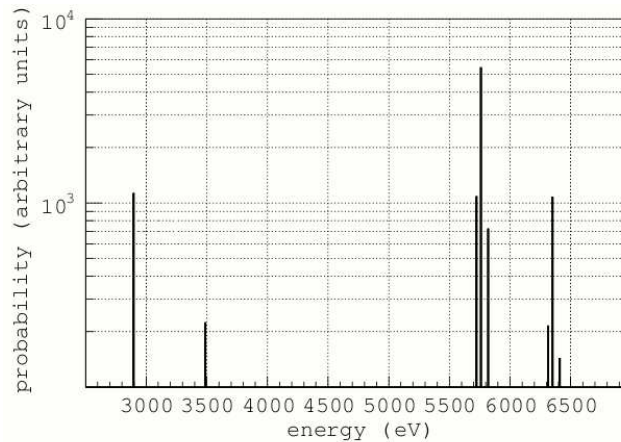


Figure 19. ^{55}Fe spectrum in argon, only main lines plotted, ratio of K_α and K_β conversion assumed to be 5, from [Che09]

2.3.2 Other gas mixtures

Helium, methane and CF_4 based mixtures are also used in gaseous detectors. For helium, the ionisation energy of the K shell is only 24.5 eV and the photo electron has a higher energy in a less dense gas. For that reason δ -electrons are more visible. As the atomic number of helium is two, the Compton effect is also likely to happen. The molecular gases methane (CH_4) and CF_4 have K shell binding energies of

around 0.3 keV compared to 3.2 keV for argon. For these low binding energies, only a photo peak is visible in the spectrum as nearly all the energy is transferred to the photo electron. In Figure 20, transverse diffusion coefficient for various gas mixtures are plotted versus the drift field.

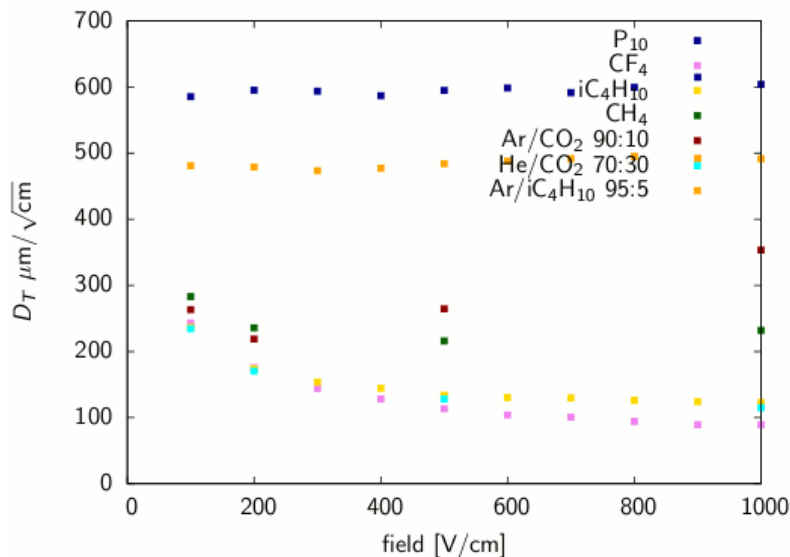


Figure 20. Transverse diffusion coefficient for various gas mixtures as function of the drift field, MAGBOLTZ simulation from [Sch10]

3 Experimental setup

In this chapter the experimental setup will be described. In section 1.2.4 the concept of micro pattern gaseous detectors was introduced. In our setup we used a Micromegas amplification structure and a highly segmented readout, the Timepix chip. The first section of this chapter will introduce this chip. The second section will focus on the detector housing, which is a gas-tight box. The electronics used for the readout will be described in the third section. The last section will describe a LASER test bench that was set up in Freiburg.

3.1 Pixel readout

MPGDs use structures of the order of one micrometer. In our experiments the readout was realised with a CMOS⁷ pixel chip with a pixel size of $55 \times 55 \mu\text{m}^2$ and 256×256 pixels. These chips are well known from digital imaging like in digital cameras or astronomy. Each pixel is a individual electron detector. In our case the chips were produced by IBM using the $0.25 \mu\text{m}$ CMOS technology. The chips are wire-bonded to a readout printed circuit board (PCB).

3.1.1 Medipix2

The Medipix chip [ABB+99] was designed and produced by the Medipix collaboration mainly for medical

⁷ Complementary Metal Oxide Semiconductor

application and available in 1997. The second version, the Medipix2 chip has a total size of $14 \times 16 \text{mm}^2$ where $14 \times 14 \text{mm}^2$ are equipped with pixels. Each pixel contains a circuit with preamplifier, shaper, discriminators, a 14 bit counter and communication logic using 500 transistors and 13 internal 8 bit Digital-to-Analog-Converters (DACs). The chip was designed for single photon detection. For this application the photon-electron converter is a *X-ray* semiconductor that is bump bonded to the pixel surface. For that reason the sensitive pixel surface is made of an octagonal aluminium bump bonding pad of approximately $20 \times 20 \mu\text{m}^2$. The remaining surface is passivated.

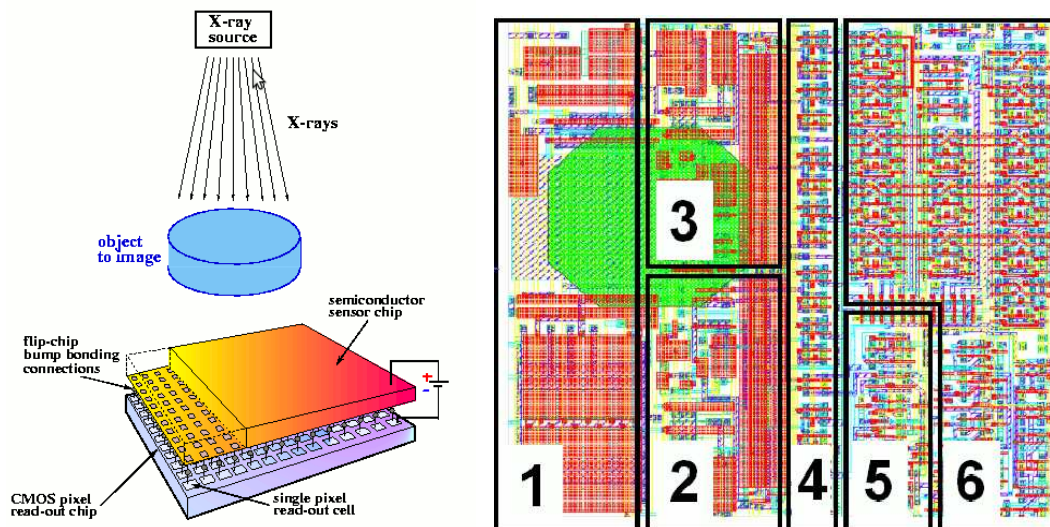


Figure 21. Schematic of a Medipix *X-ray* image detector (left), pixel layout (right): Preamplifier(1), High threshold discriminator(2), Low threshold discriminator(3), 8 bit configuration register(4), double discriminator logic(5), shift register and control logic(6).

For particle detector applications the chip is used without the photon converter. The pixel pads are used as anodes in a gas amplification structure. It is possible to record 2D images of particle tracks on the chip plane. The third coordinate of a track point can not be reconstructed as there is no time information available. The number of hits per pixel in the acquisition time can also be recorded. A upper and a lower threshold can be set by the two internal discriminators. The electronic noise in each pixel is around 1000 electrons.

3.1.2 Timepix

The Timepix chip [Llo06],[LBC+07] is a modification of the Medipix2 chip for TPC applications. The Medipix chip is able to record 2D tracks and count the number of hits per pixels using a 14 bit counter. For the TimePix chip the 14 bit counter is not used to count hits but to count cycles of a clock that is transferred to each pixel. The frequency can be tuned up to 150 MHz. The block diagram of the electronics in each pixel is shown in Figure 22. The Timepix chip uses only one discriminator. The input is the signal from the sensitive surface of the pixel. There is a second input from a capacitance that can be driven by test pulses for the calibration, see sections 3.3.2 and 3.3.3.

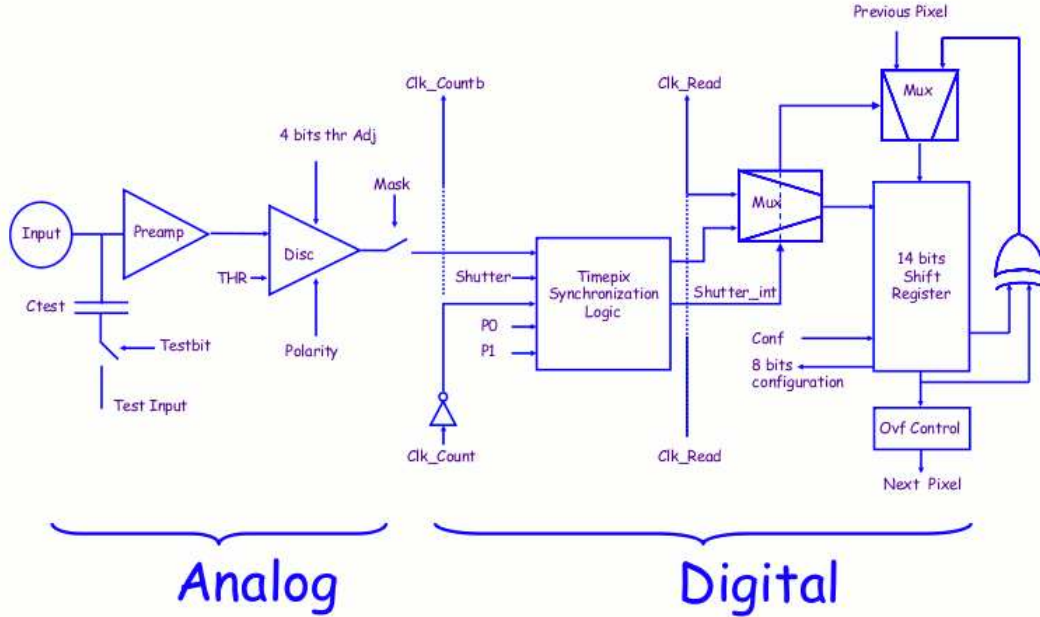


Figure 22. Pixel electronics block diagram, from [Llo06]

A charge coming from the pixel is collected in an integration capacitance of the preamplifier. The output signal is a voltage signal. The time constant of the capacitance can be regulated with the IPream DAC such that the rising edge of the output voltage has a time constant between 90 and 140 ns. The signal is a pulse with a fast rise and a slow falling edge. The time constant of the falling edge can be set externally with the Ikrum DAC. The offset voltage of the output can be set by the FBK DAC to enlarge the dynamic range.

The discriminator is transforming the analog voltage signal coming from the preamplifier V_{in} to a signal that can be used in the digital section of the pixel. It compares the input voltage V_{in} with a voltage V_{THL} that can be set externally via the THL and THLcoarse DACs. THL stand for threshold. V_{THL} and the referring DAC value is the THL level of the pixel and can be calibrated to a number of electrons, see section 3.3.2. The output voltage of the discriminator is a logic signal that is high (logic 1) as long as $V_{in} > V_{THL}$, for the time the signal is over the threshold. Time over threshold will be shortly called TOT.

In the digital section the external clock cycles are counted. As the counter has 14 bit and some positions are reserved for other information the maximum number of counts is 11810. There are 4 different modes of operation, see Figure 23. A pixel can count clock cycles depending on the two configuration bits P0 and P1.

- Medipix mode (P0=0, P1=0): Every time the discriminator signal changes from logic 0 (low) to logic 1 (high) the counter is increased by one. The number of charge pulses during the shutter time is counted that way.
- Time over threshold (TOT) mode (P0=1, P1=0): As long as the discriminator signal is high the clock cycles are counted. If the discriminator signal goes to low the counting is stopped and continued if it becomes high again within the same shutter window. The length of the discriminator signal is proportional to the voltage of the preamplifier output voltage which is proportional to the charge deposited in the pixel. A charge-to-TOTcounts calibration can be done using external test pulses, see 3.3.3.
- Time mode (P0=1, P1=1): The clock cycles are counted in the following way: If the discriminator signal goes to logic 1 for the first time during the shutter window the counter starts. The counting is finished at the end of the shutter window. Changes of the discriminator signal to logic 0 can not stop the counter. The time of arrival with respect to the end of the shutter signal can be measured that way. The time information is essential for the reconstruction of the z -coordinate of track points. The shutter can be opened and closed by an external trigger signal or by the software.

- 1st hit mode (P0=0, P1=1): The counter is set to one by the first clock cycle when the discriminator signal is high. All other clock cycles or changes of the discriminator signal are ignored.

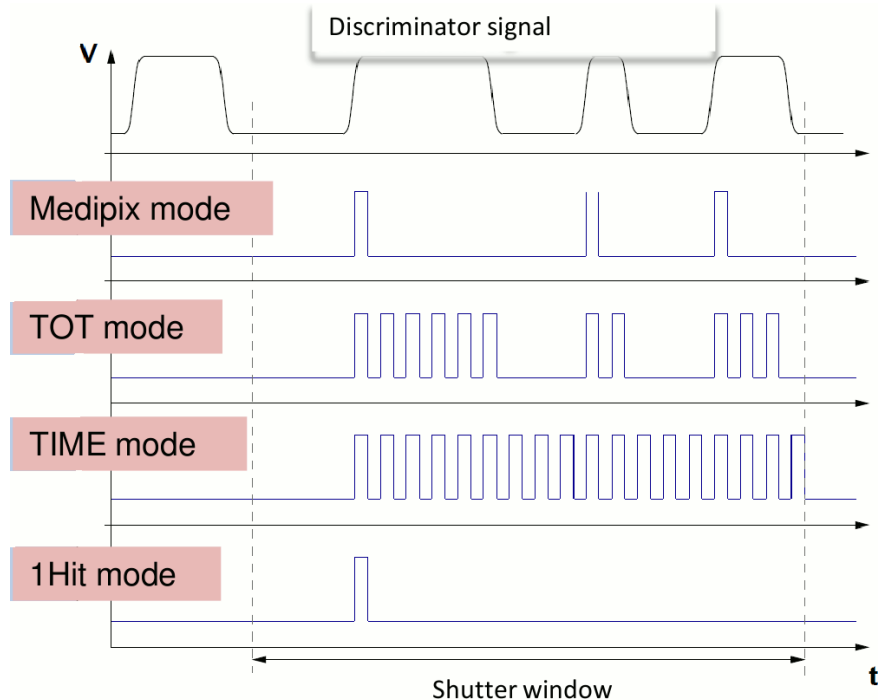


Figure 23. Different operation modes of the Timepix chip

There are two CMOS control line M1 and M2 responsible for setting the chip to read, write or counting mode. More information about the signal transition, fast shift register and chip layout can be found in the Timepix manual [Llo06].

A second version, the Timepix2 chip, is under development [CBH+07]. It will be able to record Time and TOT at the same time. It will be constructed in $0.13\ \mu\text{m}$ CMOS technology, have a higher time precision by a pixel intern oscillator, a faster rise time of 25 ns and a shaping time of 100 ns. The external trigger system and the readout speed ($>250\ \text{MHz}$) will also be improved. To construct large area readout modules the chip should be designed such that silicon-wafer-through-technology⁸ can be applied and the readout from the rear side of the chip is possible.

3.1.3 Threshold equalisation

In TOT mode the clock cycles as long as the signal is higher than the threshold are counted. In Time mode the clock cycles from the first rise over threshold to the end of the shutter are counted. For that reason the threshold level of the discriminator in the analog part of each pixel is the most important value to give a correct TOT and Time information. However due to small differences in fabrication or on-chip voltage variations, the threshold level can vary from pixel to pixel and is a Gaussian distribution around the overall chip threshold level that can be controlled by the THL and THLcoarse DAC.

This differences can be compensated with a 4-Bit current DAC, called thrAdj (threshold adjustment). The range of this DACs is controlled by the global THS DAC. Chips with a low internal variation of threshold levels need a lower THS DAC level and a better equalisation can be achieved.

⁸. Wafer through technology allows close to 100% sensitive surface on the front side of the chip. The readout is done on the rear side of the chip.

A threshold equalisation can be done using the Pixelman software [HJP+06]. During the scan test pulses are injected to each pixel. First the thrAdj DAC is set to 0. The THL is lowered and the value a pixel responds is recorded. The pixel is masked for the next THL step. The same is done with thrAdj DAC =15. The intermediate values for the thrAdj DACs are calculated using linear interpolation. Every pixel gets an adjustment DAC value such that its response is as close to the mean value as possible. The 256×256 matrix of the thrAdj values for the pixels is called the correction mask or threshold equalisation mask. In Figure 24 the distribution from the two THS values and the final distribution of the equalised pixels is shown.

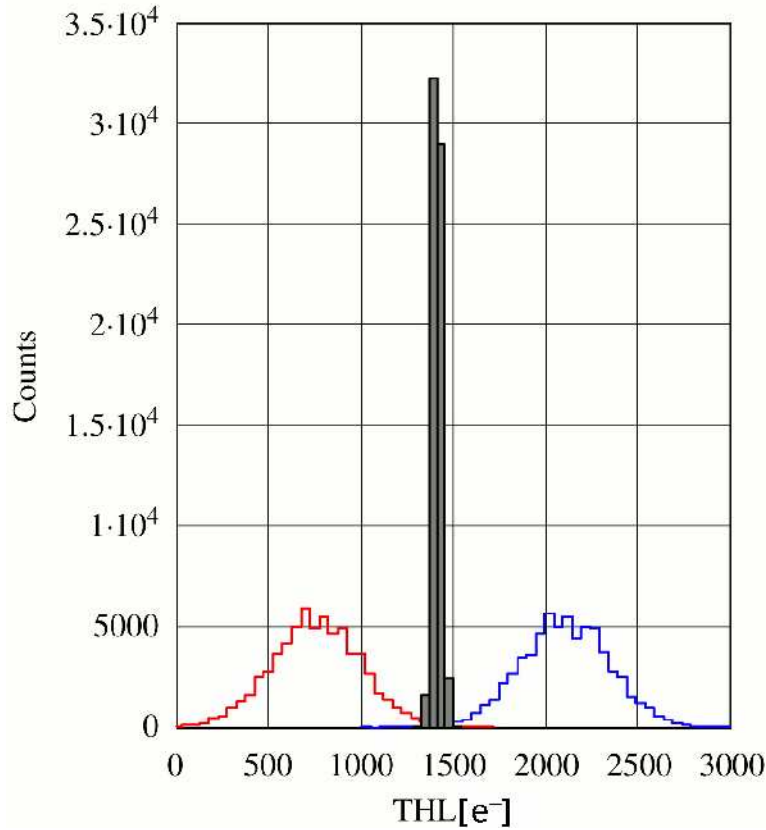


Figure 24. Threshold equalisation: THS= 0 (red, left) distribution, THS = 16 (blue, right) distribution and distribution of equalised pixels (black). The variance is reduced from ≈ 10 DAC values to ≈ 2 DAC values or $\approx 300e^-$ to $\approx 50e^-$, from [LBC+07].

3.1.4 InGrid

The Timepix chip is the anode and the device to read out the detector. Its threshold level is about 1000 electrons. An amplification structure is necessary to detect primary electrons. The GEM and Micromegas concepts explained in section 1.2.4 are used for this purpose. When the Timepix chip was used with a Micromegas the grid was first stretched over the chip surface and set on top of the chip using pillars. The grid holes were not aligned to the pixels and the distance between the chip and the grid was not constant along the surface. The results were spatial efficiency and gain variations [Che09]. A Moiré effect⁹ was visible. A process was developed to solve this problem. During this process the grid is built on the Timepix chip using a lithographic procedure. A grid constructed this way is called integrated grid (InGrid). In Figure 25 the image from Pixelman of a Timepix combined with a grid on pillars and an InGrid is shown. For the combination (left) the pillars are visible as dead area. The misalignment of pixels and grid holes leads to the Moiré pattern. For comparison on the right an image from a InGrid is shown. The ineffective area on the top left is the pad, where the HV connection of the grid was placed.

9. The Moiré effect is a periodic pattern that occurs when two periodic patterns are combined but misaligned.

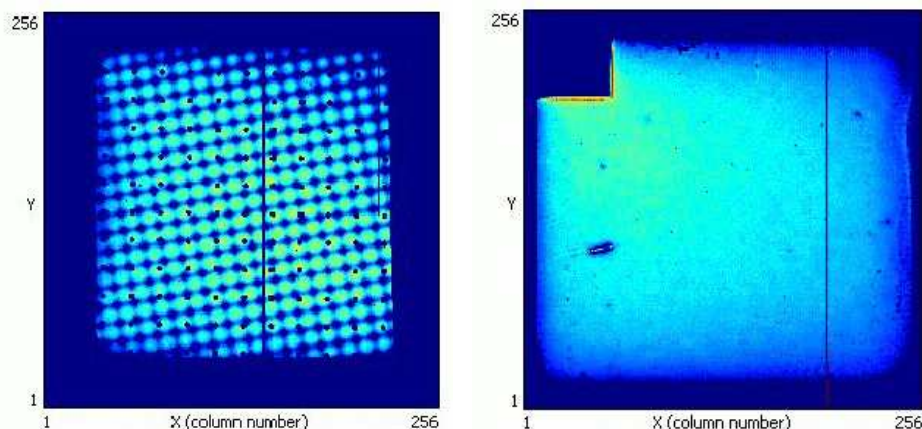


Figure 25. Moiré effect at the combination of a Timepix chip and a Micromegas grid (left), uniform efficiency of a Timepix+InGrid structure, grid defects, bonding pad and dead Timepix columns visible (right)

The different steps in the fabrication of an InGrid are:

- 1. The substrate in Figure 25 could be a naked wafer, a segmented anode or a Timepix chip. In the case of a Timepix chip an additional layer called SiProt (silicon protection) is put on top of the chip before. This layer will be explained in the next section. On top of the SiProt a photo resistive layer is deposited by spin coating. It highly absorbs UV light. For the chips used in our experiment the photoresist was SU8. The gap size can be regulated in this step.
- 2. The pillars for the grid are built by exposing the photoresist with UV light using a mask.
- 3. A $1\ \mu\text{m}$ thin layer of aluminium is evaporated on top of the partly exposed photoresist. The holes are etched in this layer to build the grid holes. The grid geometry like hole size, diameter and distance can be chosen in this step.
- 4. The non exposed photoresist is washed out in a chemical bath. The exposed pillars stay.

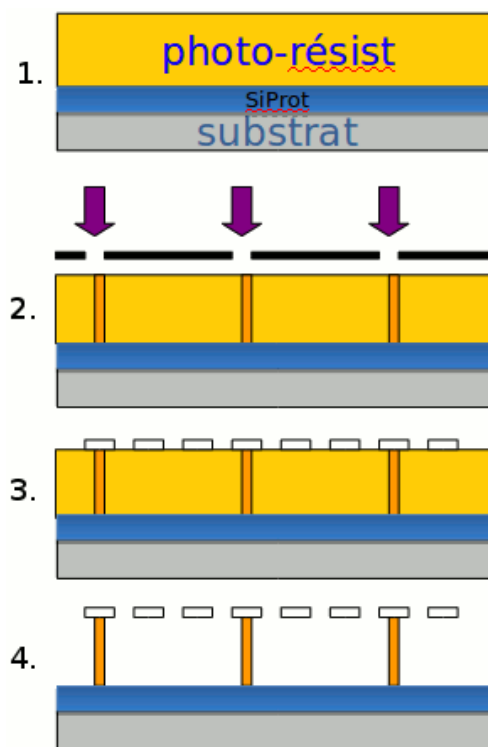


Figure 26. Steps in the fabrication of a InGrid

During the fabrication process the grid and gap geometries can be controlled. Varying the time of etching or spin coating leads to different hole or gap sizes. The gap size (typically between $10\ \mu\text{m}$ and $200\ \mu\text{m}$) can be arranged with a precision of $10 - 20\%$ on a scale of the order of micro meters during the fabrication. The statistical variations in gap size for one chip is less than 1% rms. For the hole size (of the order of $20\ \mu\text{m}$) the precision is $1 - 8\ \mu\text{m}$ with a variation of less than $1\ \mu\text{m}$ [Che09].

The silicon protection layer SiProt is necessary for Timepix+Micromegas structures like InGrid. For

the Micromegas concept the gas amplification takes place directly on top of the readout structure which is the anode. There is a potential difference of about $400V$ over a distance of $\approx 50\mu m$ to provide a strong electric field for gas amplification. Discharges (sparks) are likely in this region. For Micromegas detectors using anodes pads the electronic circuit is designed to handle this discharges. A Timepix chip however would immediately be destroyed after the first spark. A high resistive layer is added to protect the chip. It is made of amorphous silicon $a\text{-Si:H}$ or silicon nitride Si_3N_4 . The influence of this additional layer on the behaviour of InGrids will be discussed in section 4.4.

Six chips were available for our experimental investigation studies. They are named by the position and the waver they are coming from. The ID is branded in chip electronics and detected when the chip is connected to Pixelman. Each chip is tested before the wafer dicing and classified by A (no dead column) to D (more than 2 dead columns), E (bad DACs) and F (dead chip) The grid geometry was measured under the microscope. In Figure 27 an example is shown.

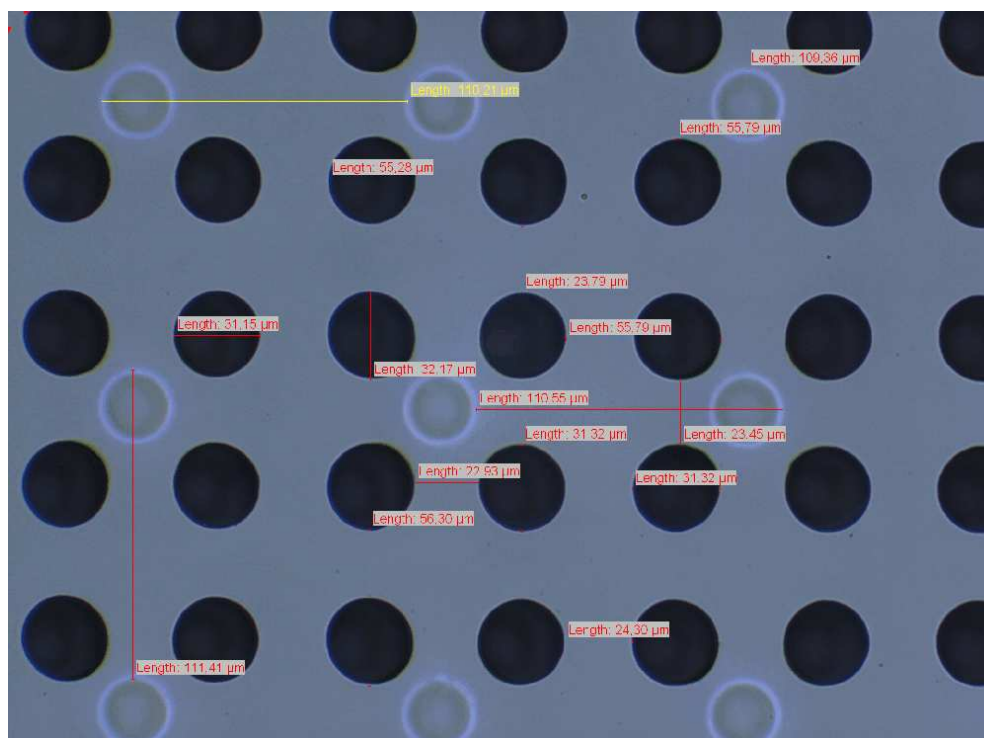


Figure 27. Microscope image of the grid of the G06-W0096 chip. Geometry measurements: Distance between pillars: $110\mu m$, distance hole centres: $55\mu m$, distance between hole borders: $24\mu m$, hole diameter: $32\mu m$ all with small variations of the order of $0.5\mu m$.

The six chips were tested and the high voltage was applied on the grid if the chips worked. In Table 4 the status of the chips is listed.

Chip ID	Chip class	Grid status	Chip status	HV bond status
G06-W0096	A	good	perfect	detached, but 2/3 still touch surface
L07-W0013	n.a.	perfect	dead from beginning	2/3 ok
I03-W0013	C	one big scar, corners wavy some holes	dead after first spark current between chip and grid	1/3 ok
H01-W0013	C	top left corner wavy	2244 pixels masked current between chip and grid top left corner	2/3 ok
K09-W0016	C	perfect	not dead, but can't be used due to electrical problems	0/2 ok
L09-W0032	D	perfect	detected as Medipix 98% bad pixels	2/3 ok

Table 4. Status of the six available Timepix Ingrid chips

The chip G06-W0096 was used for all the measurements. It has a SiProt layer of $8\ \mu\text{m}$ thickness consisting of Si_3N_4 . After several sparks first three, later nine columns died. After one strong spark at the end of the measurements the chip had to be recalibrated completely and the uniformity of the response was not as good as before. The chip H01-W0013 has a connection between the grid and the pixels. With this chip a current of some tens of nA at a voltage of 300 V was measured. It can only be used with care and is used as spare chip.

A critical point is the high voltage connection for the grid. A pad of $300 \times 300\ \mu\text{m}^2$ is foreseen for this connection. The grid is an aluminium layer of $1\ \mu\text{m}$ thickness supported by soft SU8. Bonding is a difficult task under this conditions. The wire bond will penetrate the aluminium layer and push into the SU8. A fixation of the wire on top of the grid was possible with some experience. Many wire bonds were disconnected in operation, see Figure 28. For that reason the HV connection of the grid was done using two or three wires on different positions. For the G06-W0096 chip the HV wires were disconnected but still touched the surface as they were twisted and pushed on the surface. Lately the bonding connection on the grid has additionally been fixed with a small drop of silver glue.



Figure 28. Microscope image of the bonding pad of the grid on chip G06-W0096. The big hole on the pad on the left was the place where a wire bond was fixed. The other holes come from several attempts of bonding.

3.2 Detector

With a Timepix InGrid detector the readout and amplification structure is given. In this section the remaining parts of the detector will be explained. Two gas-tight boxes were used for the experiments. They host the Timepix Ingrid chip on a PCB and the drift cathode. Gas pipe connections, voltage connections for the cathode and grid voltage are available as well as data cable connected to the readout interface.

3.2.1 Saclay gas box

The gas box used in Saclay is made of aluminium and has a volume of 1,5 l (inner dimensions $230 \times 130 \times 50 \text{ mm}^3$). The cover is a 10mm thick acrylic glass window. Photons from an ^{55}Fe source would strongly be absorbed by the glass window. The part of the window directly on top of the detector is made of a $12 \mu\text{m}$ Mylar® foil. There are three safe high voltage (SHV) connections, two gas connections, and two side windows for α particles available. The readout cable connecting the Timepix PCB with the MUROS interface is fed through the aluminium wall.

Inside the box the PCB is fixed on a plastic carrier. The drift cathode is a circular frame with a stainless steel mesh held by three pillars at a drift distance of at most 24mm on top of the Timepix Ingrid chip.

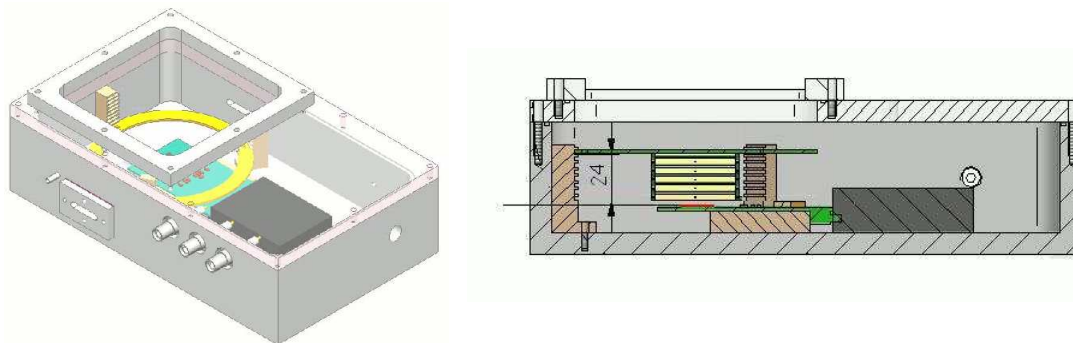


Figure 29. Schematic of the Saclay gas box (left) and cross section (right)

For field uniformity a six-stage voltage degrader ring is installed between the cathode grid and the chip. Each ring has a height of 3mm with a isolation of 1mm between to ring segments. The segments are connected by 10M Ω resistors. The top segment is connected to the cathode, the last segment via the third SHV connection to a variable resistance outside the box and connected to ground. This variable resistance is chosen such that the last ring segment is on the same potential as the InGrid. The other two SHV connections support the cathode voltage U_{cath} and the grid voltage U_{grid} . This gas box was used for all the measurements with the InGrid detectors. The Timepix PCB hosted the InGrid chips. A ^{55}Fe source was used to produce the primary electrons. The source was placed inside the box directly on top of the drift cathode or on top of the Mylar $^{\text{®}}$ foil. The primary electrons from the photon conversions between cathode and chip were drifted towards the InGrid chip and amplification structure.



Figure 30. Saclay laboratory setup: NIM rack with HV (background), computer with Pixelman software, InGrid storage box, experiment box, Micromegas box, MUROS interface (see section 3.3) and gas mixer (in the front).

During the measurements it was discovered that the 24mm drift distance were not sufficient to obtain enough diffusion to separate the primary electrons. An enlargement for the box has been constructed with a drift distance up to 80mm, see Figure 31. The advantage of this longer drift distance will be explained in section 4.2.4.

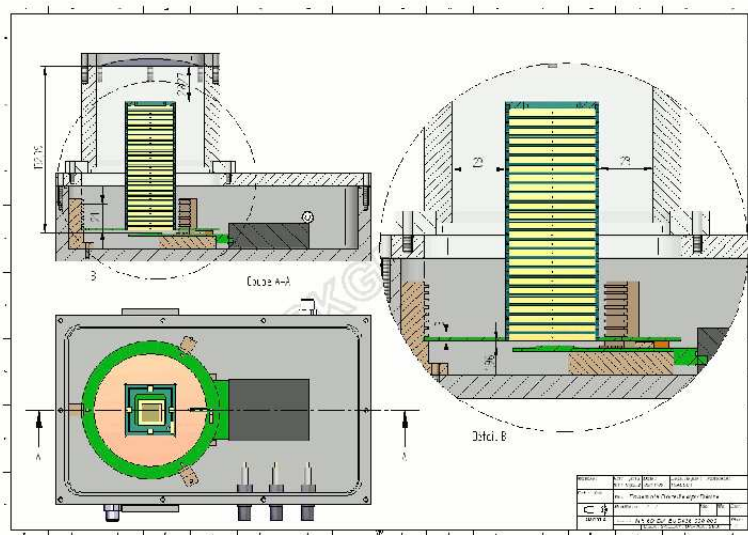


Figure 31. Schematic of the Saclay gas box with enlarged drift distance

Another gas box was used for Micromegas gain measurements, see Figure 32. This box is a transparent plastic box of $23 \times 23 \times 8 \text{ cm}^3$. The detector inside this box is a standard Micromegas ($5 \mu\text{m}$ copper mesh) with an unsegmented anode and a $50 \mu\text{m}$ amplification gap. The mesh has a size of $10 \times 10 \text{ cm}^2$, the drift distance is 1.3cm. This detector was used for gain measurements of the standard Micromegas inside the box. As it has the same gap size of $50 \mu\text{m}$ the results can be compared to the gain measurements of the InGrids.

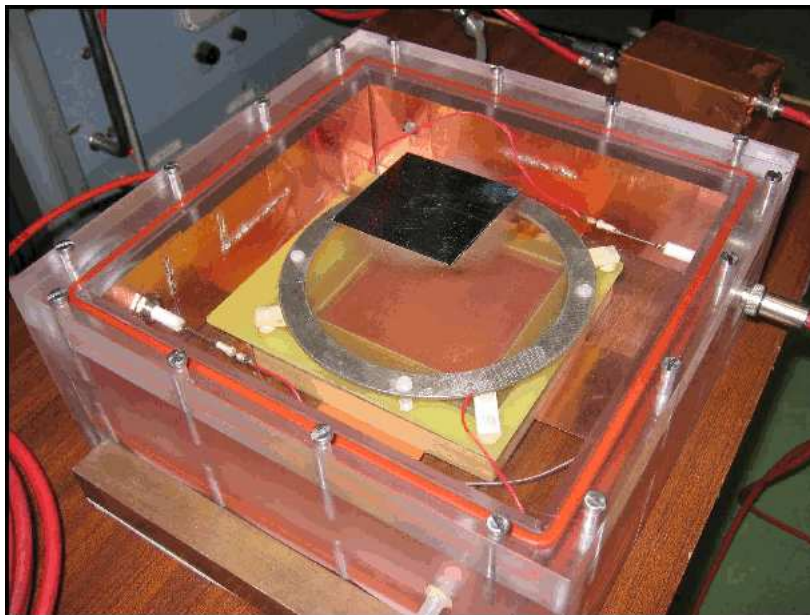


Figure 32. Standard Micromegas gas box

3.2.2 Freiburg gas box

A modular, non magnetic gas box has been constructed in Freiburg [Köh10] using stainless steel. It has a gas volume of 3.1l. The main body cylinder has an inner radius of 100 mm and a height of 100mm. Nine SHV connections, four gas connections and two beam windows are available. They can be equipped with fused silica windows with a transmission for light wavelengths between 185 and 3100 nm for LASER measurements. The chamber is also equipped with a pressure sensor with a precision of 0.5 mbar and temperature sensors with a precision of 0.5K. The data connection is done with a gas-tight PCB on the bottom. For the top cover a Plexiglas window as well as a stainless steel cover is available.

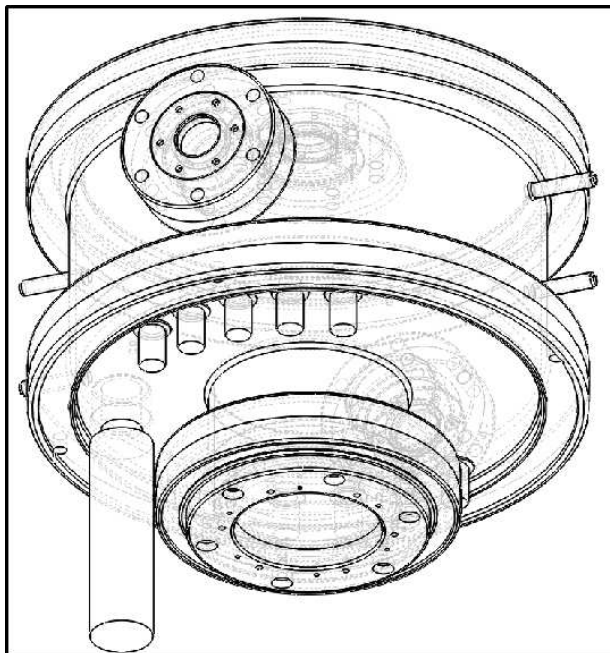


Figure 33. Schematic of the Freiburg gas box

3.3 MUROS Readout

The Medipix re-Usable Readout System (MUROS) [Bel03], produced at the National Institute for Nuclear Physics and High Energy Physics (NIKHEF) in Amsterdam, is an interface between the Medipix PCB and a National Instrument DIO-653X PC card. It can handle the signals of up to eight chips. For that amount of chips there has to be an additional power supply for the chips. Timepix chips can be used with the second version MUROS2. The clock frequency for the Timepix can also be set with the MUROS. For the measurements 36 MHz, 47.6 MHz and 60 MHz were used. The Pixelman software [HJP+06] was used to control the chip and visualise and register the data.

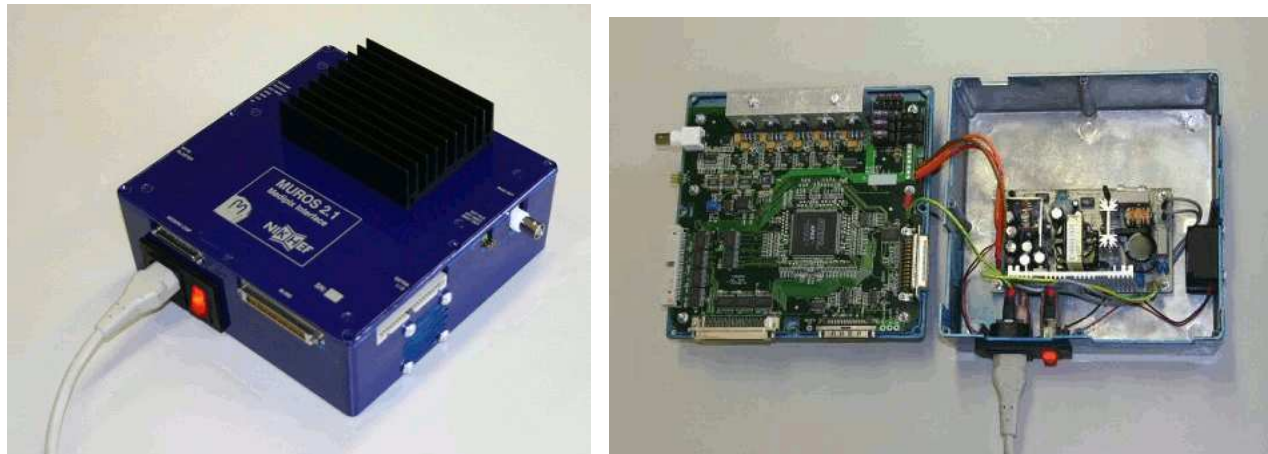


Figure 34. The MUROS 2.1 interface (left: closed, right: open), from [NIK]

3.3.1 Test pulses

The charge deposited in a pixel can be measured by the TOT counts as shown in Figure 23. A calibration is necessary to convert the TOT counts back to the number of electrons. Each pixel is equipped with a capacitor $C_f \approx 8\text{fF}$ in front of the preamplifier (Figure 22), such that an incoming electron signal from a pixel can be simulated:

$$Q = CU \Rightarrow Q_{\text{test}}[e^-] = U_{\text{test}}[\text{V}] \times 50000 \quad (33)$$

The test pulses can be applied if the TestBit on the chip gets a high signal from the ENABLE_TPULSE line coming from the MUROS. The test pulses are applied as analog signals from TEST_IN connected to an impedance converter. Only test pulses referring up to ≈ 40 k electrons can be simulated within the linear region of TEST_IN connection. However simulations showed that the linear range for signals coming from a pixel goes up to 200 k electrons [Llo06]. The calibration curve will hence saturate at around 40 k electrons. This is not due to the pixel electronics but to the test pulses. For charge coming from the pixel this linearity would go on until 200 k electrons. As every pixel has a slightly different behaviour (capacitor, preamplifier, discriminator), a pixel per pixel calibration would be preferable.

The MUROS interface can be used to apply this test pulses through the PCB to the chip (internal test pulses). The pulses are generated on the PCB. Test pulses can also be applied using a test pulse generator. The internal test pulse line needs to be cut on the PCB and the pulse generator is connected to the line going to the chip (external test pulses). For our measurements internal test pulses have been used. They show a good agreement to the measurements in [LBC+07] and [Umm08] who used external test pulses.

3.3.2 Threshold calibration

For the discriminator in the analog part of a pixel a threshold can be set by the 4 bit THLcoarse and 10 bit THL DAC. For the measurements the THLcoarse DAC was never changed and is set to the default DAC value of 7 for the G06-W0096 and H01-W0013 chip. To obtain a transformation between THL DAC values und the threshold level in number of electrons the s-curve method is used [Llo06]. The chip was set to Medipix mode and 5000 internal test pulses (period $28.1\ \mu\text{s}$, spacing 4) of different height at different THL DAC settings where applied using the Pixelman software. Spacing 4 means that every fourth pixel column in one run gets test pulses to avoid pixel cross talk. Four runs are needed to test all the pixels. The MUROS interface frequency was set to 36 MHz, 47.6 Mhz or 60 MHz. No frequency dependence of the threshold levels has been observed. If the threshold is lower then the noise, the counter will overload during the time of measurement. For a threshold higher than the noise, but lower than the pulse height

5000 pulses will be counted. If the threshold reaches the pulse high, the number of pulses counted will decrease to zero. The effective threshold is reached, when 50% of the pulses are counted. Figure 35 shows a s-curves measurement with the G06-W0096 chip for 5 different test pulse voltages.

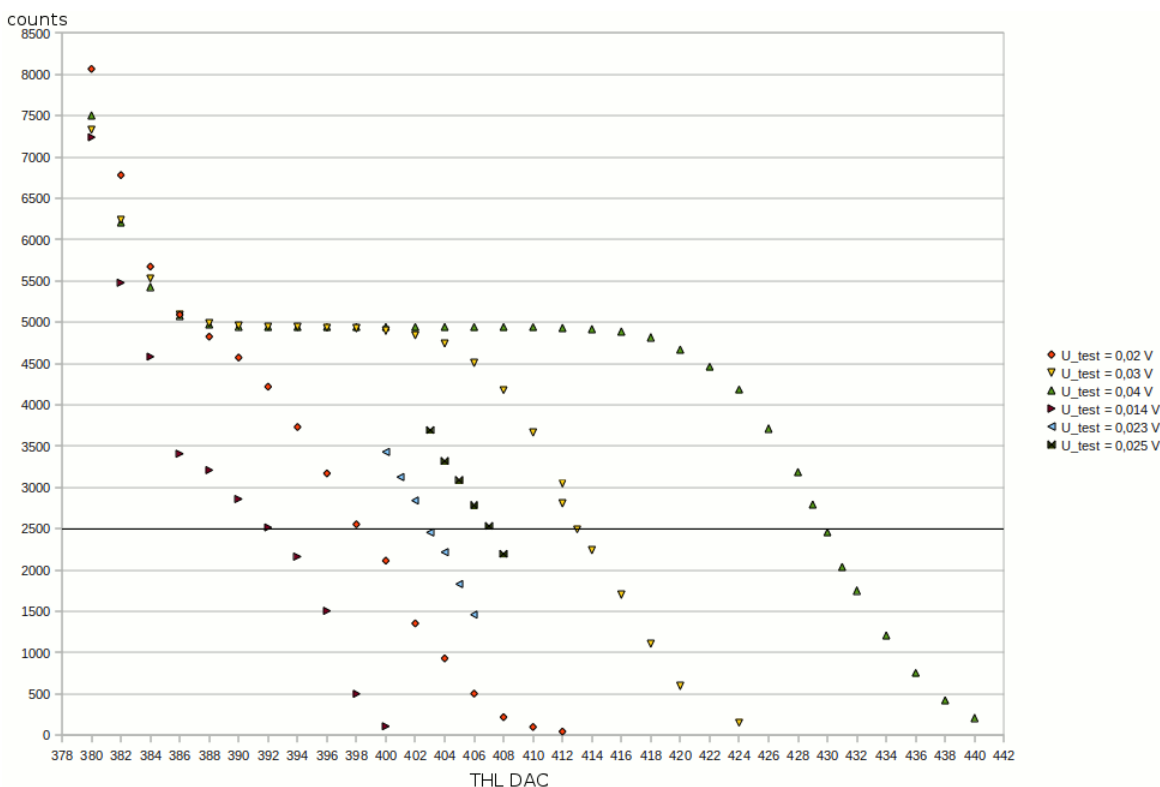


Figure 35. S-curves for different pulse voltages for the G06-W0096 chip. Registered counts as function of THL DAC values

In Figure 36 the 50% effective thresholds are plotted versus the number of electrons corresponding to the pulse height, which is obtained from the equation $Q_{\text{test}}[e^-] = U_{\text{test}}[V] \cdot 50000$. The result for this particular measurement was a value of $(31.8 \pm 0.6) e^-/\text{DAC step}$. The noise level was measured to be at $(367 \pm 1) e^-$, see Figure 36.

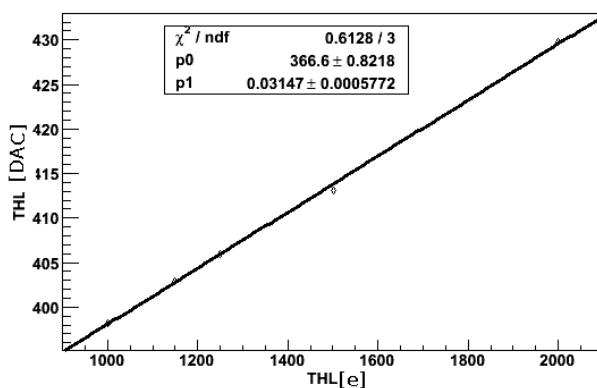


Figure 36. Threshold calibration curve for the G06-W0096 chip with linear fit

The DAC value 405 used for the measurements after this calibration corresponds to $1220 e^-$. This value was chosen because the noise was strongly suppressed at this threshold level for the typical acquisition times of 0.0001 s. The threshold calibration was done several times during the measurements. As recalibrations were necessary after some strong sparks the threshold level also changed. The lowest threshold level achieved was 1150 electrons.

3.3.3 TOT calibration

Test pulses are applied with the Pixelman software and a MUROS interface at 36 MHz, 47.6 MHz or 60 MHz to each pixel. For the different MUROS frequencies f_{Muros} the calibration curves are different. The distribution of the TOT counts from the whole Pixel matrix were recorded. The TOT counts can be converted to TOT time with the clock frequency f_{Muros} :

$$\text{TOT}[s] = \text{TOT counts} \times \frac{1}{f_{\text{Muros}}}. \quad (34)$$

In Figure 37 the mean of the distribution in TOT counts is plotted against the simulated number of incoming electrons for a MUROS frequency of 36 MHz. The curve shows a linear behaviour above ≈ 5000 electrons. It can be described by the formula

$$f(x) = ax + b - \frac{c}{x-d} [\text{Cze}]. \quad (35)$$

Note that the fit parameter d in number of electrons, which is an indicator for the threshold, is in good agreement with the threshold level of 1150 electrons. The TOT calibration was used in the analysis code to convert measured TOT values into electrons using the inverse function of Equation 35 and the fitted parameters:

$$x = f(y) = \frac{1}{2a} \left(ad + y - b + \sqrt{(-b + da + y)^2 + 4a(c + bd - dy)} \right) \quad (36)$$

The range of this fit curve was taken from 0 to 40 k electrons because at that level the charge from the pulses is not linear any more (see the measured TOT counts at the upper end of the curve in Figure 37).

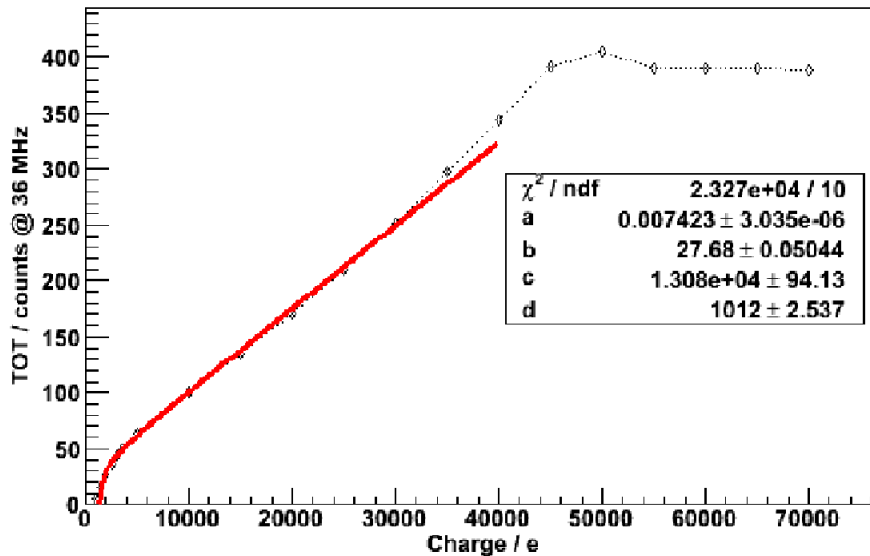


Figure 37. TOT calibration curve fitted by $f(x)$ for the Timepix chip G06-W0096 for $f_{\text{Muros}} = 36$ MHz

3.4 Laser test bench

A LASER¹⁰ test bench for MPGD has been build in Freiburg by myself. Its aim is to produce primary electrons by photo ionisation on the drift cathode. The position of the primary electrons can be chosen by the point the LASER is focused on the cathode. The number of primary electrons can be regulated with the laser intensity. I installed an optic rail with several components, see figure 38. The different components of the setup are:

- A PRA LN103 nitrogen LASER [PRA85] was used as light source. The LASER has a wavelength of 337nm, a peak power of 400kW and with pulses of 300ps length with a adjustable repetition rate up to about 30Hz. The beam divergence is 0.04 rad.
- Photo diodes (PDs) of the type Hamamatsu S1223.
- A beam splitter window with a reflection coefficient of 50% for the LASER wavelength measured with the PDs.
- An attenuation wheel with 20 steps of attenuation with transparencies from 100 – 16%.
- Additional attenuation windows with transparencies from 100 – 10%. Attentions down to 0.2% have been measured with combinations of windows and the wheel.
- A beam redirector consisting of two mirrors.
- Focusing lenses with focal lengths of 13 cm, 21 cm, and 39cm.
- The final focusing lens is installed on a rotatable mount.

The LASER beam is parallel to the optical table going in x -direction. The height (z -position) of the beam can be adjusted with the beam redirector. The y -position of the beam is fixed. See Figure 38 for the axes. The angle between the table plane and the beam can be adjusted by the last component on the rail. The final focusing lens installed at that element can be rotated around the y -axis. In Figure 39 a photo of the setup is shown.

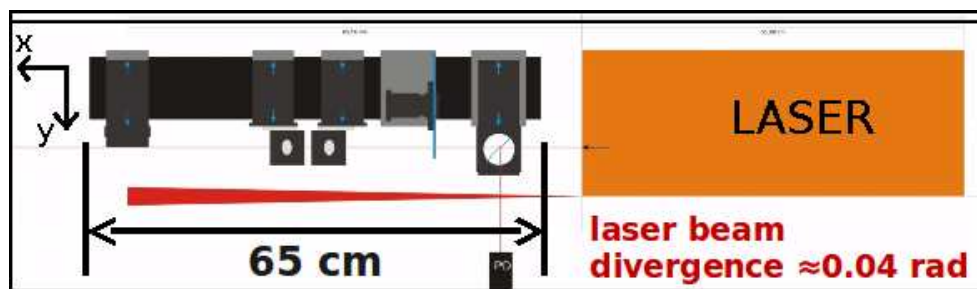


Figure 38. Schematic of the LASER bench setup (top view) with LASER, beam splitter, trigger PD, attenuator wheel, beam redirector and final focusing (from right to left). The optical bench has a length of 65cm. The beam divergence is 0.04 rad.

¹⁰. The principle of Light Amplification by Stimulated Emission of Radiation LASER is explained in many textbooks, for example in [Dem05].

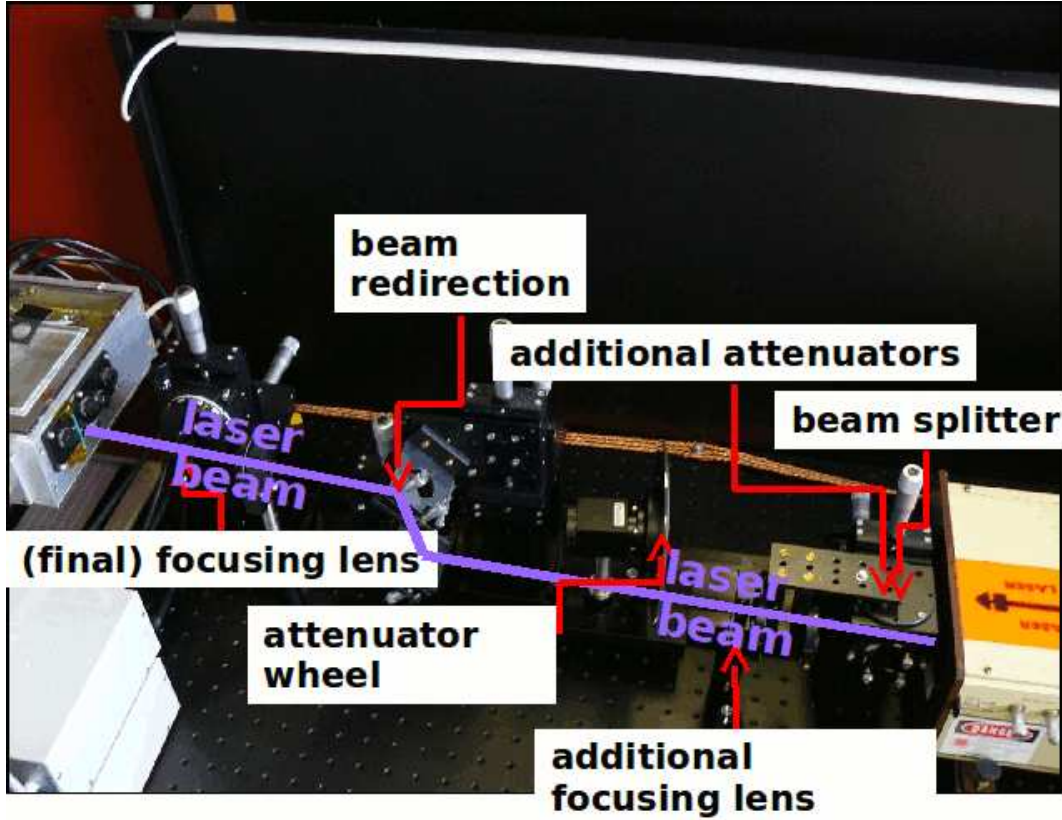


Figure 39. Photo of the LASER bench setup with LASER, beam splitter, additional focusing lens, attenuator wheel, beam redirector, final focusing lens and GEM gas box

We performed first test with the LASER test bench using a triple GEM amplification structure with Timepix readout using a GEM gas box [Bam07]. The primary electrons were detached from a nickel cathode photo effect. Ni has a work function of $W = 5.01\text{eV}$. The energy of a photon in the LASER beam is

$$E_{\text{Laser}} = \frac{hc}{\lambda} = 3.68\text{ eV}. \quad (37)$$

The photo electrons are detached by multiple photo effect or single photo effect from the tails of the electron energy distribution. The contribution of multiple photo effect increases with the illumination intensity. The probability for single photo effect depends on the temperature and the energy difference of W and E_{Laser} [ABF77].

The GEM gas box (Figure 40) has a quartz glass window with a diameter of 8.0mm for the LASER beam. The bottom side of the cathode is placed 5.5mm over the lowest point of the window (see Figure 40). The beam needs to be focused on the bottom side of the cathode over the Timepix chip. This position at the centre of the cathode is 86mm away from the entrance window. The cathode is a quadratic metal plate with a length of 124mm. The area where the LASER beam hits the cathode is made of a Ni grid with a lattice spacing of $220\mu\text{m}$. The drift gap size for this measurements was 6mm. The maximum angle for the beam incidence of the cathode is given by

$$\tan \alpha_{\text{max}} = \frac{5.5\text{mm}}{86\text{mm}} = 0.06395 \Rightarrow \alpha_{\text{max}} = 3.659^\circ. \quad (38)$$

Due to this small angle the focusing in x -direction is not possible. The top mirror of the beam redirection to be rotated by $\alpha_{\max}/2$ to redirect the beam off the optical bench axis.

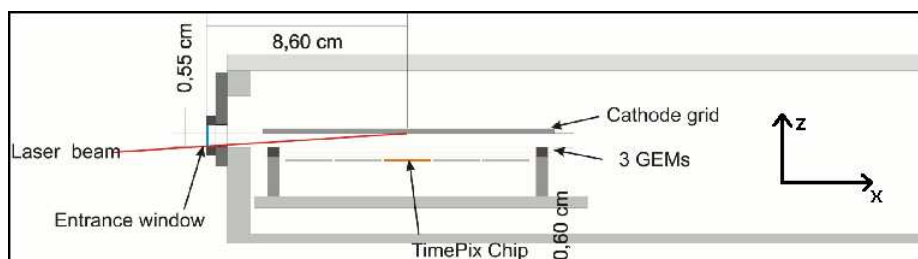


Figure 40. Schematic of the GEM gas box [Bam08] with a triple GEM setup (side view). The LASER beam has to be sent through a 55 mm quartz window into the 6 mm drift volume and is focused on the drift cathode grid.

As the laser beam can not be seen the adjustment of the laser beam and the focusing in the drift cathode was difficult. For that reason I first used a dummy cathode made of paper to adjust the position of the focal point. Later optical fibres, that absorbed the LASER light and emitted light in the visible part of the spectrum, were used. Figure 41 shows a photo that I took with 60 s of exposure time in an almost dark laboratory. The focal spot is visible through the paper.

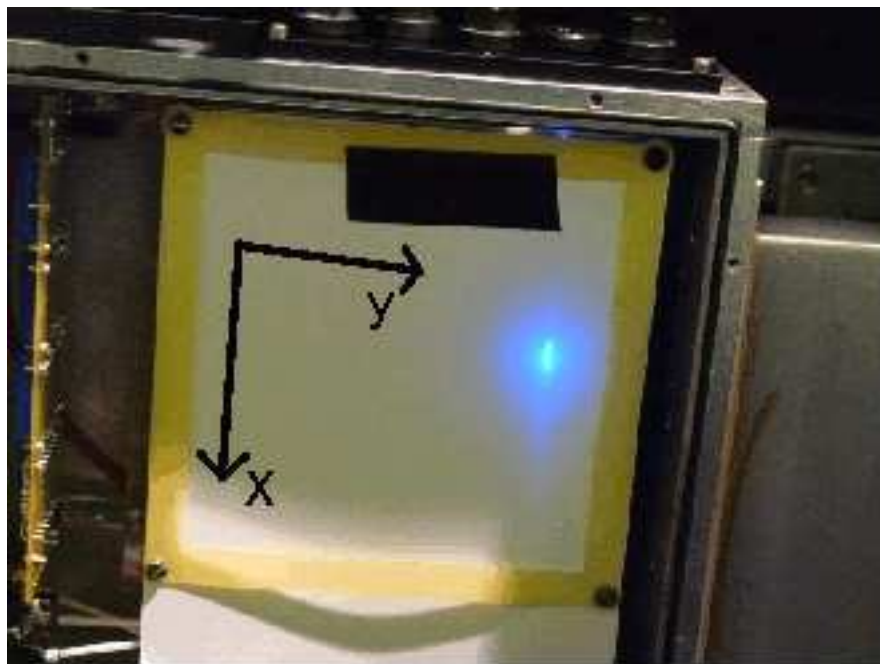


Figure 41. Photo from the top of the GEM box with a dummy cathode made of paper. Fluorescence light of the LASER beam focused on the cathode. The exposure time is 60 s.

The GEM gas box was mounted on a table movable in y - and z -direction. The z -direction was not changed once the beam was focused on the cathode. Changing the y -position led to different positions where primary electrons were created. The photo electrons were amplified in the triple GEM structure and registered on the Timepix chip. Figure 42 shows event displays from the Pixelman software of 4 different y -positions. The beam is focused in y -direction and defocused in x -direction due to the small angle of incidence.

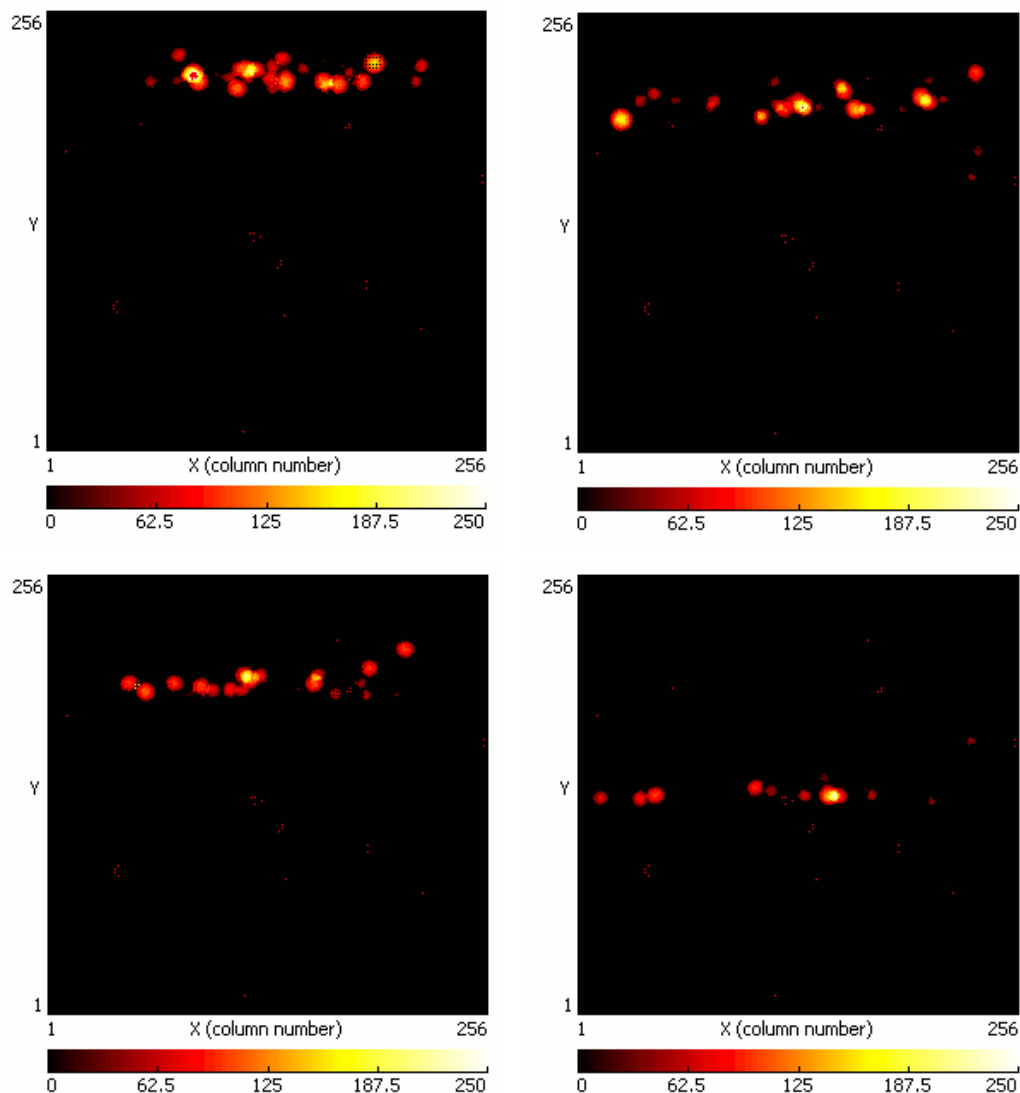


Figure 42. Pixelman event displays for different y positions of the LASER beam. The table with the GEM box was moved from in y -direction. The focus in y -direction and the refocusing in x -direction by the small angle of incidence is visible.

This first test measurements with a tripple GEM setup showed that the production of single electrons by photo effect on the cathode is possible. The beam can be focussed on the cathode on top of the Timepix chip. The setup was later used for measurements with a Timepix InGrid detector. The aim of this measurements was to produce primary electrons on a defined position with a defined frequency. The position could be defined by the focal point on the cathode, the frequency the primary electrons were generated could be set by the repetition rate of the laser pulses. Moreover the number of generated primary electrons could be defined by the LASER intensity using the attenuators shown in Figure 39. The results of this measurements will be presented in Section 4.5.5.

4 Measurements and results

In this chapter the results of the measurements performed will be presented. There have been two fields of

interest which were investigated. In Section 4.2 the measurement of the number of electrons in the ^{55}Fe spectrum is presented. The aim of this measurement was to measure the number of primary electrons in a photon conversion in ArIso 95/5 and possibly other gases. These measurements were carried out in TIME mode of the Timepix chip as, in this mode, several events in one Frame can be separated using the time information. This is important as the number of primary electrons per electron cloud has to be measured. Section 4.3 deals with the gain curve measurements, where for the first time the TOT information from the Timepix chip was used to calculate the gain of the InGrid detector. The TOT calibration curve from Section 3.3.3 was used to convert TOT counts to charge. The aim of this measurements were to measure the gain curve (dependency of the gain on the voltage in the amplification gap) with a Timepix InGrid detector and compare the results to a standard Micromegas detector. In the first section of this chapter the data acquisition and analysis will be explained.

4.1 Data acquisition and analysis

The data collected with the Timepix chips were read out by the MUROS interface connected to a National Instrument card in the PC. The Pixelman software was used to control the chip and register the data. As no external trigger was used, the chip recorded the events during an acquisition time that could be set with the software. The event display with the recorded clock cycles per pixel was illustrated as an event display of a coloured 256×256 matrix. One set of values from the 256×256 pixel matrix recorded for in one single acquisition is called frame. For each run several thousands of frames were recorded. The frames were saved in an ASCII file that consists of three rows: the x and y position of a hit pixel and the number of clock cycles it counted. This counted clock cycles could be TOT counts or TIME counts depending on the mode the chips was set to for the run. These files (one data sample) were saved together with a note file with the run parameters. The parameters changed in the measurements were:

- The grid voltage to obtain a different gain.
- The cathode voltage to obtain different field ratios $E_{\text{drift}}/E_{\text{amp}}$ where $E_{\text{drift}} = (U_{\text{Cath}} - U_{\text{Grid}})/d_{\text{drift}}$ is the electrical field in the drift region and $E_{\text{amp}} = U_{\text{Grid}}/d_{\text{amp}}$ is the electrical field in the region of amplification. U_{Cath} is the voltage of the drift cathode, U_{grid} is the grid voltage, $d_{\text{drift}} = 24\text{mm}$ is the drift distance and $d_{\text{amp}} = 50\ \mu\text{m}$ is the amplification gap size.
- The gas mixture and flux: Mainly Ar/Iso 95/5 with a flux of $10\text{l}/h$ was used, but also Ar/Iso 80/20, P10, CF_4 and CH_4 with different fluxes.
- The ^{55}Fe source position to change the rate. The acquisition time was adapted to the source rate in order to register approximately one photon conversion per frame.

A list with all the runs and the most important parameters can be found in appendix D.

The LASER test bench explained in Section 3.4 was also used to produce primary electrons by photo effect. These measurements needed different specifications as no ^{55}Fe source was used. They will be presented in Section 4.5.5. In the following the conditions for the experiments with the radioactive source will be explained.

4.1.1 Data acquisition

The acquisition time of the Pixelman software was set such that in each frame only one or two photon conversion events (shortly called events) are recorded. One event produces hits on several pixels. They come from the primary electrons produced in the photon conversion. All the electrons of one event and also the pattern of hit pixels are called an electron cloud. To reject frames that contain only noise, addi-

tionally only frames with more than 10 hit pixels were registered. Usually one run took between 20 min and 2h or was set such that 45000 frames were recorded. Some long term measurements were also performed.

4.1.2 Data analysis and cuts

The ASCII files of the frames were analysed with a C++ code using the ROOT analysis package. Several cuts were used to reject unusable events like cosmics or clusters that were coming from a conversion that was too close to the chip to provide enough separation of the primary electrons by diffusion. The code is slightly different for measurements in TIME and in TOT mode. This is due to the fact that in TIME mode it is possible to use the TIME information to separate two events in one frame. An event display example for both modes is shown in Figure 43.

Photon separation (for TIME data) For the analysis of the number of electrons per photon conversion it is important to have just one event per frame. Sometimes one frame contains two or more electron clouds. They can be identified by the time of arrival on the chip. In the spectrum of the TIME counts peaks are searched for. These peaks typically had a width of not more than 10 clock cycles (time bins) (some 100ns), depending on the MUROS clock frequency. One acquisition (recording time of one frame) was of the order of 100 μ s long. The peaks were clearly separated in the time spectrum. All pixels in an interval of 30 time bins around a peak are grouped to one photon conversion. Frames with several events are split such that each frame has just one event. This is the first step in the TIME analysis code. For the TOT mode this is not possible as no drift time information is available. The acquisition time in the TOT mode was set by a factor 3 shorter than for the TIME mode to be sure that most of the frames contain at most one event.

RMSratio cut (for TOT data) To be sure that in a frame of TOT mode only one electron cloud is present the circularity of the electron cloud is checked in the first step of the analysis code. The RMS of the electron cloud in x and y direction, rmsX and rmsY, is taken from a two dimensional histogram that has the number of clock cycles as entries. The rms ratio $\text{rms}_{\text{ratio}} = \text{rms}_x / \text{rms}_y$ is calculated. The cut variable is called $\text{rms}_{\text{ratio,max}}$ and was set to 0.2. Only electron clouds with

$$1 - \text{rms}_{\text{ratio,max}} = 0.8 < \text{rms}_{\text{ratio,max}} < 1.2 = \text{rms}_{\text{ratio,max}} + 1 \quad (39)$$

are accepted. In Figure 44 the histogram of the rmsRatios for one data sample is shown. The value of $\text{rms}_{\text{ratio,max}} = 0.2$ was chosen because it rejects most of the not circular events in the tails and accepts most of the almost circular events from one single photon conversions. The highlighted area in Figure 44 is the region where the cut condition is met. The event in Figure 43 on the left hand side is rejected, it consists of two photon conversions in one frame.

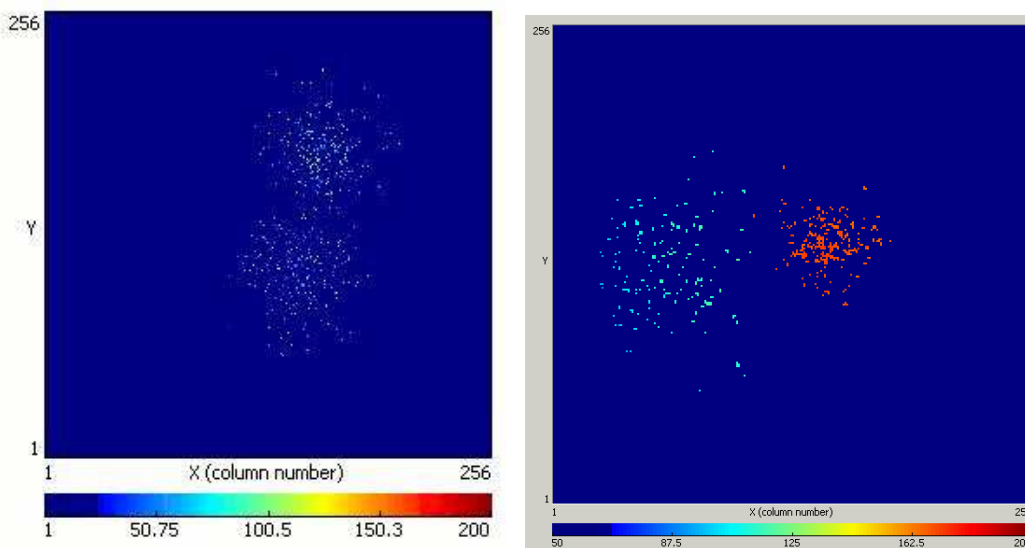


Figure 43. Pixelman event displays of TOT mode (left) and TIME mode (right). The colour code is the number of counted clock cycles equivalent to charge in TOT mode and arrival time in TIME mode.

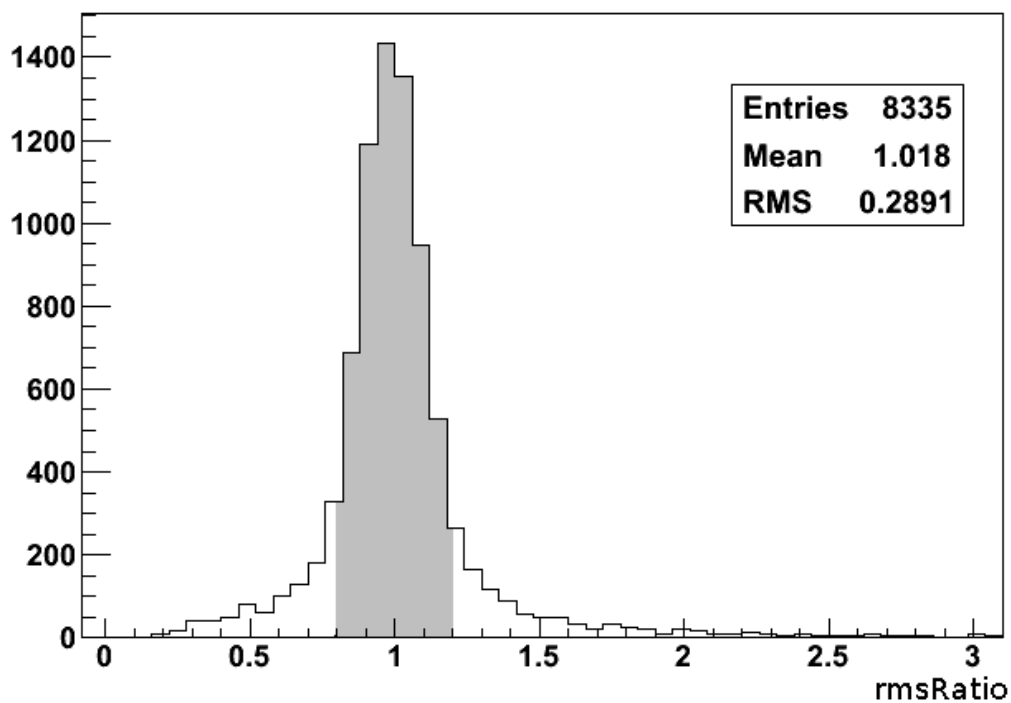


Figure 44. Histogram of the rmsRatios of the electron clouds in one data sample. The highlighted area is the region where the cut conditions are met.

Centre cut (for TIME and TOT data) As there is no guard ring around the Timepix Ingrid chip the electric field on top of the borders of the grid is not homogeneous. Electrons can be lost for events close to the borders. For that reason only electron clouds with their centroid (\bar{x}, \bar{y}) close to the middle of the

chip are accepted. The cut variables are \bar{x}_{cut} and \bar{y}_{cut} and the cut is done using

$$|\bar{x} - N_{\text{pixel}}/2| < \bar{x}_{\text{cut}} \quad (40)$$

where N_{pixel} is the number of pixels in x -direction (256 for a single Timepix chip). The same is done in y -direction. For \bar{x}_{cut} and \bar{y}_{cut} a value of 48 pixel was used. This value was chosen because it is three times the rms of an electron cloud with a sufficient diffusion (see next cut variable). This means that the centre of an electron cloud has to be within an area of 96×96 pixels in the centre of the chip, see Figure 45.

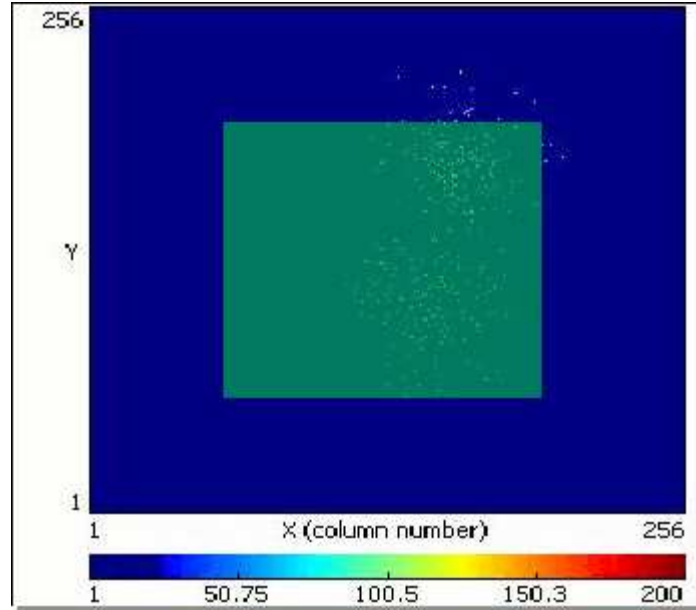


Figure 45. Pixelman event display with the area highlighted where the centre of an electron cloud has to be in order to be accepted by the centre cut.

RMS cut (for TIME and TOT data) It is the aim of the measurements in TIME mode to count the number of primary electrons and to measure the gain in the TOT mode. For both measurements it is important that an electron cloud is wide enough such that the primary electrons are clearly separated. If this would not be the case, the signal from several primary electrons would end up in one pixel. Not all the primary electrons would be counted and the TOT signal from that pixel would not be the gain of a single electron. Only in the case of clear separation every avalanche process is triggered by one primary electron and every primary electron enters through a different hole in the grid. Then every hit pixels (or cluster, see next paragraph) is equivalent to one primary electron. The electron cloud is spread by the diffusion along the drift through the drift volume. If a photon conversion takes place very close to the grid the electron cloud can not widen enough. A cut on $\text{rms}_{xy} = (\text{rms}_x^2 + \text{rms}_y^2)^{1/2}$ was done using the cut variable Rms_{cut} . Only electron clouds with $\text{rms}_{xy} > \text{Rms}_{\text{cut}}$ are accepted as highlighted in Figure 46. A value of $\text{Rms}_{\text{cut}} = 16.4$ was used.

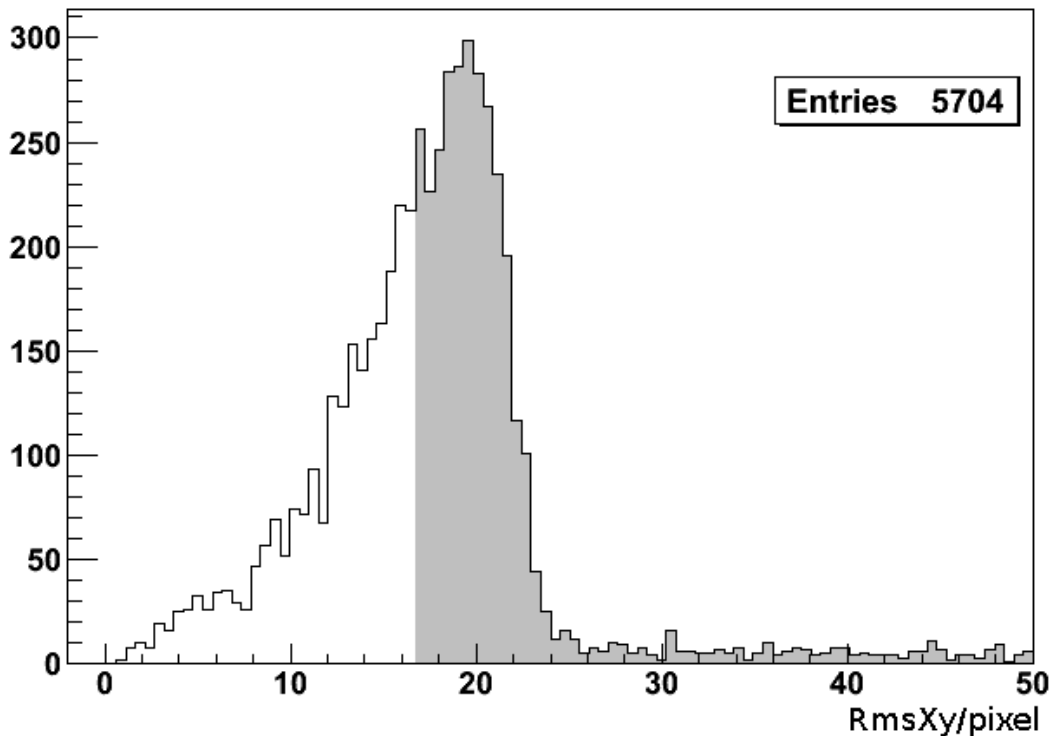


Figure 46. Histogram of the Rmsxy of the electron clouds in one data sample (no cuts applied). The highlighted area is the region where the cut conditions are met. The events with high Rmsxy are mainly cosmics and several photon events that would be sorted out by the other cuts.

The cut variable Rms_{cut} is related to the distance an electron cloud had to drift to become wide enough. In Section 2.1.5 the formula for the diffusion was introduced (Equation 20):

$$\sigma = D \sqrt{L} \quad (41)$$

where σ is the rms of the electron cloud, D is the transverse diffusion coefficient and L is the drift length. From Figure 46 we can see that the centre of the peak of the Rms_{xy} distribution is close to 20 pixel = $Rms_{xy,mean}$. The shape of the distribution in Figure 46 is an exponential increase until the peak around $Rms_{xy,mean}$ is reached. This comes from the exponential decrease of photons entering deeper into the gas. The events around $Rms_{xy,mean}$ are coming from photon conversion close to the cathode. This events have the longest drift distance and the highest diffusion when they arrive at the grid. The cut variable $Rms_{xy,cut}$ was chosen such that most of the events close to and higher than $Rms_{xy,mean}$ are accepted. Each pixel is $55 \mu m$ wide. Taking a diffusion constant of $480 \mu m/\sqrt{cm}$ (see Figure 20) one gets for the drift distance L those electrons are coming from:

$$L = \left(\frac{Rms_{xy,mean} \times 55 \frac{\mu m}{pixel}}{\sqrt{2} D} \right)^2 \approx 2.6 cm \quad (42)$$

which is in good agreement with the maximum drift distance of 2.4cm. The factor $\sqrt{2}$ comes from the fact that Rms_{xy} is defined as $Rms_{xy} = \sqrt{rms_x^2 + rms_y^2}$ but should be $Rms_{xy} = \sqrt{(rms_x^2 + rms_y^2)/2}$ to be comparable to σ .

Clustering (For TIME and TOT data) For high gains the secondary electrons produced in an avalanche can induce a signal on several pixels (charge sharing). For this reason attached pixels were connected to one cluster and the number of clusters were counted to obtain the number of primary electrons. Two

pixels are combined in one cluster only if they have one border in common. Pixels having a same corner are not combined to one cluster, see Figure 47. In the data most of the clusters have size one (they consist of just one pixel). At most every fifth cluster consists of two pixels, this is due to charge sharing or due to not enough diffusion, as will be explained in Section 4.2.4.

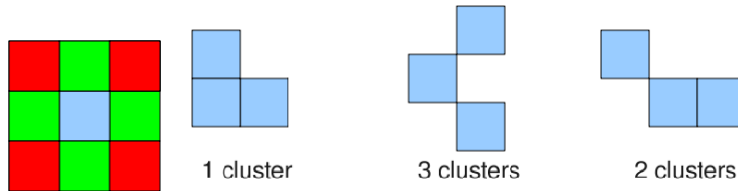


Figure 47. The clustering algorithm combines attached pixels to one cluster if they have the same border (left), some examples of clusters (right)

4.2 Primary electron counting

The aim of this measurement was to record the spectrum of the number of primary electrons per electron cloud. The measurements were performed using the TIME mode because in this mode several events in one frame can be separated. An ^{55}Fe source was used to produce the primary electrons. In Section 2.3 we have seen that a photon from the decay of ^{55}Fe ionises the atoms of the gas. A certain number of primary electrons is produced in the photon conversion depending on the gas. For argon-based mixtures a photo peak (where all the energy of the photon is transferred to ionisation) and an escape peak (a fraction of the energy is missing because a photon produced in the conversion escapes the detector) are expected. The number of primary electrons in the escape and photo peak are a Gaussian distribution around a mean value. The width of this distribution, the rms, depends on the statistical effects during the photon conversion (see Section 2.1.3) and the resolution of the detector. The measurements of the ^{55}Fe spectrum will be presented in Section 4.2.1. The efficiency of counting all the primary electrons will be presented in Section 4.2.4 and 4.5.4.

To absorb the K_β photons coming from the iron source a Cr foil was used, see Section 2.3. The effect on the spectrum is shown in Figure 48 for a data sample taken in ArIso 95/5 with a grid voltage of $U_{\text{Grid}} = 330\text{V}$ and a cathode voltage of $U_{\text{Cath}} = 2040\text{V}$. The RMS and centre cut are applied in the analysis. The shoulders on the right of the photo and escape peak, which are coming from the K_β photons are suppressed when the Cr foil is installed.

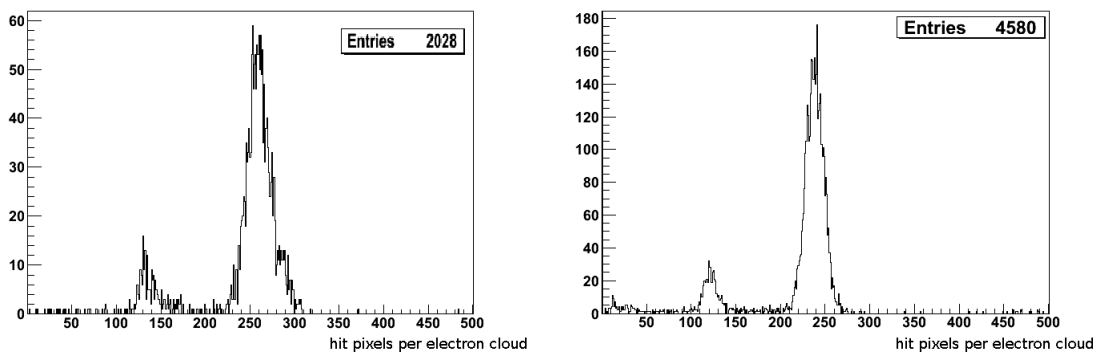


Figure 48. Histogram of the hit pixels per electron cloud with RMS and Centre cut without (left) and with (right) Cr foil. The effect of the K_β photons is visible in the left edge of the photo peak in the spectrum without Cr foil. Parameters for this measurements: ArIso 95/5, $U_{\text{Grid}} = 330\text{V}$, $U_{\text{Cath}} = 2040\text{V}$, RMS and centre cut are used in the analysis. Note the different number of entries.

4.2.1 Remark to the measured ^{55}Fe spectrum for the primary electron counting

The number of hit pixels and clusters per electron cloud were counted and histograms for one run was produced. The effects of the cuts will be demonstrated using a typical data sample. The parameters for this run were: ArIso 95/5 gas, $U_{\text{Grid}} = 330\text{ V}$, $U_{\text{Cath}} = 2040\text{ V}$.

In Figures 49-51 histograms of the number of hit pixels per electron cloud are presented. From the number of entries in the first histogram the number of photons in this run can be extracted. The photo and escape peak are clearly visible in the spectrum. Applying the RMS and centre cut reduces the number of entries from 44128 to 16427.

<i>Cuts</i>	no cut	RMS cut	RMS and centre cut
<i>Entries</i>	44128	34231	16427

The events with only a few hit pixels at the low end of the spectrum is clearly reduced by the RMS cut as this electron clouds are typically small. The centre cut clearly separates the two peaks. Events at the borders of the chip, where electrons can be lost, are sorted out by this cut. In Figure 51 Gauss curves are fitted to the escape and photo peak. The mean and sigma values for the two peaks are extracted and stored for further analysis. In 51 the parameters of the Gauss fit are given. The mean value of the photo peak in this data sample is 239 ± 0.1 with a sigma of 10.04 ± 0.07 . The error on the mean value of the peak position is of the order of 0.1 electron. This number is coming from the fit and the number of events in the peak. It can not be taken as an error of the position of the peak. This error was estimated by the repetition of runs under the same conditions. The result was an error of 1 pixel or cluster for the peak positions.

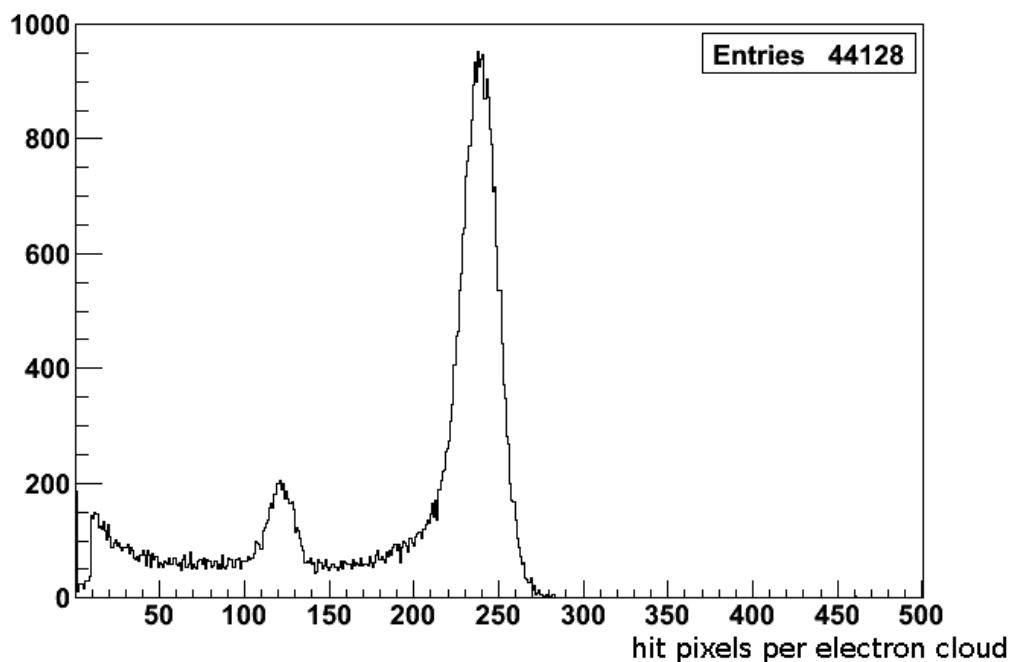


Figure 49. Histogram of the number of hit pixels, no cuts applied

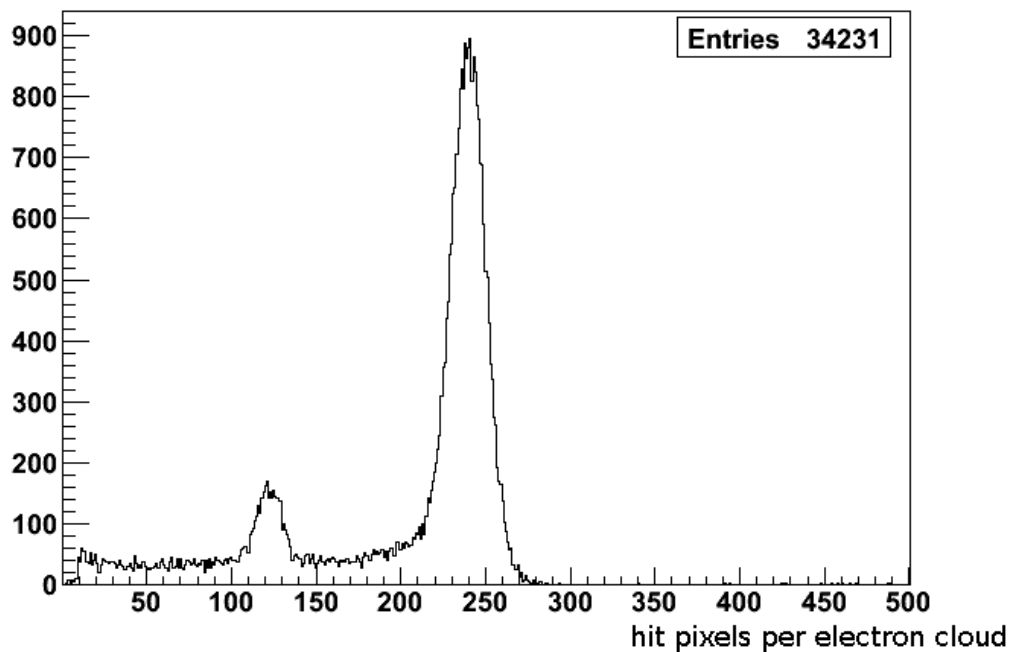


Figure 50. Histogram of the number of hit pixels, RMS cut applied

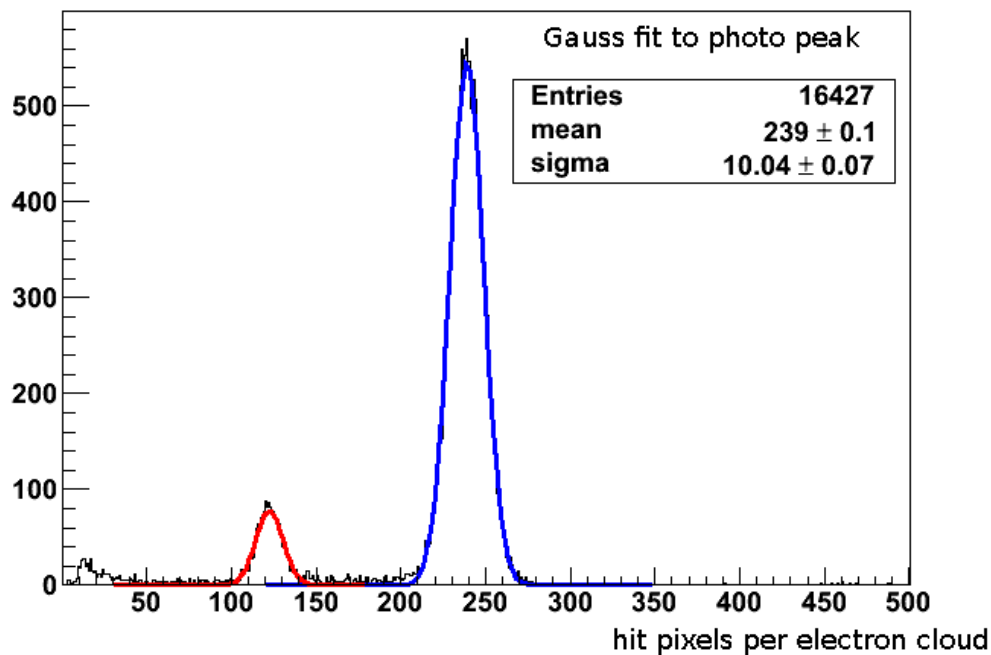


Figure 51. Histogram with fits of the number of hit pixels, RMS and centre cut applied

The same histograms are shown in Figure 52-55 for the number of clusters per electron cloud. The number of entries is the same, but the positions of the peaks are shifted to lower values as some pixels are combined to one cluster. The changes of the histograms when applying the cuts and the fit of Gauss

curves are shown. The increase of events is the same as for the pixels. The results of the Gauss fit for the photo peak in this data sample are a mean of 195.3 ± 0.1 clusters and a sigma of 11.13 ± 0.08 .

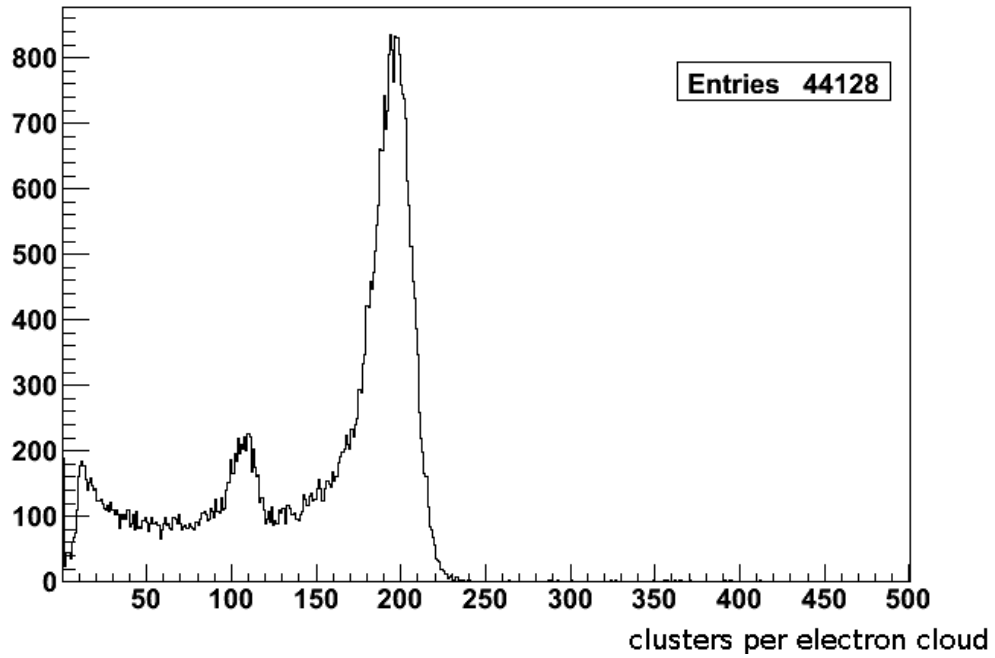


Figure 52. Histogram of the number of clusters, no cuts applied

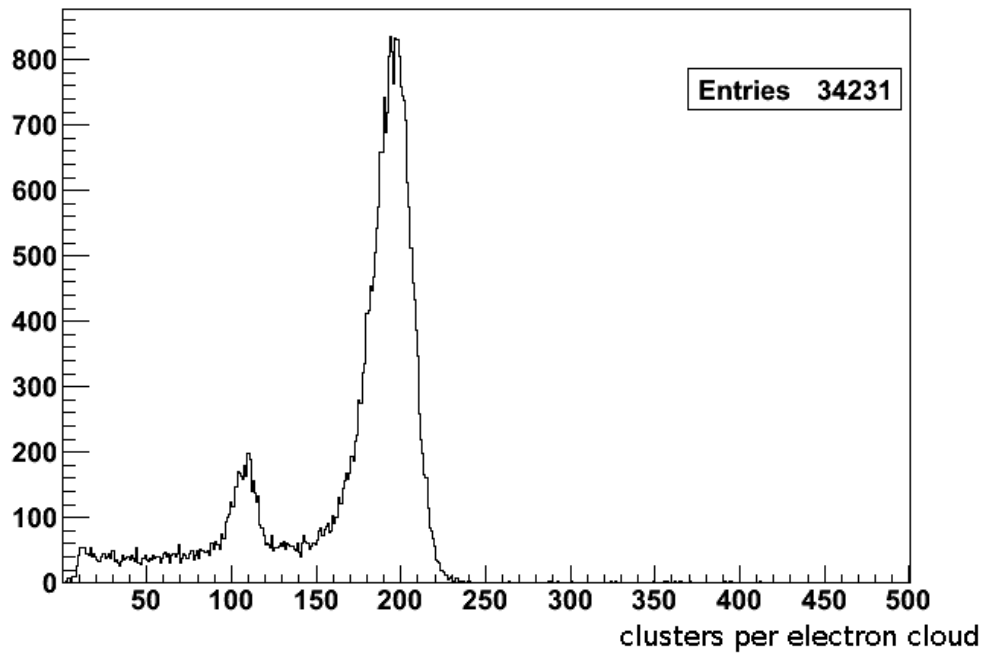


Figure 53. Histogram of the number of clusters, RMS cut applied

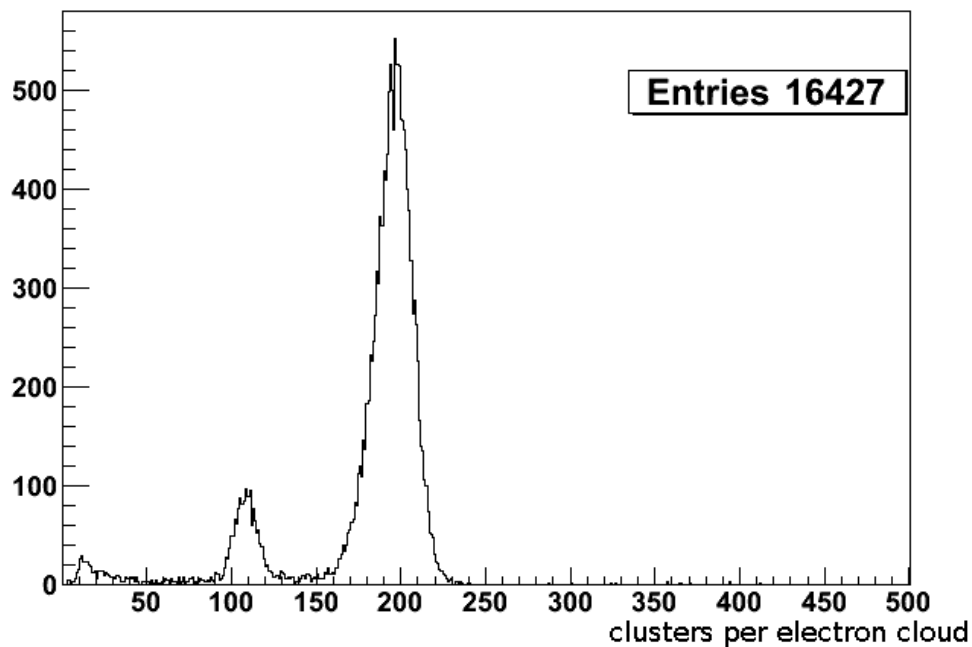


Figure 54. Histogram of the number of clusters, RMS and centre cut applied

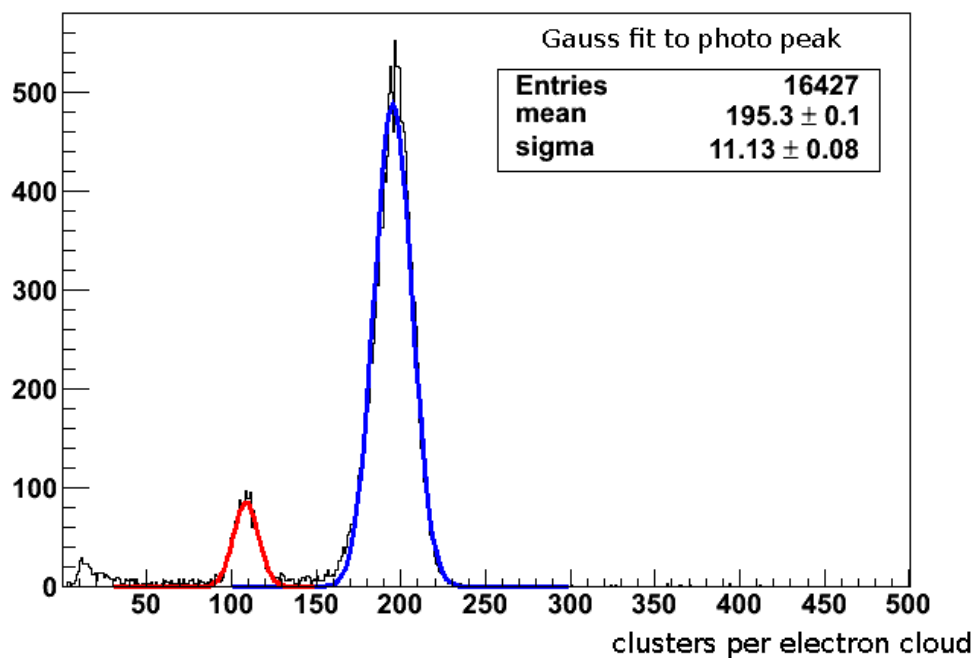


Figure 55. Histogram and fit of the number of clusters, RMS and centre cut applied

In Figure 56 cluster size histograms are shown with (right) and without (left) cuts. After the cuts

about 83.8% of the clusters consist of one pixels and $\approx 11.4\%$ of two and $\approx 2.5\%$ of more than three. The ratio of one pixel size clusters to two pixel size clusters was also extracted from the analysis. It can be used as an indicator for the separation of the electrons and the charge sharing.

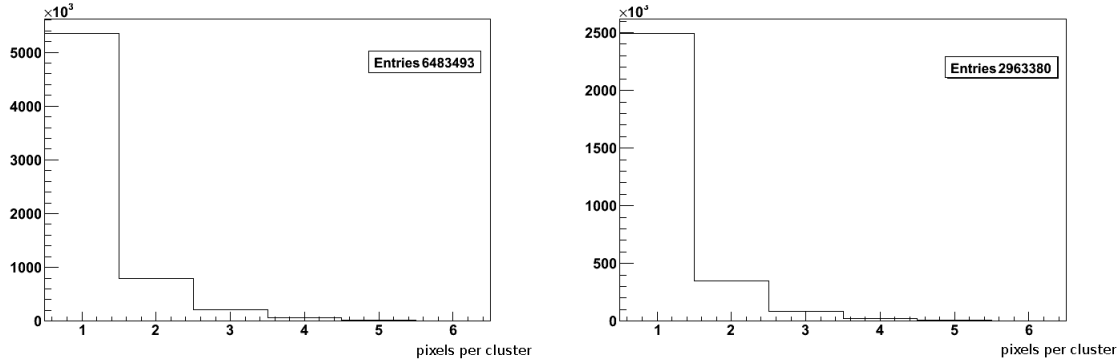


Figure 56. Histogram of the cluster size without (left) and with (right) centre and rms cuts. For the data without cuts about 82.1% of the clusters consist of one pixel. 11.9% of the clusters consist of two pixels and less than 2.9% of three pixel. After the cuts the distribution is: 83.8% size one clusters; 11.4% size two clusters and 2.5% size three clusters.

Other plots were produced to have an overview about the quality of the measurement and to verify if the source was placed on top of the centre of the chip. In this plots no cuts were applied such that all the events are included. They are presented in Figure 57. The control plots were:

- (1): A two dimensional matrix of 256×256 bins with all the centres (\bar{x}, \bar{y}) of the electron clouds. The distribution of the events can be seen in this plot to identify ineffective areas of the detector.
- (2): The circularity of the clusters can be checked in a histogram of the Rms_{ratio} . In this plot the effect of the Rms cut can be seen.
- (3): In a histogram of Rms_{xy} vs. the number of hits the relation between cloud size and hit pixels can be seen. The two accumulations of the escape and photo peak are clearly visible. The rise of the number of hits in bigger electron clouds can also be seen.
- (4): The circularity of the electron clouds and the size can be checked in the rms_x vs. rms_y plot. Circular clouds are accumulated on the line with $rms_x = rms_y$.
- (5): The distribution of hits in the x and y direction is checked to see if the source was placed in the centre on top of the Timepix chip or to find out if some regions of the detector were inefficient.
- (6): A three dimensional histogram with the hits in x and y direction shown the distribution of the hits on the chip.

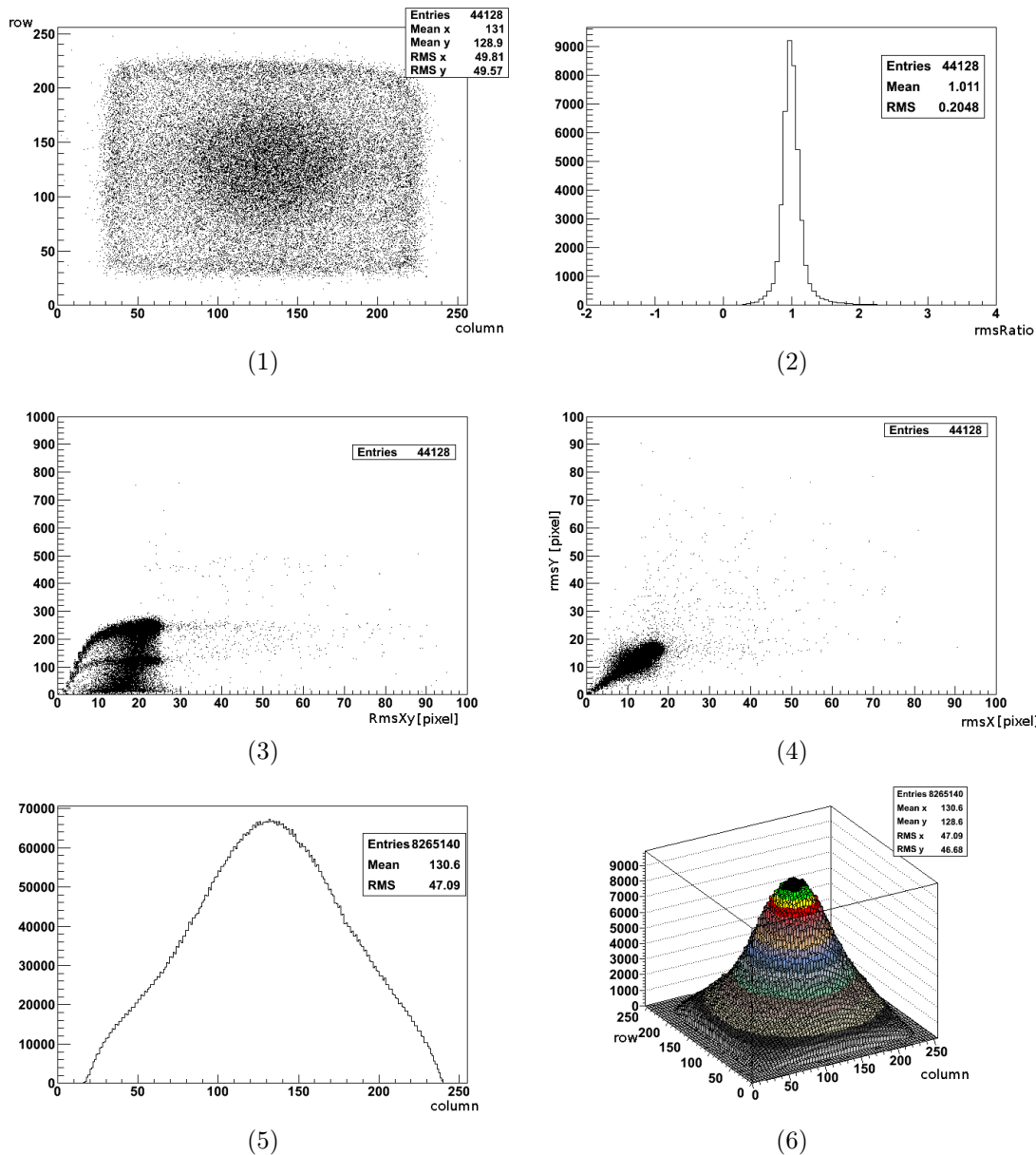


Figure 57. Control plots in the analysis of the electron spectrum measurements, all plots without cuts. (1) Positions of the centre of the electron clouds, dead or inefficient parts of the detector can be identified in this plot. (2) RmsRatio plot: The circularity of the electron clouds can be checked with this plot. (3) Number of hit pixels vs RMS: this plot shows the RMS values and the number of hit pixels in the electron clouds. The effect of the cut variable in the RMS cut can be checked. The rise at small RMS values is visible. (4) The RmsX vs RmsY plot shows the circularity of the electron clouds. (5) The distribution of the hit pixels in x -direction is shown in this plot. If the source is not placed in the centre on top of the chip this curve is not symmetric. The efficiency of the centre cut can be seen in this plot. (6) is a three dimensional plot of the distribution of the hits on the 256×256 pixel matrix but using only 64 bins for a better visualisation.

However from the pixel and cluster histograms of the ^{55}Fe spectra a general problem of the measurements is visible. In Figure 58 (top left), the spectrum of clusters for a data sample with ArIso 95/5, $U_{\text{Grid}} = 350\text{V}$, $U_{\text{Cath}} = 2060\text{V}$ is shown. The photo peak is placed at 204 ± 1 cluster (error not from fit, but by repetitions of experiments) as can be seen from the fit. For the escape peak the fit would lead to a mean value of 116 ± 1 . The escape peak is placed at a position of $(56.7 \pm 0.5)\%$ of photo peak, hence

higher than half the value of the photo peak.

In Section 2.3 the position of the escape and photo peak in argon based mixtures was calculated. The photo peak originates from a photon of 5.899 keV, the escape peak from a deposit of 2.9 keV in the detector. The ratio of these two values is 0.491. The escape peak should hence contain half the number of primary electrons compared to the photo peak. This is not the case in the measurements. The reason is that the drift distance in our measurements was not long enough to widen the electron cloud by diffusion such that all the primary electrons enter through individual holes in the grid and end up in individual pixels. An evidence can be seen in Figure 57 (3). The RMS of an electron cloud is an indicator for the drift distance. In the plot of RMS vs hits per electron cloud the number of hit pixels still rises with the RMS for the large accumulation at around 250 hit pixels (the events responsible for the photo peak). The accumulation finishes at RMS values of 25 pixels because the drift distance was not long enough to achieve higher diffusions.

Harder rms cuts were applied to the spectrum what resulted in significant loss of statistics see Figure 58 and Figure 59. With a drift distance of 2.4cm as in our experiment a diffusion leading to an rms of 20 pixels can be achieved. But as diffusion is a statistical process this value is just the centre of a Gaussian distribution. Electron clouds with higher rms values are less and less likely. The fit results for the escape and photo peak at different cut values are listed in the following table.

Rms _{cut}	16.4	20.1	23.2	25.9
Photo peak position	204±1	209±1	216±1	227±6
Escape peak position	116±1	117±1	117±1	-
ratio of positions	0.567±0.005	0.561±0.005	0.542±0.005	-

Table 5. Fit results for the position of the escape and photo peak for different Rms_{cut} variables for a data sample with ArIso 95/5, $U_{\text{Grid}} = 350V$, $U_{\text{Cath}} = 2060V$

It can be seen that the position of the photo peak changes when harder cuts are applied. This is due to the fact that with harder rms cuts only electron clouds with a better separation of the primary charge are selected. The position of the escape peak is not changing significantly when harder cuts are applied. In Figure 58(3) the accumulation responsible for the escape peak at around 100 pixels has a horizontal shape. This is due to the fact that in the escape peak only half of the number of primary electrons are present compared to the photo peak. The hit density on the chip in an escape peak event is only half of the value as in a photo peak event. For escape peak events the probability that the avalanches of two primary electrons end up on the same pixels with the given drift distance is smaller. In Section 4.2.4 we will see that the diffusion is large enough to detect all the primary electrons and arrive at a single electron detection efficiency (the efficiency to count all the primary electrons) better than 97%. For this reason the number of clusters in the escape peak is an important value in the analysis. Even for the hardest rms cut the position of the escape peak at half the value of the photo peak could not be achieved. The photo peak is not at the right position and can not be taken into account for the analysis of the number of primary electrons, hence only the escape peak will be used. Another argument for not using the photo peak to calculate the number of primary electrons can be found in Appendix A. It uses the cluster size in the photo peak, which is a direct indicator for low diffusion.

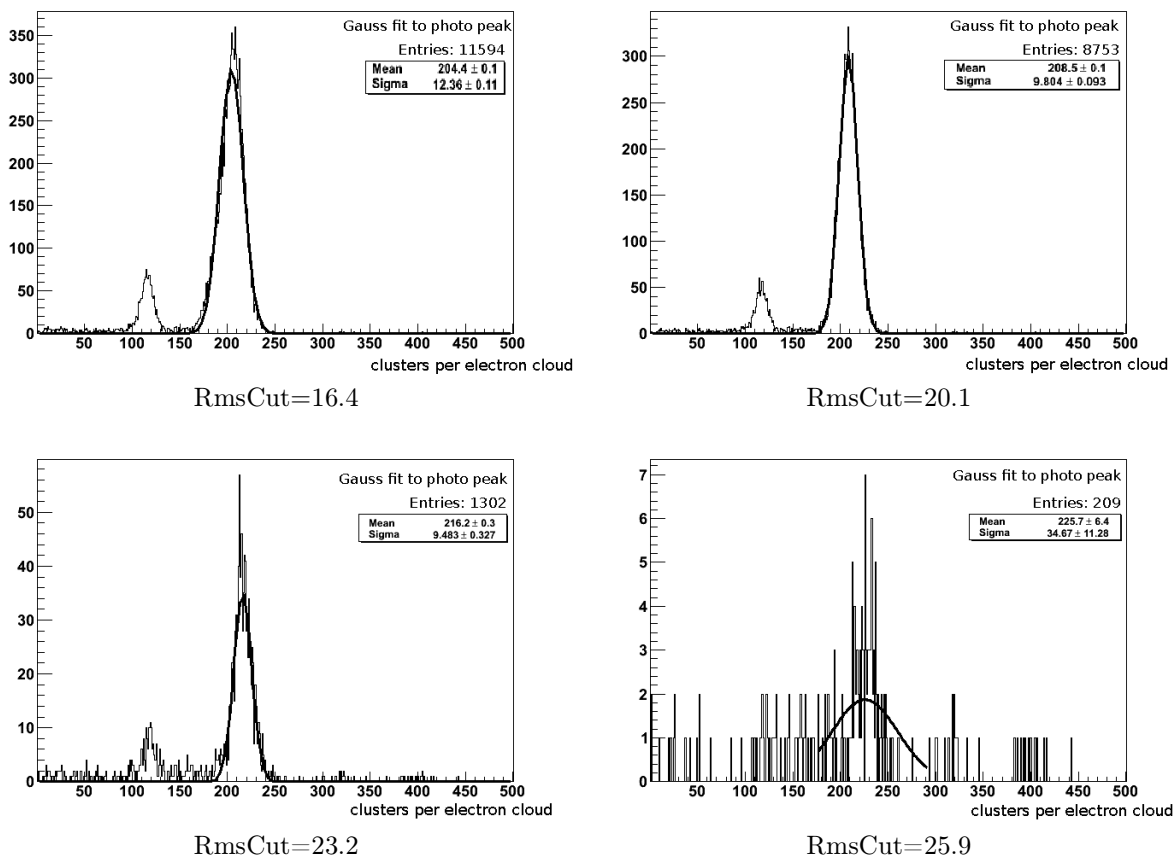


Figure 58. Spectrum of the number of clusters per electron cloud with RMS and centre cut at ArIso 95/5, $U_{\text{Grid}} = 350\text{V}$, $U_{\text{Cath}} = 2060\text{V}$. The number of photons in the run was 32545. Harder cuts on rms leads to a higher mean value of the Gaussian fitted to the photo peak but also to a significant loss in statistics. The position of the escape peak is not affected by harder cuts.

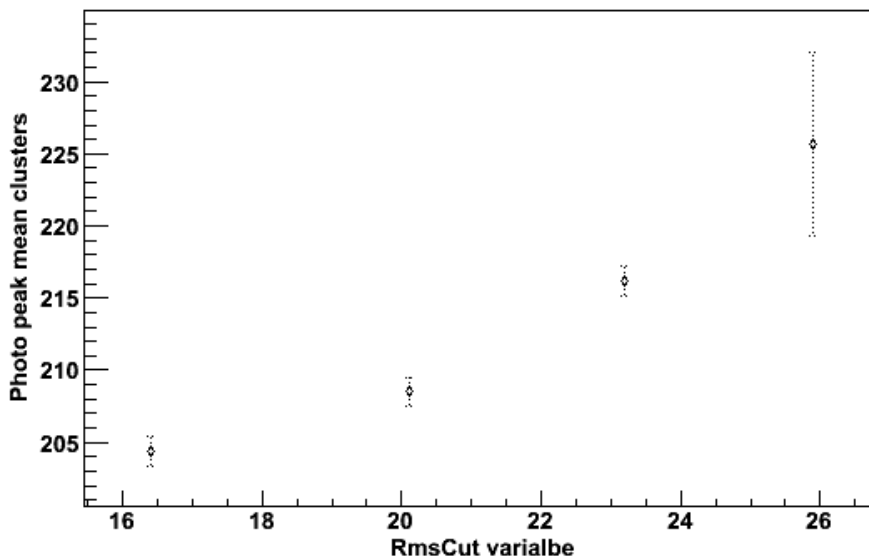


Figure 59. Position of the photo peak with RMS and centre cut depending on the RmsCut parameter for ArIso 95/5, $U_{\text{Grid}} = 350\text{V}$, $U_{\text{Cath}} = 2060\text{V}$. The errors on the peak positions is 1 cluster for the three lowest RmsCut variables and 6.4 for the highest one because in this case the error is dominated by small statistics.

4.2.2 Field ratio

Detector	Gas	$U_{\text{grid}}[\text{V}]$	$U_{\text{cath}}[\text{V}]$	Source	Aim of measurements
InGrid	ArIso 95/5	330	930 – 2530	^{55}Fe : weak	effect of field ratio on peak position

In ([Che09], Section 6.3.2) a dependence of the single electron detection efficiency on the field ratio $E_{\text{drift}}/E_{\text{amp}}$ is reported. In the measurements in [Che09] the current on an unsegmented anode was measured using a preamplifier and a MCA to get a spectrum. The gap size between InGrid and anode was $90\ \mu\text{m}$. Various grid geometries were used, the results are shown in Figure 60. For comparison the InGrids used in our measurements have a pitch of $24\ \mu\text{m}$ and a diameter of $32\ \mu\text{m}$. This values are a result of an optimisation process carried out in [Che09].

Before the measurement of the primary electrons were done, the effect of the field ratio has been studied. In our preliminary measurements for the given region of field ratios between 72 and 264 no significant variations of single electron detection efficiency were observed, see Figure 61. However for high field ratios (equivalent to low drift fields) the rate of the events arriving on the chip significantly dropped and the area where events are registered shrinks to a smaller and smaller rectangles in the centre of the chip. In Figure 62 the same histogram as in 57(5) is shown for a cathode voltage of 930V (field ratio 264) compared to 2040V (field ratio 93) in 57(5). The reasons for the loss of signals on the borders of the chip are field inhomogeneities because there is no guard ring around the chip to provide a uniform field.

For the main measurements of the primary electrons the cathode voltage was chosen such that $U_{\text{cath}} = U_{\text{grid}} + 1710\text{V}$. The grid voltage was changed in a range from $U_{\text{grid}} = 260\text{V}$ to $U_{\text{grid}} = 365\text{V}$. That results in a constant drift field of $712.5\text{V}/\text{cm}$ and field ratios between 72.98 (for lowest grid voltages of 260V) and 102.46 (for highest grid voltages of 365V). For the chosen drift field the area on the chip where signal are registered is as large as possible. Within this region of field ratios the single electron detection efficiency is assumed to be independent of the field ratio and only depends on the grid voltage. The geometry of the grid of InGrids (gap size, pitch, hole diameter) has been optimised using the results in [Che09] to arrive at the highest single electron detection efficiency.

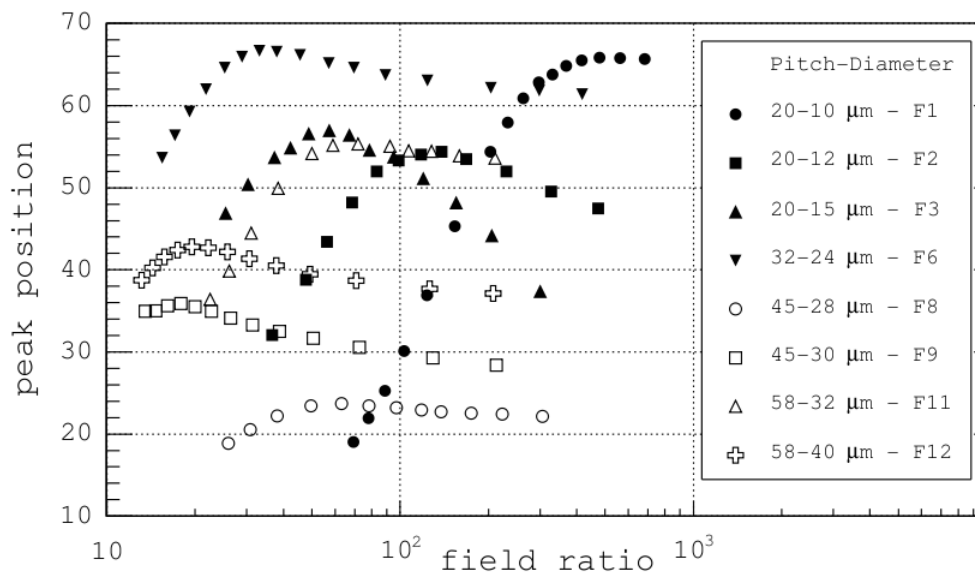


Figure 60. From [Che09]: Peak position and field ratio measured with InGrids of various hole pitches and diameters in Ar/Iso 95/5 at an amplification field of 41 kV/cm. For the measurements InGrids with a gap of $90\mu\text{m}$ on a unsegmented anode were used. The photo peak position is measured from the charge arriving on the anode.

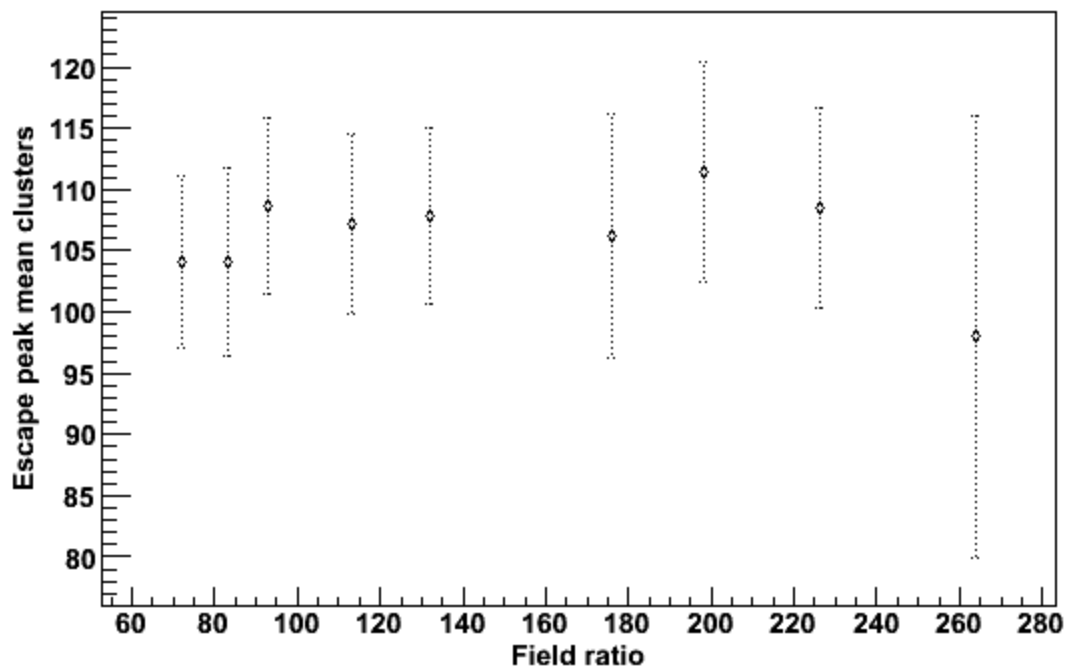


Figure 61. Field ratio scan with a Timepix InGrid detector with a gap of $55\mu\text{m}$ in Ar/Iso 95/5 with an amplification voltage of 330V (66 kV/cm amplification field). Number of clusters in the escape peak with RMS and centre cut as function of the field ratio. The error bars in the diagram are the rms values of the escape peak. The error on the peak positions is 1 cluster for the low field ratios up to 132 and 2 clusters for the the higher field ratios due to small statistics (only signal in the chip centre).

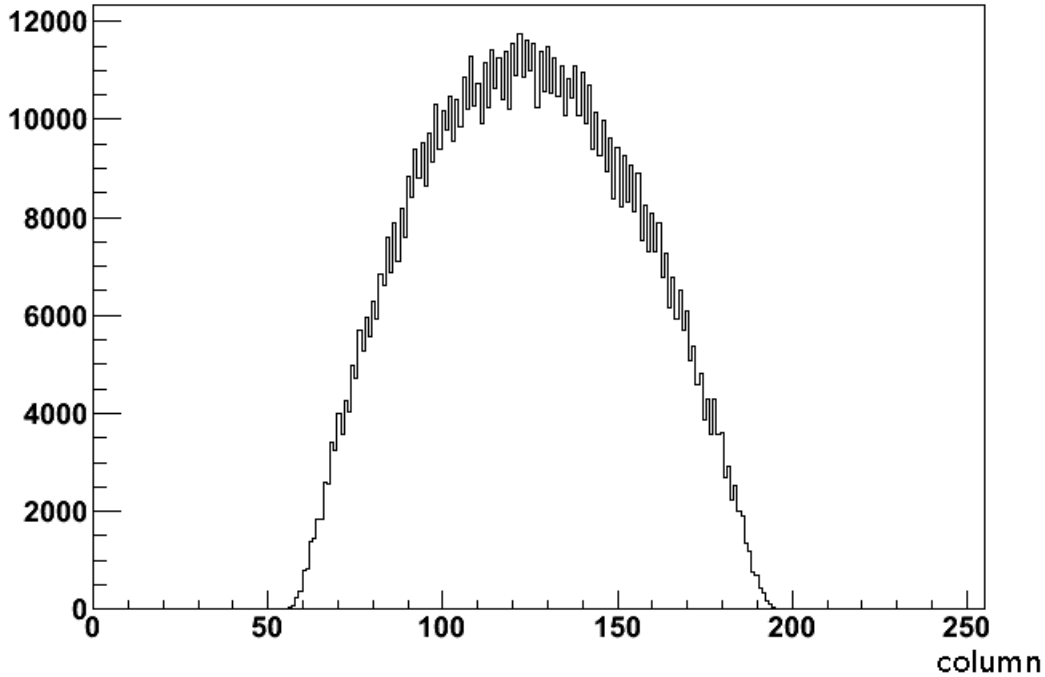


Figure 62. Distribution of the hits in x -direction for ArIso 95/5, $U_{\text{Grid}} = 330\text{V}$, $U_{\text{Cath}} = 930\text{V}$, no cuts applied.

4.2.3 Gas flux

<i>Detector</i>	<i>Gas</i>	$U_{\text{grid}}[\text{V}]$	$U_{\text{cath}}[\text{V}]$	<i>Source</i>	<i>Aim of measurements</i>
InGrid	ArIso 95/5	330	2040	^{55}Fe : weak	effect of gas flux on peak position

Preliminary measurements with different gas fluxes were done to check whether there are no differences in the number of counted clusters caused by contamination of the gas. Oxygen is known to capture free electrons and to reduce the number of primary charge. The positions of the peaks in the cluster spectrum are shown in Table 6. Except for a gas flux of 5l/h no significant variations of the mean number of clusters in the peaks is visible. The gas flux for the main measurements chosen to be 10l/h after the preliminary measurements presented in this section.

Gas flux	mean escape peak
5l/h	105 ± 1
10l/h	109 ± 1
20l/h	108 ± 1
30l/h	107 ± 1

Table 6. Cluster spectrum peak positions for different gas fluxes in ArIso 95/5, $U_{\text{Grid}} = 330\text{V}$, $U_{\text{Cath}} = 2040\text{V}$.

4.2.4 Single Electron detection efficiency

<i>Detector</i>	<i>Gas</i>	$U_{\text{grid}}[\text{V}]$	$U_{\text{cath}}[\text{V}]$	<i>Source</i>	<i>Aim of measurements</i>
InGrid	ArIso 95/5	280-365	$U_{\text{grid}} + 1700$	^{55}Fe : weak	number of primary electrons

The main measurements of the number of primary electrons is presented in this section. The single electron detection efficiency depends on the capability of the detector to measure the signals of the avalanches triggered by individual primary electrons. This capability depends on the ratio of signal to threshold of the detector. The threshold level has been measured in the detector calibration, see Section 3.3.2. The signal level is the mean value of the gain (\bar{G}). Let $p(g)$ be the normalised gain distribution with $g = G/\bar{G}$ and t the threshold level. The detection efficiency κ can be written as:

$$\kappa = \int_t^\infty p(g) dg \quad (43)$$

where κ is the fraction of avalanches that contains more secondary electrons than the threshold. Assuming a Polya like gain distribution $p(m, g)$ (Section 2.2.5) one gets:

$$\kappa(m, G, t) = \int_t^\infty \frac{m^m}{\Gamma(m)} \frac{1}{G} \left(\frac{g}{G}\right)^{m-1} \exp\left(-m\frac{g}{G}\right) dg \quad (44)$$

The parameter $m = \Theta + 1$ of the Polya function can be measured by fitting this curve to the measured detection efficiency (the number of counted primary electrons as function of the grid voltage). For these measurements it is necessary to know the gain G for each grid voltage. The gain measurements will be presented in Section 4.3 where also the detection efficiency will be discussed again. However in this section the measurements of the number of primary electrons from a photon conversion will be discussed. As explained in the previous section the number of clusters in the escape peak is a good value for this measurements. The single electron detection efficiency should be a function of only the grid voltage and arrive at a plateau of 100% for sufficiently high grid voltages or gains.

In Figure 63 the number of clusters in the escape peak for grid voltages U_{grid} from 280V to 365V are shown. A saturation curve of the form $f(x) = c - \exp(a + bx)$ is fitted to the data. The error bars in the plot are the rms of the escape peak for comparison. For the fit the error of the number of clusters in the peak of 1 cluster was used. The saturation occurs at 117.9 ± 0.7 clusters.

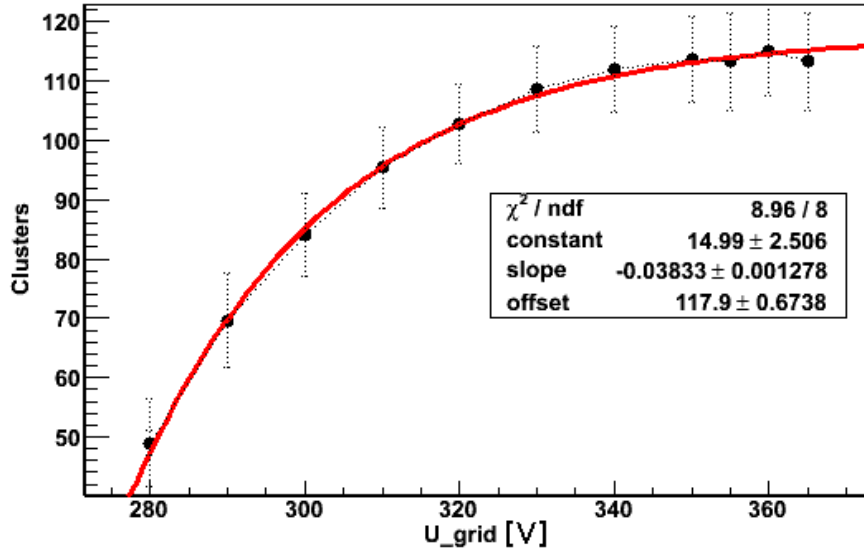


Figure 63. Clusters in the escape peak (RMS and Centre cut applied) as function of the grid voltage in Ar/Iso 95/5. Error bars are the rms of the escape peak. The error bars for the peak position (one cluster) would be smaller than the dots. For the fit a saturation curve of the for $f(x) = c - \exp(a + b x)$ was used. For the fit the error of the peak positions of one cluster was used.

The number of pixels in the escape peak is shown in Figure 64 for the same grid voltages. The saturation curve leads to a value of 144 ± 1 pixels. Again the error bars in the fit are the rms of the escape peak, but the for the fit an error of 1 pixel for the peak position was used.

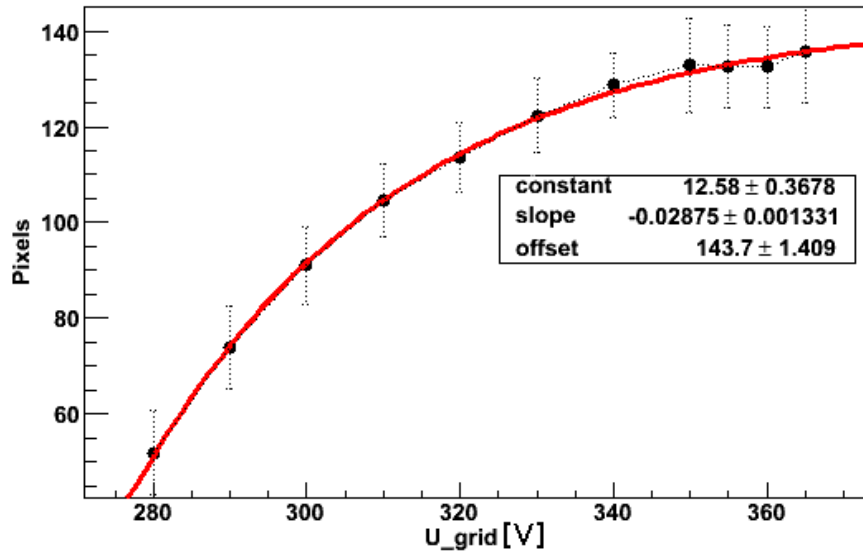


Figure 64. Pixels in the escape peak (RMS and Centre cut applied) as function of the grid voltage in Ar/Iso 95/5. Error bars are the rms of the escape peak. The error bars for the peak position would be smaller than the dots. For the fit a saturation curve of the for $f(x) = c - \exp(a + b x)$ was used. For the fit the error of the peak positions of one cluster was used.

The real mean number of primary electrons has to be between the number of clusters and the number of hit pixels. We have seen in Section 4.2.1 and Appendix A that the number of clusters in the escape

peak is a good indicator for the number of primary electrons. Charge sharing is present in the escape peak and leads to a higher number of hit pixels. A single electron detection efficiency of 97.8% has been achieved for the highest gains assuming that 117.9 clusters correspond to 100%.

The number of primary electrons in the photo peak can be calculated to 236 ± 1 by multiplying the value for the escape peak by two. The results of the measurement of the primary electrons are summarised in Table 7.

Peak	Primary electrons
Escape	117.9 ± 0.7
Photo	236 ± 1

Table 7. Results of the measurements of the primary electrons in ArIso 95/5

In the literature values from 220 [Che09] to 250 [BLRS10] primary electrons in the photo peak can be found for ^{55}Fe conversions in argon. In simulations the photo peak is located between 227 (HEED) and 233 (MAGBOLTZ) electrons [Sch10], see Figure 65. For the escape peak the mean values are 107 (HEED) and 116 (MAGBOLTZ).

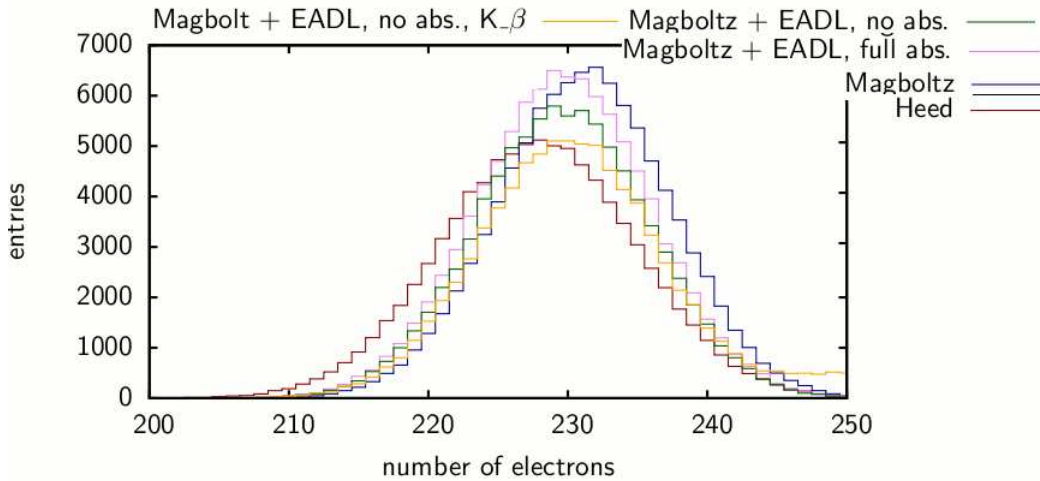


Figure 65. Simulation of the of primary electron spectrum from a photon of 5.9 keV in argon, zoom on the photo peak, from [Sch10].

4.2.5 Number of primary electrons in ArIso 80/20

Detector	Gas	$U_{\text{grid}}[\text{V}]$	$U_{\text{cath}}[\text{V}]$	Source	Aim of measurements
InGrid	ArIso 80/20	340-460	$U_{\text{grid}} + 1900$	^{55}Fe : weak	number of primary electrons

Measurements of the peak position were also performed in a mixture of Ar/Iso 80/20 for grid voltages U_{grid} between 340V and 460V. The cathode voltage was set such that $U_{\text{cath}} = U_{\text{grid}} + 1900\text{V}$ to achieve approximately the same field ratios as in the measurements in ArIso 95/5. In ArIso 80/20 mixture the diffusion constant is smaller than the one in Ar/Iso 95/5. The number of primary electrons should not change significantly as argon is still the main component of the gas. In Figure 66 the mean number of clusters in the escape peak is shown for different grid voltages. A saturation is not visible and the counted number of clusters is not in agreement with the number of counted clusters in Ar/Iso 95/5. The number of counted clusters in Ar/Iso 80/20 is smaller. The reason is that the diffusion is not enough to spread the primary electrons even in the escape peak to count every single electron. In the photo peak this effect is even stronger and only 128 clusters and 234 pixels were counted for the highest voltages.

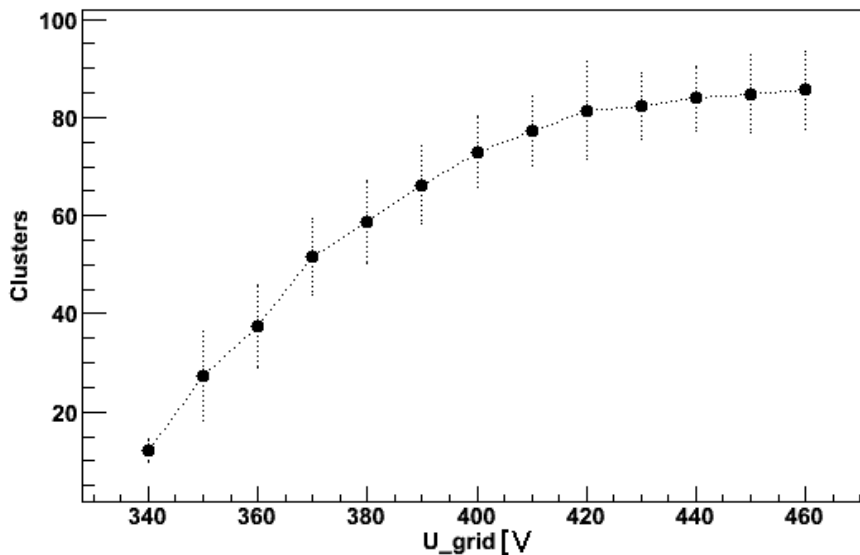


Figure 66. Clusters in the escape peak (RMS and Centre cut applied) as function of the grid voltage in Ar/Iso 80/20. Error bars are the rms of the escape peak. The error bars for the peak position would be smaller than the dots.

4.2.6 Peak resolution and Fano factor

<i>Detector</i>	<i>Gas</i>	$U_{\text{grid}}[\text{V}]$	$U_{\text{cath}}[\text{V}]$	<i>Source</i>	<i>Aim of measurements</i>
InGrid	ArIso 95/5	340	$U_{\text{grid}} + 1710$	^{55}Fe : weak	upper limit for Fano factor

In Section 2.1.3 we have seen that from the width of the peaks in the ^{55}Fe spectrum the Fano factor can be calculated:

$$F = \frac{\sigma_{N_e}^2}{N_e} \quad (45)$$

where N_e is the mean number of primary electron distribution and $\sigma_{N_e}^2$ is the rms. Now the detector will not for all gains be able to detect all the primary electrons. We have already seen that the single electron detection efficiency κ depends on the gain. Additionally there is a collection efficiency for primary electrons η that takes the loss of primary electrons, for example, by collection on the grid into account. For our InGrid we assume a collection efficiency of $\eta = 1$ [Col10] for the field ratios used in our experiments. The mean number of detected electrons N_d is given by

$$N_d = \kappa \eta N_e \text{ or } \kappa \eta = \frac{N_d}{N_e} \quad (46)$$

The Fano factor is then given by [Che09]:

$$F = \left(\frac{\sigma_{N_d}}{N_d} \right)^2 \frac{N_d}{\kappa \eta} + \frac{\kappa \eta - 1}{\kappa \eta} \quad (47)$$

To calculate the Fano factor either the number of primary electrons or the efficiencies η and κ have to be known. For the following calculations we assume that $N_{e,e} = 117.9$ in the escape peak and $N_{e,p} = 235.8$ in the photo peak as the saturation values of the number of clusters indicate. The Fano factors calculated here can just be an upper limit. Other factors apart from the intrinsic peak width can affect the width of

the peak. For example fluctuations of the gain due to temperature and pressure variations have been observed in long term measurements. The best resolution in the escape as well as in the photo peak was observed in a data sample recorded in a long term measurement of 14h in ArIso 95/5 at $U_{\text{Grid}} = 340\text{ V}$, $U_{\text{Cath}} = 2050\text{ V}$. The goal of this measurement was to record far more photons than in a two hours measurement (283345 compared to ≈ 10000 photons). A hard rms cut (RmsCut=23.2) was applied. After this cut the number of entries in the histogram was still larger than in a two hours measurement. The spectrum is shown in Figure 67 and the calculated Fano factors for the two peaks in Table 8. The two values are different but consistent with the results in [Che09] of $F \leq 0.21 \pm 0.06$.

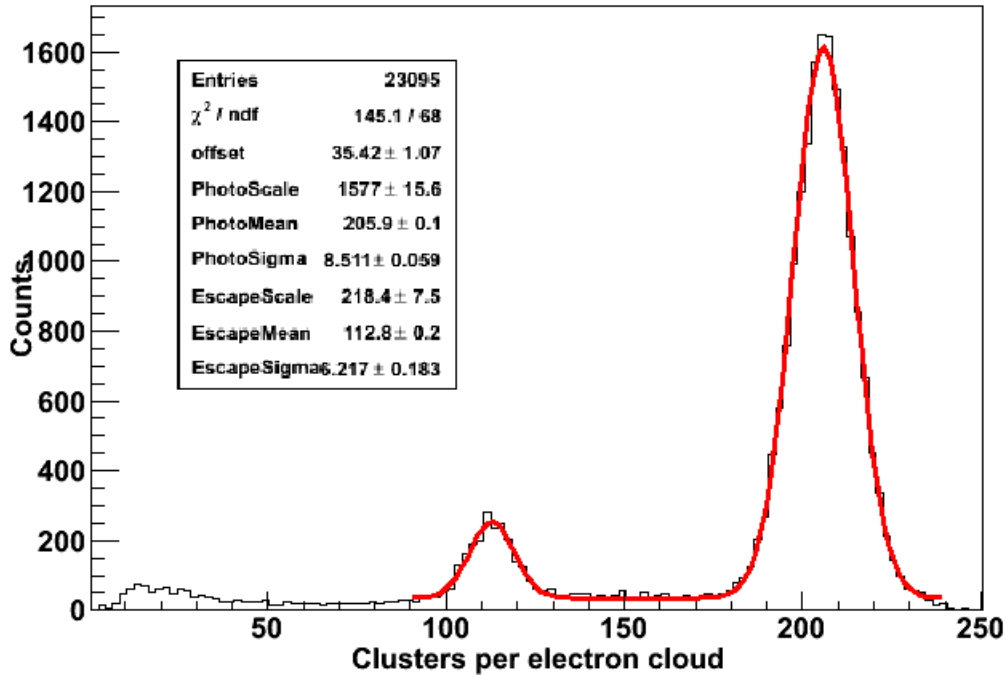


Figure 67. Cluster spectrum with the best resolution in photo and escape peak (RMS and Centre cut applied). ArIso 95/5, $U_{\text{Grid}} = 340\text{ V}$, $U_{\text{Cath}} = 2050\text{ V}$. A large data sample has been recorded in a night measurement and hard rms cuts (RmsCut=23.2) were applied.

The full width at half maximum (FWHM) of the photo peak is $\text{FWHM} = 2 \sqrt{2 \ln 2} \sigma \approx 20.04$ clusters or 9.73%. For the escape peak it is $\text{FWHM} = 12.98\%$.

Peak	Fano factor
Escape	0.31 ± 0.02
Photo	0.26 ± 0.01

Table 8. Calculated upper limits for the Fano factors for the spectrum with the best resolution, see Figure 67.

4.3 Charge measurements

In TOT mode the charge arriving in each pixel was measured. This experiments were the first, where the gas amplification was measured with a Timepix+Ingrid detector. The recorded TOT values were con-

verted to a number of electrons using the TOT calibration curve, see Section 3.3.3. The measured charge in each pixel corresponds to the number of secondary electrons. If the avalanche of the secondary electrons arriving in one pixel is triggered by one primary electron and no charge sharing occurs, the number of counted secondary electrons is equal to the gain. As the gain is a statistical process the number of counted electrons in one event in different pixels is different. A gain distribution can be recorded. Histogram of the charge per pixel were created. The number of entries in this histogram is the number of hit pixels in one run. The mean value of the gain distribution \bar{G} , simply called gain, has been measured for different grid voltages. The gain curve, the relationship between U_{grid} and \bar{G} , has been measured with a Timepix Ingrid detector and for comparison also with a standard Micromegas detector.

4.3.1 Ingrid gain measurements

Detector	Gas	$U_{\text{grid}}[\text{V}]$	$U_{\text{cath}}[\text{V}]$	Source	Aim of measurements
InGrid	ArIso 95/5	290-365	$U_{\text{grid}} + 1710$	^{55}Fe : weak	gain curve

In Figure 69 the measured TOT curves are shown for a data sample with ArIso 95/5 gas, $U_{\text{Grid}} = 330\text{V}$, $U_{\text{Cath}} = 2040\text{V}$. In the first histogram (1a) the raw TOT distribution, as it was recorded with the Pixelman software, is plotted. In (1b) the RMS ratio cut was applied, in (1c) additionally the RMS cut. In (1d) the RMS ratio, RMS cut and Centre cut are applied. The mean value and the rms of the distribution also get smaller especially if the RMS cut is applied. This is due to the fact that if the RMS cut is applied the diffusion of the electron clouds gets larger and not so many avalanches of different primary electrons end up in the same pixel such that the secondary electrons are added up what results in a higher TOT value. On the right hand side of Figure 69 the same histograms are shown for clusters. The TOT volume of a cluster is the sum of the TOT values of the pixels of the clusters. The mean value of the TOT distribution is hence larger for every histogram compared to the same cuts in the pixels histogram.

The aim of the TOT measurements was to record the TOT value of the pixels. As there are of the order of 200 hit pixels per electron cloud it was not necessary to record as many frames as in TIME mode. For crosscheck reasons histograms of the number of hit pixels and clusters per electron cloud were created. These spectra (see Figure 68 (left)) serve as control plots for the TOT measurements. The other control plots shown in Figure 57 for the TIME mode were also generated for the TOT mode. To check the reasonability of the TOT values an additional spectrum called TOT sum was generated. It is a histogram of the sum of all TOT counts in a electron cloud (Figure 68, right).

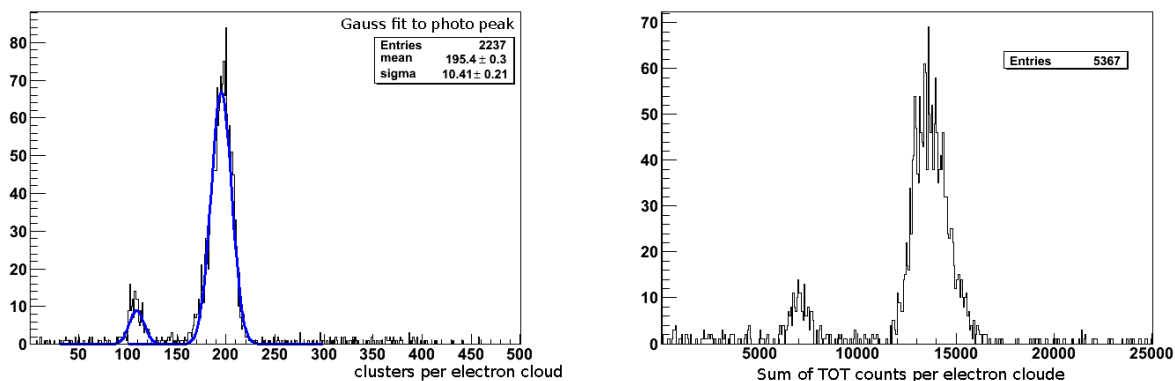


Figure 68. Spectra of the ^{55}Fe source in TOT mode (RMS, RMSratio and Centre cut applied). Number of clusters per electron cloud (left) with all cuts. Sum of TOT counts per electron cloud (right) without cuts. ArIso 95/5 gas, $U_{\text{Grid}} = 330\text{V}$, $U_{\text{Cath}} = 2040\text{V}$

For the analysis of the TOT distribution only the histogram of clusters with all cuts was studied. An

additional condition had to be met by clusters used for the gain studies. They had to consist of just one pixel to be sure that no charge sharing was present. Using the calibration curve from Section 3.3.3 the TOT counts were converted to number of electrons. In Figure 70 the spectrum of number of electrons is shown. Polya functions (see Section 2.2.5) were fitted to the spectra. The fit was done for the whole spectrum starting from 0 electrons and also starting from 4000 electrons. Reasons for that had been that the TOT calibration curve is not very accurate in for low charge pulses that correspond to fewer than 4000 electrons. The advantage of the fit starting from 0 is that it also takes the curvature of the distribution at the low end of the spectrum into account. But this could also be a disadvantage as the calibration can be wrong for low number of electrons, the Θ parameter ($p1$ in Figure 70) might also be wrong. For the mean value of the Polya curve at low voltages the fit starting from 0 electrons is more accurate and also more stable as the curve is fixed to 0 at 0 electrons. However for higher number of electrons the fitted curve differs from the data as it is mainly influenced by the curvature at the low end of the spectrum. The advantage of the fit starting at 4000 electrons is that the calibration and hence the shape of the electron spectrum is correct in this region. For high grid voltages (or high gains) when most of the spectrum is located higher than 4000 electrons and also the rise at the low end still continues at 4000 electrons this fit gives more accurate results. For high gains where also the curvature is taken into account with this fit the resulting Θ parameter should be accurate. In Section 2.2.4 and 2.2.5 where the gain distribution curves had been discussed we saw that the gain curves are not Polya distributed. A Polya distribution is chosen as fit function because it can be expressed analytically. For that reason the χ^2 values of the fits did not give good results.

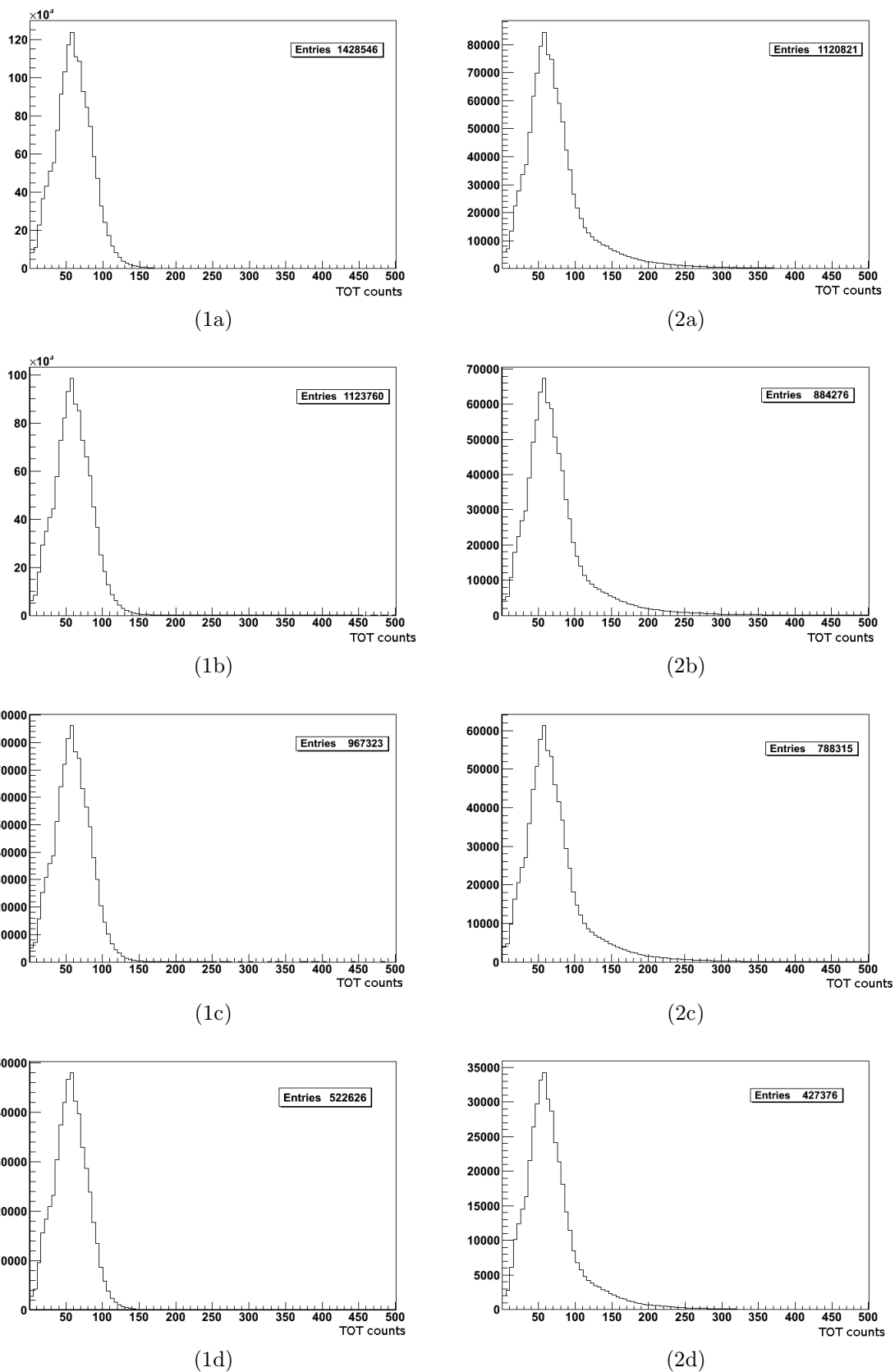


Figure 69. Histograms of TOT distributions for pixels (1, left) and clusters (2, right) with different cuts. In (a) no cuts are applied, in (b) only the RMS ratio cut, in (c) additionally the RMS cut and in (c) the RMS ratio, RMS and centre cut are applied. ArIso 95/5 gas, $U_{\text{Grid}} = 330V$, $U_{\text{Cath}} = 2040V$

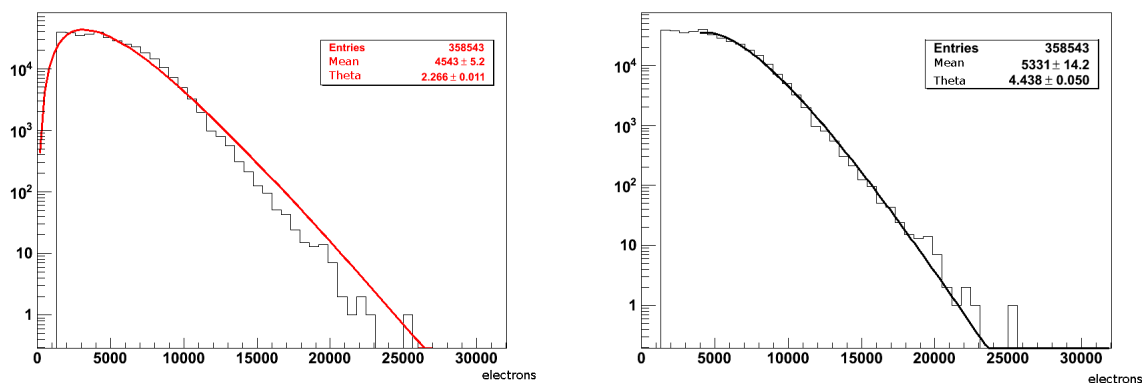


Figure 70. TOT spectra in number of electrons (RMS, RMSRatio and Centre cut applied) with logarithmic y -axis. The calibration from 3.3.3 is used for clusters of size one. Polya curves are fitted to the data starting from 0 electrons (left) and 4000 electrons (right). The fit parameter p_0 is the Mean, p_1 is Theta and p_3 is a scaling factor of the Polya curve. ArIso 95/5 gas, $U_{\text{Grid}} = 330V$, $U_{\text{Cath}} = 2040V$

In Figure 71 TOT spectra for different grid voltages are shown in one plot. To compare the different measurements the number of electrons G has been divided by the mean number of electrons \bar{G} for each voltage. The x -axis in Figure 71 is in G/\bar{G} . Also for comparison the TOT spectra were normalised to an integral of 1. Polya curves are fitted to the data starting at 4000 electrons for each data sample. Noise does not play any role in the TOT spectra. The threshold level was set such that only in 1000 frames only 100 pixels gave a noise signal. Moreover only frames with more than 10 hit pixels were registered. The detector was covered to prevent signals from UV light.

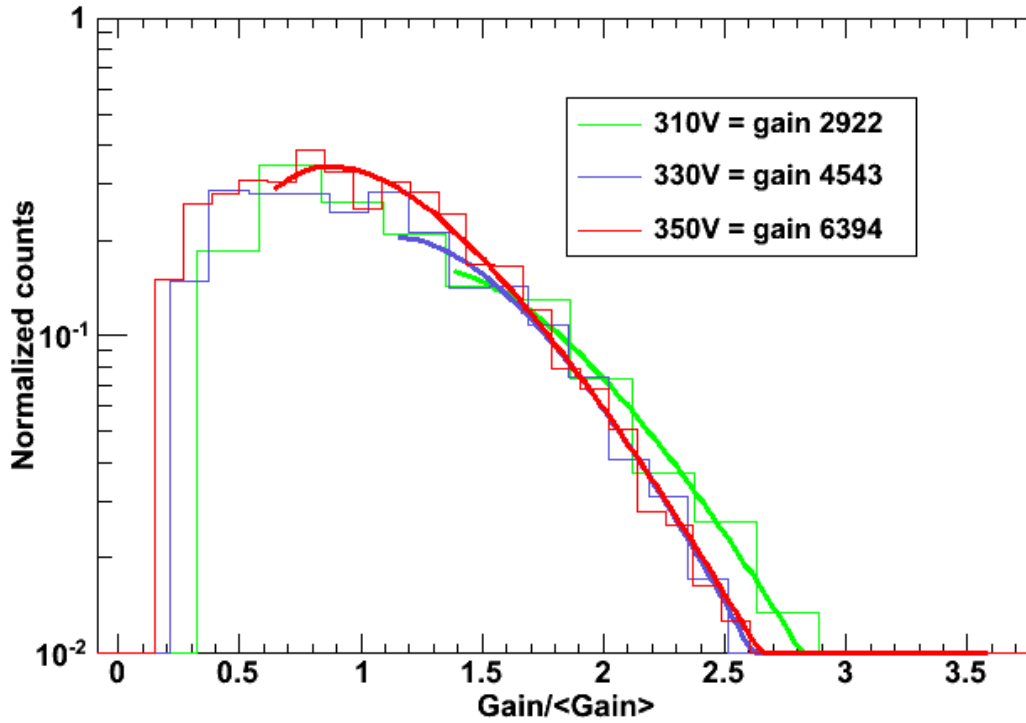


Figure 71. TOT spectra for different grid voltages (RMS, RMSratio and Centre cut applied). The histograms are normalised to an integral of 1. The x -axis is in G/\bar{G} . For each voltage the mean value \bar{G} of the distribution was calculated. The y -axis is in logarithmic scale. The lines are fitted Polya curves starting at 4000 electrons. The calculated gain in the legend corresponds to a gain

The gain distribution had been recorded for several grid voltages with a Timepix InGrid detector. For low voltages up to 300V the turn over at the low end of the spectrum was not visible and only the tails of the distribution could be fitted. For very low gain the fit starting from 4000 electrons could not be performed as there were only a few avalanches with more than 4000 electrons. The fitted mean and Θ parameters of the Polya curves are shown in Figure 72 for different grid voltages.

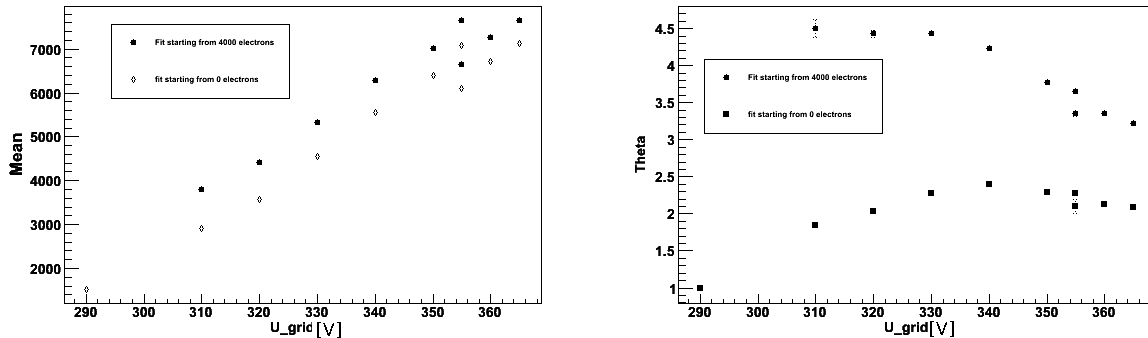


Figure 72. Fitted mean (left) and Θ parameter in dependence of the grid voltage (RMS, RMSratio and Centre cut applied). Fit parameters for the fit starting at 0 electrons and for the fit starting at 4000 electrons.

In Figure 72 a first problem of the measurements can be seen. The measurements have been performed

under the same conditions, only the grid and cathode voltage were changed. However a difference of the mean value for $U_{\text{grid}} = 355V$ of 1000 is visible indicating a change of an, at the time, unknown parameter. The measurements of $U_{\text{grid}} = 290V, 310V, 320V, 330V$ and $340V$ were performed consecutive. The measurements of $U_{\text{grid}} = 350V$ and $355V$ (with higher mean value) four days later. Within this time the conditions were stable. The three data points at $U_{\text{grid}} = 355V, 360V$ and $365V$ were recorded two weeks after the first measurements. Within this time some environmental variable must have changed. The effect is not so clearly visible in the plot of the Θ values. An explanation of this effect will be given in Section 4.4.

The Θ parameters for the different fits vary significantly. For low grid voltages the fit starting at 4000 electrons is not expected to give good results as only few events contribute to the fit. For high grid voltages two fits should lead to the same results. In Figure 72 we can see that the fitted Θ values for the both fits converge, but for the highest voltages they still differ by 1. The reason for the lower Θ values in the fit starting at 0 electrons is the low end of the spectrum. There the TOT calibration is not reliable. Also the mean values of this fit for low grid voltages can only be an approximation of the real mean number of electrons in an avalanche. The three last data points have been measured under different conditions. As the Polya distribution is not the exact gain distribution, but only an approximation the Θ value does not need to be constant for all grid voltages. A reliable Θ value can only be measured for high gains where the turn over point of the distribution is higher than 4000 electrons. In this case the fit starting from 4000 electrons can take the curvature of the turn over into account without being influenced by the calibration problems. Even at the highest grid voltage of $U_{\text{grid}} = 365V$ the gain was not high enough to arrive at this conditions. In Section 4.5.3 measurements with higher gain will be presented and the Θ value will be discussed again.

The mean value of the gain distribution \bar{G} is simply called gain. Form the theory (Section 2.2.1) we know that $\text{Mean} = \bar{G}$ should be an exponential function of the voltage in the amplification gap. From Figure 72 (left) we can see that the recorded gain curve is rather linear than exponential. The same curve is shown in Figure 73 with logarithmic y -axis. The reason for the non linearity will be explained in section 4.4.

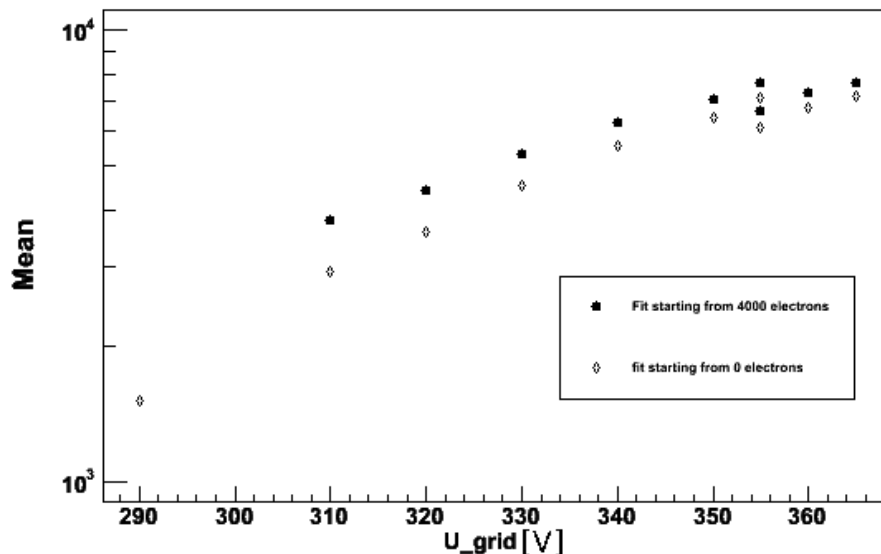


Figure 73. Fitted mean (left) parameter in dependence of the grid voltage with logarithmic y -axis (RMS, RMSratio and Centre cut applied). Fit parameters for the fit starting at 0 electrons and for the fit starting at 4000 electrons.

Gain measurements with the InGrid Timepix chip were also performed in CF_4 and P10 gases. In CF_4

the diffusion was too small and after the cuts not enough events were left to produce comparable results. In P10 measurements with four different voltages were carried out. The chip was hit by several sparks at a grid voltage of 430V (Micromegas gain of less than 10000). The run had to be stopped. After this measurement the chip needed to be calibrated and the homogeneity of the response was not as good as before. Only the data of two ($U_{\text{grid}} = 380\text{V}$ (Micromegas gain 1921) and $U_{\text{grid}} = 400\text{V}$ (Micromegas gain 3678)) of the four measurements could be used for analysis. The fitted mean values of the gain distributions \bar{G} are shown in Table 9. No further measurements were performed in this gas as the InGrid detector was still needed for other measurements.

U_{grid}	\bar{G} (fit from 0)	\bar{G} (fit from 4000)
380 V	1559	2071
400V	2538	3328

Table 9. Mean values of the fits to the gain distributions in P10 gas.

4.3.2 Micromegas gain measurements

<i>Detector</i>	<i>Gas</i>	$U_{\text{grid}}[\text{V}]$	$U_{\text{cath}}[\text{V}]$	<i>Source</i>	<i>Aim of measurements</i>
Micromegas	ArIso95/5 & 80/20, CH ₄ , CF ₄ , P10	different	$U_{\text{grid}} + 286$	⁵⁵ Fe: strong	gain curves

To compare the InGrid gain measurements with a standard Micromegas detector (Section 3.2.1) measurements of the gain in a Micromegas with the same gap size were performed. The gain was measured by recording the current on the grid using a Ortec Preamplifier 142B¹¹ and Ortec spectroscopic amplifier 672 and an Amptec Multi Channel Analyser (MCA) connected to the PC to record the spectrum. For this measurements the photo peak was used as the current from the grid does not depend on the diffusion and no number of primary electrons needs to be measured. The photo peak position channel ch_{peak} was fitted in the recorded spectrum. The gain was calculated with the equation

$$\bar{G}_{\text{mm}}(U_{\text{grid,mm}}) = \frac{\text{ch}_{\text{peak}}}{\text{ch}_{\text{MCA}}} \frac{U_{\text{MCA}}}{G_{\text{Amp}} \times c_{\text{Preamp}} \times N_g} \quad (48)$$

where $\text{ch}_{\text{MCA}} = 1024$ is the number of channels of the MCA, $U_{\text{MCA}} = 5\text{V}$ or 10V is the maximal range of the MCA, G_{Amp} is the amplification factor of the main amplifier, c_{Preamp} is the charge to voltage transformation factor of the preamplifier and N_g is the number of primary electrons in the photo peak in the particular gas. The ⁵⁵Fe source used for the measurements was stronger than the source used in the InGrid measurements. The drift field was set to 220V/cm. For comparison the gain curve in ArIso 95/5 was measured with both of the sources. No significant difference has been observed.

In Figure 74 the gain curve in ArIso 95/5 is shown for grid voltages from 290V to 355V. An exponential function $G(U_{\text{grid}}) = \exp(A + B \cdot U_{\text{grid}})$ was fitted to the data points. The two fit parameters A (constant of the fit) and B (slope of the fit) describe the gain curve. As shown in Table 10 together with the parameters for the other gases, the results for ArIso 95/5 are $A = -3.47 \pm 0.001$ and $B = (3.6911 \pm 0.0004) \times 10^{-2}$. The function agrees well with the measurements. The errors on the fit values are only coming given by the fit and are hence so small. They were not used for further calculations. The fit parameters from the fit were used for further calculations of Micromegas gains from the grid voltage.

¹¹. The preamplifier has to be adapted for the capacitance of the amplification gap to get a signal. For the InGrid amplification gap no adequate preamplifier was available to directly measure the gain by the grid current and the TOT at the same time.

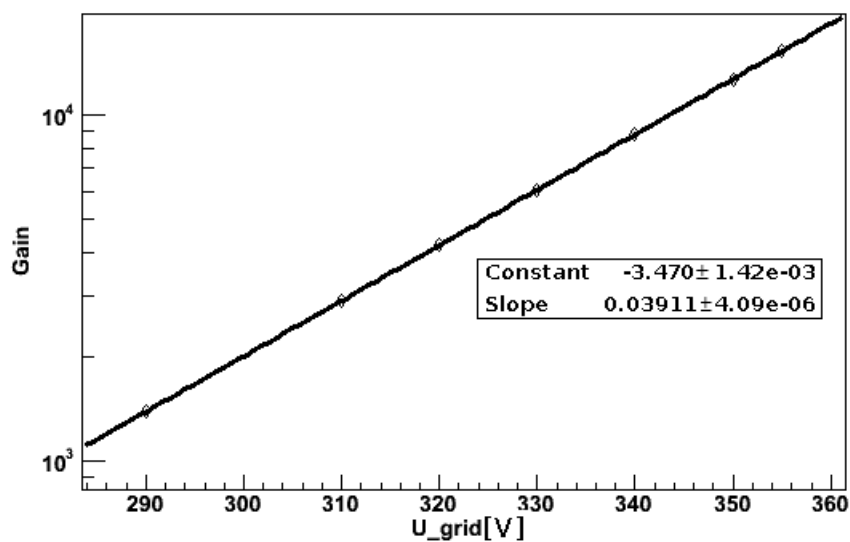


Figure 74. Gain curve in ArIso 95/5 measured with a standard Micromegas detector with an exponential fit function.

Gain measurements were also performed in other gases. The gain curves are shown in Figure 75.

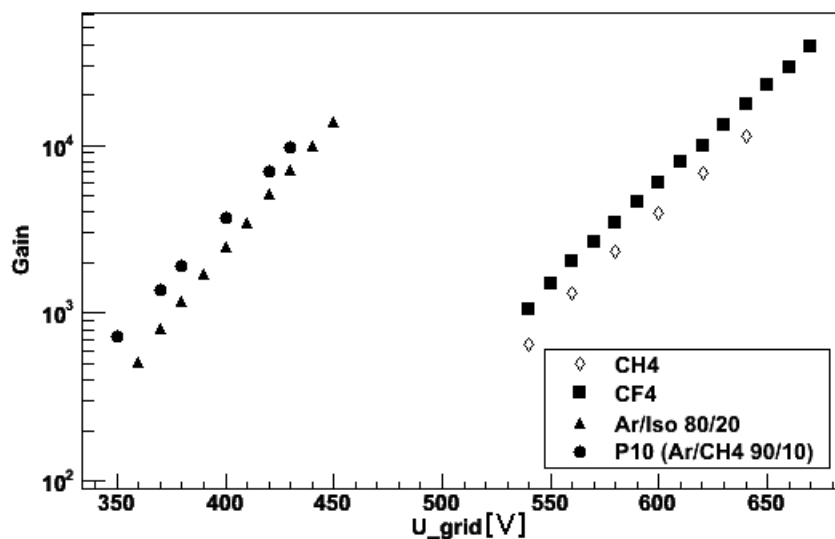


Figure 75. Gain curve in CH₄, CF₄, ArIso 80/20 and P10 measured with a standard Micromegas detector.

Gas	A	B
ArIso 95/5	-3.470 ± 0.001	$(3.6911 \pm 0.0004) \times 10^{-2}$
ArIso 80/20	-5.804 ± 0.002	$(3.4084 \pm 0.0004) \times 10^{-2}$
CH ₄	-7.505 ± 0.003	$(2.6319 \pm 0.0004) \times 10^{-2}$
CF ₄	-7.384 ± 0.0006	$(2.67853 \pm 0.00009) \times 10^{-2}$
P10	-4.776 ± 0.003	$(3.2466 \pm 0.0006) \times 10^{-2}$

Table 10. Fit parameter results for the Micromegas gain measurements, error from fit only.

The gain measurements with the InGrid detector and the standard Micromegas detector with same amplification gap size are compared in Figure 76 for ArIso 95/5. The mean value of the Polya fits is taken as gain for the InGrid detector. For low grid voltages the gain of the InGrid detector is higher than the one of the Micromegas detector ($\approx 110\%$). This could be due to the TOT calibration problems for small gains. For higher grid voltages the gain of the InGrid detectors drops and reaches a value of 50% of a Micromegas detector for $U_{\text{grid}} = 355\text{ V}$ (Figure 76, top). The Figure on the bottom shows the mean value of the gain distribution for the InGrid detector as function of the gain of a standard Micromegas detector (U_{grid} has been transformed to $G(U_{\text{grid}}) = \exp(A + B \cdot U_{\text{grid}})$ by the fit parameters A and B of the Micromegas gain curve). The line in the plot is the line of equal gain. Two data points from measurements in P10 gas are also included in this plot.

The main difference between the amplification structure of the InGrid and the standard Micromegas is the silicon protection layer on top of the Timepix chip inside the amplification gap. The effect of gain drop as well as the change of conditions during the measurements even if the environment variables are kept constant are probably due to this layer. This will be explained in the next section.

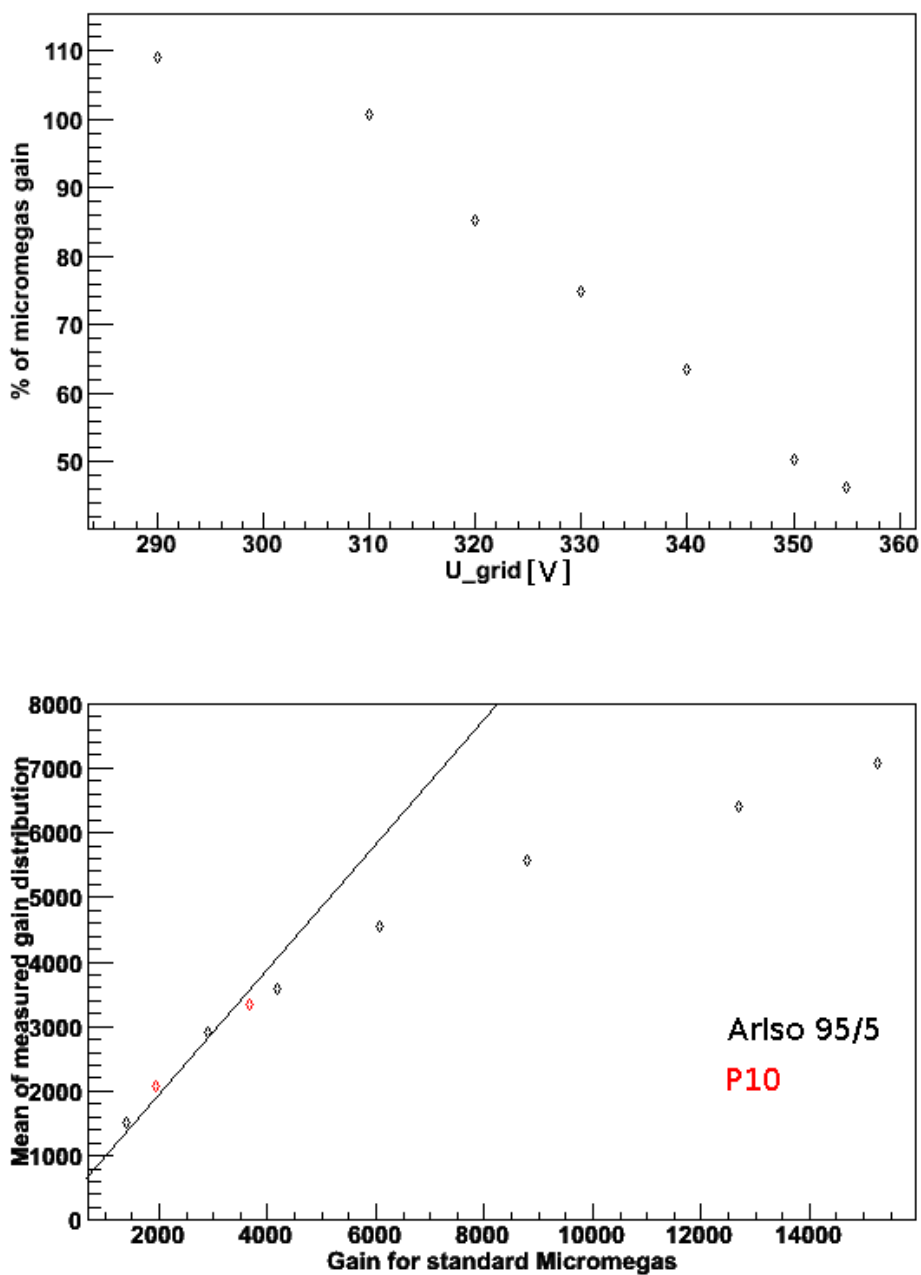


Figure 76. Compression of the gain curves of the Micromegas and InGrid detectors in ArIso 95/5. Percentage of Micromegas gain for the InGrid detector (top). Ingrid gain as function of the Micromegas gain (bottom) with also two measurements in P10(Ar/CH₄ 90/10) included (red). The line in the plot is the line of equal gain. (RMS, RMS-ratio and Centre cut applied for InGrid gain values)

4.4 Theory of the Influence of SiProt on gas amplification in an InGrid setup

The naked TimePix Chips are covered by a silicon layer to protect them from sparks in the amplification

region. This is a significant difference between a Standard Micromegas and an InGrid Detector. This layer lowers the gain of an InGrid detector. The model, which I developed, describes the influence of this additional layer. In the following I will describe a simple model for this layer and derive a formula for the reduction of the gain.

There are two different SiProt types: hydrogenated amorphous silicon (a-Si:H) and silicon nitride (Si_3N_4 , as for the G06-W0096 chip used in the measurements). Both layers have different properties in resistivity ρ and permittivity ε shown in Table 11.

	a-Si:H	Si_3N_4
$\rho/[\Omega\text{cm}]$	10^{11} [Che09]	10^{14} [Sil]
ε	11.8 [Dea93]	7.5 [Sil]

Table 11. Resistivity and permittivity of a-Si:H and Si_3N_4

This layer acts as a capacitor on top of each pixel that is instantaneously charged by an avalanche and discharged with a time constant τ . In the following calculation we assume that the silicon layer thickness d is small or in the same order (it is about $8\mu\text{m}$ for our chip) with respect to the sensitive pixel pad size of $20\mu\text{m}$. The protection layer surface and the sensitive area build a capacitor with resistivity ρ and permittivity ε as show in Figure 77.

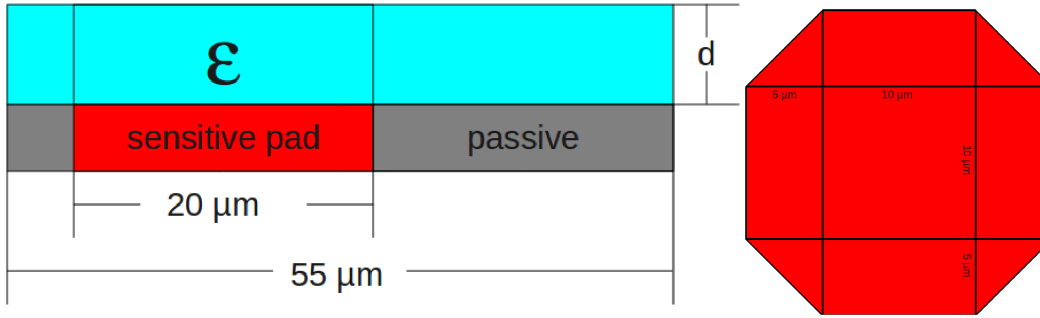


Figure 77. Capacitor on sensitive pixel pad (left) and pixel sensitive pad geometry

The time constant τ can be calculated from the material properties:

$$C = \varepsilon_0 \varepsilon \frac{A}{d} \quad (49)$$

$$R = \rho \frac{d}{A} \quad (50)$$

$$\tau = RC = \varepsilon_0 \rho \varepsilon \quad (51)$$

where C is the capacitance, R is the resistance, ε_0 is the vacuum permittivity constant and A is the sensitive pad area of $350\mu\text{m}^2$. Values obtained for a-Si:H and Si_3N_4 are $\tau_{\text{a-Si:H}} = 0.10448\text{s}$ and $\tau_{\text{Si}_3\text{N}_4} = 66.405\text{s}$ respectively from the resistivity and permittivity given in Table 11. Note that this values can just be approximations as, for example, for the resistivity just the order of magnitude is given. For the SiProt in our measurements, which consists of Si_3N_4 a time constant τ of the order of 1 min is expected. The surface of the silicon layer will be charged after an avalanche. The equivalent circuit is shown in Figure 78. The capacitance C_1 is the amplification gap, C_2 is the capacitance of the SiProt layer that is connected to ground with the resistance R .

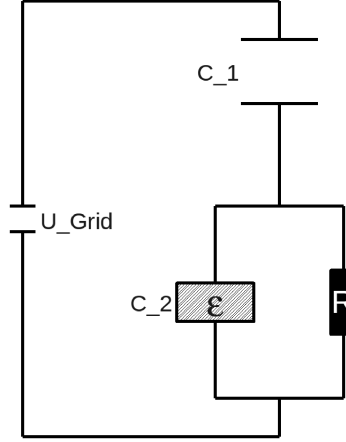


Figure 78. Equivalent circuit of the amplification gap of an InGrid with SiProt. The capacitance C_1 is the amplification gap, C_2 is the capacitance of the SiProt layer that is connected to ground with the resistance R .

If the pixel is hit with a constant rate f with (for the first simple model) pulses of charge G (G in Coulomb¹²) the surface of the SiProt layer will reach a voltage level U_{Sat} :

$$\text{decrease of charge on surface: } \frac{dQ}{dt} = -I_{\text{ch}} = -\frac{U}{R} = -\frac{Q}{RC} \quad (52)$$

$$\text{increase of charge on surface: } \frac{dQ}{dt} = J = Gf \quad (53)$$

$$\Rightarrow \frac{dQ}{dt} = Gf - \frac{Q}{RC} \quad (54)$$

For $t \rightarrow \infty$ this will lead to a saturation $Q_{\text{Sat}} = C U_{\text{Sat}}$:

$$\frac{dQ}{dt} = 0 \Rightarrow J = I_{\text{ch}} \Rightarrow \frac{U_{\text{Sat}}}{R} = Gf \quad (55)$$

Now the charge of the incoming pulse G is not constant. It is the gain called G of a single electron, which depends on the voltage difference between the grid and the silicon surface $\Delta U = U_{\text{grid}} - U_{\text{Si}}$, where U_{Si} is the voltage on top of the silicon protection layer:

$$G[C](U_{\text{Si}}) = e \exp(A + B \times \Delta U(U_{\text{Si}})) \quad (56)$$

e is the electron charge. The constants A and B are obtained from gain curve measurements for the particular gas with a Micromegas detector with pad readout (no protection layer, $50 \mu\text{m}$ amplification gap) by a fit (see Table 10). As the gain drops when the voltage on the silicon surface U_{Si} rises there will be a value of G and U_{Si} where $\frac{dU_{\text{Si}}}{dt} = 0$ for $t \rightarrow \infty$. This was not included in our first simple model where G was constant. We have to expand our model and let G be dependant on the voltage on top of the silicon protection layer. In the first simple model this voltage was called U_{Sat} . We can take the formula from the first model, but now G depends on U_{Sat} or U_{Si} as we will call it in this case. We take Equation 55 with $U_{\text{Sat}} = U_{\text{Si}}(t \rightarrow \infty)$ and $G = G(U_{\text{Si}}(t \rightarrow \infty)) = e \exp(A + B \times (U_{\text{grid}} - U_{\text{Si}}(t \rightarrow \infty)))$:

$$\frac{U_{\text{Si}}(t \rightarrow \infty)}{R} = G(U_{\text{Si}}(t \rightarrow \infty)) f \Rightarrow \frac{U_{\text{Si}}(t \rightarrow \infty)}{R f e} = \exp(A + B \times (U_{\text{grid}} - U_{\text{Si}}(t \rightarrow \infty))) \quad (57)$$

This equation is self dependant in $U_{\text{Si}}(t \rightarrow \infty)$. The solution for U_{Si} is the Lambert W-function (see Figure 79):

$$U_{\text{Si}}(t \rightarrow \infty) = \frac{W(B R f e \exp(A + B \times U_{\text{grid}}))}{B} \quad (58)$$

¹² G is in this calculation just a variable in units of Coulomb, but it is not by chance called G as it corresponds the the gain of the InGrid detector.

Note that $e \exp(A + B \times U_{\text{grid}}) = G_{\text{orig}}[e^-]$ is the original gain without taking the charging of the silicon layer into account. For the gain of an InGrid detector at a grid voltage U_{grid} that is irradiated such that every pixel is charged with frequency f we get:

$$G_{\text{real}}(U_{\text{grid}}, f) = \exp \left[A + B \times \left[U_{\text{grid}} - \frac{W(B R f e \exp(A + B \times U_{\text{grid}}))}{B} \right] \right] = \frac{G_{\text{orig}}}{\exp \left[\frac{W(B f R G_{\text{orig}})}{B} \right]} \quad (59)$$

In this model we just looked on the effect of one single pixel. Usually in an InGrid detector an avalanche occurs in some area of the chip and only some pixels are effected. This geometrical effects have not been studied here.

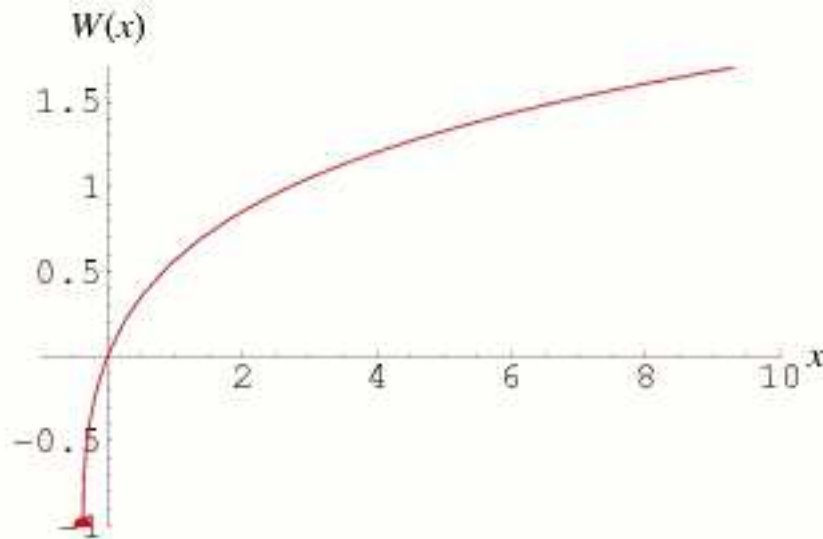


Figure 79. Lambert W-function

Using Equation 59 the gain of the InGrid detector with silicon protection layer can be calculated from the gain a standard Micromegas detector would have for the same voltage. The critical value in the calculation is the frequency f with which avalanches arrive on top of the SiProt layer. It is related to the activity and position of the source, the attenuation by the Cr foil and the drift field configuration. Additionally for a radioactive source the frequency is not fixed and also the position where avalanches occur is random. This makes it difficult to keep all the conditions for the measurements constant. The significant shift of the mean value of the TOT spectrum in Figure 72 for high grid voltages, that indicated a change of conditions, can be explained by this effect. In the following the two data points at $U_{\text{grid}} = 355V$ are discussed. The conditions concerning drift and cathode voltage and field configuration are the same for both measurements. The rate of avalanches was different for the measurements. The run leading to a higher mean value had a lower rate (7016 frames recorded in 1h 15min) compared to the run with the lower mean value (9383 frames in 29 min). From the histogram of the number of hits in x -direction (like the one in Figure 57(5)) a shift of the source can be seen. A source rate can not be calculated by the recorded data as there is an unknown dead time during the chip readout. The conclusion is that for the two data point the voltage difference ΔU between SiProt and grid and hence the gain $G(\Delta U)$ was different because of a different rate of avalanches.

Figure 80 shows a plot of the measured gain (same as 72(left)). Additionally a curve of calculated gain $G_{\text{real}}(U_{\text{grid}}, f = 0.8\text{Hz})$ as a function of U_{grid} in ArIso 95/5. A frequency of $f = 0.8\text{Hz}$ was chosen to fit the measurements and is reasonable compared to the avalanche rate in the centre of the chip.

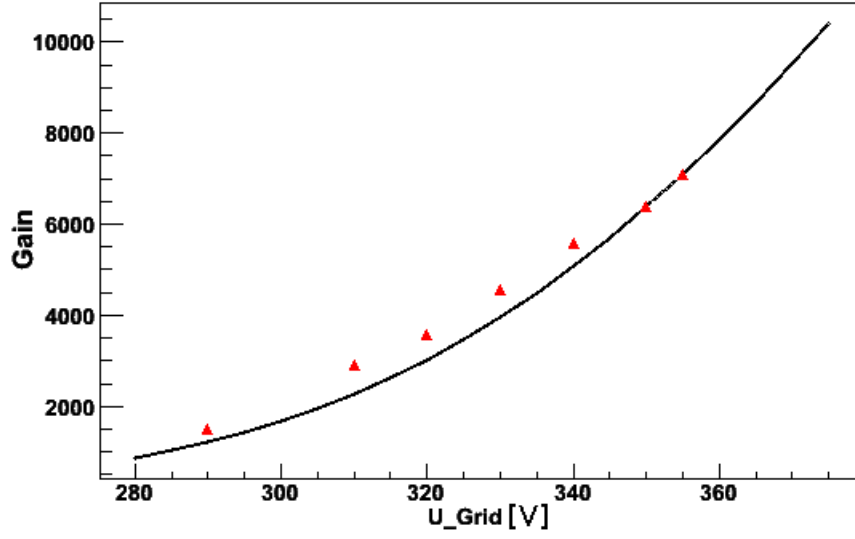


Figure 80. Corrected gain curve. Data (red) and calculation (black) using $f = 0.8\text{Hz}$

From the gain difference between the InGrid and the Micromegas detector the voltage on top of the SiProt layer U_{Si} can be calculated:

$$G_{\text{InGrid}} = \exp(A + B \cdot \Delta U) \Rightarrow \Delta U = \frac{\ln(G_{\text{InGrid}}) - A}{B}, U_{\text{Si}} = U_{\text{grid}} - \Delta U \quad (60)$$

where G_{InGrid} is the measured InGrid gain (the mean of the measured Polya distribution) and A and B are the constants from the gain curves in the gas (see Table 10). The result for the same measurements as in Figure 76 in ArIso 95/5 are shown in Figure 81.

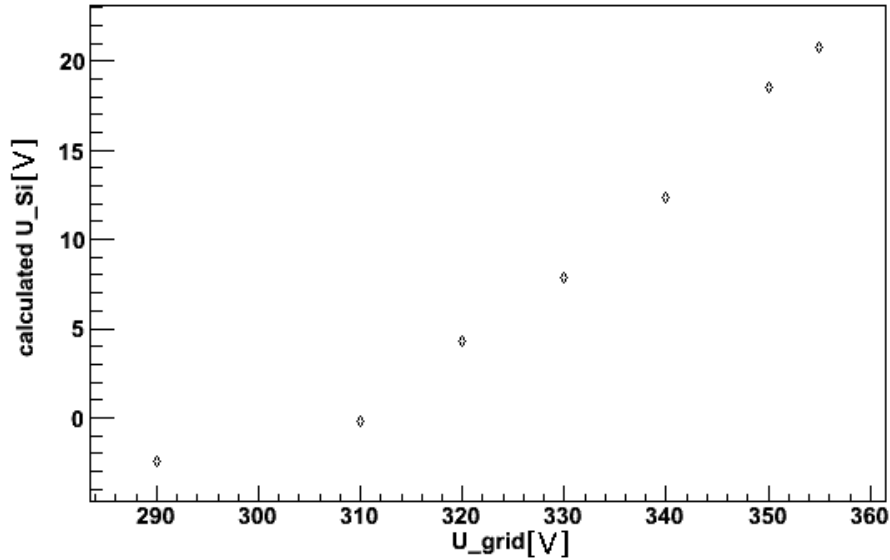


Figure 81. Calculated voltage on top of the SiProt layer (Equation 60) from the difference of gain of the InGrid and Micromegas detectors. The negative values for the low grid voltages might be due to the incorrect TOT calibration for low gains.

As the gain is an exponential function of the voltage ΔU in the amplification gap the charging up effects of the SiProt layer have a serious influence on the gain. The gain depends not only on the grid voltage U_{grid} but also on the frequency of avalanches.

4.5 Measurements of the time constant of SiProt

In order to validate the model I developed in the previous section, additional TOT measurements had been carried out with the aim to measure the same gain as a Micromegas detector. However one needs to produce avalanches to measure the gain, but producing avalanches changes again the gain to lower values. A low rate of avalanches is necessary to arrive at highest gains. A first confirmation of the theory would be to measure the correct time constant τ of the SiProt layer that was predicted to be of the order of 1 min. The measurements will be presented in Section 4.5.1. To measure the same gain with an InGrid detector as with a Standard Micromegas Detector low avalanche frequencies were necessary. Measurements of the gain and the Θ value of the gain distribution, where the source was placed in a larger distance from the detector, are presented in Section 4.5.2 and 4.5.3.

For the analysis it was necessary to separate the data into packages of short duration such that the change of the gain with the time could be inspected. The time intervals should be as short as possible to get many data points of the rising or falling edge with time constant τ . However for shorter time intervals the number of events decreases and an analysis will not give stable results. Time intervals of one minute were chosen. The rate of the source should not be chosen too small as there has to be enough statistics for the analysis. To get a larger number of events, even for low source rates, the acquisition time was increased. The data sample of one run was split in packages of one minute. The analysis code evaluated this packages. The only output of this analysis were the mean and the Θ value of the two fits (one from 0 electrons and one from 4000 electrons). This values were plotted in a time to mean or time to Θ diagram to see the time dependence of these fit parameters.

4.5.1 Measurements of the time constant

<i>Detector</i>	<i>Gas</i>	$U_{\text{grid}}[\text{V}]$	$U_{\text{cath}}[\text{V}]$	<i>Source</i>	<i>Aim of measurements</i>
InGrid	ArIso 80/20	420 and 440	$U_{\text{grid}} + 1900$	^{55}Fe : weak and strong	τ of SiProt

For the measurements of the gain of a Micromegas detector a different, stronger source was available. The weaker source used for the InGrid gain measurements was also available. During one run the sources were exchanged resulting in a change of the rate of avalanches. If the weak source was in place first and exchanged by the stronger one (or both sources) the gain dropped as expected. If first both sources were in place and the strong source was taken away the gain had risen. The time constant of the rise or drop was evaluated from a fit of an exponential function. This measurements performed in ArIso 80/20. In Figure 82 and 83 the result of the two measurements is presented. From the fit parameter slope s of the exponential function the time constant τ can be calculated:

$$\tau = 1/s \quad (61)$$

The results for the two measurements are:

$$\tau_{420\text{V}} = (1.1 \pm 0.4) \text{ min}$$

$$\tau_{440\text{V}} = (1.27 \pm 0.05) \text{ min}$$

For comparison in the theory a time constant of the order of $\tau_{\text{theo}} = 1 \text{ min}$ was calculated using the permittivity ϵ and the magnitude of the resistivity ρ of Si_3N_4 . The measurements are in good agreement with this calculations which is a first confirmation of the theory.

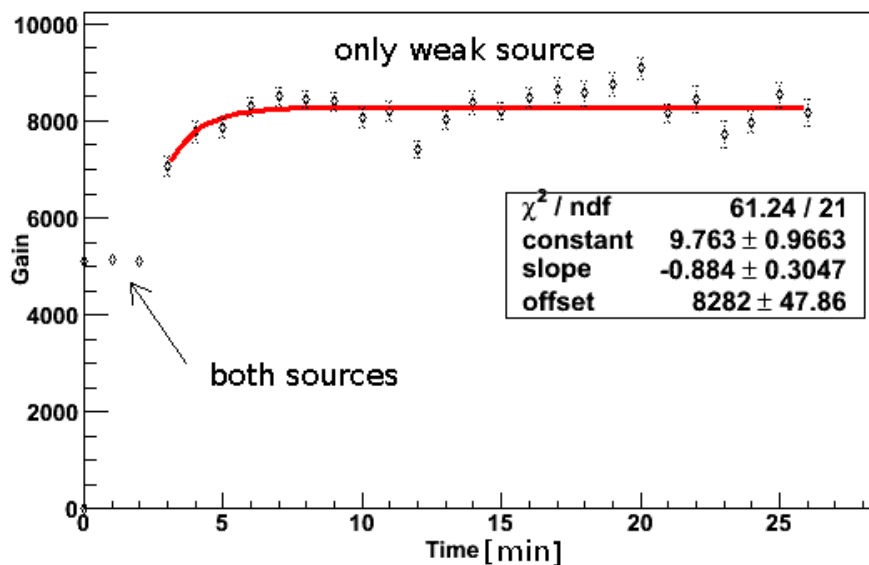


Figure 82. Mean value (RMS, RMSratio and Centre cut applied) of the Polya fits (here called Gain) as function of the time. Measurements in ArIso 80/20 at $U_{\text{cath}} = 2320\text{V}$, $U_{\text{grid}} = 420\text{V}$. First both sources were in place on top of the Mylar window outside the detector box. After three minutes of measurement the strong source was taken away. Fit of exponential function to the data points.

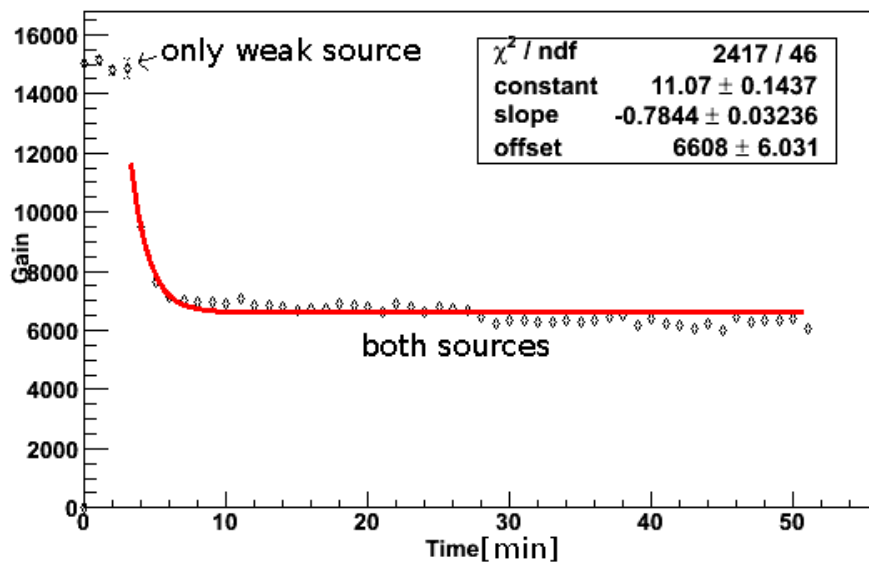


Figure 83. Mean value (RMS, RMSratio and Centre cut applied) of the Polya fits (here called Gain) as function of the time. Measurements in ArIso 80/20 at $U_{\text{cath}} = 2340\text{V}$, $U_{\text{grid}} = 440\text{V}$. First only the weak source was in place on top of the Mylar window outside the detector box. After three minutes of measurement the strong source was added. Fit of exponential function to the data points.

4.5.2 Low frequency gain measurements

Detector	Gas	$U_{\text{grid}}[\text{V}]$	$U_{\text{cath}}[\text{V}]$	Source	Aim of measurements
InGrid	ArIso 95/5	300, 320,330 and 340	$U_{\text{grid}} + 1700$	^{55}Fe : weak	arrive at Micromegas gain

The gain was measured at various frequencies to see whether it approaches the gain of a Micromegas detector. This measurements were again carried out in ArIso 95/5 such that the results can be compared to the measurements at higher rates. The source position was changed to get different avalanche rates. For the measurements at high rates the weak source was placed directly on top of the cathode mesh inside the detector box. Lower rates were obtained by placing the weak source on top of the Mylar window outside the box. The lowest rate was achieved by putting a collimator between the Mylar window and the weak source. For every measurements the Cr foil was also present. The low rate measurements were done for four grid voltages: $U_{\text{grid}} = 300V, 320V, 330V$ and $340V$. The drift voltage was set such that $U_{\text{drift}} = U_{\text{grid}} + 1700V$. The acquisition time was adapted to still record at least one event in 10 frames ($0.001s$ and $0.05s$ compared to $0.0001s$ for the high rate measurements). As a result of the improvement of the measurement conditions a MUROS frequency of $f_{\text{MUROS}} \approx 60$ MHz was used for this measurements. Higher frequencies lead to a higher TOT binning and hence higher precision. The data were split into packages of one minute and each packages was analysed separately. The average gain for one run was taken from the average of the mean values of the plateau in the mean vs. time diagram (see Figure 84 as an example) be sure that no charging up effects of the SiProt layer had an influence.

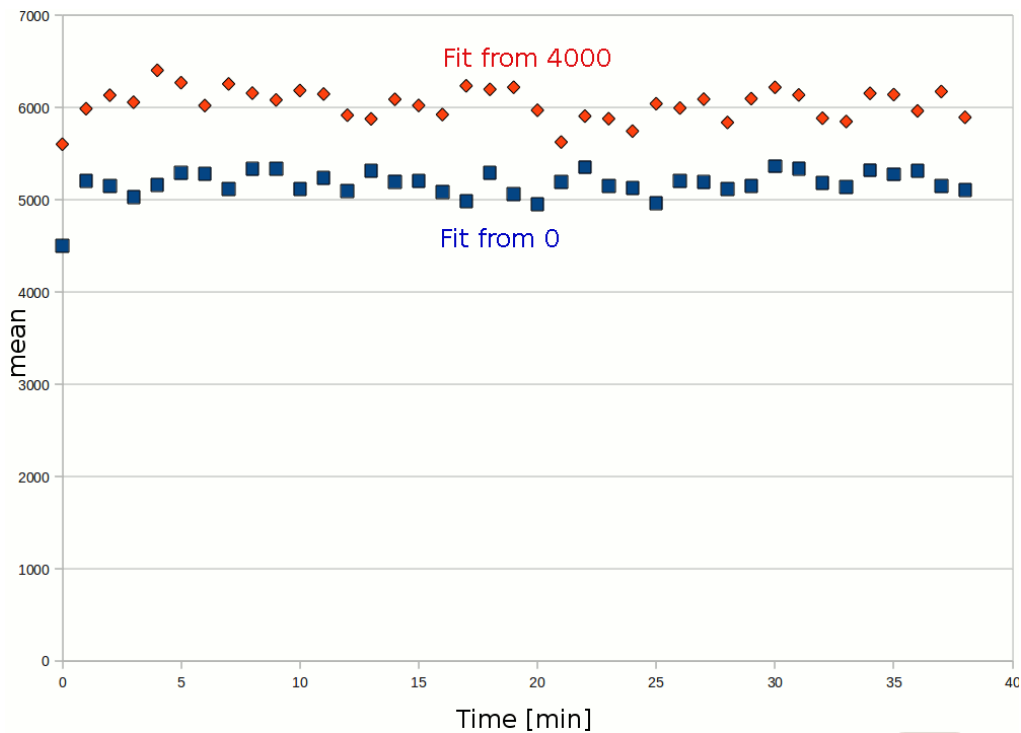


Figure 84. Fit parameter mean (RMS, RMSratio and Centre cut applied) as function of the time for the fit starting from 0 and 4000 electrons for the data sample with $U_{\text{grid}} = 330V$, $U_{\text{cath}} = 2030V$, ArIso 95/5. The average gain (for each fit) of this run was taken from the average of the mean values of the flat plateau, in this case starting after 1 minute.

The results from the fit starting at 0 and at 4000 electrons were taken. In Figure 85 the results are shown.

	Micromegas gain	InGrid source inside	InGrid source outside	InGrid source outside collimator
$U_{\text{grid}}[V]$	calc. from U_{grid}	fit from 0 (4000)	fit from 0 (4000)	fit from 0 (4000)
300	2004	n.a.	1414 (3097)	1584 (3569)
320	4193	3578 (4413)	3904 (4869)	3875 (5306)
330	6064	4543 (5331)	5185 (6070)	5835 (6766)
340	8772	5562 (6275)	7403 (7944)	8123 (8707)

Table 12. Calculated Micromegas gains and measured average gains of an InGrid for different source positions.

The x -axis in Figure 85 is given not in U_{grid} but in the gain of the standard Micromegas detector $G_{\text{mm}}(U_{\text{grid}}) = \exp(A + B \times U_{\text{grid}})$. The constants A and B are obtained from the Micromegas gain curve. For simplicity not all the data points for both of the fits are shown. This would have led to six points for each Micromegas gain. An unusual way of presentation was chosen: The “error” bars in Figure 85 indicate the range between the two fits. The mean gain values of the points G_{mean} in the plot are the intermediate value: $G_{\text{mean}} = (G_{\text{fit}0} + G_{\text{fit}4000})/2$, where $G_{\text{fit}0}$ and $G_{\text{fit}4000}$ are the results of the fits starting at 0 and 4000 electrons respectively. The bars have the total length $l = |G_{\text{fit}0} - G_{\text{fit}4000}|$. That means that the point for $G_{\text{fit}0}$ (this fit always gives a lower value than $G_{\text{fit}4000}$) would be placed at the low end of the bar and the point for $G_{\text{fit}4000}$ at the top.

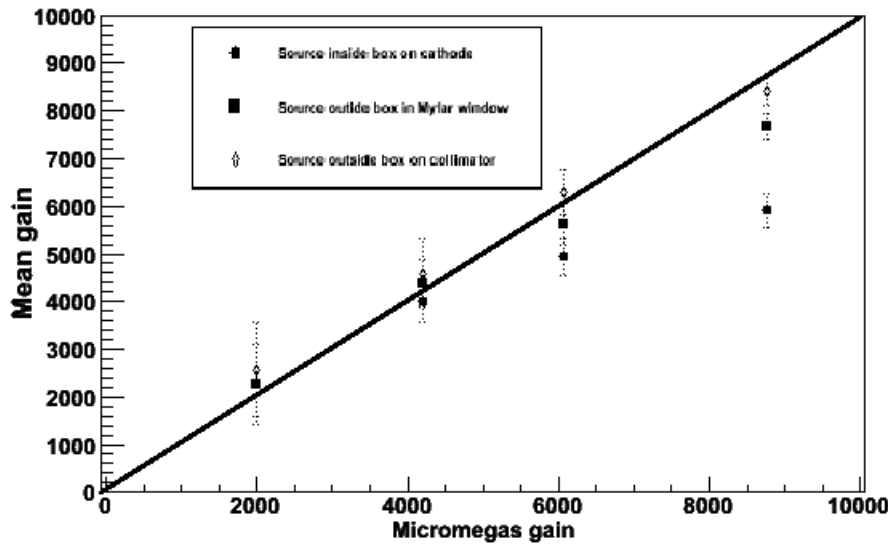


Figure 85. Mean InGrid gain (RMS, RMSratio and Centre cut applied) as function of the Micromegas gain (calculated from U_{grid} used for the InGrid measurement). The points are at the intermediate value of mean value from the fit starting at 0 and 4000 electrons. The bars have the length corresponding to the difference between the results of the two fits. The continuous line marks the gain of a standard Micromegas detector. The highest source rate was obtained if the source was placed inside the box. The lowest rate was obtained if the source was put outside the detector on the Mylar window with an additional collimator.

From Figure 85 we can see that the bars are getting smaller for higher Micromegas gains. That means that the results of the two fits converge. This results was already expected as for higher gains the influence of events with less than 4000 electrons to the fits gets smaller. It is also visible that the mean gain value approaches the value for a standard Micromegas (continuous line) for measurements with lower source rates. For the lowest Micromegas gains the measured InGrid gain is higher than the Micromegas gain. This can be due to problems with the fits for low gains. Another possibility is that the amplification gap of the detectors is different, even if both of the gaps are specified to be $50 \mu\text{m}$ wide.

4.5.3 Low frequency Θ measurements

Detector	Gas	$U_{\text{grid}}[\text{V}]$	$U_{\text{cath}}[\text{V}]$	Source	Aim of measurements
InGrid	ArIso 95/5	340	$U_{\text{grid}} + 1700$	^{55}Fe : weak	measure Θ for highest gains

Putting the source outside the detector results in a lower rate of avalanches. Higher gains can be achieved with the same grid voltages U_{grid} than before. The potential difference in the amplification gap $\Delta U = U_{\text{grid}} - U_{\text{Si}}$ is bigger as the potential on top of the SiProt layer U_{Si} is smaller. A problem in this (and only in this) measurements had been, that noise was significantly visible. The acquisition time was

adapted to the low rate and hence longer. For that reason the probability that noisy pixels appear in a frames had increased. In Figure 86 TOT spectra are shown for the two measurements at low rate at a grid voltage of $U_{\text{grid}} = 340\text{V}$. For both measurements the source was put outside the detector box and additionally a collimator was used for the measurements in the histogram in Figure 86 (right). The effect of noise is stronger in the histogram on the right as the acquisition time was divided by two referred to the measurements without collimator (from 0.001s to 0.05s). The mean value had also increased as ΔU and hence the gain increased for a lower rate. In the plots the fit starting at 4000 electrons is shown. In this measurement the highest gain in ArIso 95/5 was reached with an InGrid detector. The Θ -parameters in this measurements were $\Theta_1 = 2.60 \pm 0.02$ (for the measurement with collimator, mean = gain = 8777 ± 14) and $\Theta_2 = 2.68 \pm 0.04$ (for the measurement without collimator, mean = gain = 7902 ± 22).

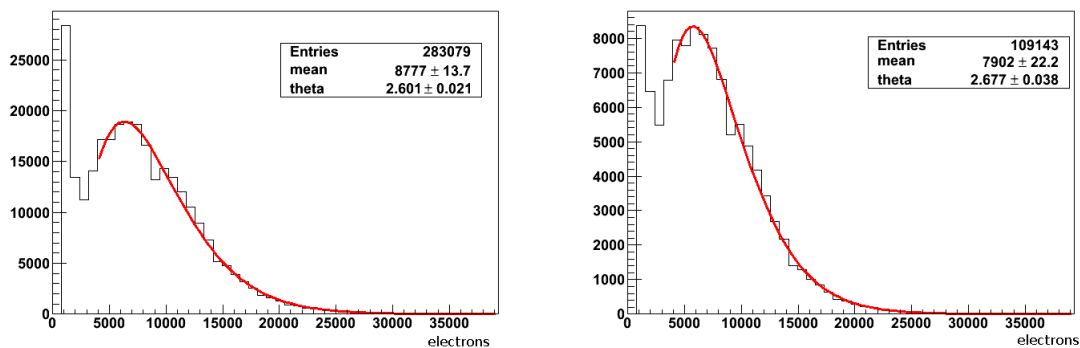


Figure 86. TOT spectra (RMS, RMSratio and Centre cut applied) for low rate measurements at $U_{\text{grid}} = 340\text{V}$, $U_{\text{cath}} = 2040\text{V}$ in ArIso 95/5. For both measurements the source was put outside the detector box. For the spectrum on the left additionally a collimator was used such that the rate was decreased further. The acquisition time were 0.05s (right) and 0.001s (left). The signals from noisy pixels are clearly visible at the low end of the spectra. For the measurement with longer acquisition time (right) the effect from noise is stronger.

4.5.4 Single electron detection efficiency

Detector	Gas	$U_{\text{grid}}[\text{V}]$	$U_{\text{cath}}[\text{V}]$	Source	Aim of measurements
InGrid	ArIso 95/5	290 - 365	$U_{\text{grid}} + 1700$	^{55}Fe : weak	derive Θ from det. eff. curve

In Section 4.2.4 the capability of the detector to measure the signals of the avalanches triggered by the primary electrons was discussed. The number of detected primary electrons depends on the gain. Equation 44 describes the relation between the detection efficiency and the gain. The detector threshold t is known from the calibration. The integral from Equation 44:

$$\kappa(m, G, t) = \int_t^\infty \frac{m^m}{\Gamma(m)} \frac{1}{G} \left(\frac{g}{G}\right)^{m-1} \exp\left(-m\frac{g}{G}\right) dg \quad (62)$$

was solved for different values of the Θ parameter. The curves are shown in Figure 87 as function of \bar{G}/t , where \bar{G} is the mean of the gain distribution.

From the TIME measurements the efficiency $\kappa_{\text{data}} = N_{\text{cluster,escape}}/N_{\text{cluster,escape,Sat}}$ was calculated, where $N_{\text{cluster,escape}}$ is the number of counted clusters in the escape peak. The saturation value of $N_{\text{cluster,escape,Sat}} = 117.9$ was taken as 100% from the measurement of primary electrons, see Section 4.2.4. The gain/threshold is the mean of the TOT spectrum divided by the threshold of the Timepix chip. Therefore a TOT measurement was performed directly after a TIME measurement for the same grid voltages. The efficiency is calculated from the TIME, the gain/threshold from the TOT measurement.

The gain was obtained from the fit starting at 0 electrons for all the data points for consistency. For the lowest gains only this fit gave results. As the calibration curve had not been very accurate for low gains (highest gain value 7137) an error of 20% was assumed for the gain value. This value is taken as an average from the difference between the results of the fit starting from 0 electrons and 4000 electrons. The statistical errors in y -direction are of the order of 2% and are not shown in the plot. $\Theta = 0$ (exponential gain curve) is excluded for all gains. For the lowest gains Θ from 0.5 are possible. For the highest gains no conclusion can be drawn as the theoretical curves for different Θ approach one another. Θ between 1 and 3 are reasonable. The medium gains in the region between 2 and 5 gain/threshold are the most interesting in this plot. The measurements indicate $0.5 \lesssim \Theta \lesssim 2$. Threshold in our measurements was of the order of 1000 electrons. But as the calibration curve from TOT to electrons becomes reliable from 4000 electrons onwards, the Θ of the gain distributions could not be measured directly for this region. The results from this method can not be compared to the direct measurements of Θ from the gain distribution at gains of 7902 and 8777.

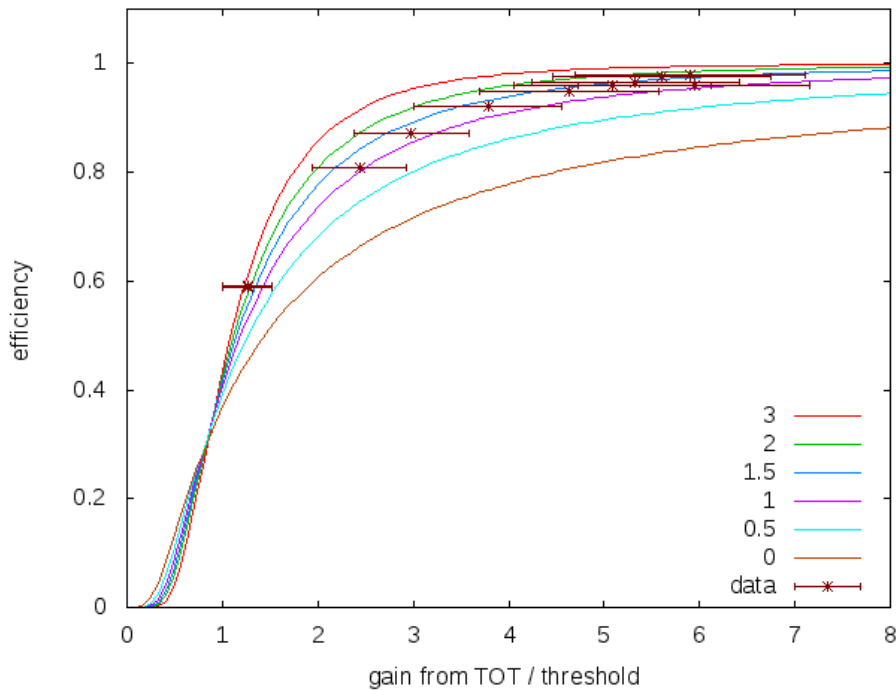


Figure 87. Detection efficiency with theoretical curves for Polya distributions with different Θ parameters and data points. 117.9 counted clusters are assumed as 100% efficiency. The error on the gain from TOT is assumed to be 20%. Error bars in y -direction are of the order of 2% and not shown in the plot.

4.5.5 LASER test bench measurements

<i>Detector</i>	<i>Gas</i>	$U_{\text{grid}}[\text{V}]$	$U_{\text{cath}}[\text{V}]$	<i>Source</i>	<i>Aim of measurements</i>
InGrid	ArIso 95/5	300, 320,330 and 340	$U_{\text{grid}} + 779$	Photo electrons (LASER)	measure $G_{\text{InGrid}}(f)$

The LASER test bench I built in Freiburg was used to produce primary electrons by photo effect which were then amplified and registered with an InGrid detector. As mentioned in the introduction to this chapter, the specifications for the experiment, as well as the analysis and cuts had to be modified to meet the different conditions compared to an experiment with radioactive source.

The aim of the LASER measurements was, to produce a few avalanches at a defined area of the drift cathode, where the LASER had been focused on. The frequency of avalanches could be controlled by the LASER pulse repetition rate. Repetition rates of 9Hz, 5.7Hz, 3.3Hz and 1.6Hz were used. The threshold

calibration gave a threshold level of the chip of $1100e^-$ for this measurements. The referring DAC value used was 416. The acquisition time was set to $0.2s$. Within this time, signals from noise hits were unlikely and the signal from the photo electrons was clearly visible.

Also tracks from cosmic particles could be seen in the Pixelman event display. The filter for the data registration was adapted such that almost only events from the photo electrons were stored. This was done by setting a minimum and maximum number of pixels that have to be hit per frame such that it is registered. The minimum number was set to 2 pixels on a complete frame of 256×256 pixels to suppress frames that only contain noise or no hit pixels. The maximum number was set to 40 pixels per frame to suppress cosmics. The maximum number of hit pixels from an event coming from the LASER was usually not higher than 35 hit pixels per frame.

The clustering was also done for this measurement, but as only a few primary electrons were generated almost every cluster contained just one pixel. The highest value for the ratio of size 1 cluster to size 2 clusters found was $(\#1/\#2)_{\max} = 19$. As typically in the focal point of the LASER (area of $\approx 30 \times 30$ pixels) 5 pixels were hit this is most likely an effect of charge sharing.

ArIso 95/5 with a gas flux of $15l/h$ was used for all of the measurements. The flux had to be higher than for the other measurements because a different gas box was used. The drift distance in this detector was $d_{\text{drift}} = 1.1\text{cm}$. To obtain a similar drift field and field ratio as in the measurements with the ^{55}Fe source, the cathode voltage was set such that $U_{\text{cath}} = U_{\text{grid}} + 779$. The MUROS frequency of $f_{\text{MUROS}} = 60\text{MHz}$ was used. All the parameters that were kept constant in these measurements are listed in Table 13.

Acq. time	Threshold	Min.#hit pixels/frame	Max.#hit pixels/frame	gas	gas flux	f_{MUROS}
$0.2s$	$1100e^-$	2	40	ArIso 95/5	$15l/h$	60 MHz

Table 13. Parameters kept constant for the measurements with the LASER in Freiburg

The threshold and TOT calibration was done directly before the measurements. As the LASER was focused on a small spot on the cathode, only the area of the Timepix chip underneath this spot was used for analysis. The threshold calibration was done by using only the pixels in this area. The TOT to charge calibration curve is shown in Figure 88.

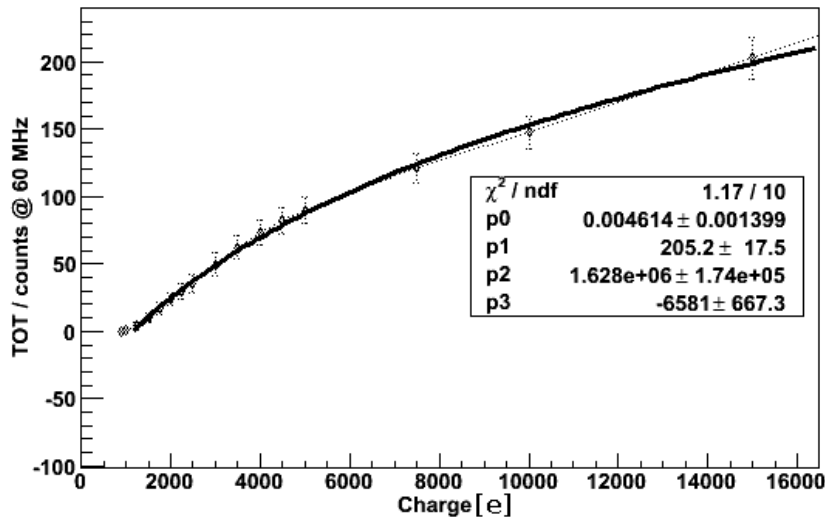


Figure 88. TOT calibration curve for the measurements with the LASER

The analysis code was modified for this measurements as no signals from ^{55}Fe electron clouds were registered. The RMS, centre and Rms ratio cuts were removed. Instead, a fiducial area of pixels was chosen as a cut (area cut). Only the pixels inside this selected area were used for the analysis. The area was chosen such that all the pixels between 88 and 115 pixels (included) in x -direction and 138 and 170 pixels (included) in y -direction were selected by the cut.

In Figures 89 some of the control plots are shown for a data sample at a LASER repetition rate of $f_{\text{laser}} = 5.7\text{Hz}$, a grid voltage of $U_{\text{grid}} = 340\text{V}$ and a cathode voltage of $U_{\text{cath}} = 1119\text{V}$.

- In (a) the distribution of the hit pixels in y -direction is shown without cuts. It consists of one peak with a shoulder. The peak is due to the well focused LASER beam in y -direction. It has a Gaussian shape and reaches its half maximum at 138 and 170 pixels. That interval was chosen for the area cut in y -direction. The shoulder on the left of the peak is due to the fact that the LASER beam was not parallel to the x -direction in the measurements, what can be seen in Figure 90 where the hits are shown in a three dimensional plot. The number of entries in this plot corresponds to the number of hit pixels in the run.
- In (b) the distribution of the hits in x -direction is shown. The LASER beam can not be focused in x -direction due to the small angle of incidence, see Section 3.4. Nevertheless a peak with a plateau is visible in the plot. The wide shoulders of this plateau, filling the whole spectrum, are due to the defocused beam. The interval in x -direction for the area cut was chosen between 88 and 115 pixels, which corresponds to the plateau.
- In (c) the spectrum of the number of hit pixels per frame with area cut is shown. The low value in the bin from 0 to 2 comes from the filter that stored only frames with more than 2 pixels in the whole matrix. It is only filled if 1 or 2 pixels are hit inside the selected area with additional hits outside. The distribution is similar to a Poisson distribution, what could have been expected. It should be remarked that for that data sample the LASER repetition rate (5.7Hz in this case) was higher than the readout rate (shutter length 0.2 s). Therefore one frame contains the piled up signal of photo electrons of several LASER shots. For a repetition rate of 1.6Hz, which is lower than the readout rate, most of the frames contained only a few hit pixels or clusters. The number of entries in this frame correspond to the number of frames that have at least one hit pixel inside the area selected by the area cut.
- The spectrum shown in (d) is the same as the one in (c) but for the number of clusters per frame with area cut.
- In (e) the centre of the electron clouds without cuts is shown. An electron cloud in this measurements is different to one from a ^{55}Fe photon conversion. For the LASER measurements it an electron cloud are all the pixels in one frame. The number of entries in this plot hence is the number of frames registered in the run.
- In (f) the TOT spectrum for clusters of size 1, with the area cut applied, is shown. The number of entries is the number of clusters inside the selected area in the run.

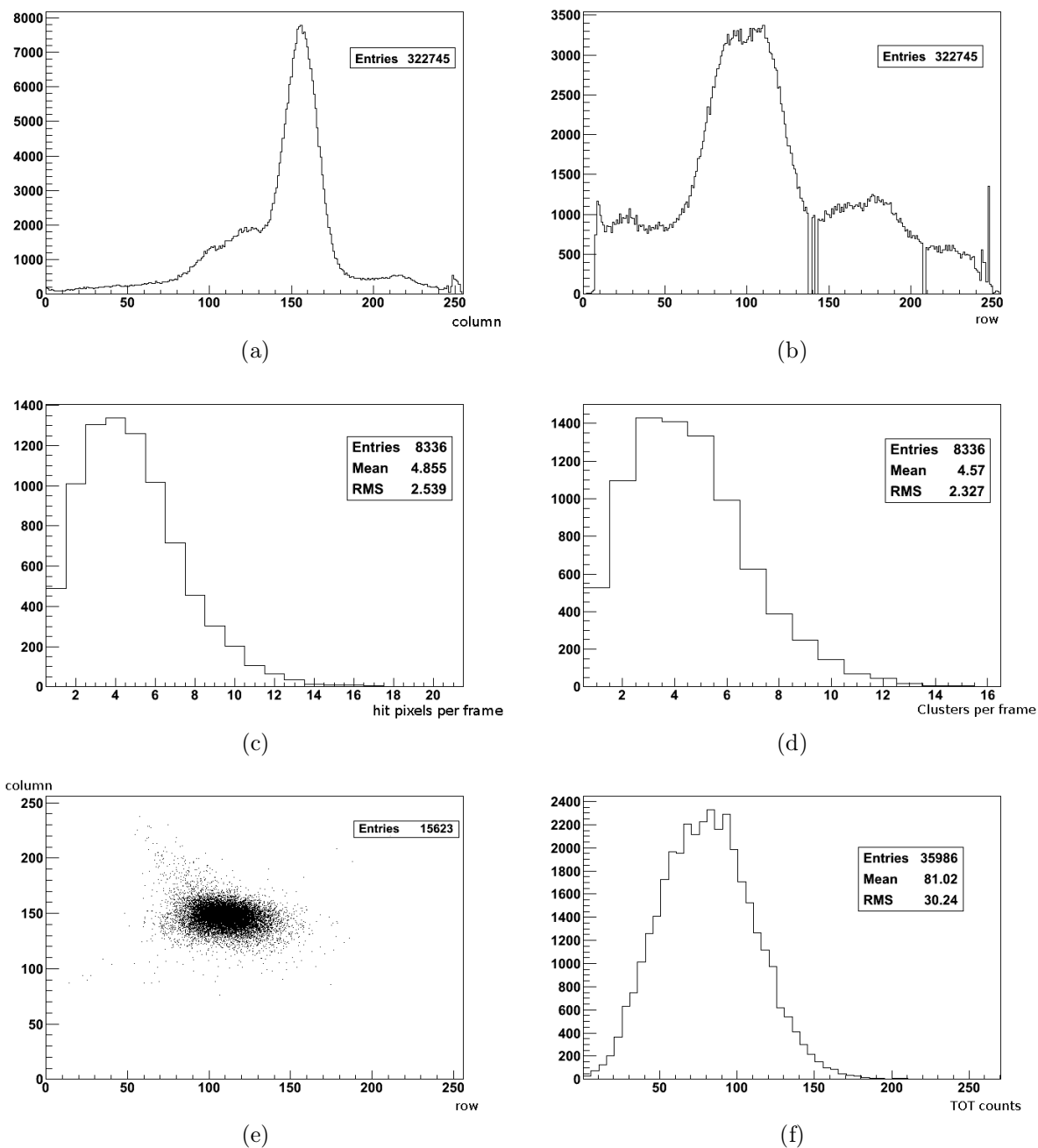


Figure 89. Control plots for the LASER measurements: (a) histogram of hits in y -direction without cuts; (b) histogram of hits in x -direction without cuts; (c) spectrum of hit pixels with area cut; (d) spectrum of clusters with area cut; (e) electron cloud centres without cuts; (f) TOT spectrum in TOT counts for clusters of size 1 with area cut. Data sample with $f_{\text{laser}} = 5.7\text{Hz}$, $U_{\text{grid}} = 340\text{V}$, $U_{\text{cath}} = 1119\text{V}$.

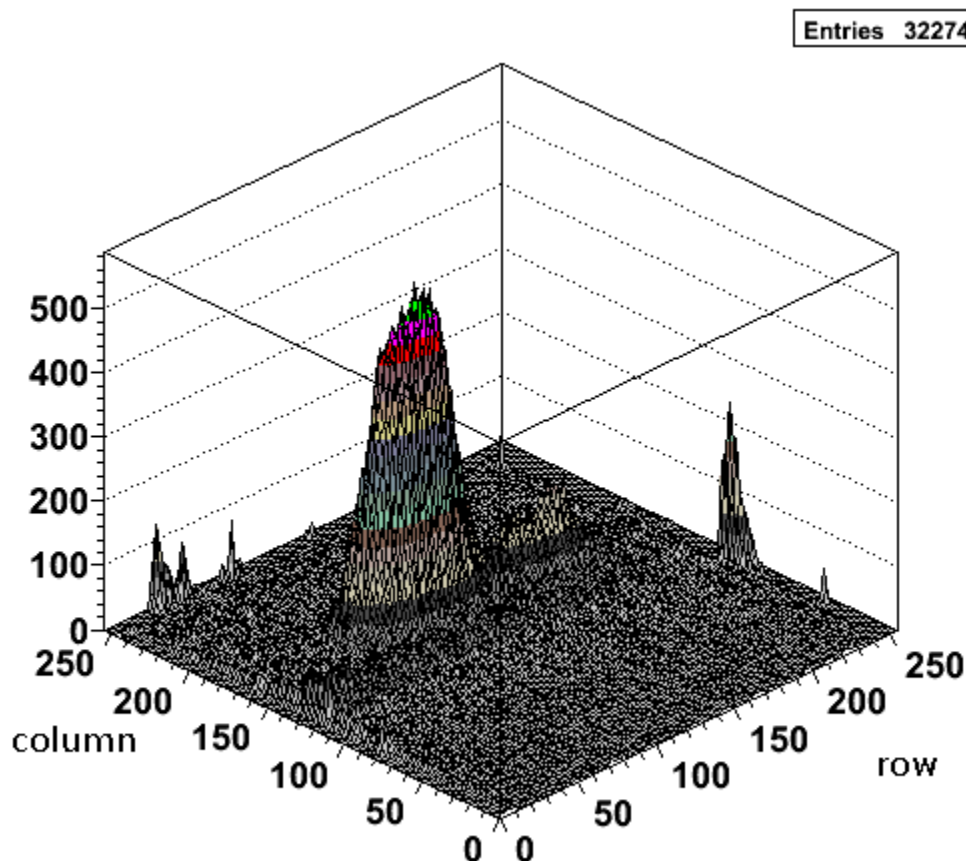


Figure 90. Three dimensional plot of the hit pixel distribution. The peak corresponds to the area where the LASER was focused on the cathode. Data sample with $f_{\text{laser}} = 5.7 \text{ Hz}$, $U_{\text{grid}} = 340 \text{ V}$, $U_{\text{cath}} = 1119 \text{ V}$.

In Figure 90 a three dimensional plot of the hit pixel distribution is shown. The area that was selected for the area cut corresponds to the peak that comes from the position the LASER was focused on at the cathode. Hits from sparks are visible at the borders of the chip. Dead columns and masked pixels can also be seen. They are due to masked areas on the chip.

Before the main measurements were carried out some test measurements with the same parameters had been performed. It was observed that within an acquisition time of 0.2 s , which is long compared to the acquisition times used for the ^{55}Fe measurements, critical areas of the InGrid became clearly visible. Defective parts of the InGrid, where current between grid and chip is present, could be seen. In Figure 91 a Pixelman image from a test measurement is shown that is an integral of 100 frames with an acquisition time of 2 s ($f_{\text{laser}} = 9 \text{ Hz}$, $U_{\text{grid}} = 330 \text{ V}$, $U_{\text{cath}} = 1500 \text{ V}$). The signal from the LASER but also hot spots from currents, especially in the top right corner and the centre, are visible. These hot spots have already been seen in the measurements with ^{55}Fe , but less pronounced. Ageing and oxidations have been reported from earlier measurements [Col10] and could be the reasons for the degradations of the grid, as it was stored in air for several months between the measurements. For the measurements the hot spot pixels were masked to allow the noise and cosmic suppression by the filter.

The aim of these measurements was to study the charging up effects of the SiProt by avalanches from the photo electrons. As can be seen from Figure 91 the TOT counts from the hot spots are significantly higher than the ones from the photo electron avalanches. The charging up of the SiProt is hence mainly an effect of the current from the grid at the hot spots. Note that the model developed in Section 4.4 can

only be applied to individual pixels. Spatial effects like the influence of avalanches or current at a different position of the chip are not described in the model.

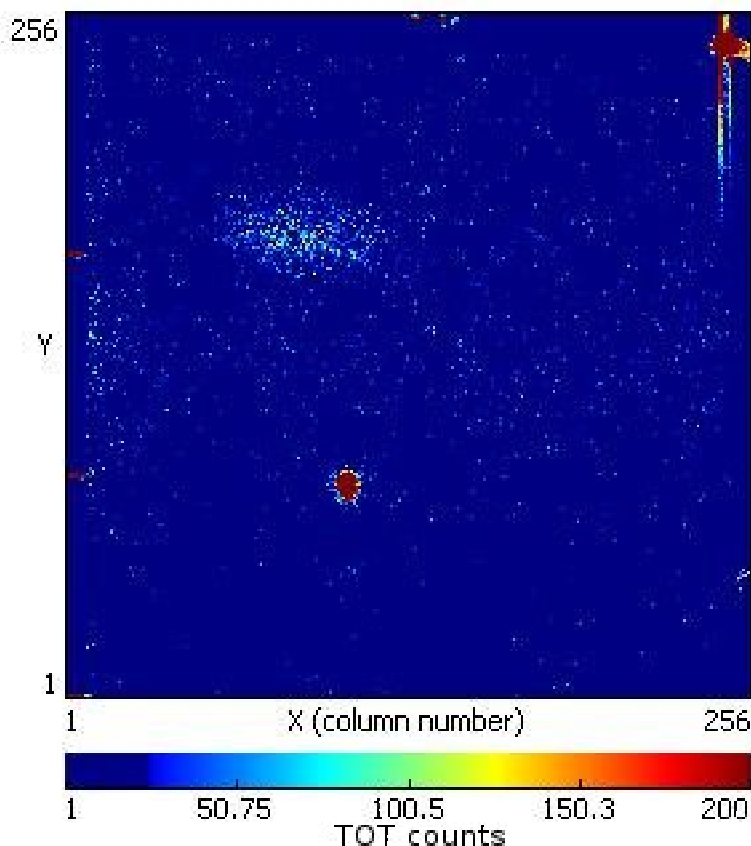


Figure 91. Pixelman image as an integral of 100 frames at an acquisition time of 2 s ($f_{\text{laser}} = 9\text{Hz}$, $U_{\text{grid}} = 330\text{V}$, $U_{\text{cath}} = 1500\text{V}$). The signals from the LASER are visible, especially at the top left. Hot spots from current between grid and chip are visible especially on the top right corner and the centre.

The TOT spectrum was transformed to the number of electrons using the TOT calibration, see Figure 88. A histogram for the data sample with $f_{\text{laser}} = 5.7\text{Hz}$, $U_{\text{grid}} = 340\text{V}$ and $U_{\text{cath}} = 1119\text{V}$ is shown in Figure 92. The transformation to electrons was done for the clusters of size 1 (see Figure 89(f)) with area cut. The Polya fit starting from 0 electrons gives a mean values of 4904 that is taken as the gain of the InGrid detector. The standard Micromegas gain for that grid voltage would be $G_{\text{mm}}(340\text{V}) = 8772$, for comparison. This gain drop is in mainly due to the current between grid and chip and not to the avalanches triggered by the LASER. The Θ value is high compared to the measurements with ^{55}Fe indicating a narrow gain distribution. This has been seen in all of the LASER measurements but might be due to an incorrect TOT calibration curve for lower than 4000 electrons. In fact the calibration curve is flat compared to other calibration curves. The aim of the measurements was, to evaluate how the InGrid gain depends on the avalanche rate. But as the main influence of the charging up effect of the SiProt is caused by the current of the hot spots this effect could not be studied.

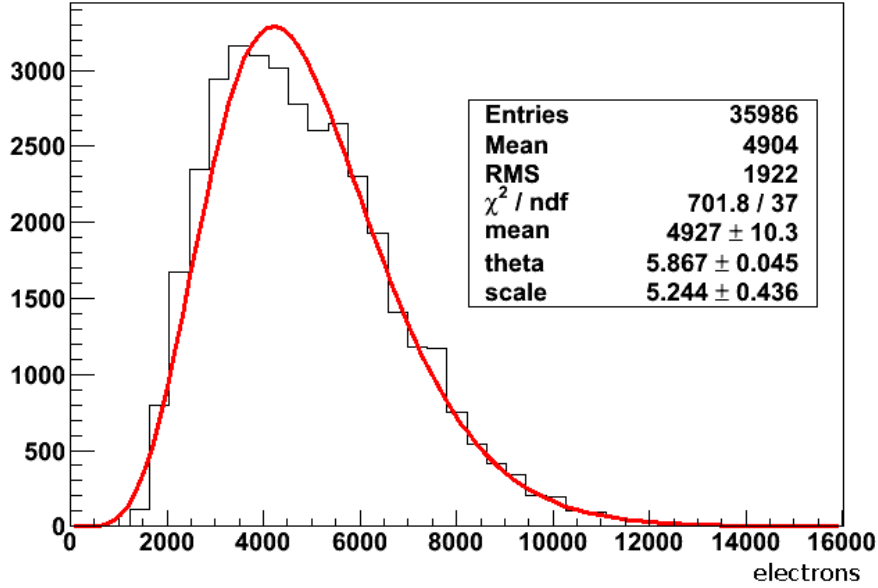


Figure 92. Electron spectrum of the LASER measurements with Polya fit, transformed from clusters of size 1 with area cut for $f_{\text{laser}} = 5.7\text{Hz}$, $U_{\text{grid}} = 340\text{V}$ and $U_{\text{cath}} = 1119\text{V}$.

For the analysis of the influence of the laser frequency, not the electron spectrum, but the TOT spectrum was used. The change of gain can also be seen on the TOT counts and this comparison is independent of the calibration. The mean of the TOT spectrum for clusters of size one with area cut (called $\overline{\text{TOT}}$) was taken for the analysis. In Figure 93 the TOT counts for the four different grid voltages are shown in dependence of the LASER repetition rate f_{laser} . The drop of the gain for higher frequency is small compared to the absolute $\overline{\text{TOT}}$ value and not clearly visible in the figure.

$U_{\text{grid}}[\text{V}]$	$f_{\text{laser}}[\text{Hz}]$	$\overline{\text{TOT}}[\text{TOT counts}]$	Error[TOTcounts]
300	9	42.02	0.25
320	9	58.13	0.35
330	9	69.15	0.41
340	9	81.98	0.49
300	5.7	43.01	0.26
320	5.7	59.34	0.36
330	5.7	75.00	0.45
340	5.7	81.03	0.49
300	3.3	43.47	0.26
320	3.3	60.34	0.36
330	3.3	72.04	0.43
340	3.3	84.50	0.51
300	1.6	44.47	0.27
320	1.6	60.80	0.36
330	1.6	72.17	0.43
340	1.6	82.84	0.50

Table 14. Mean TOT counts in the TOT spectrum of clusters of size 1 with area cut.

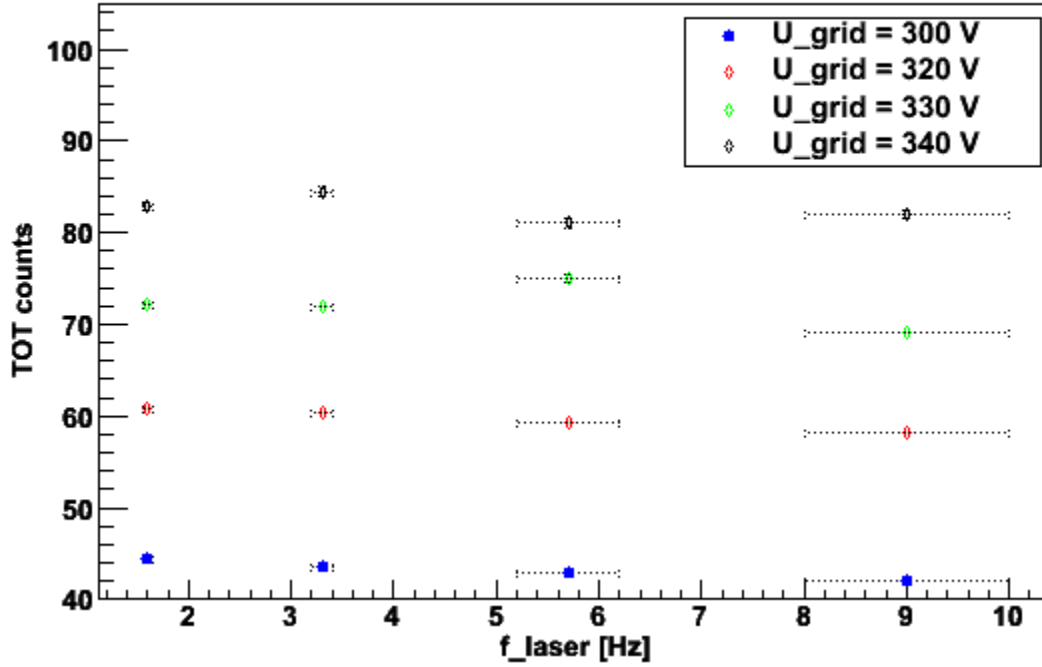


Figure 93. TOT counts for the four grid voltages in dependence of the laser repetition rate f_{laser} .

To compare all the values for the different LASER repetition rates f_{laser} the sum $\overline{\text{TOT}}_{\text{sum}}$ of all $\overline{\text{TOT}}$ for the same f_{laser} was calculated:

$$\overline{\text{TOT}}_{\text{sum}} = \overline{\text{TOT}}_{300\text{V}} + \overline{\text{TOT}}_{320\text{V}} + \overline{\text{TOT}}_{330\text{V}} + \overline{\text{TOT}}_{340\text{V}} \quad (63)$$

where $\overline{\text{TOT}}_{U_{\text{Grid}}}$ are the $\overline{\text{TOT}}$ for the different grid voltages, but same f_{laser} . The result is shown in Table 15 and Figure 94. Errors are included here. The errors on the LASER repetition rate f_{laser} are caused by the accuracy of the oscilloscope or the stopwatch to measure the frequency. The errors on the $\overline{\text{TOT}}_{\text{sum}}$ are statistical errors coming from the errors on the $\overline{\text{TOT}}$ values.

$f_{\text{laser}}/\text{Hz}$	Error/Hz	$\overline{\text{TOT}}_{\text{sum}}[\text{TOTcounts}]$	Error[TOTcounts]
9	1	251.28	1.6
5.7	0.5	258.38	1.6
3.3	0.1	260.35	1.6
1.6	0.05	260.28	1.6

Table 15. $\overline{\text{TOT}}_{\text{sum}}$ for the different LASER repetition rates

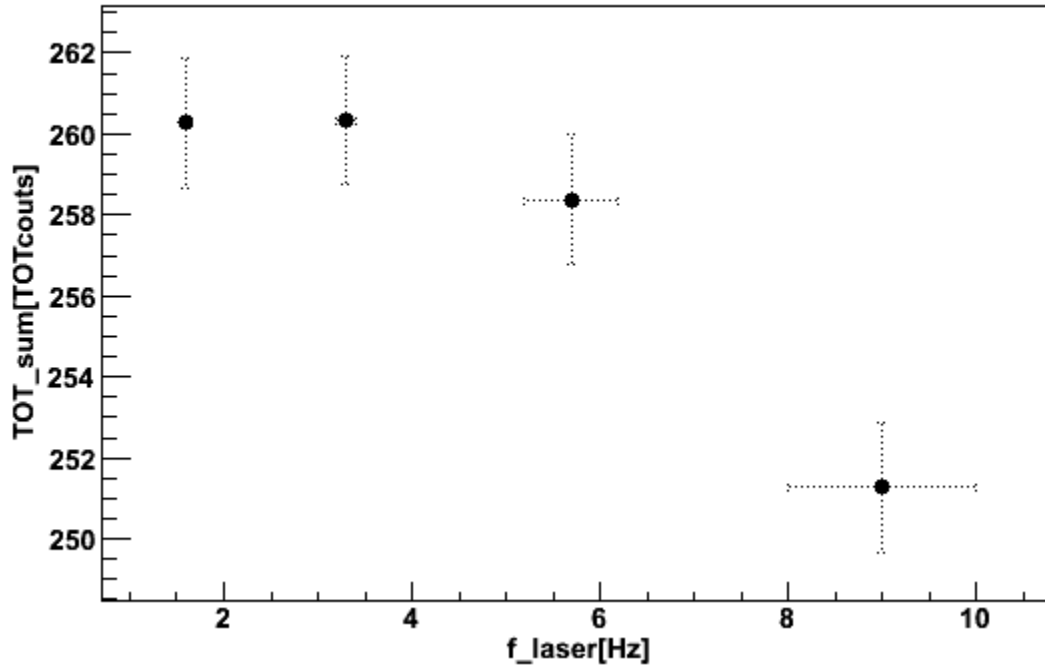


Figure 94. $\overline{\text{TOT}}_{\text{sum}}$ as function of the LASER repetition rate f_{laser} .

The gain drop measured was not as significant as expected, but is visible in the Figure showing TOTsum. As a result of the LASER measurements it was observed that the charging up effects were mainly influenced by currents between grid and chip. As can be seen from Figure 94 a small drop of the gain for a repetition rate of 9Hz has been observed. A possible interpretation of this results is, that at higher rates the number of avalanches becomes more and more comparable to the current between grid and chip.

5 An eight chip panel for the large LC TPC prototype

The long term aim in the development of a TPC using pixel chips as readout is to construct large surface readout structures. At the moment the MUROS readout is capable to read eight chips at the same time. Panels with four InGrid chips have been constructed by NIKHEF. A panel equipped with eight InGrid chips called Octopuce (Octo for eight, puce (french) for chip) has been build in Saclay for the detection of tracks in the large LC TPC prototype [Deh08] at DESY.

5.1 The LC TPC prototype

The Linear Collider TPC (LCTPC) collaboration has constructed a large prototype (LP) of a TPC at DESY, see Figure 95 top. The barrel has a diameter of 75cm and a length (z -coordinate) of about 60cm. It is embedded in a 1.25T permanent current magnet (PCMAG), placed in the DESY II test beam area and can be moved such that the beam traverses the TPC on a different z position. The beam consist of

electrons with an energy up to $6 \text{ GeV}/c$. The endplate (Figure 95 bottom) can be equipped with up to seven modules of any technology (Micromegas or GEM using pads or Timepix as readout).

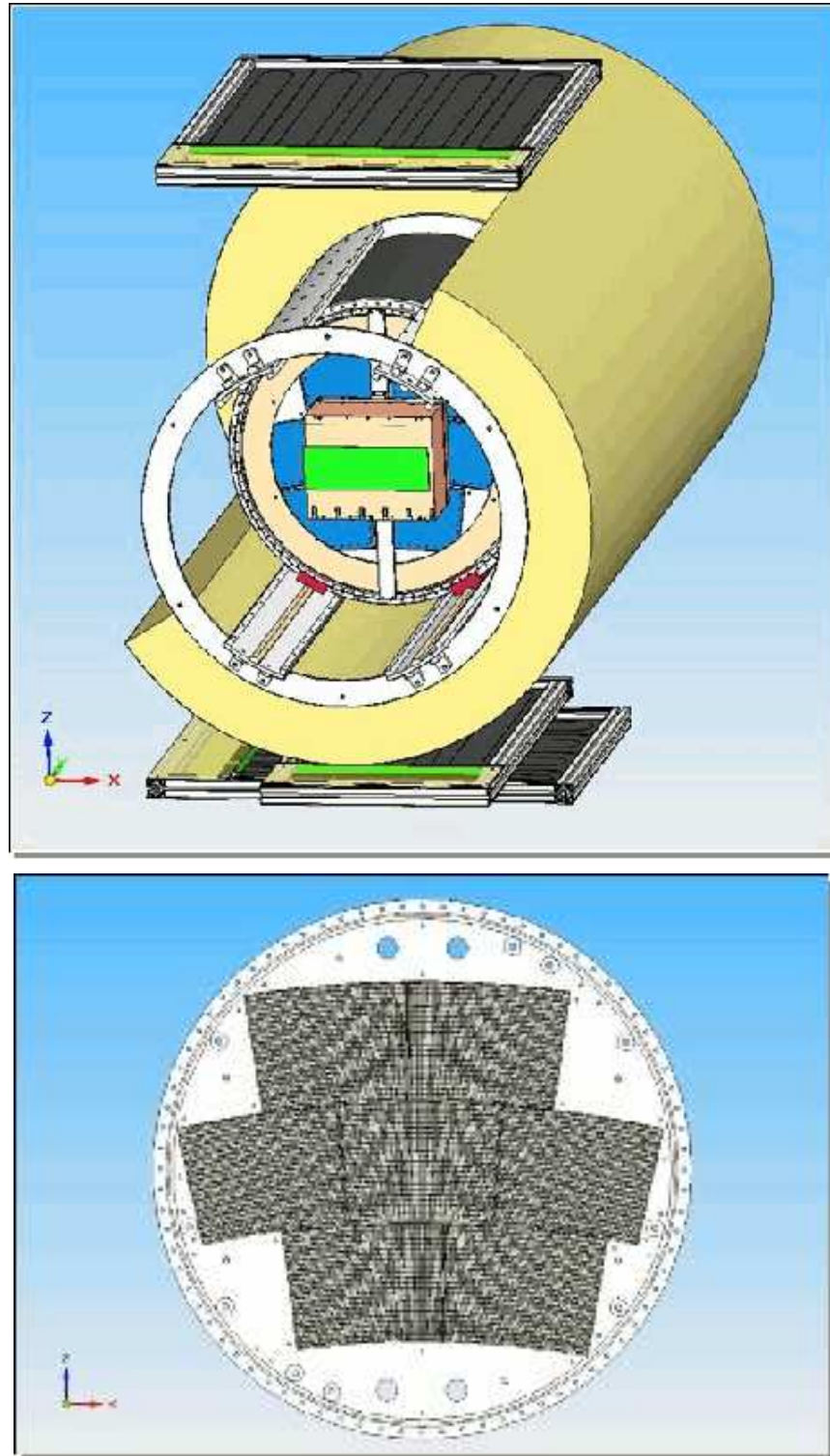


Figure 95. Schematic of the LCTPC prototype (top) and endplate (bottom)

5.2 Octopuce

One module for the LCTPC prototype was prepared to hold eight InGrid chips. The setup consists of a frame that can be mounted on the endplate of the LCTPC prototype, a mother PCB that carries the electronics for the power supply of the chips and the readout, a daughter PCB that carries the chips and a guard plate to provide a uniform electric field in the TPC, see Figure 96.

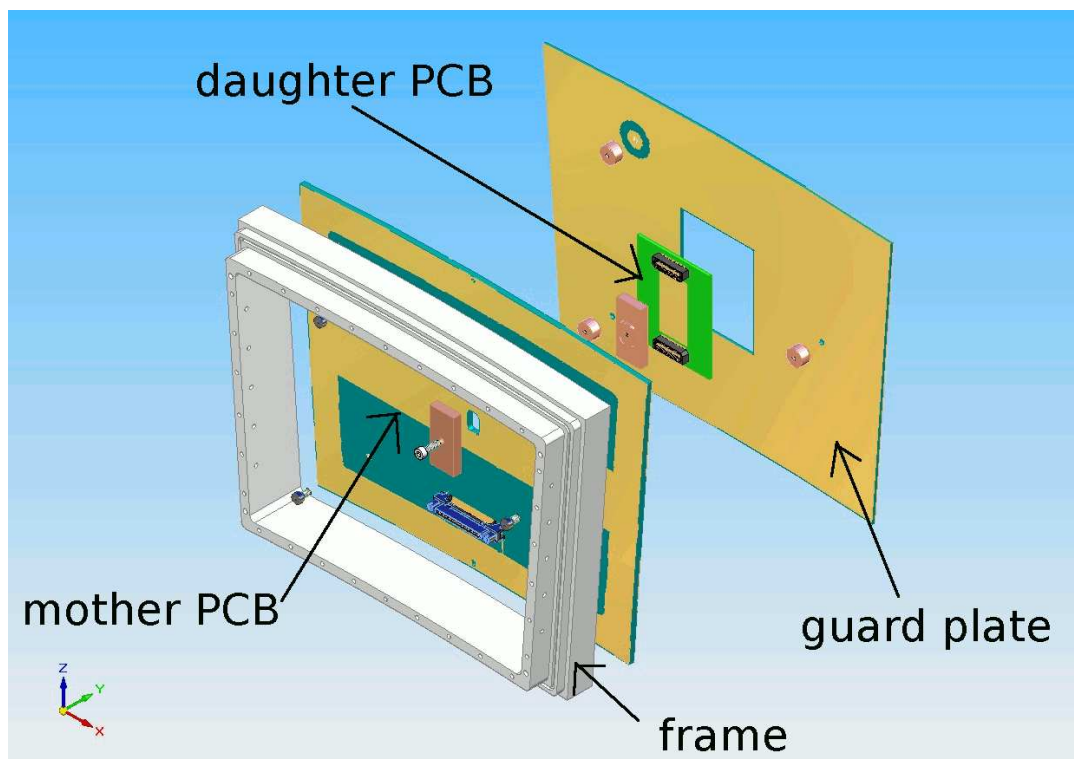
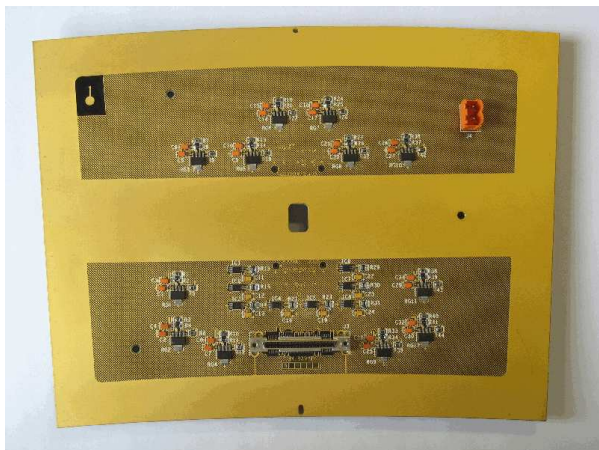
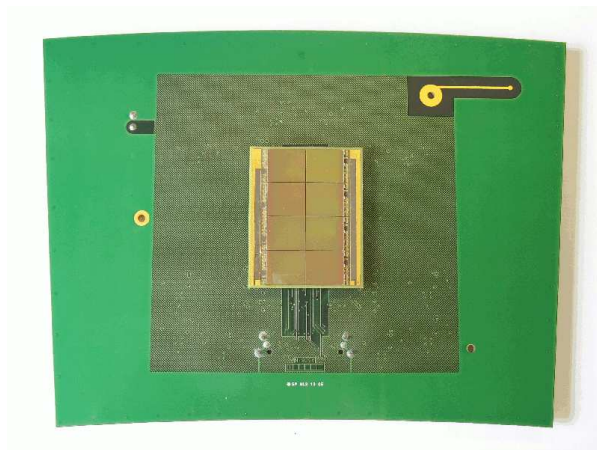


Figure 96. Octopuce module for the LCTPC prototype. Aluminium frame, mother PCB, daughter PCB and guard plate.

The PCBs were designed by the CEA Saclay SEDI electronics department. As the MUROS can only read out eight chips but not support the power an external power supply was also connected to the mother PCB. The data from the chips is shift from one chip to the next one. If one chip is damaged it can be bypassed. This is not possible for the first and the last chip. The power supply was the biggest challenge of the setup. The voltage levels of the different circuits have to be correct such that the chips work and the data readout is possible. The power consumption (≈ 6 W) and heating were also not negligible. The heat was transported to the rear side of the mother PCB by a copper block that was connected to the rear side of the daughter PCB with heat conducting paste. The PCB cards, voltage supply and power consumption were first tested using Timepix chips on the first daughter PCB. Later eight InGrid chips were glued and bonded on a second daughter PCB. The HV connections of the InGrids were additionally fixed with a drop of silver glue (see Figure 97 (5)). The grids have not been perfect. In Figure 97 (6) a microscope picture of a big hole in one of the grids is shown. At some of the corners the grids have been wavy.



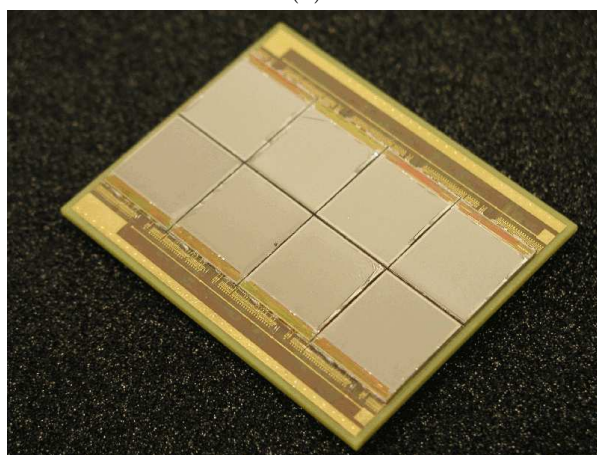
(1)



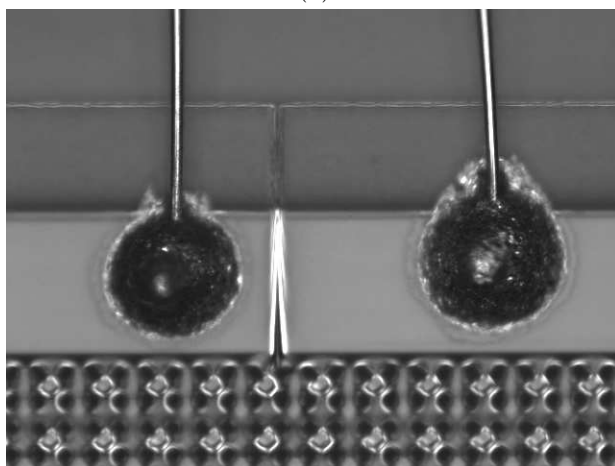
(2)



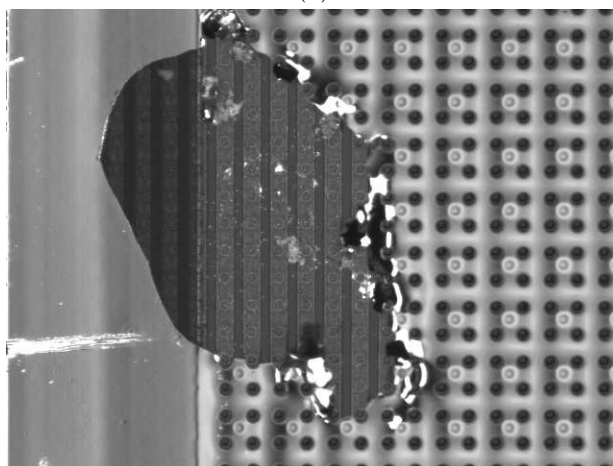
(3)



(4)



(5)



(6)

Figure 97. Images of the Octopuce: (1): Rear side of the mother PCB with electronic circuits for power support and readout; (2): Daughter PCB mounted on the front side of the mother PCB, here equipped with eight Timepix chips; (3): Guard plate mounted on the mother PCB, the daughter PCB and the eight chips are visible in the window in the centre; (4): Daughter PCB equipped with eight InGrid chips; (5): HV wire bonds on the grid of one of the InGrids additionally fixed with a drip of silver glue; (6): Hole in one of the InGrid grids.

5.3 Detector tests

The Timepix chips of each InGrid were working correctly. In Figure 98 some images from the Pixelman software are shown. There were nine dead columns on all the chips (1: map of masked pixels). The threshold equalisation map is shown in (2). The different colours correspond to different values of the thrAdj bits. Test pulses in TIME (3) and TOT (4) were sent to the chip. In (3) the distribution of the test pulses can be seen from the colour code. A darker blue means a later time of test pulse arrival. The Octopuce chips worked electronically. The condition of the amplification structure was tested in a gas box for LCTPC module tests.

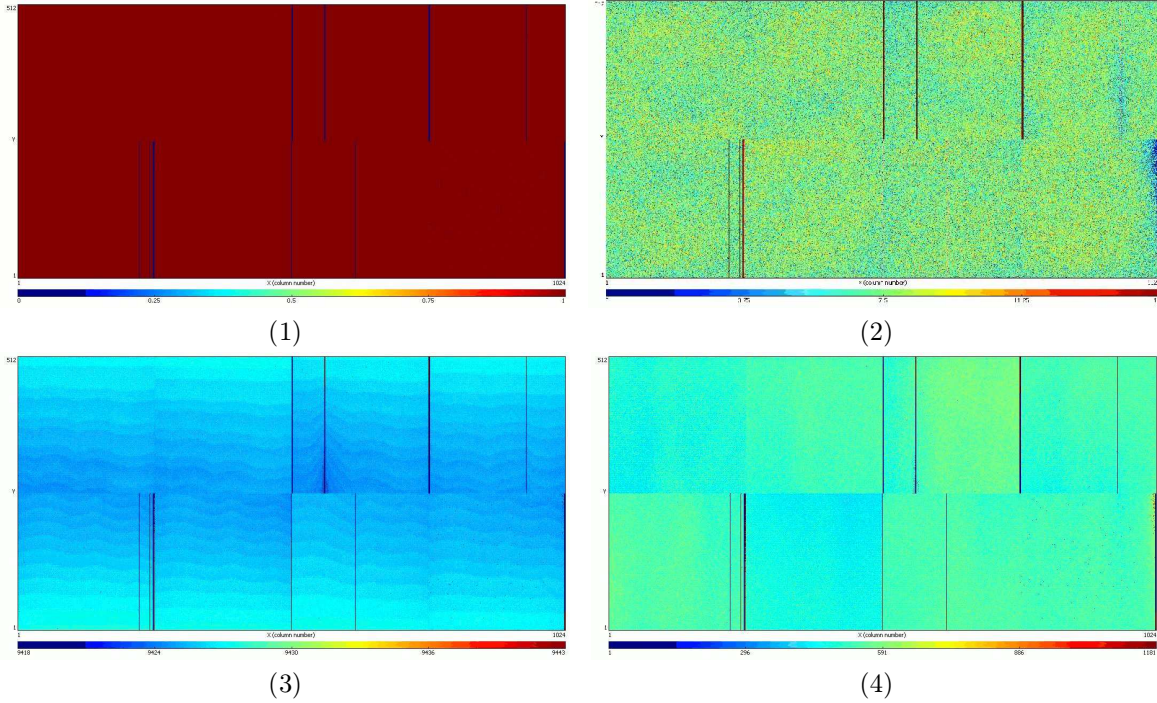


Figure 98. Pixelman images from the electrical test of the Timepix chips of the InGrids. (1): Map of the masked pixels (dark). Nine columns were dead. (2) Threshold adjustment map. The colour code corresponds to the values of the thrAdj bits. (3) Signal from test pulses in TIME mode. The dark blue corresponds to a later time of signal arrival. (4) Signal from pulses in TOT mode.

The drift distance in this detector was 3cm. The cathode was put on a potential of 800V. The grid voltage was raised with care to prevent sparks. At the voltage supply NIM as well as in the Pixelman image a current between grid and chip was registered. The current was stable and of the order of 20nA at voltages not higher than $U_{\text{grid}} = 275V$. In Figure 99 the track of an alpha particle in TOT mode at $U_{\text{grid}} = 275V$ in ArIso 95/5 with an acquisition time of 0.5s is shown. As the acquisition time was that long no external trigger was necessary. In this Pixelman image the signals from the current between grid and chip are also clearly visible (marked in red). The current occurs at the border of one of the chip and also in the centre area of two chips. The largest spot is at the same position as the big hole in one of the InGrids shown in Figure 97 (6). Due to the current between grid and chips no measurement at voltages higher than 275V (gain lower than 1000) can be presented here. Recently a grid voltage of 300V and a stable operation of the Octopuce has been achieved. The panel will be used in a test beam at DESY in the large LCTPC prototype to detect tracks from electrons of up to 6 GeV/c.

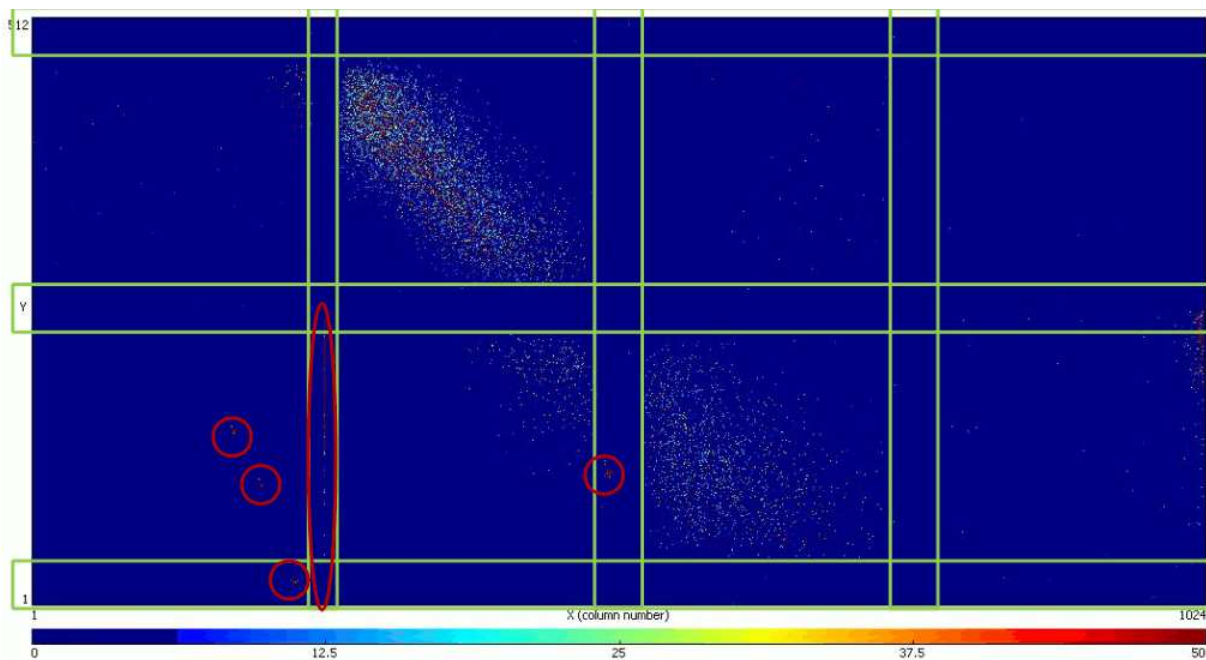


Figure 99. Pixelman image in TOT mode from the Octopuce in ArIso 95/5 with a grid voltage of 275V. No trigger system for cosmics was used. The acquisition time was set to 0.5s. A track from a alpha particle and some is visible. The edges of the chips are marked in green. In this region no signal is registered. Signals from discharges or current between grid and chip are marked in red.

6 Summary and outlook

In this last chapter the results of this thesis are summarised. The two main fields of investigation will be given two individual section (Section 6.1.1 and 6.1.2). Other outcomes like the LASER test bench and the Octopuce are also summarised in Section 6.1. The final section of this thesis is an outlook on future activities in this this field of research.

6.1 Summary

A Laser test bench has been constructed in Freiburg to test and characterise MPGDs. With this setup electrons from the drift cathode can be released and used as primary charge. First measurements had been performed with a GEM+Timepix setup.

A panel hosting eight InGrid chips has been constructed in Saclay. The PCB cards were shown to support the InGrid with power and transfer the data. It was successfully read out with the MUROS interface. The grids of the detector have not been in a condition to arrive at gains of higher than 2000. Tracks of cosmic particles were measured in the laboratory in ArIso 95/5. The panel will be taken to the DESY and plugged into the large prototype of the LCTPC collaboration for measurements with electrons of up to 6 GeV/c.

Measurements with a single InGrid chip were performed mainly in ArIso 95/5 gas. Measurements in ArIso 80/20 had also been performed but could only give limited results as the diffusion is lower in this mixture. Other gases (CH_4 , CF_4 , P10) were also used. In this gases higher grid voltages were necessary to arrive at a sufficient gain. The probability for sparks is higher in this gases. The Timepix chip G06-W0096 has been used as readout in an InGrid detector in a period of one year. At highest grid voltages of 365V in ArIso 95/5 and especially in a P10 gas mixture it has suffered from many sparks and discharges. Nine columns had been destroyed during the measurements. The behaviour of the columns next to the destroyed ones has also been affected. A recalibration and new threshold equalisation has been necessary

after the strongest sparks. The quality of the chip (electronic noise level, TOT variations after the threshold equalisation) had not been affected by the sparks. The chip could still be used after recalibrations. Two main topics have been investigated: the measurement of the gas gain and the counting of single electrons with a InGrid detector.

6.1.1 Avalanche statistics

An InGrid is a Micromegas like detector. It consists of an amplification gap that is placed directly on top of the readout structure. Additionally a protection layer (SiProt) is necessary to protect the pixel readout from sparks. This layer leads to a different behaviour of an InGrid compared to a standard Micromegas. The gain of an InGrid detector was measured using primary electrons from the conversion of photons from a ^{55}Fe source. Gains of down to 50% compared to a standard Micromegas detector was measured in ArIso 95/5. The gain of the Micromegas detector had been measured for ArIso 95/5, ArIso 80/20, CH_4 , CF_4 and P10. A theory describing the effect of the SiProt layer has been developed. The smaller gain of the InGrid detectors is based on charging up effects of the SiProt layer. The newly developed theory predicts voltages of up to 20V on top of this layer at grid voltages of 365V in ArIso 95/5 have been calculated. The drop of gain is strongly dependent on the frequency of avalanches. A time constant of the order of $\tau_{\text{theo}} = 1 \text{ min}$ has been predicted from the theory. A time constant $\tau_{\text{meas}} = (1.27 \pm 0.05) \text{ min}$ was measured using the change of voltage on top of the SiProt layer if the avalanche rate is changed. The rate of the avalanches was changed by placing the source in larger distances from the detector. At lowest rates the gain of the InGrid detectors approaches the Micromegas gain. The gain of an InGrid detector can be calculated from the TOT counts and agrees with the gain of a Micromegas detector if the effects of the SiProt layer are taken into account.

The Θ value of the Polya function fitted to the gain distribution was measured. At highest gain of 8777 ± 14 and 7902 ± 22 values of $\Theta = 2.60 \pm 0.02$ and $\Theta = 2.68 \pm 0.04$ respectively was measured directly from the gain distributions. An evaluation of the single electron detection efficiency of the InGrid detector indicates $0.5 \lesssim \Theta \lesssim 2$ for gains from ≈ 2000 to ≈ 5000 . A dependence of Θ of the gain is possible.

The LASER test bench in Freiburg was used to produce photo electrons as primary charge. Tests with low avalanche rate were performed to measure a dependence between the rate and the gain. Due to currents between grid and chip, that might result from ageing of the grid, no quantitative measurements could be done. There are hints for a drop of the gain for the highest repetition rates.

6.1.2 Single electron counting

To investigate the number of primary electrons in a conversion of a photon of ^{55}Fe in Argon based mixtures a high diffusion is necessary. The highest diffusion in a gas, that allows stable measurements, was achieved in ArIso 95/5. The spectrum of the number of hit pixels and clusters per electron cloud had been recorded. Different cuts were applied, among others a cut on the electron cloud size. The position of the photo peak changes for different cut values. The diffusion is not sufficient to separate all the electrons leading to this peak. The escape peak was used for the analysis. Tests at different ratios between drift and amplification field (field ratio) and different gas fluxes were performed to verify that the used and fixed parameters of a field ratio of the order of 100 and a gas flux of 10 l/h assure optimum detector performance. The number of electrons in the escape peak was investigated at different gains (single electron detection). A saturation of 144 ± 1 hit pixels and 117.9 ± 0.7 clusters was measured. The number of clusters is assumed to represent the primary electrons and that the saturation appears at 100% single electron detection efficiency. More than 97.8% single electron detection efficiency have been reached for the highest gains. Simulations using MAGBOLTZ lead to a value of 116 primary electrons in the escape peak.

From the resolution of the escape and photo peak an upper limit of the Fano factor can be calculated. In a long term measurement a spectrum with the best resolution was measured. A resolution of $\text{FWHM}_{\text{photo}} = 9.73\%$ for the photo peak and $\text{FWHM}_{\text{escape}} = 12.98\%$ for the escape peak was achieved. The limits for the Fano factor from the escape and photo peak are $F_{\text{escape}} \leq 0.31 \pm 0.02$ and $F_{\text{photo}} \leq 0.25 \pm 0.01$ respectively. In [Che09] an upper limit of $F \leq 0.21 \pm 0.06$ is reported.

6.2 Outlook

Pixelated readout structures are an interesting technology for the next generation of TPCs. It has been shown that the Timepix works with GEM and Micromegas amplification structures. The Timepix chip has a sensitive surface of $1.4 \times 1.4 \text{ cm}^2$. At the present the aim is to construct large area arrays of Timepix chips. Two modules with 4 Timepix chips read out simultaneously were build end tested in Bonn using GEMs as amplification structure. The modules were installed in the Large Prototype TPC at DESY and tracks of electrons have been recorded. The analysis is still ongoing. First results are presented in [Bre10].

The Octopuce presented in this thesis will be tested in the Prototype at DESY possibly at the end of 2010. At the present only gains lower than 2000 can be achieved with this module due to damages of the grids. If this defects can be fixed tracks at gains of the order of 5000 could be recorded. The analysis of this measurements will give interesting results concerning the number of ionisations per track length (that can directly be seen by means of the number of hit pixels), the track and point resolution and the charging up effect of the SiProt in a real detector environment.

The MUROS interface can read out eight chips at the same time. The Octopuce arrives at this limit. A new interface is necessary to build large area detectors with of the order of 100 Timepix chips. There are efforts at Bonn, Mainz and NIKHEF to develop such an interface.

On the chip side the Timepix2 chip is under development at CERN. To avoid dead area on the front side, an implementation for the readout from the back side would be preferable. This is necessary to get as much sensitive surface as possible on an endplate consisting of many chips.

For the production of InGrid chips the fabrication process needs to be improved. The grids are very fragile and currents between grid and Timepix chip have been detected. In some of the cases this lead to the destruction of the chip, in others the gain was limited. Until now InGrid structures on top of Timepix chips have only been produced one by one in the laboratory [Bla09]. The automation of the fabrication and the development of robuster chips are reasons for the cooperation between the Bonn and Twente groups and the IZM (Fraunhofer-Institut für Zuverlässigkeit und Mikrointegration) in Berlin and the Saclay group with LAAS (Laboratoire d'Analyse et d'Architecture des Systèmes) in Toulouse. The mass production of InGrids on the wafer is necessary to build large detector arrays.

Within this Diploma thesis the effect of the SiProt layer has been studied. It was shown that the gain of an InGrid structure depends on the rate of avalanches. If InGrid structures should be used in regions of the detector where high rates are expected a new concept of chip protection has to be developed.

Résumé et perspectives

Ce chapitre est un résumé du mémoire. Les deux domaines principaux sont présentés dans des sections séparées (Section 6.3.1 et 6.3.2). Les autres résultats comme l'installation de mesure LASER et l'octopuce sont résumés dans la Section 6.3. Le chapitre final du mémoire discute des perspectives sur les activités futures à conduire dans ce domaine de recherche.

6.3 Résumé

Les détecteurs gazeux à micro-structures (Micro Pattern Gaseous Detectors, MPGS) sont de nouveaux détecteurs gazeux avec des structures de l'ordre de quelques dizaines de micromètres. Dans nos expériences, un détecteur InGrid-Timepix était utilisé. La puce Timepix est finement pixelisée. Chaque pixel fait office d'anode pour collecter la charge des avalanches créées dans le gaz, et est équipé d'un amplificateur et d'un discriminateur. Le signal de chaque pixel est un nombre de cycles d'une horloge qui correspond à la charge déposée dans le pixel (mode Time Over Threshold TOT) ou au temps d'arrivée du signal. $50 \mu\text{m}$ au-dessus de la puce se trouve une grille avec un potentiel de $\approx 400 \text{ V}$. Le détecteur entier se situe dans une atmosphère de gaz. Dans un champ électrique fort entre grille et puce (région d'amplification), des électrons primaires qui entrent dans les trous de la grille sont accélérés. Ils peuvent ioniser des atomes du gaz dans la région d'amplification et produisent des électrons secondaires (gain de gaz). Les électrons de cette avalanche sont collectés dans les pixels et mesurés par l'électronique connectée. Pour une puce InGrid chaque trou se trouve exactement au-dessus d'un pixel. Ainsi, une avalanche d'un électron qui entre dans un trou se dépose sur un pixel au-dessous. Les électrons primaires proviennent d'une région au-dessus de la grille (région d'ionisation). Ils sont dus à la conversion d'un photon dans le gaz du

détecteur ou à l'ionisation créée par le passage d'une particule chargée. Grâce à un champ électrique, les électrons sont évacués vers la grille. Dans la plupart de nos expériences, les photons étaient produits par une source de fer radioactif (^{55}Fe).

Le but des expériences était d'une part la mesure des distributions de nombres d'électrons primaires. Ces derniers étaient diffusés dans le volume de dérive en direction de la grille. Dans le cas optimal, seul un électron primaire entraînait dans un trou de la grille. Dans ce cas, chaque pixel allumé correspondait à un électron primaire. A gain élevé il est possible qu'une avalanche se dépose sur quelques pixels voisins (partage de charge). Le nombre des clusters (ensemble de pixels connexes) est compté dans les mesures.

D'autre part, nous avons analysé le processus de multiplication. Comme pour une diffusion forte, un seul électron primaire entre dans un trou de la grille, le nombre d'électrons secondaires compté correspond au facteur de gain. Comme le processus de multiplication est un processus statistique, le gain suit une certaine distribution. Le but des mesures était de mesurer cette distribution pour différents gains (ou tension de grille). La distribution de gain suit approximativement une fonction Polya.

Une installation de mesure LASER a été construite à Freiburg pour tester et caractériser des MPGDs. Ce montage expérimental consiste à l'émission des électrons primaires de la cathode par l'effet photoélectronique. Des mesures ont été effectuées avec un détecteur GEM+Timepix.

Un panneau qui porte huit puces InGrid a été construit à Saclay. Les cartes électroniques fonctionnent et assurent la transmission des données et de l'alimentation. Les puces ont été lues avec succès grâce à l'interface MUROS. Les grilles du détecteur n'ont pas été en état d'arriver à un gain supérieur à 2000. Les traces de rayons cosmiques ont été mesurées dans le laboratoire dans un mélange d'Argon et d'Isobutane 95/5. Le panneau va être apporté au DESY pour effectuer des mesures en faisceaux d'électrons d'énergie allant jusqu'à $6\text{ GeV}/c$.

Les mesures avec une seule puce ont été effectuées principalement dans Argon-isobutane 95/5. Des mesures ont également été effectuées dans ArIso 80/20 mais ont seulement donné des résultats limités à cause d'une diffusion plus faible dans ce gaz. D'autres gaz (CH_4 , CF_4 , P10) ont été utilisés, pour lesquels des voltages plus forts ont été nécessaires afin d'atteindre un gain suffisant. La production d'étincelle est plus fréquente dans ces gaz. La puce Timepix G06-W0096 était utilisée comme système de lecture dans un détecteur InGrid pendant une période d'un an. Aux voltages les plus grands de 365 V dans ArIso 95/5 et particulièrement dans le mélange P10, elle a subi beaucoup de sparks et de décharges. Neuf colonnes ont été détruites pendant les mesures. Le fonctionnement des colonnes voisines des colonnes détruites a aussi été affecté. Un re-calibrage et une nouvelle adaptation de seuil se sont avérés nécessaires après les étincelles les plus fortes. Cependant, la qualité de la puce (seuil électronique, variations de TOT après adaptation) n'a pas été notablement influencée par les étincelles. La puce pouvait encore être utilisée après un re-calibrage.

Deux thèmes principaux ont été étudiés: la mesure de gain de gaz et le comptage des électrons avec un détecteur InGrid.

6.3.1 Statistique des avalanches

Un détecteur InGrid est un Micromegas intégré sur silicium. Il se compose d'un espacement d'amplification qui se trouve directement sur la structure de lecture. Il y a une couche supplémentaire (SiProt) qui est nécessaire pour protéger les pixels des étincelles. Cette couche change l'attitude du détecteur InGrid comparé avec le un Micromegas standard. Le gain d'un détecteur InGrid était mesuré avec des électrons primaires d'une source de ^{55}Fe . Des gains jusqu'à 50% en regard d'un Micromegas standard ont été mesurés dans ArIso 95/5. Le gain du détecteur Micromegas standard était mesuré dans ArIso 95/5, ArIso 80/20, CH_4 , CF_4 , et P10. Une théorie qui décrit les effets de la couche SiProt a été développée. La perte de gain du détecteur InGrid était dû au chargement de la couche SiProt. Avec cette théorie des voltages jusqu'à 20 V sur la couche ont été calculés à des voltages de 365 V sur la grille dans ArIso 95/5. La diminution du gain dépend fortement de la fréquence des avalanches. Une constante de temps de $\tau_{\text{theo}} = 1\text{ min}$ est prédite par la théorie. Une constante de temps de $(1.27 \pm 0.05)\text{ min}$ était mesurée à la suite d'un changement de voltage sur la couche si la fréquence des avalanches changeait. La fréquence des avalanches était changée en éloignant la source. Aux taux les plus faibles, le gain du détecteur InGrid se rapproche au gain du détecteur Micromegas sans SiProt. Le gain du détecteur InGrid peut être calculé à partir du TOT et est en accord avec le gain du détecteur Micromegas si les effets de la couche SiProt sont pris en compte.

La valeur du paramètre Θ de la courbe d'ajustement Polya à la distribution de gain a été mesurée. Aux gains les plus hauts de 8777 ± 14 et 7902 ± 22 des valeurs de $\Theta = 2.60 \pm 0.02$ et $\Theta = 2.68 \pm 0.04$ respectivement, ont été mesurées des distributions de gain. Une évaluation de l'efficacité de détection des électrons du détecteur InGrid indique $0.5 \lesssim \Theta \lesssim 2$ pour des gains de ≈ 2000 à ≈ 5000 . Une dépendance de Θ en fonction du gain est possible.

L'installation de mesure LASER à Freiburg a été utilisée pour produire des électrons photoélectronique comme charge primaire. Des test aux fréquences faibles ont été effectuées pour mesurer la relation fonctionnelle entre la fréquences et le gain. A cause de courants entre la grille et la puce, qui peuvent résulter du vieillissement, des mesures quantitatives n'étaient pas possibles. La perte de gain pour les taux les plus hautes était visible.

6.3.2 Comptage des électrons

Pour étudier le nombre d'électrons primaires dans la conversion de photons de ^{55}Fe dans des mélanges basés sur l'Argon, une diffusion forte est nécessaire. La diffusion la plus forte dans un gaz qui assure des mesures stables a été trouvée dans ArIso 95/5. Le spectre du nombre de pixels touchés et de clusters dans un nuage d'électrons a été mesuré. Des coupures différentes ont été appliquées, dont une sur la taille des nuages. La position du pic photo-électrique change pour des valeurs différentes de coupure. La diffusion n'est pas suffisante pour séparer tous les électrons primaires qui composent ce pic. Le pic d'échappement était utilisé pour les analyses. Des mesures pour différentes valeurs du rapport entre le champ de dérive et le champ d'amplification et aux différent flux des gaz ont été effectuées. pour tester la stabilité des résultats vis-à-vis de ces paramètres. Pour les mesures un rapport de champ d'environ 100 et un flux de gaz de 10 l/h a assuré une efficacité optimale. Le nombre d'électrons dans le pic d'échappement a été étudié pour des gains différents (détection des électrons séparés). Une saturation à 144 ± 1 pixels et 117.9 ± 0.7 clusters était mesurée. Il est supposé que le numéro de clusters correspond aux électrons primaires et la saturation apparaît efficace à 100% pour la détection des électrons séparés. Pour les gains les plus hauts, une efficacité de 97.8% de détection des électrons séparés était observée. Les simulations avec MAGBOLTZ donnent une valeur de 116 électrons primaires pour le pic d'échappement.

Une limite supérieure pour le facteur Fano peut être calculée à partir de la résolution des pics. Dans une mesure pendant la nuit, un spectre avec la résolution la plus haute a été mesuré. Une résolution de $\text{FWHM}_{\text{photo}} = 9.73\%$ pour le pic photo et de $\text{FWHM}_{\text{echap}} = 12.98\%$ était obtenu. Les limites pour le facteur Fano de pic photo et pic d'échappement sont $F_{\text{photo}} \leq 0.25 \pm 0.01$ et $F_{\text{echap}} \leq 0.31 \pm 0.02$ respectivement. Dans [Che09], une limite supérieure de $F \leq 0.21 \pm 0.06$ est mentionnée.

6.4 Perspective

Les structures de lecture avec pixel sont une technologie intéressante pour une TPC de la nouvelle génération. Il a été démontré que le Timepix fonctionne avec des GEM et Micromegas comme système d'amplification. La puce Timepix a une surface sensible de $1.4 \times 1.4 \text{ cm}^2$. Actuellement, le but est de construire des systèmes de grande surface avec des puces Timepix. Deux modules à 4 puces Timepix lues par deux MUROS a été construit à Bonn avec des GEMS. Le module a été testé dans le Grand Prototype à DESY et des traces des électrons ont été enregistrées. L'analyse est encore en cours. Les premiers résultats sont présentés dans [Bre10].

L'Octopuce présentée dans ce mémoire va probablement être testée dans le Grand Prototype à DESY à la fin de l'année 2010 Pour le moment, seuls des gains allant jusqu'à 2000 peuvent être atteints avec ce module à cause de défauts des grilles. Si ces défauts peuvent être réparés et la connection entre grille et puce peut être coupée, des traces aux gains d'environ 5000 peuvent être enregistrées. L'analyse de ces mesures va donner des résultats intéressants sur le numéro des ionisations par longueur de trace (qui peut directement être vu des numéros de pixels allumés), la résolution de trace et de point et l'effet de chargement de SiProt dans un environnement réel.

L'Octopuce avec des InGrid arrive à la limite de l'interface MUROS de huit puces. Une nouvelle interface est nécessaire pour construire des détecteurs à grande surface avec un ordre de grandeur de 100 puces Timepix. Il y a des efforts à Bonn, Mainz et au NIKHEF pour développer une nouvelle interface.

Concernant la puce Timepix, le Timepix2 est en développement au CERN. Une implémentation de lecture par l'arrière serait préférable pour éviter la surface morte de côté détecteur. Cela s'avère nécessaire pour obtenir la surface sensible maximale sur l'endplate qui comporte beaucoup de puces.

Pour la production des puces InGrid, le processus de fabrication doit être perfectionné. Les grilles sont très fragiles et des courants entre grille et Timepix ont été détectés. Parfois les puces étaient détruites, parfois le gain était limité. Pour l'instant les InGrids+Timepix étaient produits en petite série dans le laboratoire [Bla09]. L'automatisation de la fabrication et le développement de puces plus robustes sont des raisons pour des collaborations entre les groupes de Bonn et Twente et IZM (Fraunhofer-Institut für Zuverlässigkeit und Mikrointegration) à Berlin et le groupe de Saclay et LAAS (Laboratoire d'Analyse et d'Architecture des Systèmes) à Toulouse. La fabrication en grande série des InGrid sur le wafer est nécessaire pour la construction de détecteurs de grande surface. Dans ce mémoire, l'effet de la couche SiProt a été étudiée. Il a été constaté que le gain d'une structure InGrid dépend de la fréquence des avalanches. Si des structures InGrid étaient utilisées dans des régions de détecteur où des hautes fréquences sont espérées, un nouveau concept de protection de puces devrait être développé.

Zusammenfassung und Ausblick

In diesem letzten Kapitel werden die Ergebnisse der Diplomarbeit zusammengefasst. Den beiden Hauptgebieten der Arbeit wird dabei jeweils ein eigener Abschnitt eingeräumt (Abschnitt 6.5.1 und 6.5.2). Die anderen Ergebnisse wie der LASER Messstand und der Octopuce werden in Abschnitt 6.5 erläutert. Der letzte Abschnitt stellt einen Ausblick auf zukünftige Aktivitäten auf diesem Forschungsgebiet dar.

6.5 Zusammenfassung

Microstrukturierte Gasdetektoren (Micro Pattern Gaseous Detectors MPGS) sind neuartige, gasgefüllte Detektoren, deren Strukturen in der Größenordnung von einigen Mikrometern liegen. In unseren Experimenten wurde ein InGrid-Chip verwendet. Dieser Chip besteht aus einer hoch segmentierten, pixelierten Anode, die gleichzeitig das Auslesesystem des Detektors darstellt (Timepix-Chip). Der Timepix-Chip hat eine sensitive Fläche von $1.4 \times 1.4 \text{ cm}^2$. Das Ausgangssignal jedes einzelnen Pixels ist eine Anzahl von Zeitzyklen, die entweder der im Pixel deponierten Ladung (im Time Over Threshold, TOT-Modus) oder der Ankunftszeit der Ladung (im TIME-Modus) entsprechen. $50 \mu\text{m}$ über den Chip befindet sich ein Gitter, welches auf einem Potential von ca. 400 V liegt. Der gesamte Detektor befindet sich in einem Gasvolumen. In dem starken elektrischen Feld zwischen Gitter und Chip (Verstärkungsregion) werden primäre Elektronen, die durch die Löcher des Gitters eindringen, beschleunigt, sodass sie die Atome des Gases in der Lücke ionisieren und Sekundärelektronen erzeugen (Gasverstärkung). Die Elektronen dieser Ladungswave werden im Pixel gesammelt und von der angeschlossenen Elektronik gemessen. Der InGrid-Chip ist so aufgebaut, dass sich über jedem Pixel genau ein Loch des Gitters befindet, sodass sich die Ladungswave eines durch das Loch fliegenden Elektrons im zugehörigen Pixel niederschlägt. Die Primärelektronen stammen aus einem Gebiet oberhalb des Gitters (Ionisationsregion) und werden durch Konversion eines Röntgen-Photons im Detektorgas erzeugt. Mit einem elektrischen Feld werden die entstandenen Elektronen in Richtung des Gitters geführt. In unseren Versuchen stammen die Photonen meist aus einer radioaktiven Eisenquelle (^{55}Fe).

Das Ziel der Messungen war es zum einen, das Spektrum der Anzahl der Primärelektronen zu vermessen, zum anderen wurde der Prozess der Gasverstärkung zu untersuchen. Für erstere wurden die Primärelektronen durch Diffusion entlang des Driftweges zum Gitter aufgestreut, sodass nur im optimalen Fall nur noch ein Primärelektron durch ein Gitterloch gelangt. Jeder getroffene Pixel entspricht in diesem Fall einem primären Elektron. Bei hohen Gasverstärkungen kann es allerdings zur Ausbreitung der Elektronenlawine auf Nachbapixel kommen (charge sharing), sodass in den Messungen auch die Anzahl der Cluster (zusammenhängende Pixel) gezählt wurde.

Zur Untersuchung der Gasverstärkung wurde ebenfalls die hohe Diffusion ausgenutzt. Da ein Primärelektron durch ein Loch im Gitter gelangt entspricht die Anzahl der gemessenen Sekundärelektronen in der Elektronenlawine gerade dem Verstärkungsfaktor. Da es sich bei der Gasverstärkung jedoch um einen statistischen Prozess handelt schankt die Anzahl der erzeugten Sekundärelektronen. Ziel der Messungen war es, deren Verteilung bei verschiedenen Gasverstärkungen (bzw. entsprechenden Gitterspannungen) zu messen. Beschrieben werden diese Fluktuationen in erster Näherung durch eine Polya-Verteilung.

In Freiburg wurde von mir ein LASER-Messstand zur Charakterisierung von MPGDs aufgebaut. Bei diesem Aufbau werden Elektronen aus der Driftkathode ausgelöst, die dann als Primärelektronen dienen. Erste Messungen mit einem Aufbau bestehend aus GEM+Timepix wurden durchgeführt.

In Saclay wurde eine Trägerplatte entwickelt, welche mit acht InGrid-Chips bestückt werden kann. Es wurde gezeigt, dass die PCB Karten die InGrids mit Strom versorgen und die Daten transferieren können. Das Panel wurde erfolgreich mit dem MUROS Interface ausgelesen. Die Gitter der Detektoren waren auf Grund von Beschädigungen nicht in der Lage Gasverstärkungen von mehr als 2000 zu erreichen. Spuren von Cosmics wurden im Labor in ArIso 95/5 gemessen. Das Panel wird am DESY in den Großen Prototypen der LCTPC-Kollaboration eingebaut werden. Dort werden Messungen mit 6 GeV/c Elektronen durchzuführen.

Die Messungen mit einem einzelnen Chip wurden hauptsächlich in ArIso 95/5 durchgeführt. Messungen in ArIso 80/20 wurden auch durchgeführt, konnten jedoch nur beschränkte Ergebnisse liefern, da die Diffusion in dieser Mischung geringer ist. Andere Gase (CH_4 , CF_4 , $P10$) wurden ebenfalls verwendet. In diesen Gasen war eine höhere Gitterspannung nötig um eine ausreichende Gasverstärkung zu erreichen. Die Durchschlagwahrscheinlichkeit ist in diesen Gasen größer. Der Timepix-Chip G06-W0096 wurde über einen Zeitraum von einem Jahr als Auslese in einem InGrid-Detektor verwendet. Bei höchsten Gitterspannungen von 365V in ArIso 95/5 und insbesondere in einer P10 Gasmischung erlitt er zahlreiche Funkenüberschläge und Gasentladungen. Neun Spalten wurden während der Messungen zerstört. Das Verhalten der benachbarten Spalten wurde ebenfalls beeinflusst. Nach den stärksten Durchschlägen war eine Neukalibrierung und erneute Threshold Equalisierung nötig. Die Qualität des Chips (elektronische Rauschschwelle, Variationen des TOT nach der Equalisierung) wurde durch die Durchschläge nicht beeinflusst. Nach einer Neukalibrierung konnte der Chip weiter verwendet werden. Zwei Hauptfragestellungen wurden untersucht: Die Messung der Gasverstärkung und die Zählung einzelner Elektronen mit einem InGrid-Detektor.

6.5.1 Lawinenstatistik

Gegenüber einem Standard Micromegas Detektor ist bei einem Ingrid zusätzlich ist eine Schutzschicht (SiProt) nötig, um die Pixel vor Durchschlägen zu schützen. Diese Schicht führt zu einem unterschiedlichen Verhalten eines InGrid-Detektors im Vergleich zu einem Standard Micromegas Detektor. Die Gasverstärkung eines InGrid-Detektors wurde gemessen indem Primärelektronen der Photokonversion von ^{55}Fe Photonen benutzt wurden. Diese Messungen wurden mit den Ergebnissen eines Standard Micromegas Detektors verglichen. Gasverstärkungen bis herunter zu 50% im Vergleich zu einem Standard Micromegas-Detektor wurden in ArIso 95/5 gemessen. Die geringere Gasverstärkung der InGrid-Detektoren ist auf Ladungseffekte der SiProt-Schicht zurückzuführen. Es wurde eine Theorie entwickelt, die die Effekte der SiProt-Schicht beschreibt. Aus der Theorie konnten Spannungen auf der Oberseite der Schicht bis zu 20V bei einer Gitterspannung von 365V in ArIso 95/5 berechnet werden. Dies bedeutet, dass in diesem Fall die für die Gasverstärkung verantwortliche Spannung in der Verstärkungsregion lediglich 345V beträgt. Die Abschwächung der Gasverstärkung hängt stark von der Frequenz der Elektronenlawinen und damit verbundenen Aufladung der Schutzschicht ab. Eine Zeitkonstante in der Größenordnung von $\tau_{\text{theo}} = 1\text{min}$ wurde von der Theorie vorhergesagt. Eine Zeitkonstante von $\tau_{\text{meas}} = (1.27 \pm 0.05)\text{min}$ wurde gemessen indem ausgenutzt wurde, dass sich die Spannung an der Oberseite der SiProt-Schicht ändert, wenn sich die Rate der auftretenden Elektronenlawinen ändert. Diese Rate wurde verändert, indem die Quelle in einem weiteren Abstand vom Detektor platziert wurde. Bei geringsten Raten nähert sich die Gasverstärkung des InGrid-Detektors der des Micromegas-Detektors an. Die Gasverstärkung des InGrid Detektors kann aus den TOT-Werten berechnet werden und stimmt mit der Gasverstärkung eines Micromegas-Detektors überein, wenn die Auswirkungen der SiProt-Schicht berücksichtigt werden.

Der sogenannte Θ -Wert der an die Gasverstärkungsverteilung gefitteten Polya-Funktion wurde gemessen. Bei größter Gasverstärkung von 8777 ± 14 und 7902 ± 22 wurden Werte von $\Theta = 2.60 \pm 0.02$ beziehungsweise $\Theta = 2.68 \pm 0.04$ in den Gasverstärkungsverteilung gemessen. Eine Auswertung der Einzelelektronennachweiseffizienz des InGrid-Detektors deutet auf $0.5 \lesssim \Theta \lesssim 2$ für Gasverstärkungen von ≈ 2000 bis ≈ 5000 hin. Eine Abhängigkeit Θ s von der Gasverstärkung ist möglich.

Zum Vergleich der Gasverstärkung eines InGrid- und eines Micromegas-Detektors wurde die Gasverstärkung des Micromegas-Detektors in ArIso 95/5, ArIso 80/20, CH_4 , CF_4 , und $P10$ gemessen.

Der LASER-Messstand in Freiburg wurde zur Erzeugung einzelner Primärelektronen benutzt. Es wurden Tests mit niedriger Wiederholrate der Ladungslawinen durchgeführt, um die Abhängigkeit zwischen Rate und Gasverstärkung zu messen. Wegen eines elektrischen Stromes zwischen dem Gitter und dem Chip, die ihren Grund in Alterungsprozessen haben könnten, konnten keine quantitativen Messungen durchgeführt werden. Es gibt Anzeichen eines Abfalls der Gasverstärkung bei höchsten Raten.

6.5.2 Einzelelektronenzählung

Um die Anzahl der Primärelektronen in einer Konversion eines ^{55}Fe Photons in auf Argon basierenden Gasgemischen zu ermitteln ist eine hohe Diffusion nötig. Die größte Diffusion in einem Gas, welches eine stabile Messung erlaubte, wurde in ArIsO 95/5 erreicht. Das Spektrum der Anzahl getroffener Pixel und Cluster pro Elektronenwolke wurde aufgenommen. Verschiedene Schnitte wurden angewendet, unter anderem ein Schnitt auf die Größe der Elektronenwolke. Die Position des Photopeaks ändert sich für unterschiedliche Werte des Schnittparameters. Die Diffusion ist nicht ausreichend um alle Elektronen, die zu diesem Peak führen, aufzutrennen. Der Escapepeak wurde für die Analyse verwendet. Es wurden Tests bei unterschiedlichen Verhältnissen zwischen Drift- und Gasverstärkungsfeld und unterschiedlichen Gasflüssen durchgeführt um sicherzustellen, dass die verwendeten Parameter eines Feldverhältnisses um 100 und eines Gasflusses von 10 l/h einen optimalen Detektorbetrieb garantieren. Die Anzahl der Elektronen im Escapepeak wurde für unterschiedliche Gasverstärkungen untersucht (Einzelelektronenzählung). Eine Sättigung von 144 ± 1 getroffene Pixel und 117.9 ± 0.7 Cluster wurde gemessen. Es wird angenommen, dass die Anzahl der Cluster den Primärelektronen entsprechen und die Sättigung bei 100% Einzelelektronennachweiswahrscheinlichkeit eintritt. Für die höchste Gasverstärkung wurde eine Einzelelektronennachweiswahrscheinlichkeit von höher als 97.8% erreicht. MAGBOLTZ Simulationen führen zu einem Ergebnis von 116 Primärelektronen im Escapepeak.

Aus der Auflösung der Peaks lässt sich eine obere Schranke für den Fano Faktor berechnen. Die beste Auflösung wurde in einer Langzeitmessung gemessen. Es wurde eine Auflösung von $\text{FWHM}_{\text{photo}} = 9.73\%$ für den Photopeak und $\text{FWHM}_{\text{echap}} = 12.98\%$ für den Escapepeak erreicht. Die Grenzen für den Fano Faktor ergeben sich zu $F_{\text{echap}} \leq 0.31 \pm 0.02$ für den Escape- und $F_{\text{photo}} \leq 0.25 \pm 0.01$ für den Photopeak. In [Che09] ist eine obere Grenze von $F \leq 0.21 \pm 0.06$ angegeben.

6.6 Ausblick

Pixelierte Auslesestrukturen sind eine interessante Technologie für TPCs der nächsten Generation. Es wurde gezeigt, dass Pixelchips zusammen mit GEM und Micromegas Gasverstärkungsstrukturen funktionieren. Momentan ist es das Ziel großflächige Arrays von Timepix-Chips zu bauen. Zwei Module mit 4 Timepix-Chips, welche gleichzeitig ausgelesen wurde, wurde in Bonn gebaut und getestet. Als Gasverstärkung wurden GEMs benutzt. Die Module wurde in den Großen Prototypen der TPC am DESY eingebaut und damit Spuren von Elektronen aufgezeichnet. Die Auswertung ist noch in Gange. Erste Ergebnisse sind in [Bre10] aufgeführt.

Der Octopuce, der in dieser Arbeit vorgestellt wurde, wird wahrscheinlich Ende 2010 im Prototype am DESY getestet. Momentan können mit diesem Modul nur Gasverstärkungen bis 2000 erreicht werden da die InGrids beschädigt sind. Wenn diese Defekte repariert werden können könnten Spuren bei Gasverstärkungen um 5000 aufgezeichnet werden. Von den Auswertung dieser Messungen erwartet man interessante Ergebnisse zur Anzahl der Ionisationen pro Spurlänge (kann direkt aus der Anzahl der getroffenen Pixel erkannt werden), zur Punkt- und Spurauflösung und zur Auswirkung der SiProt Schicht in einer echten Detektorumgebung.

Mit dem Octopuce ist die Maximalzahl der mit dem MUROS Interfaces gleichzeitig auslesbaren Chips erreicht. Um großflächige Detektoren mit um 100 Timepix-Chips zu bauen ist ein neues Interface notwendig. In Bonn, Mainz und am NIKHEF gibt es Bestrebungen ein solches Interface zu bauen.

Auf der Seite der Chips wird am CERN gerade der Timepix2 entwickelt. Um Totfläche auf der Vorderseite zu vermeiden ist geplant alle notwendigen Verbindungen auf der Rückseite des Chips auszuführen. Dies ist nötig um so viel sensitive Fläche wie möglich auf einer Endplatte, die aus vielen Chips besteht, zu erhalten.

Was die Produktion von InGrid-Chips angeht muss der Herstellungsprozess verbessert werden. Die Gitter sind sehr zerbrechlich und es wurden Ströme zwischen Gitter und dem Timepix-Chip gemessen. In einigen Fällen führte dies zur Zerstörung des Chips, in andern war dadurch die Gasverstärkung eingeschränkt. Bisher wurden InGrid nur einzeln im Labor hergestellt [Bla09]. Die Automatisierung der Herstellung und die Entwicklung robusterer InGrids ist der Grund für die Zusammenarbeit der Gruppen in Bonn und Twente mit dem IZM (Fraunhofer-Institut für Zuverlässigkeit und Mikrointegration) in Berlin und der Gruppe in Saclay mit LAAS (Laboratoire d'Analyse et d'Architecture des Systèmes) in Toulouse. Die Massenproduktion von InGrids auf Wafer-Basis ist nötig, um große Detektorarrays bauen zu können.

In dieser Diplomarbeit wurde die Auswirkung der SiProt Schicht studiert. Es wurde gezeigt, dass die Gasverstärkung einer InGrid-Struktur von der Rate der Elektronenlawinen abhängt. Sollten InGrid-Strukturen in Regionen von Detektoren verwendet werden, in denen hohe Raten zu erwarten sind, muss ein neues Konzept zum Schutz des Chips entwickelt werden.

Bibliography

- [ABB+99] S.R. Amendolia, E. Bertolucci, M.G. Bisogni, U. Bottigli, A. Ceccopieri, M.A. Ciocci, M. Conti, P. Delogu, M.E. Fantacci, P. Maestro, V. Marzulli, E. Pernigotti, N. Romeo, V. Rosso, P. Rosso, A. Stefanini, and S. Stumbo. Medipix: a vlsi chip for a gaas pixel detector for digital radiology. *Nuclear Instruments and Methods in Physics Research Section A: Accelerators, Spectrometers, Detectors and Associated Equipment*, 422(1-3):201 – 205, 1999.
- [ABF77] S.I. Anisimov, V.A. Benderskii, and G. Farkas. Nonlinear photoelectric emission from metals induced by a laser radiation. *Soviet Physics Uspekhi*, 20(6):467, 1977.
- [Adl08] C. Adloff et al. Development of MicroMegas for a Digital Hadronic Calorimeter. *Proc. of Linear Collider Workshop Chicago*, 2008.
- [AKV67] G.D. Alkhozov, A.P. Komar, and A.A. Vorob'ev. Ionization fluctuations and resolution of ionization chambers and semiconductor detectors. *Nuclear Instruments and Methods*, 48(1):1 – 12, 1967.
- [Alk70] G.D. Alkhozov. Statistics of electron avalanches and ultimate resolution of proportional counters. *Nuclear Instruments and Methods*, 89:155 – 165, 1970.
- [Ams08] C. Amsler et al. (particle data group). *Physics Letters B667*, 1, 2008. and 2009 partial update for the 2010 edition.
- [Ang90] F. Angelini et al. Further progress in the development of the microstrip gas chamber. 4-9 October 1990. Prepared for ECFA Large Hadron Collider (LHC) Workshop: Physics and Instrumentation, Aachen, Germany.
- [Bam07] A. Bamberger et al. Readout of gem detectors using the medipix2 cmos pixel chip. *Nucl. Instr. Meth.*, A573, 361, 2007.
- [Bam08] A. Bamberger et al. Si-tpc with gems. <http://www.eudet.org/e26/e28/e615/e851/eudet-memo-2008-40.pdf>, 2008.
- [Bel03] D.S.S. Bello. Muros2 user's manual. *NIKHEF, Amsterdam*, July 2003.
- [Bla09] V.M. Blanc Carballo. *Radiation Imaging Detectors Made by Wafer Post-processing of CMOS Chips*. PhD thesis, Univ. of Twente, June 2009.
- [BLRS10] G.J. Barker, P.K. Lightfoot, Y.A. Ramachers, and N.J.C. Spooner. Optical readout tracking detector concept for future large volume liquid argon detectors. *Nuclear Instruments and Methods in Physics Research Section A: Accelerators, Spectrometers, Detectors and Associated Equipment*, 619(1-3):140 – 142, 2010. Frontiers in radiation physics and applications: Proceedings of the 11th International Symposium on Radiation Physics.
- [BR93] W. Blum and L. Rolandi. Particle detection with drift chambers. *Springer-Verlag Berlin Heidelberg*, 1993.
- [Bra07] J. Brau et al. International Linear Collider reference design report. 1: Executive summary. 2: Physics at the ILC. 3: Accelerator. 4: Detectors. 2007. ILC-REPORT-2007-001.
- [Bre10] C. Brezina et al. First data taking of the sitpc module at the large tpc prototype. *EUDET-Memo-2009-14*, February 2010.
- [Cam06] M. Campbell et al. GOSSIP: A vertex detector combining a thin gas layer as signal generator with a CMOS readout pixel array. *Nucl. Instrum. Meth.*, A560:131–134, 2006.
- [CBH+07] M. Campbell, R. Ballabriga, E. Heijne, X. Llopart, L. Tlustos, and W. Wong. Requirements/ideas/proposal for a future gas detector pixel readout device. *EUDET-Memo-2007-24*, November 2007.
- [Cha68] G. Charpak et al. The use of multiwire proportional counters to select and localize charged particles. *Nucl. Instrum. Methods* 62, 262, 1968.
- [Che09] M. Chefdeville et al. *Development of micromegas-like gaseous detectors using a pixel readout chip as collecting anode*. PhD thesis, Univ. of Twente, January 2009.
- [Col02] P. Colas et al. Electron drift velocity measurements at high electric fields. *Nuclear Instruments and Methods in Physics Research Section A: Accelerators, Spectrometers, Detectors and Associated Equipment*, 478(1-2):215 – 219, 2002.
- [Col10] P. Colas. Personal correspondence. 2010.
- [CRS70] G. Charpak, D. Rahm, and H. Steiner. Some developments in the operation of multiwire proportional chambers. *Nuclear Instruments and Methods*, 80(1):13 – 34, 1970.
- [Cze] Czech Technical University in Prague. <http://aladdin.utef.cvut.cz/ofat/Methods/TimePixCalibration/index.htm>.
- [Dea93] S.C. Deane et al. Field-effect conductance in amorphous silicon thin-film transistors with a defect pool density of states. *Journal of applied physics*, vol. 74, no11, pp. 6655-6666, 1993.
- [Deh08] K. Dehmelt. Status of the large tpc prototype. *EUDET-Memo-2008-46*, December 2008.

- [Dem04] Demtröder. *Kern-, Teilchen- und Astrophysik*. Springer, 2004.
- [Dem05] Demtröder. *Atome, Moleküle und Festkörper*. Springer, 2005.
- [Gar05] C. Garabatos et al. Mwpc rate capability measurements with an x-ray tube. *Scientific Report, FAIR-QCD-CBM-13*, 2005.
- [Gio96] Y. Giomataris. Micromegas: a high-granularity position-sensitive gaseous detector for high particle-flux environments. *Nucl. Instr. Meth.*, A376, 29, January 1996.
- [GS08] C. Grupen and B. Shwartz. *Particle Detectors*. Cambridge University Press, second edition, 2008.
- [HJP+06] T. Holy, J. Jakubek, S. Pospisil, J. Uher, D. Vavrik, and Z. Vykydal. Data acquisition and processing software package for medipix2. *Nuclear Instruments and Methods in Physics Research Section A: Accelerators, Spectrometers, Detectors and Associated Equipment*, 563(1):254 – 258, 2006. Proceedings of the 7th International Workshop on Radiation Imaging Detectors - IWORID 2005.
- [ILD09] ILD Concept Group. The international large detector. *Letter of intent*, 2009.
- [Köh10] M. Köhli. tba. Master's thesis, Universität Freiburg, November 2010.
- [LBC+07] X. Llopart, R. Ballabriga, M. Campbell, L. Flustos, and W. Wong. Timepix, a 65k programmable pixel readout chip for arrival time, energy and/or photon counting measurements. *Nuclear Instruments and Methods in Physics Research Section A: Accelerators, Spectrometers, Detectors and Associated Equipment*, 581(1-2):485 – 494, 2007. VCI 2007 - Proceedings of the 11th International Vienna Conference on Instrumentation.
- [Leg55] W. Legler. Zur Statistik der Elektronenlawinen. *Zeitschrift für Physik*, 140:221–240, March 1955.
- [Lin] Linearcollider. <http://www.linearcollider.org>.
- [Llo06] X. Llopart. Timepix manual v1.0. *CERN, Geneva, Switzerland*, August 2006.
- [NIK] NIKHEF. <http://www.nikhef.nl/pub/experiments/medipix/muros.html>.
- [Nyg75] D.R. Nygren. A time projection chamber - 1975. *presented at 1975 PEP Summer Study, PEP 198, and included in proceedings*, 1975.
- [Oed88] A. Oed. Position sensitive detector with microstrip anode for electron multiplication with gases. *Nucl. Instrum. Meth.*, A263:351–359, 1988.
- [Phy] Physicsmasterclasses. <http://www.physicsmasterclasses.org/exercises/keyhole/it/detectors/DELPHI.html>.
- [PRA85] PRA. *LN103 Nitogen LASER operating manual*, July 1985.
- [PS75] V. Palladino and B. Sadoulet. Application of classical theory of electrons in gases to drift proportional chambers. *Nuclear Instruments and Methods*, 128(2):323 – 335, 1975.
- [Ren07] U. Renz. Development of a gem bases gas detector with medipix2 pixel readout. Master's thesis, Universität Freiburg, March 2007.
- [RK41] M.E. Rose and S.A. Korff. An investigation of the properties of proportional counters. I. *Phys. Rev.*, 59(11):850–859, Jun 1941.
- [Sau97] F. Sauli. Gem: A new concept for electron amplification in gas detectors. *Nucl. Instr. Meth.*, A386, 531, 1997.
- [Sch10] H. Schindler. Personal correspondance. 2010.
- [Sil] Siliconfareast. <http://www.siliconfareast.com/sio2si3n4.htm>.
- [Sip79] H. Sipila. The Statistics of Gas Gain in Penning Mixtures. *IEEE Transactions on Nuclear Science*, 26:181–185, 1979.
- [Sny47] H.S. Snyder. *Phys. Rev.*, 72:181, 1947.
- [Umm08] M. Ummenhofer. Inbetriebnahme einer zeitprojektionskammer mit pixel-auslese. Master's thesis, Universität Bonn, July 2008.
- [Wag67] E.B. Wagner et al. Time-of-flight investigations of electron transport in some atomic and molecular gases. *J. Chem. Phys.* 47, 3138, 1967.
- [XCO] XCOM: Photon Cross Sections Databas NIST Standard Reference Database 8 (XGAM). <http://physics.nist.gov/PhysRefData/Xcom/Text/XCOM.html>.

Appendix A Primary electrons in the photo peak

In Figure 100 the number of clusters in the photo peak is shown as a function of the grid voltage. The function arrives at a plateau of 210.0 ± 0.7 clusters using the fit of a saturation function of the form $f(x) = c - \exp(a + bx)$. From Section 4.2.1 we know that the position of the photo peak changes to higher number of clusters when harder RmsCuts are applied. Moreover the photo peak is not at the right position in the spectrum that should be at double the value of electrons in the escape peak. This plateau is not the 100% single electron detection efficiency. The reason is that the diffusion is not big enough to separate all the electrons in for events in the photo peak.

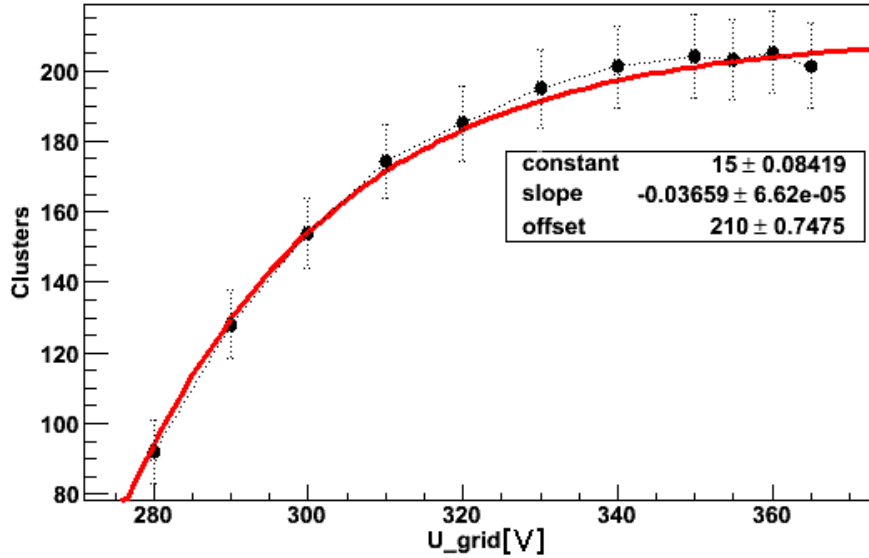


Figure 100. Clusters in the photo peak (RMS and Centre cut applied) as function of the grid voltage in Ar/Iso 95/5. Error bars are the rms of the escape peak. The error bars for the peak position (one cluster) would be smaller than the dots. For the fit a saturation curve of the form $f(x) = c - \exp(a + bx)$ was used. For the fit the error of the peak positions of one cluster was used

In Figure 101 the ratio of clusters consisting of one pixel to clusters consisting of two pixels is plotted. Higher values of cluster size ratio correspond to more size one clusters. For low grid voltages almost every cluster consists of one pixel. This is due to the fact that even in the photo peak the hit pixel density is low as not so many primary electrons are detected. For high voltages the cluster size ratio seems to saturate at a value of 6. An evidence that charge sharing effects are not prominent in the photo peak and that the size two and bigger clusters are mainly an effect of not enough diffusion is the following calculation.

Assuming there are just size one and size two clusters. Taking a saturation function of the form $f(x) = c - \exp(a + bx)$ and fitting it to the curve leads to a value of 210.0 ± 0.7 clusters in the photo peak as saturation value and a value of 6.0 ± 0.8 for the saturation of the cluster size ratio. The 210 clusters consist of size one and size two clusters. The number of size two clusters (#2) is

$$\#2 = \frac{210}{(1+6)} = 30. \quad (64)$$

The number of size one clusters (#1) is

$$\#1 = 210 - \#2 = 180. \quad (65)$$

The total number of hit pixels should be

$$\#1 + 2 \times \#2 = 180 + 2 \times 30 = 240 \quad (66)$$

A fit to the measured data in Figure 102 leads to 284 ± 2 pixels which is far more. To get this larger number of hit pixels the clusters need to contain more pixels. This means that the clusters with many pixels are concentrated in the photo peak. For low grid voltages the number of cluster (91.8) is almost the same as the number of hit pixels (98.2).

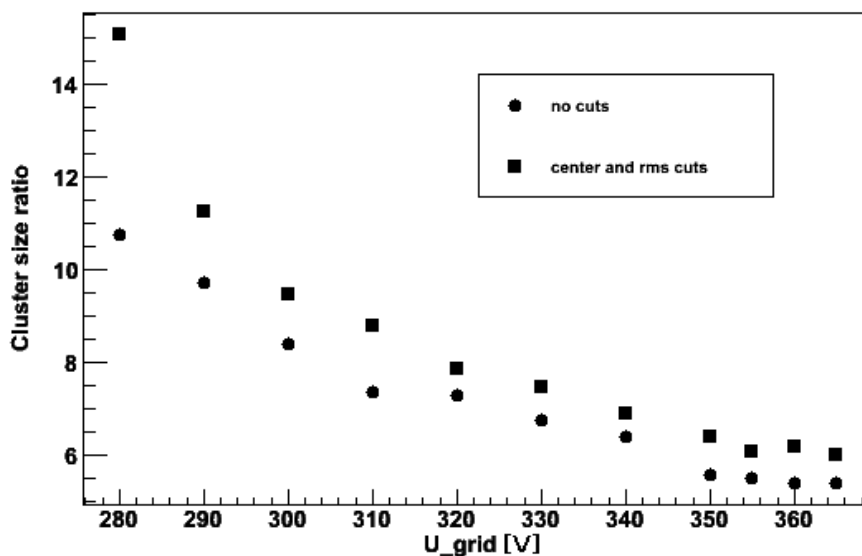


Figure 101. Ratio of clusters (without cuts) of size 1 to clusters of size 2 as function of the grid voltage in Ar/Iso 95/5

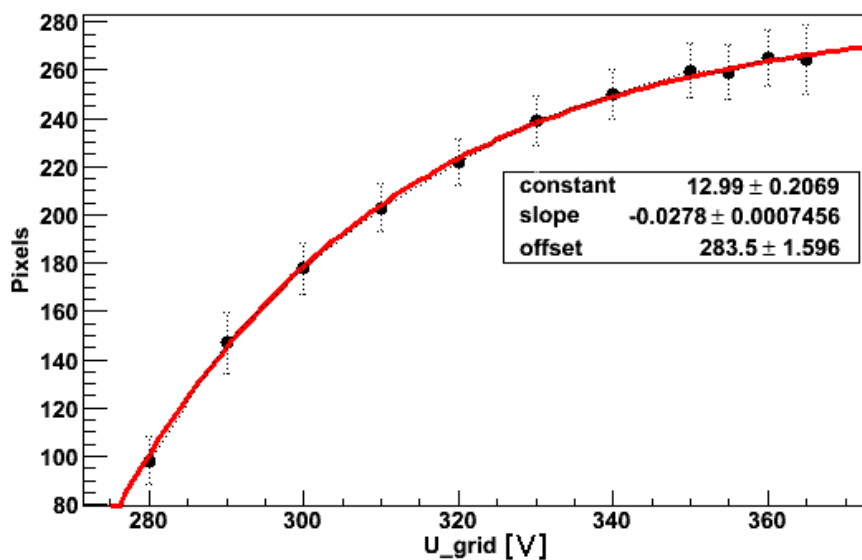


Figure 102. Pixels in the photo peak (RMS and Centre cut applied) as function of the grid voltage in Ar/Iso 95/5. Error bars are the rms of the escape peak. The error bars for the peak position (one pixel) would be smaller than the dots. For the fit a saturation curve of the form $f(x) = c - \exp(a + bx)$ was used. For the fit the error of the peak positions of one cluster was used.

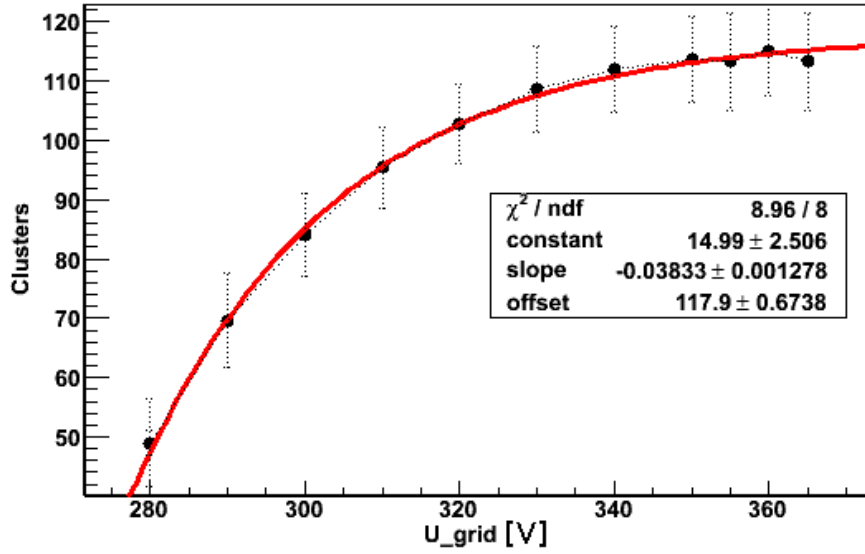


Figure 103. Clusters in the escape peak (RMS and Centre cut applied) as function of the grid voltage in Ar/Iso 95/5. Error bars are the rms of the escape peak. The error bars for the peak position (one cluster) would be smaller than the dots. For the fit a saturation curve of the for $f(x) = c - \exp(a + bx)$ was used. For the fit the error of the peak positions of one cluster was used.

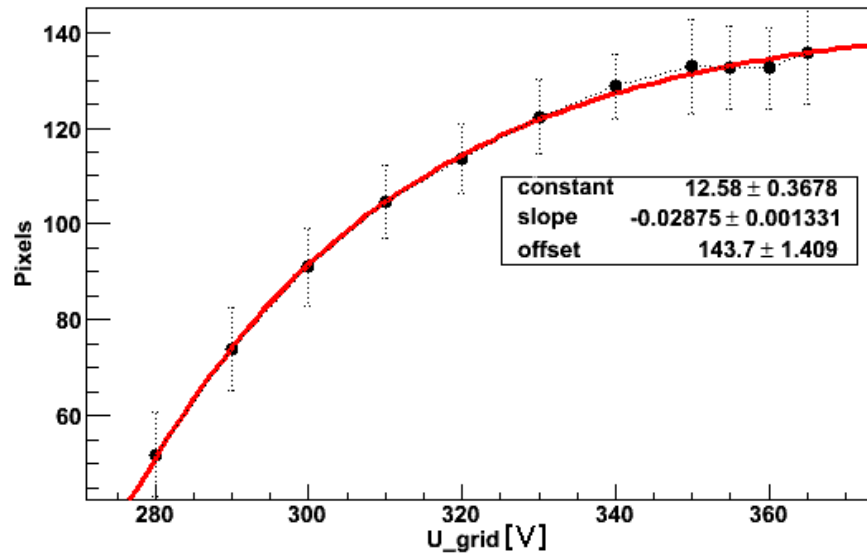


Figure 104. Pixels in the escape peak (RMS and Centre cut applied) as function of the grid voltage in Ar/Iso 95/5. Error bars are the rms of the escape peak. The error bars for the peak position would be smaller than the dots. For the fit a saturation curve of the for $f(x) = c - \exp(a + bx)$ was used. For the fit the error of the peak positions of one cluster was used.

For the escape peak the number of clusters saturates at 117.9 ± 0.7 , see Figure 103. For the number of pixels the saturation is not so clearly visible, see Figure 100. A fit with a saturation function leads to 144 ± 1 pixels. With the same calculation as before for the photo peak we arrive at

$$\#2 = \frac{117.9}{1+6} \approx 16.8 \quad (67)$$

size two pixels in the escape peak,

$$\#1 = 117.9 - 16.8 = 101.1 \quad (68)$$

size one pixels and

$$\#1 + 2 \times \#2 = 101.1 + 2 \times 16.8 = 134.7 \quad (69)$$

hit pixels if only size one and size clusters would contribute. This value is in better agreement with the measured number of hit pixels of 144 ± 1 . The conclusion is that in the escape peak the clusters are rather small and mainly consist of size one pixels. The hit pixel density is low and the number of clusters in the escape peak is a good approximation for the number of primary electrons.

Appendix B Long term measurements and temperature effects

Usually measurements for the data presented in this thesis was taken in a time not longer than two hours. However some long term effects have also been studied. In Figure 105 the mean of the Polya distribution (gain) is shown for a four day measurements. Every half an hour one data point was calculated. The grid voltages was set to $U_{\text{grid}} = 310V$ in ArIso 95/5. In the same Figure the temperature registered at the Saclay weather station at the same site is illustrated. A correlation between gain and temperature is visible. Higher temperatures lead, with some delay, to higher gains. A monitoring of temperature and pressure in the laboratory would be desirable.

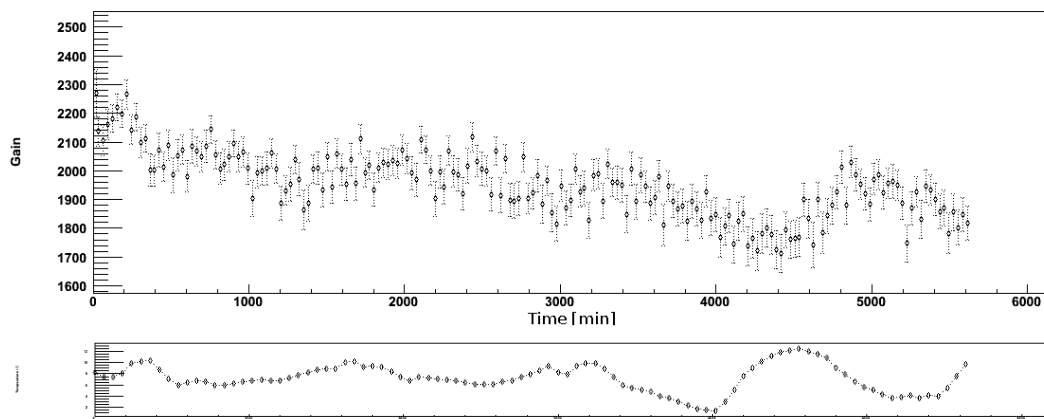


Figure 105. Long term measurements in ArIso 95/5 with $U_{\text{grid}} = 310V$, $U_{\text{cath}} = 2010V$, temperate data (bottom) from Saclay weather station

Appendix C SiProt influence on electric field without avalanches

In this section the effects in the protection layer when switching on the grid voltage are discussed. We will treat the area between the grid and the anode as a capacitor separated into two. One with vacuum permittivity $\varepsilon_{\text{vac}} = 1$ and one with permittivity ε . The equivalent circuit diagram is shown in Figure 106.

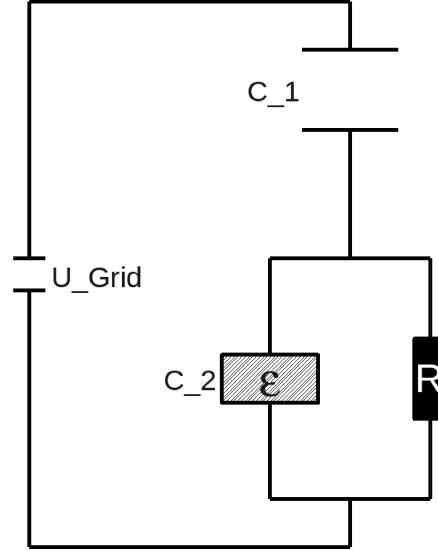


Figure 106. Equivalent circuit diagram of the amplification gap

At $t = t_0$ the voltage U_{Grid} will be switched on. The question now is what the voltage U_2 on the surface of the protection layer will be and the voltage $\Delta U = U_{\text{Grid}} - U_2$ responsible for the avalanche.

At $t < t_0$ the voltage on the surface of the protection layer will be $0V$ as everywhere else. When at $t = t_0$ the grid voltage is switched on the field lines will end on the protection layer. The dielectric will start to polarise. If it is be a perfect insulator we would have:

$$\frac{1}{C} = \frac{1}{C_1} + \frac{1}{C_2} \quad (70)$$

$$Q = C U_{\text{Grid}} = \text{const} \quad (71)$$

$$\Delta U = \frac{Q}{C_1} = \frac{C U_{\text{Grid}}}{C_1} = \frac{C_1 C_2}{C_1 + C_2} \frac{U_{\text{Grid}}}{C_1} = \frac{C_2}{C_1 + C_2} U_{\text{Grid}} \quad (72)$$

$$U_2 = \frac{C_1}{C_1 + C_2} U_{\text{Grid}} \quad (73)$$

The protection layer surface will be charged by the polarisation immediately ($t_0 + \Delta t$).

Now as the dielectric is not a perfect insulator but has a finite resistance R , there will be a current inside the dielectric until there are no more field lines inside the dielectric. This means that the surface voltage U_2 will return to $0V$ as the pixels are also on ground level. The capacitance C_2 will discharge via the resistance R with the time constant $\tau = RC$.

$$U_2(t_0 + \Delta t + t) = U_2(t_0 + \Delta t) \exp\left(-\frac{t}{\tau}\right) \quad (74)$$

For the voltage between the grid and the protection layer ΔU this means:

$$\Delta U(t_0 + \Delta t + t) = U_{\text{Grid}} - U_2(t_0 + \Delta t) \exp\left(-\frac{t}{\tau}\right) \quad (75)$$

The time constant $\tau = \varepsilon_0 \varepsilon \rho$ is of the order of one minute for a SiProt layer of Si_3N_4 .

Appendix D Measurement summary table

Date (yymmdd)	U_grid / V	U_kath / V	Mode	THL	Chrom foil, source in box	field cage	Chip	Acq.time /s	F_MUROS / MHz	Analysis with cut	Gas flux	Remark
091029		TOT calib		410, 405					35.89			
100106		TOT calib		410 (check if same as before)					35.99			
100106	280	2500	TIME	405	n	n	G06-W0096	0.000320		y	Ar/iso 95/5 5 l/h	
100106	280	2000	TIME	405	n	n	G06-W0096	0.000320	35.9857	y	Ar/iso 95/5 5 l/h	
100107	290	2000	TIME	405	n	n	G06-W0096	0.000320		y	Ar/iso 95/5 5 l/h	
100107	290	2000	TOT	405	n	n	G06-W0096	0.000320		y	Ar/iso 95/5 5 l/h	
100107	300	2000	TIME	405	n	n	G06-W0096	0.000320		y	Ar/iso 95/5 5 l/h	
100107	300	2000	TOT	405	n	n	G06-W0096	0.000320		y	Ar/iso 95/5 5 l/h	
100108	310	2020	TIME	405	n	n	G06-W0096	0.000320	35.97	y	Ar/iso 95/5 5 l/h	
100108	310	2020	TOT	405	n	n	G06-W0096	0.000320		y	Ar/iso 95/5 5 l/h	
100108	320	2030	TIME	405	n	n	G06-W0096	0.000320		y	Ar/iso 95/5 5 l/h	
100108	320	2030	TOT	405	n	n	G06-W0096	0.000320		y	Ar/iso 95/5 5 l/h	
100111	Ar bottle exchanged											
100111		TOT calib		405					0.000320			
100111	330	2040	TOT	405	n	n	G06-W0096	0.000320	35.86			
100111	330	2040	TIME	405	n	n	G06-W0096	0.000320	35.89	y	Ar/iso 95/5 10 l/h	
100112	340	2050	TOT	405	n	n	G06-W0096	0.000320		y	Ar/iso 95/5 10 l/h	
100112	340	2050	TIME	405	n	n	G06-W0096	0.000320	35.97	y	Ar/iso 95/5 10 l/h	
100112	345	2055	TIME	405	n	n	G06-W0096	0.000320	35.0967, 35.5648	y	Ar/iso 95/5 10 l/h	UVBackground strong 350 tried before (discharge)
100112	345	2055	TOT	405	n	n	G06-W0096	0.000320		y	Ar/iso 95/5 10 l/h	
100113	330	330	TOT	405	n	n	G06-W0096	0.000320		y	Ar/iso 95/5 0 l/h (blocked)	Noise
100113	290	2000	TOT	405	n	n	G06-W0096	0.000320		y	Ar/iso 95/5 0 l/h (blocked)	Noise
100113	310	2020	TOT	405	n	n	G06-W0096	0.000320		y	Ar/iso 95/5 0 l/h (blocked)	Noise
100113	330	2040	TOT	405	n	n	G06-W0096	0.000320		y	Ar/iso 95/5 0 l/h (blocked)	Noise
100113	330	0	TOT	405	n	n	G06-W0096	0.000320		y	Ar/iso 95/5 0 l/h (blocked)	Noise
100113	0	0	TOT	405	n	n	G06-W0096	0.000320		y	Ar/iso 95/5 0 l/h (blocked)	Noise
100113	330	2040	TOT	405	n	n	G06-W0096	0.000320		y	Ar/iso 95/5 0 l/h (blocked)	repeat of 100111 TOT
100113	350	2060	TOT	405	n	n	G06-W0096	0.000320		y	Ar/iso 95/5 0 l/h (blocked)	
100114	330	2040	TOT	405	n	n	G06-W0096	0.000100	35.97	y	Ar/iso 95/5 10 l/h	
100114	330	2040	TIME	405	n	n	G06-W0096	0.000320		y	Ar/iso 95/5 10 l/h	
100114	350	2060	TOT	405	n	n	G06-W0096	0.000100		y	Ar/iso 95/5 10 l/h	
100114	350	2060	TIME	405	n	n	G06-W0096	0.000320		y	Ar/iso 95/5 10 l/h	
100114	355	2065	TOT	405	n	n	G06-W0096	0.000100		y	Ar/iso 95/5 10 l/h	
100114	355	2065	TIME	405	n	n	G06-W0096	0.000320		y	Ar/iso 95/5 10 l/h	
100115	Install preamp for grid gain measurements											
100115	280	1990	TOT	405	n	n	G06-W0096	0.000100		y	Ar/iso 95/5 10 l/h	MCA, empty
100115	preamp deinstalled											
100115	310	1700	TOT	405	n	n	G06-W0096	0.000100		y	Ar/iso 95/5 10 l/h	
100118	320	1710	TOT	405	n	n	G06-W0096	0.000100		y	Ar/iso 95/5 10 l/h	
100118	330	1720	TOT	405	n	n	G06-W0096	0.000100		y	Ar/iso 95/5 10 l/h	
100118	340	1730	TOT	405	n	n	G06-W0096	0.000100		y	Ar/iso 95/5 10 l/h	
100118	UV Photon effect detected => cover detector from now on											
100118	340	1730	TIME	405	n	n	G06-W0096	0.000320		y	Ar/iso 95/5 10 l/h	
100118	340	1530	TIME	405	n	n	G06-W0096	0.000320	35.95	y	Ar/iso 95/5 10 l/h	
100120	340	930	TOT	405	n	n	G06-W0096	0.000100		y	Ar/iso 95/5 10 l/h	
100120	340	930	TIME	405	n	n	G06-W0096	0.000320		y	Ar/iso 95/5 10 l/h	
100120	340	2500	TIME	405	n	n	G06-W0096	0.000320	35.95	y	Ar/iso 95/5 10 l/h	
100120	340	2500	TOT	405	n	n	G06-W0096	0.000100		y	Ar/iso 95/5 10 l/h	
100120	340	1130	TIME	405	n	n	G06-W0096	0.000320		y	Ar/iso 95/5 10 l/h	
100121	340	1130	TOT	405	n	n	G06-W0096	0.000100	35.97	y	Ar/iso 95/5 10 l/h	
100121	340	1030	TOT	405	n	n	G06-W0096	0.000100		y	Ar/iso 95/5 10 l/h	
100121	340	1030	TIME	405	n	n	G06-W0096	0.000320		y	Ar/iso 95/5 10 l/h	
100127	300	2010	TIME	405	y	y	G06-W0096	0.000320		y	Ar/iso 95/5 10 l/h	
100127	340	1000	TIME	405	y	y	G06-W0096	0.000360	35.97	y	Ar/iso 95/5 10 l/h	
100127	280	2000	TIME	405	y	y	G06-W0096	0.000360		y	Ar/iso 95/5 10 l/h	
100128	290	2000	TIME	405	y	y	G06-W0096	0.000360	35.96	y	Ar/iso 95/5 10 l/h	
100128	290	2000	TOT	405	y	y	G06-W0096	0.000100		y	Ar/iso 95/5 10 l/h	
100128	310	2020	TIME	405	y	y	G06-W0096	0.000360		y	Ar/iso 95/5 10 l/h	
100128	310	2020	TOT	405	y	y	G06-W0096	0.000100		y	Ar/iso 95/5 10 l/h	
100128	320	2030	TIME	405	y	y	G06-W0096	0.000250		y	Ar/iso 95/5 10 l/h	
100128	320	2030	TOT	405	y	y	G06-W0096	0.000100		y	Ar/iso 95/5 10 l/h	over night
100129	330	2040	TOT	405	y	y	G06-W0096	0.000100		y	Ar/iso 95/5 10 l/h	
100129	330	2040	TIME	405	y	y	G06-W0096	0.000250		y	Ar/iso 95/5 10 l/h	
100129	340	2050	TOT	405	y	y	G06-W0096	0.000100		y	Ar/iso 95/5 10 l/h	
100129	340	2050	TIME	405	y	y	G06-W0096	0.000250		y	Ar/iso 95/5 10 l/h	
100129	350	2060	TOT	405	y	y	G06-W0096	0.000100	35.94	y	Ar/iso 95/5 10 l/h	

100129 Ar bottle exchanged, Chip H01-W0013 tested								Ar/iso 95/5 10 l/h			
100204	340	2050	TIME	405	y	G06-W0096	0.000250	y	Ar/iso 95/5 10 l/h		
100204	350	2060	TIME	405	y	G06-W0096	0.000250	y	Ar/iso 95/5 10 l/h		
100204	350	2060	TOT	405	y	G06-W0096	0.000100	y	Ar/iso 95/5 10 l/h		
100204	355	2065	TOT	405	y	G06-W0096	0.000100	y	Ar/iso 95/5 10 l/h		
100204	355	2065	TIME	405	y	G06-W0096	0.000250	y	Ar/iso 95/5 10 l/h		
100204	330	2040	TOT	405	y	G06-W0096	0.000100	y	Ar/iso 95/5 5 l/h	over night	
100205	330	2040	TIME	405	y	G06-W0096	0.000250	y	Ar/iso 95/5 5 l/h		
100205	330	2040	TIME	405	y	G06-W0096	0.000250	y	Ar/iso 95/5 20 l/h		
100205	330	2040	TOT	405	y	G06-W0096	0.000100	y	Ar/iso 95/5 20 l/h		
100205	330	2040	TIME	405	y	G06-W0096	0.000250	y	Ar/iso 95/5 30 l/h		
100205	330	2040	TOT	405	y	G06-W0096	0.000100	y	Ar/iso 95/5 30 l/h		
100129	340	2050	TIME	405	y	G06-W0096	0.000250	y	Ar/iso 95/5 30 l/h		
100205	330	930	TIME	405	y	G06-W0096	0.000250	y	Ar/iso 95/5 10 l/h	no peaks visible, harder centre cuts needed	
100208	330	930	TOT	405	y	G06-W0096	0.000100	y	Ar/iso 95/5 10 l/h		
100208	330	1030	TOT	405	y	G06-W0096	0.000100	y	Ar/iso 95/5 10 l/h		
100208	330	1030	TIME	405	y	G06-W0096	0.000250	y	Ar/iso 95/5 10 l/h	Cut z 10 center 20	
100208	330	1130	TOT	405	y	G06-W0096	0.000100	y	Ar/iso 95/5 10 l/h		
100208	330	1130	TIME	405	y	G06-W0096	0.000250	y	Ar/iso 95/5 10 l/h	Center 20	
100208	330	1230	TOT	405	y	G06-W0096	0.000100	y	Ar/iso 95/5 10 l/h		
100208	330	1230	TIME	405	y	G06-W0096	0.000250	y	Ar/iso 95/5 10 l/h		
100208	340	2050	TIME	405	y	G06-W0096	0.000250	y	Ar/iso 95/5 10 l/h	over night	
100209	330	1530	TOT	405	y	G06-W0096	0.000100	y	Ar/iso 95/5 10 l/h		
100209	330	1530	TIME	405	y	G06-W0096	0.000250	y	Ar/iso 95/5 10 l/h		
100209	330	1730	TOT	405	y	G06-W0096	0.000100	y	Ar/iso 95/5 10 l/h		
100209	330	1730	TIME	405	y	G06-W0096	0.000250	35.92	y	Ar/iso 95/5 10 l/h	
100210	330	2230	TOT	405	y	G06-W0096	0.000100	y	Ar/iso 95/5 10 l/h		
100210	330	2230	TIME	405	y	G06-W0096	0.000250	y	Ar/iso 95/5 10 l/h		
100210	330	2530	TOT	405	y	G06-W0096	0.000100	y	Ar/iso 95/5 10 l/h		
100210	330	2530	TIME	405	y	G06-W0096	0.000250	35.85	y	Ar/iso 95/5 10 l/h	
100211	355	2065	TOT	405	y	G06-W0096	0.000100	y	Ar/iso 95/5 10 l/h		
100211	355	2065	TIME	405	y	G06-W0096	0.000250	y	Ar/iso 95/5 10 l/h		
100211	360	2070	TOT	405	y	G06-W0096	0.000100	y	Ar/iso 95/5 10 l/h		
100211	360	2070	TIME	405	y	G06-W0096	0.000250	y	Ar/iso 95/5 10 l/h	Sparks: 1 dead collum	
100212	365	2075	TOT	405	y	G06-W0096	0.000100	y	Ar/iso 95/5 10 l/h	Sparks: 3 dead collums	
100212	365	2075	TIME	405	y	G06-W0096	0.000250	35.96	y	Ar/iso 95/5 10 l/h	
100212 DAC Threshold calibration, error in pixel matrix, chip recalibrated											
100222	270	1980	TIME	405	y	G06-W0096	0.000250	y	Ar/iso 95/5 10 l/h		
100222	275	1985	TIME	405	y	G06-W0096	0.000250	y	Ar/iso 95/5 10 l/h		
100222	280	1990	TIME	405	y	G06-W0096	0.000250	y	Ar/iso 95/5 10 l/h		
100222	285	1995	TIME	405	y	G06-W0096	0.000250	y	Ar/iso 95/5 10 l/h		
100223	265	1975	TIME	405	y	G06-W0096	0.000250	y	Ar/iso 95/5 10 l/h		
100223	260	1970	TIME	405	y	G06-W0096	0.000250	35.89	y	Ar/iso 95/5 10 l/h	
100223	340	2240	TIME	405	y	G06-W0096	0.000250	y	Ar/iso 80/20 10 l/h		
100223	350	2250	TIME	405	y	G06-W0096	0.000250	y	Ar/iso 80/20 10 l/h		
100223	360	2260	TIME	405	y	G06-W0096	0.000250	y	Ar/iso 80/20 10 l/h		
100223	370	2270	TIME	405	y	G06-W0096	0.000250	y	Ar/iso 80/20 10 l/h		
100224	380	2280	TIME	405	y	G06-W0096	0.000250	y	Ar/iso 80/20 10 l/h		
100224	390	2290	TIME	405	y	G06-W0096	0.000250	y	Ar/iso 80/20 10 l/h		
100224	400	2300	TIME	405	y	G06-W0096	0.000250	y	Ar/iso 80/20 10 l/h		
100224	410	2310	TIME	405	y	G06-W0096	0.000250	y	Ar/iso 80/20 10 l/h		
100224	420	2320	TIME	405	y	G06-W0096	0.000250	y	Ar/iso 80/20 10 l/h		
100225	430	2330	TIME	405	y	G06-W0096	0.000250	y	Ar/iso 80/20 10 l/h		
100225	440	2340	TIME	405	y	G06-W0096	0.000250	y	Ar/iso 80/20 10 l/h		
100225	450	2350	TIME	405	y	G06-W0096	0.000250	y	Ar/iso 80/20 10 l/h		
100225	460	2360	TIME	405	y	G06-W0096	0.000250	35.78	y	Ar/iso 80/20 10 l/h	
100329 DAC Threshold calibration, tot calib								35.9453, 35.9462, 39.9408, 35.9214			
100329	310	2020	TOT	405	source outsy	G06-W0096	0.000100	y	Ar/iso 95/5 10 l/h	filter problem, no data	
100330	310	2020	TOT	405	source outsy	G06-W0096	0.000100	y	Ar/iso 95/5 10 l/h	splitted in severnal runs, charging of Si	
100331	310	2020	TOT	405	source outsy	G06-W0096	0.000100	y	Ar/iso 95/5 10 l/h	over night	
100401	310	2020	TOT	405	source outsy	G06-W0096	0.000100	y	Ar/iso 95/5 10 l/h		
100401	310	2020	TOT	405	source outsy	G06-W0096	0.000100	y	Ar/iso 95/5 10 l/h		
100401	310	2020	TOT	405	source outsy	G06-W0096	0.000100	y	Ar/iso 95/5 10 l/h		
100401	310	2020	TOT	405	source outsy	G06-W0096	0.000100	y	Ar/iso 95/5 10 l/h		
100401	310	2020	TOT	405	source outsy	G06-W0096	0.000100	y	Ar/iso 95/5 10 l/h		
100402	310	2020	TOT	405	y	G06-W0096	0.000100	y	Ar/iso 95/5 10 l/h	4 days measurement	
100416	300	2010	TOT	405	y	G06-W0096	0.000100	35.9	y	Ar/iso 95/5 10 l/h	3 days measurement, sparks produced
100427	340	2050	TOT	405	y	G06-W0096	0.000100	35.9	y	Ar/iso 95/5 10 l/h	
100428	563	3350	TOT	405	y	G06-W0096	0.000100	y	CF4 6 l/h		

100428	520	3350	TOT	405	y	y	G06-W0096	0.000100	y	CF4 6 l/h		
100429	380	2080	TOT	405	y	y	G06-W0096	0.000100	y	P10 10 l/h		
100429	400	2100	TOT	405	y	y	G06-W0096	0.000100	y	P10 10 l/h		
100429	430	2130	TOT	405	y	y	G06-W0096	0.000100	y	P10 10 l/h		
100429	420	2120	TOT	405	y	y	G06-W0096	0.000100	y	P10 10 l/h	Heavy sparks 9 dead col	
100429	350	2050	TOT	405	y	y	G06-W0096	0.000100	y	P10 10 l/h	sparks: 2 dead collums	
100430 recalibration if chip after sparks, TOT calib, thl calib, new theta, theta of other chips, also for 60 MHz, MM gain curves												
100602	420	2320	TOT	405	y, source outsy	y	G06-W0096	0.000100	47.62	y	Ar/iso 80/20 10 l/h	source on directly after measurement
100602	420	2320	TOT	405	y, source outsy	y	G06-W0096	0.000100		y	Ar/iso 80/20 10 l/h	two sources, big away during measurement
100602	440	2340	TOT	405	y, source outsy	y	G06-W0096	0.001000		y	Ar/iso 80/20 10 l/h	only weak source U changed during measurement
100602	440	2340	TOT	405	y, source outsy	y	G06-W0096	0.001 for weak source 0.0001 for strong		y	Ar/iso 80/20 10 l/h	
100603 tot calib 47 mhz												
100607 tot calib 60 MHz thl calib												
100607	320	2020	TOT	405	y, source outsy	y	G06-W0096	0.001000	59.9917, 59.9968, 59.9	y	Ar/iso 95/5 10 l/h	
100607	330	2030	TOT	405	y, source outsy	y	G06-W0096	0.001000		y	Ar/iso 95/5 10 l/h	
100607	340	2040	TOT	405	y, source outsy	y	G06-W0096	0.001000		y	Ar/iso 95/5 10 l/h	
100607	300	2000	TOT	405	y, source outsy	y	G06-W0096	0.001000		y	Ar/iso 95/5 10 l/h	voltage changed at start
100608 preamps tested												
100608	300	2000	TOT	405	y, source outsy	y	G06-W0096	0.05		y	Ar/iso 95/5 10 l/h	
100609	320	2020	TOT	405	y, source outsy	y	G06-W0096	0.05		y	Ar/iso 95/5 10 l/h	
100609	330	2030	TOT	405	y, source outsy	y	G06-W0096	0.05		y	Ar/iso 95/5 10 l/h	
100609	340	2040	TOT	405	y, source outsy	y	G06-W0096	0.05		y	Ar/iso 95/5 10 l/h	
100610 CH4 connected, Gain measurements with MM												
100611	440	2500	TOT	405	y, source outsy	y	G06-W0096	0.05		y	CH4 8l/h	
100611	520	2500	TOT	405	y, source outsy	y	G06-W0096	0.05		y	CH4 8l/h	

Acknowledgement

Now it is finished! By the time you read this text I have handed in my Diploma thesis. Not only an exciting period of research but also six years of studies have come to an end! Now (or at least in two months) I can call myself a Dipl. Phys. Fortunately I did not have to manage that long time all alone. There were so many people who supported me on this path and during the time I worked on my thesis and I will not miss the chance to thank everybody.

First I want to thank the people who made it possible for me to do this Diplomarbeit and go to France to carry out the research. It is not very common to go abroad for the Diplomarbeit and a lot of obstacles had to be overcome. I thank my adviser at the University of Freiburg, Prof. Markus Schumacher for his support and confidence in me that a Diploma thesis is possible like that. I want to express my gratitude to Dr. Paul Colas who agreed to the cooperation and helped me to join TPC group at CEA Saclay. After the consent was given that we will start this project together, the bureaucracy and organisation had to be met. With the help of the Studiendekan of our faculty, Prof. Andreas Buchleitner, the "Fondation Alfred Kastler" and "Science Accueil" it was far easier to manage this process. For the financial help I am grateful to the DAAD and the "Verband der Freunde der Universität Freiburg".

But even before I went to Saclay I found excellent support at the start of my research period. This thesis would not have been possible without Uwe Renz. With his help at the very beginning of my project I found perfect access to our field of research. Uwe, you are a great person! It was always fun working with you. Don't forget 09-09!

An honourable mention goes to all my other colleges at the University of Freiburg, especially to Markus Köhli, for their candidness for my problems and their advice and help to solve them. I have had a great time with you and I will miss you.

I found an excellent environment for my research at CEA. But what would this help me without my the people there? Chers collègues, je voudrais vous remercier pour l'ambiance agréable. C'était un plaisir de travailler avec vous pendant ces derniers 9 mois. Ce séjour a été une formidable expérience pour moi. Merci à tous! En particulier je voudrais remercier ma "cobureautaire" Sephora (aussi pour le chocolat). C'était toujours plaisant de travailler avec toi.

What would I have done without my adviser Dr. David Attié? A big thank you for all the suggestion, support in the laboratory, ideas for the analysis and the french you taught me. Mes meilleurs vœux pour toi et ta famille!

I also want to thank all my advisors for the annotations and discussions before handing in this thesis.

I was also given the chance to participate in many meetings and conferences such that I got an insight into our collaboration. This was the first step into my own future as I got to know other people and groups working on the same subject. I thank Maxim Titov for his mentoring on how I can continue my scientific career.

I also want to thank all my advisors for the annotations and discussions before handing in this thesis.

During my time in Saclay there were also some people from other institutes who helped me with the progress of my own project. First I have to mention Yevgen Bilevych. Yevgen, you appeared in a time where my project was stuck. You brought the new InGrids and from that time on everything just worked perfect. But you also brought a lot of fun and advice and we had a blight night out in Paris.

Next there are our friends from the simulation side: Heinrich Schindler and Rob Veenhof. Heinrich, you can see some of your simulation results in my Diploma thesis and I hope that you can use some of my results in your thesis. Your stays at Saclay were always accompanied by big progress and new ideas.

I have been to Amsterdam so often and always found a nice atmosphere there. Thanks to our friends at NIKHEF: Joop Rövekamp, Jan Timmermans and in particular Martin Fransen.

Without the work of Maximilien Chefdeville my Diplomarbeit would not have been possible. His theses "Development of Micromegas-like gaseous detectors using a pixel readout chip as collecting anode", which is not by chance the most cited one here, is the fundament of my Diplomarbeit that is somehow a continuation of his work.

As I will continue working in this field of research we will hopefully meet from time to time. It will be a pleasure for me to work with all of you again!

I also have to mention my two native speakers for the French and English correction Amy Brogren and Sophie Renault. Thanks for the time you spend with my thesis even if you were busy with your own work.

Nine months in (or close to) Paris passed way too fast after I met such good friends. Discovering this beautiful city would not have been so funny as it was with you. I would like to thank Andreas, Daniela, Franzi, Judith, Julius, Lea, Lena, Marlene, Mille, Tini and all the others who are not mentioned here, aussi vous mes amis français, for the company and time we had together. Hopefully our friendship will never end and we will see each other again. Mädels und Andreas: Alors on a vécu chaque jour comme le dernier - parce qu'on vient de loin.

With the end of this thesis also my studies at the University of Freiburg come to an end. I can look back to exciting six years here in Freiburg. Sometimes it was not easy to cope with all the workload of the courses. Luckily I had such great fellow student and we were always a good team. Some of them became close friends. I will miss you when I leave Freiburg now but I know that we will stay in contact.

Freiburg would not have been so livable without my flatmates. Folks, you were my home and I can only write this sentences with tears in my eyes because I have to leave the WG Habsburg. I know I will never find a WG like ours again. I will miss you and at the moment I can not imagine to live without you.

But I also know that a new and interesting period of my life is waiting for me in Bonn and I am so curious. I hope you will all visit me there.

It is such a good feeling to know that there is a place and a family to go in the case that something does not work. Without that safe harbour I would never have been able to go on my adventurous trips to Aberdeen and Paris. Thank you for always being there for me!

Declaration

I hereby declare and confirm that this thesis is entirely the result of my own work except where otherwise indicated.

Je déclare sur l'honneur que ce mémoire a été écrit de ma main, sans aide extérieure sauf d'autres sources qui sont présentés comme tels.

Hiermit versichere ich, dass ich diese Arbeit selbständig verfasst und keine anderen als die angegebenen Hilfsmittel verwendet habe.

Freiburg, den _____

Michael Lupberger